Probing Inflationary Cosmology: The Atacama B-Mode Search (ABS)

Thomas Essinger-Hileman

A Dissertation

Presented to the Faculty

of Princeton University

in Candidacy for the Degree

of Doctor of Philosophy

Recommended for Acceptance

by the Department of

Physics

November, 2011

Abstract

Observations of the Cosmic Microwave Background (CMB) have provided compelling evidence for the Standard Model of Cosmology and have led to the most precise estimates of cosmological parameters to date. Through its sensitivity to gravitational waves, the CMB provides a glimpse into the state of the universe just 10^{-35} seconds after the Big Bang and of physics on grand-unification-theory (GUT) energy scales around 10^{16} GeV, some 13 orders of magnitude above the energies achievable by current terrestrial particle accelerators. A gravitational-wave background (GWB) in the early universe would leave a unique, odd-parity pattern of polarization in the CMB called B modes, the magnitude of which is characterized by the tensor-to-scalar ratio, r. A GWB is generically predicted to exist by inflationary theories, and the current generation of CMB polarization experiments will probe the interesting parameter space of $r < 0.05$ corresponding to single-field inflationary models at GUT scales.

I detail the design and construction of the Atacama B-Mode Search (ABS), which aims to measure the polarization of the CMB at degree angular scales where the primordial B-mode signal is expected to peak. ABS is a 145-GHz polarimeter that will operate from a high-altitude site in the Atacama Desert of Chile, consisting of a 60-cm crossed-Dragone telescope with cryogenic primary and secondary reflectors; an array of 240 feedhorn-coupled, transition-edge-sensor, bolometric polarimeters; and, a continuously-rotating, warm, sapphire half-wave plate (HWP) that will provide modulation of the incoming polarization of light.

In this thesis, I describe the optical, mechanical, and cryogenic design of the receiver,

including the reflector design, focal-plane layout, HWP design, and free-space lowpass filters. I describe physical-optics modeling of the reflector and feedhorn to validate the optical design. A matrix model that allows the calculation of the Mueller matrix of the anti-reflection-coated HWP for arbitrary frequency and angle of incidence is outlined. This will provide a framework for characterizing the ABS HWP in the field. Finally, the development of metal-mesh free space filters for ABS is described. ABS is anticipated to measure or place an upper limit on the tensor-to-scalar ratio at a level of $r \sim 0.03$.

Acknowledgements

The work described in this thesis would not have been possible without the support of many amazing people. First and foremost, I would like to thank my advisor, Lyman Page. His enthusiasm for what we do is infectious, and the genuine care he has for his students shows. I have learned much from Lyman about experimental techniques, cosmology, and life in general. At this point, I consider Lyman to be as much a friend as a mentor.

I also cannot thank Suzanne Staggs enough for all that she has taught me. I feel as if I have a second advisor in Suzanne. Despite all that she has on her plate, her door is somehow always open, and she is ever ready to discuss whatever problems are on my mind. Although he has now left Princeton for sunny Colorado, Joe Fowler also had a significant and positive effect on my graduate school career. I would like to thank Joe for many enjoyable talks around the espresso machine about everything from coffee-roasting tips to Ludwig's third definition.

My fellow graduate students in the research group at Princeton have helped make my work both productive and fun. I could not have asked for a better group of people to work with over the past five years. I am grateful to Ryan Fisher, Adam Hincks, Lewis Hyatt, Judy Lau, Mike Niemack, Glen Nixon, Eric Switzer, and Yue Zhao for being so welcoming to me when I joined the group. Thanks also to Emily Grace and Laura Newburgh – you have livened up the group considerably in the past year, as I am sure Akito Kusaka will as well. And most importantly John Appel, Lucas Parker, and Katerina Visnjic deserve special recognition. They have been great collaborators as we have built ABS over the past three years, but they have been even better friends. I will miss the many fun times we have

had at lab dinners and look forward to sharing some pisco sours in San Pedro with you.

When I started out at Princeton, I first worked on the Atacama Cosmology Telescope (ACT). The ACT collaboration was a ton of fun to work with. Beyond those already mentioned above, I would like to thank Mark Devlin, Rolando Dünner-Planella, Jeff Klein, Toby Marriage, Danica Marsden, Mike Nolta, Dan Swetz, and Bob Thornton. I learned a lot while working on ACT about millimeter-wave astronomy and operating a telescope at an altitude of 5200 meters - no easy task. Many in the collaboration were available to help debug problems with the telescope when I was oxygen-deprived late at night. I particularly appreciate those who were with me in Chile and made my trips to work on the telescope so enjoyable.

My work with ABS has benefited from the intellectual input of many people. I would like to thank the Quantum Sensors Group at NIST in Boulder, CO, which fabricates the detectors and SQUID readout chips for ABS. Kent Irwin and his group there seem to have an inexhaustible reservoir of ideas and helped shape much of the ABS instrument. Particular thanks to Jim Beall, Hsiao-Mei (Sherry) Cho, and Ki Won Yoon. At Princeton, Norm Jarosik has been the brainchild behind many essential ABS components and has been an endless source of expertise and knowledge on all things experimental. Bert Harrop, our master wirebonder, also aided greatly in the design and construction of the focal plane, helped by Stan Chidzik.

The ABS instrument would not exist without the excellent support staff at Princeton. I appreciate their professionalism and willingness to adapt to the whims of experimental physicists. I always enjoy my walks through A-level. Bill Dix, Glenn Atkinson, and Fred Norton in the Princeton machine shop have performed many marvels in building components of ABS. Steve Lowe and, previously, Mike Peloso in the student machine shop were fantastic resources when I needed to build something there. Geoff Gettelfinger, the department manager, has been invaluable in paving the way for us to do our work. I also got great help from Barbara Grunwerg, Claude Champagne, and previously Mary Santay in the purchasing department, as well as Darryl Johnson and previously John Washington in shipping and

receiving. Thanks to Ted Lewis for many laughs and to Angela Glenn for helping me finagle as many free meals as possible. Thanks to Jim Kukon for his expert crane operation. Abhi Gupta, Vinod Gupta, and Martin Kocinski provided very necessary computing support.

I am grateful to many others for making my time at Princeton enjoyable. Unfortunately, there are too many to name individually. I greatly enjoyed Friday beer, summer softball, and many BBQs with my fellow physics graduate students. Thanks to the members of the Popayan soccer team for many exciting games. Particular thanks to Sean Long for being the best roommate a guy could ask for. Thanks to the others in the Puerto Rico crew – Emma Bassein, Alan Johnson, Colin Parker, Audrey Sederberg, and Ben Sonday – for many tropical times. Thanks to Brian and Karen Ellis for Saturdays watching college football and a lot of good homebrew shared.

To Laura Blue, thank you for making my last year at Princeton so special, and for keeping me sane while I finished up this thesis. I love you.

Finally, I only got to Princeton in the first place due to the love and support of my family. Thanks to my grandparents Bill and Elaine Hileman and Don and Letha Essinger, and to all my extended family – aunts, uncles, and cousins. Thanks to my sisters Beth and Laura. It was great growing up with you. And I owe the biggest debt of gratitude to my parents Doug and Sandy, who have invested countless hours ensuring that I had all the tools I would need to succeed.

Contents

List of Figures

List of Tables

Chapter 1

Introduction

Cosmology is aimed at understanding the nature and origin of our universe. Cosmological questions have intrigued humankind for millenia, but only in the past two decades have observations of the cosmos become sensitive enough to allow for quantitative questions about the contents and evolution of the universe to be addressed. A coherent theoretical framework now exists that fits all known data well enough to be called a "Standard Model of Cosmology." This model applies general relativity, as well as nuclear and particle physics, to the universe as a whole. Cosmologists now firmly believe that:

The Universe is expanding. Edwin Hubble first showed in 1929 that other galaxies in our local neighborhood were receding away from us with a velocity that was roughly proportional to the distance to them [41]. This is what one would expect in a uniformly-expanding, homogeneous universe described by a Friedmann-Robertson-Walker (FRW) metric:

$$ds^2 = -dt^2 + a^2(t)\left[\frac{dr^2}{1-\kappa r^2} + r^2 d\Omega^2\right] \tag{1.1}$$

This equation has three distinct families of solutions for $\kappa = -1, 0, 1$, which describe closed, flat, and open spacetimes, respectively. All time-evolution is contained in the scale factor $a(t)$, which obeys the Friedmann equations:

$$H^2 = \left(\frac{\dot{a}}{a}\right)^2 = \frac{8}{3}\pi\rho - \frac{\kappa}{R^2} \tag{1.2}$$

$$\dot{\rho} = -3H\left(\rho + p\right) \tag{1.3}$$

These equations, along with the equations of state, $\rho\left(a\left(t\right)\right)$ and $p\left(a\left(t\right)\right)$ for the constituents of the universe, determine the evolution of the scale factor, a. The equations of state of the components of the universe are generally parametrized as

$$\rho \propto a^{-n} = a^{-3(w+1)}. \tag{1.4}$$

With this parametrization, non-relativistic matter has $w = 0$, $\rho \propto a^{-3}$; photons or relativistic species have $w = 1$, $\rho \propto a^{-4}$; and dark energy must have $w < -1/3$. If dark energy were vacuum energy, this would mean that $w = -1$ and $\rho \propto$ constant. The curvature of space, while not actually an energy density at all, sometimes has a fictitious energy density associated with it that has $w = -1/3$, $\rho \propto \kappa a^{-2}$, where κ is -1, 0, or 1 for open, flat, and closed universes.

The current best direct measurements of the Hubble Constant today, H_0, come from observations of "Standard Candles" outside our local group, so that specific velocities do not dominate the measurement, but not so far away that H will have evolved significantly. The most important standard candles are Cepheid variables and Type Ia supernovae. Both of these astronomical objects have well-calibrated absolute luminosities. By measuring their observed luminosity, one can estimate their distance from Earth. This method has yielded a measurement of the Hubble Constant of 73.8 $\pm$ 2.4 km s^{-1} Mpc^{-1} [80]. Assuming a flat universe, one can also derive H_0 from measurements of CMB anisotropies. The current best constraint on H_0 from the CMB comes from the Wilkinson Microwave Anisotropy Probe (WMAP), which estimates a value of 71.0 $\pm$ 2.5 km s^{-1} Mpc^{-1} [54], in agreement with the value inferred from distance measurements.

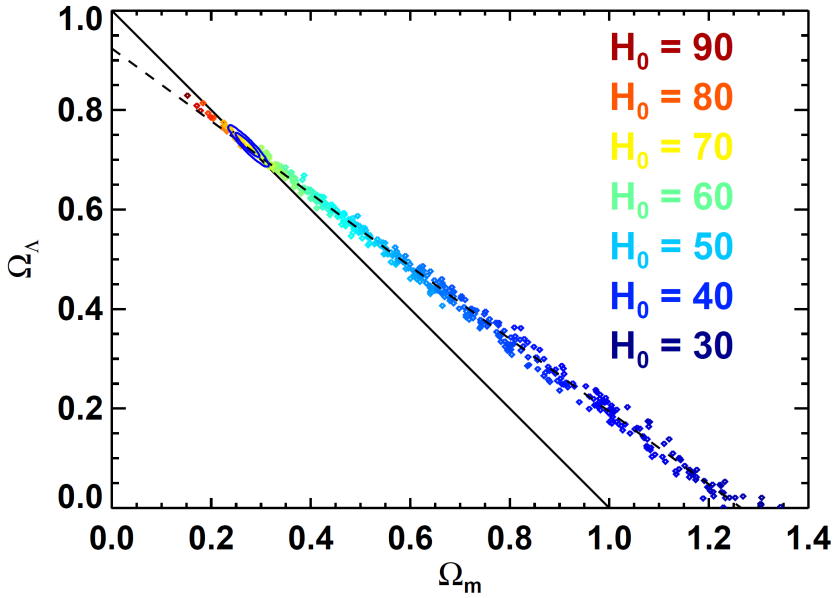

Figure 1.1: Constraints on Ω_Λ and Ω_m from WMAP seven-year data. The black line shows values consistent with a flat universe, while the colored dots show simulations for various values of H_0 indicated by their color. The units are km s^{-1} Mpc^{-1}. Combining CMB data with other probes of H_0 strongly favor a flat universe. Figure from [54]

The Universe is flat If one takes the value of H_0 from distance measurements as given, WMAP measurements of the CMB temperature anisotropies can be used to place constraints on the curvature of the universe. Inferring the redshift of the surface of last scattering from H_0, one can use the angular scale of the first acoustic peak in the CMB anisotropies to estimate the physical distance to the surface of last scattering. Assuming that w=-1 for Dark Energy and $H_0 = 73.8$, this constrains the curvature of the universe to be $-0.0178 < \Omega_\kappa < 0.0063$, consistent with a flat universe.

The early universe was hot, dense, and remarkably homogeneous. The discovery of the Cosmic Microwave Background (CMB) by Penzias and Wilson in 1958 was strong confirmation of the basic "Hot Big Bang" model of the universe. This uniform bath of radiation has a nearly perfect blackbody spectrum corresponding to a temperature of 2.725 ± 0.001 K (68% confidence), as measured by the COBE FIRAS

instrument [65]. This radiation is remnant light from decoupling, when neutral atoms were first able to form approximately 400,000 years after the Big Bang. The CMB is a particularly clean probe of the state of the universe at that early stage, and it shows that the universe was homogeneous at the level of one part in 100,000 at that time. It also shows that the universe contained a spectrum of density fluctuations that, under the influence of gravity, seeded the formation of the stars, galaxies, and clusters of galaxies that we see around us.

Most of the matter in the universe is dark. From galaxy rotation curves and probes of galaxy cluster dynamics, it has been suspected for some time that most of the matter in the universe is not visible. Measurements of cosmic abundances of light elements, most notably deuterium, suggest that the baryon density is only a small fraction of the critical density. Observations of the CMB now strongly confirm this picture. The angular power spectrum of the CMB (See Figure 1.2) exhibits a series of peaks and troughs that correspond to acoustic oscillations of the coupled photon-baryon plasma in the early universe. The peaks occur at those angular scales that have had a chance to oscillate a half-integer number of times from the Big Bang to decoupling. An overdense region will initially become denser under the force of gravity, until the photon pressure becomes great enough to reverse the flow of matter into the overdense region. Photon pressure then pushes matter out of the region until it is rarefied. The first peak at ℓ of 200 corresponds to that scale that just became overdense at decoupling. The second peak is the scale that was able to become overdense and then rarefied by decoupling, and so on. The dark matter, however, does not oscillate with this plasma. Overdense regions of dark matter simply become more and more dense over time. This means that the dark matter overdensity, which is not oscillating in this way, is augmented by the baryon density for the odd peaks, but is reduced for the even peaks. The relative heights of the odd peaks to the even peaks, and particularly the relative height of the first peak to the second and third peaks, allow a sensitive measurement of the baryon and dark matter densities from

the temperature power spectrum of the CMB.

Dark energy comprises about 73% of the effective energy density of the universe.

Observations of Type Ia supernovae provide a direct measurement of the expansion history of the universe. As mentioned above, Type Ia supernovae have well-characterized absolute luminosities that allow measurements of apparent luminosities from our position on Earth to provide a measurement of the distances to the supernovae. Type Ia supernovae can reach luminosities great enough to outshine their entire host galaxies, allowing them to be seen farther away than other standard candles. Observations of large numbers of Type Ia supernovae give strong evidence that our universe has entered a period of accelerated expansion. This accelerated expansion is driven by the so-called "dark energy."

The nature of dark energy is not known, though current observations place constraints on its equation of state, w. A combination of CMB, baryon acoustic oscillation, and Hubble constant measurements with Type Ia supernova observations imply that dark energy has w = -1.013$^{+0.068}_{-0.073}$ [89].

With suitable initial conditions and assumptions concerning the energy content of the universe, the observed properties of our universe can be reproduced within the framework of known physics. The expansion and cooling of the universe led to a series of phase changes: the formation of light nuclei in Big Bang Nucleosynthesis; the formation of neutral atoms and decoupling of the Cosmic Microwave Background (CMB); the clumping of matter into stars and galaxies via gravitational instability; and the re-ionization of the gas in the universe. The CMB has provided the most precise tests of the Standard Model to date. The current best-estimate parameters from WMAP 7-year data release are shown in Table 1.

Table 1.1: Best-Fit ΛCDM Parameters for a Flat Universe from WMAP 7-Year Data

Parameter	Description	Value
Fit Parameters		
$10^2\Omega_b h^2$	Baryon Energy Density	$2.258^{+0.057}_{-0.056}$
$\Omega_c h^2$	Cold Dark Matter Density	0.1109 ± 0.0056
Ω_Λ	Dark Energy Density	0.734 ± 0.029
$\Delta^2_{\mathcal{R}}$	Curvature Perturbation Amplitude	$(2.43 \pm 0.11) \times 10^{-9}$
n_s	Spectral Tilt	$0.963^{+0.014}_{-0.015}$
τ	Optical Depth to Recombination	0.087 ± 0.017
Derived Parameters		
t_0	Age of the Universe	13.75 ± 0.13 Gyr
H_0	Current Hubble Constant	71.0 ± 2.5 km/s/Mpc
σ_8	Amplitude of Fluctuations on 8 h^{-1} Mpc scale	0.801 ± 0.030
Ω_b	Baryon Density	0.0449 ± 0.0028
Ω_c	Cold Dark Matter Density	0.222 ± 0.026
z_{eq}	Redshift of Matter-Radiation Equality	3196^{+134}_{-133}
z_{re}	Redshift of Reionization	10.5 ± 1.2

1.0.1 Initial Conditions and Inflation

While the Standard Model is consistent with essentially all observations, it implies that we live in a special type of universe. The universe appears to be flat to roughly one part in 100, and as evidenced by CMB observations, the universe is also remarkably homogeneous on the largest scales. This is puzzling because no causal contact should have been possible on such large scales throughout the age of the universe. A number of theories of the very early universe have been put forth to address these problems, including inflationary and cyclic models.

Inflationary theories posit that the universe went through a brief stage of exponential expansion in the first 10^{-34} seconds after the Big Bang. Inflation blows quantum fluctuations, which were initially in causal contact, up to cosmological scales. This explains the homogeneity of the universe, and simultaneously gives an explanation for the origin of the inhomogeneities that seeded cosmic structure. Inflation also has the effect of flattening any curvature that the universe may have had.

Inflation is compelling for the reasons listed above, but it lacks a clear connection with other physics. One key prediction of the theory – the existence of a nearly, but not quite, scale-invariant spectrum of scalar perturbations – has been observed. However, a generic prediction of inflationary theories is that along with scalar perturbations that seed density fluctuations in the primordial plasma, tensor perturbations of the metric would also be produced. These tensor perturbations take the form of gravitational waves that would affect both the temperature anisotropies of the CMB and its polarization. The tensor-to-scalar ratio, r, is the level of tensor perturbations divided by scalar perturbations. The value of r in inflationary theories depends only on the characteristic energy scale at which it occurred. For the most straightforward single-field inflationary models, the energy scale of inflation goes as $r^{1/4}(2 \times 10^{16}$ GeV) [61].

A gravitational-wave background (GWB) from an early inflationary epoch would leave an imprint on both the CMB temperature anisotropies and polarization. A GWB would raise the level of low-ℓ temperature anisotropies, and to date the best constraints on r come from CMB temperature anisotropy measurements combined with BAO and Type Ia supernovae measurements setting a limit of $r < 0.20$ at 95% confidence [49]. However, the tensor-to-scalar ratio is degenerate with the tilt of the primordial spectrum of scalar fluctuations, making further refinement of GWB measurements via CMB temperature anisotropies alone difficult. The CMB polarization offers a particularly clean probe of r, as a GWB would leave a unique odd-parity pattern of polarization in the CMB that scalar perturbations cannot. The decomposition of CMB polarization into even- and odd-parity modes will be described in the next section.

Constraints on r from CMB polarization alone place a limit of $r < 0.72$ from the BICEP instrument [16]. The upcoming generation of CMB polarimeters will probe the interesting parameter space of $r < 0.20$ and test whether inflation occurred around the grand-unified scale of around 10^{16} GeV. ABS promises to measure the tensor-to-scalar ratio down to a level of $r \sim 0.03$. This will constrain the energy scale of inflation to be less than 0.8×10^{16} GeV. Incredibly, measurements of the low-energy, large-scale properties of the universe via

the CMB polarization can shed light on micro-physics at energies that are some 13 orders of magnitude above the reach of today's terrestrial particle accelerators! A measurement of a primordial GWB would not only be important support for inflationary theories, but would also constitute independent confirmation of the existence of gravitational waves and would provide a link between gravity and quantum processes in the early universe.

1.1 The Cosmic Microwave Background

1.1.1 CMB Temperature Anisotropies

The CMB is one of the richest sources of information available to cosmologists. The CMB that we observe today was last scattered approximately 400,000 years after the Big Bang and has streamed to us nearly unchanged from that point onward. While it is nearly perfectly homogeneous, the 2.725 K CMB does have temperature anisotropies at the level of 50μK. At large angular scales, the hot and cold spots in the CMB temperature correspond to under- and over-dense regions in the early universe, respectively. This is primarily due to the blue-shifting of CMB photons as they come down a gravitational potential hill or the corresponding red-shifting as they climb out of a gravitational potential well. As such, the CMB carries information about the distribution of matter and radiation in the universe at decoupling.

Whether or not the CMB is hot or cold at a given spot on the sky does not carry any useful cosmological information. Rather, it is the statistics of the CMB temperature anisotropies that carry information. In particular, the distribution of angular scales for the CMB temperature fluctuations carries information about the composition of the universe, the current age of the universe, the age of the universe at decoupling, and the initial distribution of scalar and tensor fluctuations. Many of these parameters are degenerate when considering the CMB temperature anisotropies alone; however, these degeneracies can be broken when CMB data are combined with other probes of cosmology such as galaxy redshift surveys, measurements of the current Hubble constant, Lyman α-Forest observations

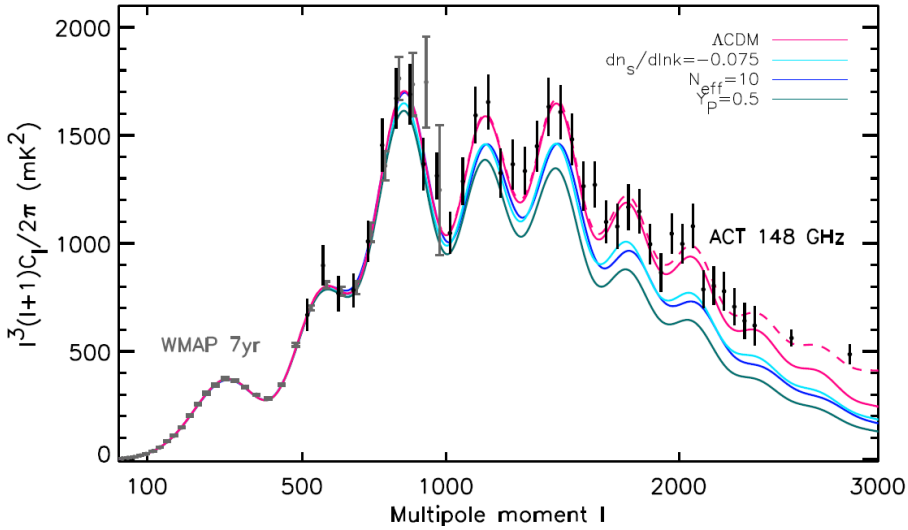

Figure 1.2: The CMB temperature power spectrum as measured by WMAP and ACT from [25]. The light grey points are from the WMAP seven-year data release [54]. The black points are from the ACT 148 GHz array. The best-fit ΛCDM model is shown, along with models incorporating a running of the spectral index $dn_s/dlnk = -0.075$, the number of relativistic species $N_{\rm eff} = 10$, and a ^{4}He fraction $Y_p = 0.5$, all of which are excluded with greater than 95% confidence by ACT data. The dashed line shows the best-fit unlensed CMB signal. The y axis has been multiplied by ℓ^2 to highlight the acoustic peaks.

and Type Ia supernovae observations. To characterize their statistical properties, the CMB temperature anisotropies on the celestial sphere are expanded using spherical harmonics, $Y_{\ell m}$ as

$$T(\hat{n}) = \sum_{\ell,m} a_{\ell m} Y_{\ell m}. \tag{1.5}$$

The CMB temperature power spectrum is derived from these by summing over all values of m for a given multipole ℓ. Higher values of ℓ correspond to smaller angular scales. The CMB temperature spectrum as measured by WMAP and the Atacama Cosmology Telescope (ACT) is shown in Figure 1.2.

1.1.2 CMB Polarization and the E/B Decomposition

Polarization in the CMB, whether sourced by scalar or tensor modes, is created by anisotropic Thomson scattering of CMB photons off of electrons at the surface of last scattering. A schematic of how polarization is generated in the CMB is shown in the left panel of Figure 1.3. Photons traveling perpendicular to our line of sight can only scatter one linear polarization, for which the electric field of the photon is oriented perpendicular to the direction of propagation and perpendicular to our line of sight. If a local quadrupole moment exists in the radiation field seen by an electron such that there are hot spots above and below the electron, and cold spots to the left and right, then more power will be radiated from the electron with horizontal linear polarization, leading to net observed linear polarization in the CMB.

While the mechanism for generating polarization is the same for both scalar and tensor modes, the symmetry properties of the resultant all-sky polarization pattern will be quite different. Scalar modes can only produce polarization patterns that are even-parity, while tensor modes can produce both even- and odd-parity patterns. One can search for the presence of a GWB background in the early universe by decomposing the polarization pattern on the sky into even- and odd-parity modes, also called E- and B-mode polarizations due to their similarity to the curl-free electric field and the divergence-free magnetic field. The Q and U Stokes parameters of the CMB polarization at each point on the sky can be combined and a decomposition performed in terms of spin-2 spherical harmonics, ${}_{\pm2}Y_{\ell m}$, such that

$$(Q \pm \imath U)(\hat{n}) = \sum_{\ell,m} (a_{\pm2,\ell m})_{\pm2}Y_{\ell m} = \sum_{\ell,m} (E_{\ell m} \pm \imath B_{\ell m})_{\pm2}Y_{\ell m}, \tag{1.6}$$

where Q and U are defined relative to a suitable spherical coordinate system such as galactic latitude and longitude. The Stokes parameters will be defined in greater detail in Section 2.1. On a sphere, the Stokes Q parameter gives the linear polarization along or perpendicular to lines of longitude, whereas the Stokes U parameter gives the linear polarization at $\pm 45°$. The $\mathrm{E}_{\ell m}$ and $\mathrm{B}_{\ell m}$ parameters can be estimated from polarization maps and power spectra

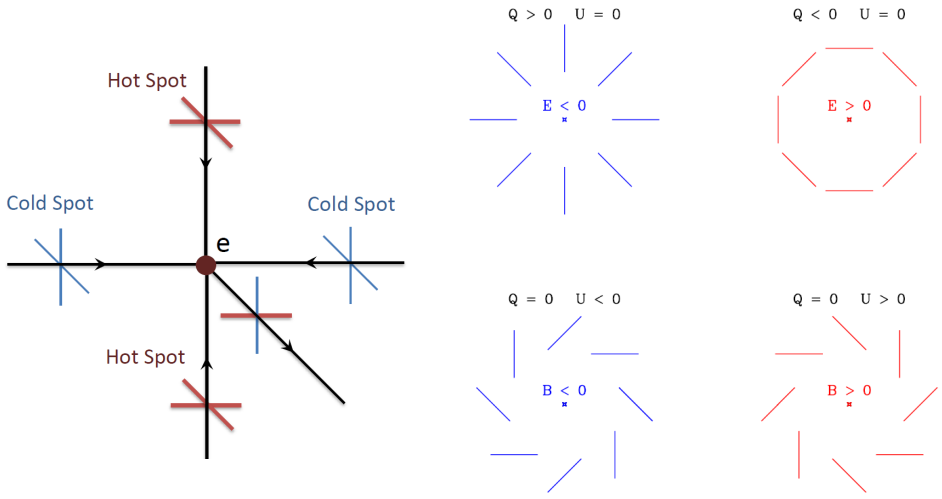

Figure 1.3: *Left:* Schematic showing the generation of CMB polarization from a local quadropole moment in the (unpolarized) radiation field seen by an electron at the surface of last scattering. Hot spots above and below the electron only scatter horizontal polarization, whereas cold spots to the left and right scatter only vertical polarization. The net result is a net horizontal linear polarization in the CMB. *Right:* Pure E- and B-mode polarization patterns. Note that the E-mode patterns remain unchanged upon reflection about a line through the center, while the B-mode patterns change sign. The Stokes Q and U parameters are defined in this figure relative to lines radiating outward from the center. Polarization which is pure Q has its electric-field vector oscillating either radially ($Q > 0$) or azimuthally ($Q < 0$). Pure U polarization states have electric-field vectors oscillating at $\pm 45°$. Figure from [106]

taken just as for the temperature anisotropy spectrum. Additionally, the cross-correlation between the temperature and the polarization can be taken. The TE, EE, and BB power spectra as measured by a number of CMB polarimeters to date and compiled in [16] are shown in Figure 1.4.

1.2 Probing Inflation with the Atacama B-Mode Search

The Atacama B-Mode Search (ABS) is a 145 GHz polarimeter which aims to measure the polarization of the CMB at degree angular scales with per-pixel sensitivity of less than 5

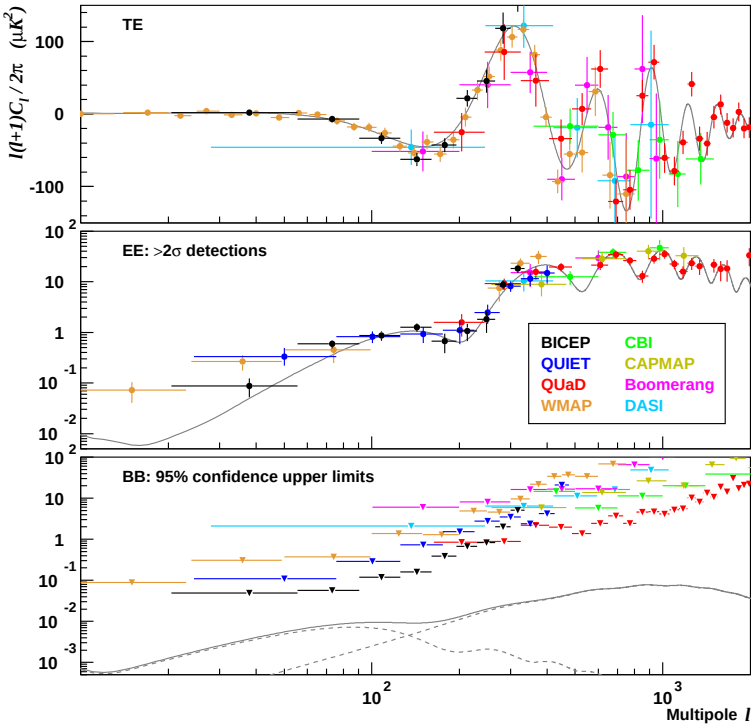

Figure 1.4: A compilation of current measurements of the TE, EE, and BB power spectra from [16]. Only upper limits have been placed on the BB power spectrum. The constraint on r from polarization data is strongest from BICEP on degree angular scales. Figure courtesy of Cynthia Chiang.

nK over the course of two seasons of observation from a high-altitude site in the Chilean Andes. With this sensitivity, the tensor-to-scalar ratio, r, will be probed down to a level of r$\sim$ 0.03, corresponding to an energy scale of inflation less than the grand-unified scale. The projected sensitivity of ABS to the E- and B-mode power spectra is shown in Figure 1.5, along with the expected levels of galactic foreqround emission and the lensed B-mode signal.

As can be seen from the sensitivity plot, the gravitational lensing of E-mode polarization into B-mode polarization by the large-scale structure in the universe is the dominant source of B modes for high ℓ. For $r = 0.03$, this occurs for scales corresponding to $\ell > 90$. This lensed B-mode signal, shown as the red curve in the plot, is guaranteed to be there and

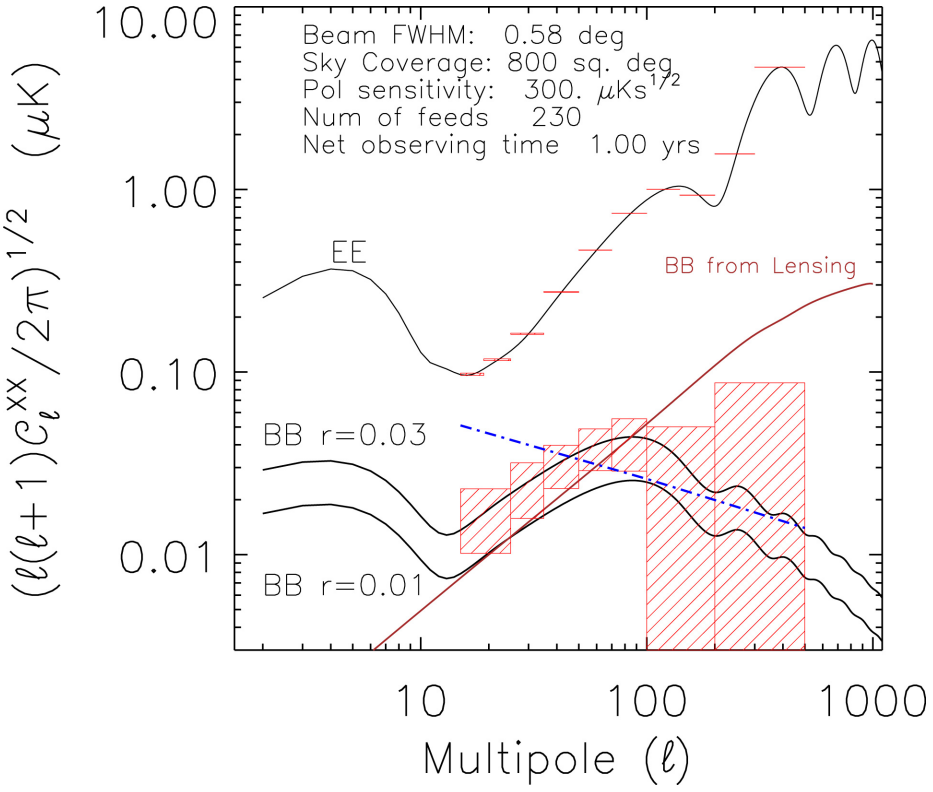

Figure 1.5: Projected sensitivity of ABS to the EE and BB power spectra. The top curve is a model EE power spectrum for a ΛCDM cosmology with parameters currently favored by WMAP data [54]. The bottom two solid black curves are the projected BB power spectra for tensor-to-scalar ratios $r = 0.03$ and $r = 0.01$ and optical depth $\tau = 0.1$. Projected foregrounds include polarized galactic dust and synchrotron emission (blue curve), estimated from [24] for galactic latitudes above 70°. Esimated binned errors for the EE spectrum and the BB spectrum with r= 0.03 are shown as hashed red boxes.

carries information about baryonic and dark matter distribution in the low-redshift universe. As such, it will be a sensitive probe of the equation of state of dark energy and the masses of the neutrinos. A number of upcoming experiments aim to measure this lensed signal. For ABS the lensed B-mode signal is a contaminant and sets the maximum value of ℓ for which the primordial signal can be measured without significant cleaning of the lensed signal. At an ℓ of 100, where the primordial B-modes peak, the primordial and lensed B modes are equal for a tensor-to-scalar ratio of r $\sim$ 0.03.

The thermal dust and synchrotron emission from our galaxy are also major sources of

contaminating polarization. The blue line in the ABS sensitivity plot shows the expected level of galactic foreground emission from [24] in the cleanest parts of the sky, where ABS will primarily be observing. Galactic emission is most significant on large angular scales. While there are prospects for cleaning of the foreground from the ABS observing patches, such as by the estimation of a template [45] using the Planck multi-frequency data once they are available, these procedures can be performed after maps have been made from the data. If ABS sees a B-mode signal, more careful investigation would be warranted to separate primordial B-modes from galactic foreground.

This thesis describes the design and construction of ABS and its current status. Chapter 2 describes the form of the data time stream. Chapter 3 describes the ABS instrument in detail, including the optics, cryogenics, focal plane and detectors, and telescope base. Chapter 4 gives an overview of the design and fabrication of the large-format, quasioptical filters used by ABS. Finally, Chapter 5 describes the current status of the instrument.

Chapter 2

Modeling the Polarization Sensitivity of ABS

The Atacama B-Mode Search (ABS) is a 150 GHz polarimeter that aims to probe for the B-mode signature of primordial gravitational waves through their imprint on the polarization of the CMB. Making precise measurements of the CMB polarization, where the signals of interest are multiple orders of magnitude below the background temperature anisotropies, requires careful control of all systematic error. At the degree angular scales ($\ell \sim 100$) where ABS is most sensitive, temperature anisotropies are on the order of 50 μK [54] and the E-mode polarization is on the order of 1 μK [16]. In contrast, for r = 0.1, the B-mode polarization peaks around $\ell = 100$ at 80 nK. If r is closer to 0.01, this level falls to 25 nK. Any systematic error that leaks temperature into polarization is particularly deleterious, because CMB temperature fluctuations are so large compared with the polarization.

This chapter lays out a formula for the expected data time stream from ABS in terms of telescope parameters. The bolometric detectors used by the ABS are intrinsically total-power, unpolarized devices. Thus it requires that other optical elements, characterized by frequency passbands and Mueller matrices described below, create the polarization sensitivity of the device. An on-chip orthomode transducer (OMT) makes each detector chip polarization sensitive. A half-wave plate (HWP) modulates the incoming polarization of

light that allows for fast (>10 Hz) modulation of the polarization signal. A matrix method for calculating the Mueller matrix for rays at oblique angles of incidence and at all frequencies is described.

2.1 Parametrizations of Polarization

The goal of the ABS instrument is to map the polarization of the sky across the frequency band 127-163 GHz as precisely as possible. The sky polarization can be parametrized in a number of ways. Coherent, monochromatic, electromagnetic (EM) radiation can be parametrized via the polarization ellipse, shown in Figure 2.1 which is the ellipse that the electric field vector traces out in the plane perpendicular to the direction of propagation. Completely linear polarization corresponds to b = 0, with the angle of the electric field vector given by ξ. Completely circularly-polarized light corresponds to $a = b$, with $h = 1$ for right-handed, and $h = -1$ for left-handed, circular polarization.

This representation falls short for partially-polarized light, in which a lack of coherence or the presence of a large spread of frequencies (both conditions are true for observations of the microwave sky) causes there to be an unpolarized component to the radiation. In this case, the EM wave over time scales of only a few oscillation periods has a well-defined polarization ellipse; however, any measurement of polarization which averages over many periods of the oscillation will see an incoherent unpolarized component combined with a polarized component. For such partially-polarized light, the Stokes parameters are commonly used to represent the state of polarization. They can be defined in a number of equivalent ways, but one of the simplest is to relate them to the components of the time-averaged, coherency matrix defined through the complex electric-field vector $E = (E_x, E_y)$ as

$$P = \langle EE^{\dagger} \rangle = I\sigma_0 + QI\sigma_3 + UI\sigma_1 + VI\sigma_2, \tag{2.1}$$

where the $\sigma_\imath$ are the Pauli matrices[1] . Here angled brackets, $\langle * \rangle$, correspond to averaging

[1]
$$\sigma_0 = \begin{pmatrix} 1 & 0 \\ 0 & 1 \end{pmatrix} \quad \sigma_1 = \begin{pmatrix} 0 & 1 \\ 1 & 0 \end{pmatrix} \quad \sigma_2 = \begin{pmatrix} 0 & -\imath \\ \imath & 0 \end{pmatrix} \quad \sigma_3 = \begin{pmatrix} 1 & 0 \\ 0 & -1 \end{pmatrix} \tag{2.2}$$

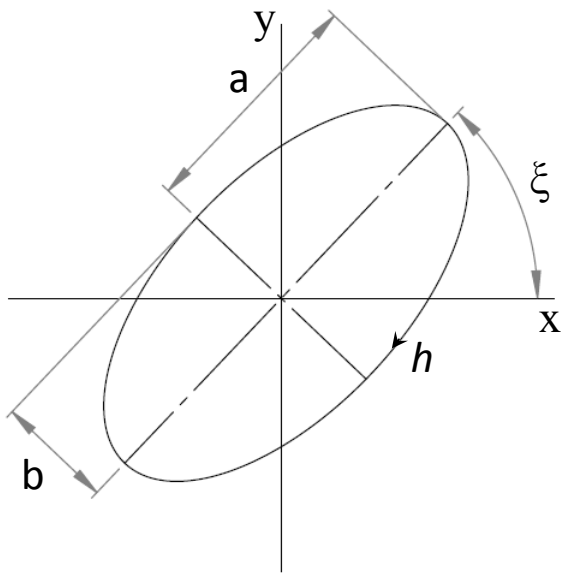

Figure 2.1: Polarization ellipse showing definitions of major axis, a, minor axis, b, ellipse angle, ξ, and handedness, h.

over a time that is long compared with the period of oscillations of the electromagnetic (EM) wave, but short compared with time scales of the measurement. This definition, while elegant, is somewhat opaque. The Stokes parameters can also be defined more intuitively. Following [36], a partially-polarized EM plane wave traveling in the z- direction can be expressed at any given time as the superposition of two plane waves with electric-field vectors oscillating in the x- and y-directions. The electric field magnitudes can be written as:

$$\begin{aligned} E_x(t) &= E_{0x}(t)e^{\imath(\omega t+\delta_x(t))} \\ E_y(t) &= E_{0y}(t)e^{\imath(\omega t+\delta_y(t))} \end{aligned} . \tag{2.3}$$

The Stokes parameters for this wave can then be expressed as:

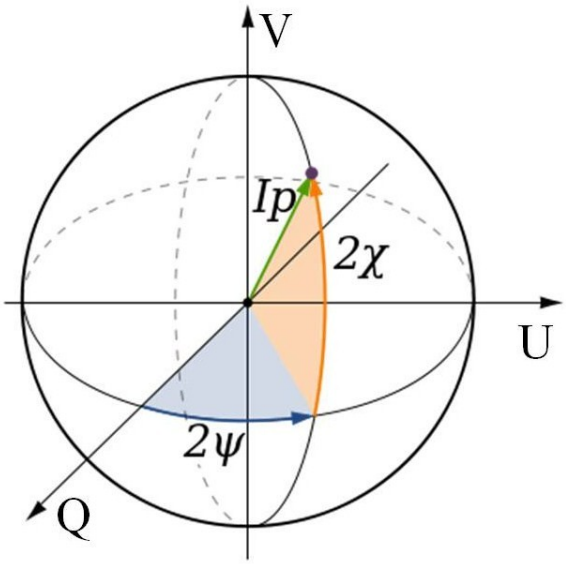

Figure 2.2: Poincare sphere. The Stokes Q, U, and V parameters form the axes. The radius of a point in the sphere is given by the polarized intensity $\sqrt{Q^2+U^2+V^2} \leq I$. The angle 2ψ defines the angle of the major axis of the polarization ellipse of Figure 2.1, while the angle 2χ gives the level of circular polarization.

$$\begin{aligned} I &= \langle E_x^2(t)\rangle + \langle E_y^2(t)\rangle \\ Q &= \langle E_x^2(t)\rangle - \langle E_y^2(t)\rangle \\ U &= 2\mathrm{Re}\langle E_x(t)E_y^*(t)\rangle \\ V &= 2\mathrm{Im}\langle E_x(t)E_y^*(t)\rangle \end{aligned} \tag{2.4}$$

Partially-polarized light is often visualized using the Poincare sphere. The Poincare sphere, as shown in Figure 2.2, represents every polarization state of light as a point on or inside a sphere of radius I. The three axes of the coordinate system are given by Q, U, and V. Any polarization state is placed at coordinate (Q, U, V). For completely polarized light $Q^2+U^2+V^2=I^2$, and the point lies on the surface of the sphere. Completely unpolarized light has $Q^2+U^2+V^2=0$, which is at the origin. Partially polarized light lies somewhere inside the sphere at a radius and polar angles given by:

$$\begin{aligned} r &= \frac{\sqrt{Q^2+U^2+V^2}}{I} \\ \psi &= \arctan\frac{U}{Q} \\ \chi &= \arctan\frac{V}{\sqrt{Q^2+U^2}} \end{aligned} \tag{2.5}$$

For a purely monochromatic, coherent plane wave, the Stokes parameters can be simply related to the polarization ellipse of the incoming light, as

$$\begin{aligned} I &= a^2 + b^2 \\ Q &= (a^2 - b^2)\cos(2\theta) \\ U &= (a^2 - b^2)\sin(2\theta) \\ V &= 2abh \end{aligned} \quad . \tag{2.6}$$

A complementary parametrization of polarized light is the Jones representation, in which the polarization state of a ray of light is given in terms of the complex electric field vectors in two orthogonal directions, as

$$J = \begin{pmatrix} E_x e^{\imath\delta_x} \\ E_y e^{\imath\delta_y} \end{pmatrix}, \tag{2.7}$$

and the action of a linear optical element on the ray can then be characterized by a 2×2 complex Jones matrix, such that incoming and outgoing rays are related by

$$\begin{pmatrix} E'_x \\ E'_y \end{pmatrix} = \begin{pmatrix} J_{xx} & J_{xy} \\ J_{yx} & J_{yy} \end{pmatrix} \begin{pmatrix} E_{0x} \\ E_{0y} \end{pmatrix}. \tag{2.8}$$

The Mueller formalism, discussed below, and Jones formalisms both have limitations. The Jones matrix is directly related to the action of an optical element on orthogonal polarization states, making it more intuitive to work with. On the other hand, the Jones formalism is incapable of dealing with partially-polarized light. The Stokes vectors of the Mueller formalism correspond to total intensities that can be measured directly; however, the Mueller formalism ignores coherence between light rays, making it impractical for calculations of the behavior of interferometers. Both formalisms will be used in Section 2.3.2 to derive the behavior of the ABS half wave plate (HWP).

2.2 Schematic of a General CMB Polarimeter

A general schematic of a CMB polarimeter is shown in Figure 2.3. The pattern of intensity and polarization on the sky is parametrized by the Stokes I, Q, and U parameters. The fourth Stokes parameter, V, parametrizes the amount of circular polarization and is expected to be zero for both the CMB and the thermal emission of the sky. The celestial polarization is a combination of the primordial CMB signal, secondary anisotropies from the interaction of the CMB with intervening large scale structure in the universe, and galactic emission. Secondary anisotropies, such as the lensing of the CMB by large scale structure, are expected to be small compared to the primordial CMB at the degree angular scales where ABS is most sensitive. As mentioned in Section 1.2, the primordial CMB can be separated from galactic foregrounds, if necessary, after maps have been made.

The telescope optics translate angle on the sky into position on the focal plane, where the polarization can be detected. The sensitivity of the optical system versus frequency, which is set by free-space filters at the aperture of the telescope and filters on each detector chip, is captured in the bandpass, $\mathrm{F}(\nu)$, of the system. The optics define copolar and crosspolar beams, $P_{\parallel}(\theta, \phi, \nu)$ and $P_{\perp}(\theta, \phi, \nu)$, which give the sensitivity of each detector to two orthogonal linear polarizations versus position on the sky.

ABS employs a warm, continuously-rotating half-wave plate (HWP) to modulate the polarized signals of interest. The HWP is made of birefringent sapphire which introduces a phase shift of 180° between orthogonal linear polarizations and rotates the incoming polarization about one of its principle crystal axes. The effects of the HWP, as well as the polarization-sensitive nature of modern bolometers, are commonly modeled using Mueller matrices, described in Section 2.3.1, which represent linear transformations between incoming and outgoing Stokes parameters. The Stokes I parameter gives the total intensity of a beam, the Q and U parameters parameterize the linear polarization state, and the V parameter gives the amount of circular polarization present. The four parameters can be placed in a vector, and the 4×4 Mueller matrix gives the effect of a linear optical element on the Stokes vector. For instance, an ideal HWP with its fast axis along the x-axis (corresponding

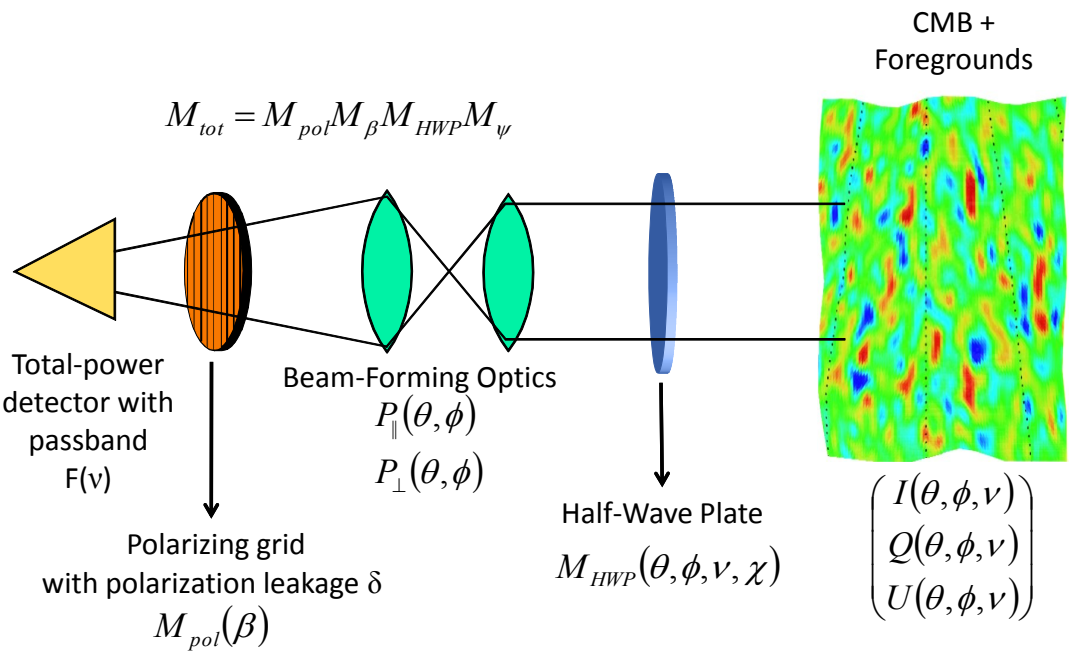

Figure 2.3: Overview of components considered in the instrument model. The CMB combined with galactic foregrounds form a static pattern of intensity I and linear polarization Q and U that vary with angles θ and ϕ on the sky, as well as frequency ν. The incoming Stokes vector for a given detector is then transformed by the Mueller matrix of the HWP, which depends on the angle (θ, ϕ) of the beam on the sky, frequency ν, and the rotation angle of the HWP, χ. The reflectors focus this light down onto the detector, or in the time-reversed sense, create copolar and crosspolar beams on the sky, $P_{\parallel}(\theta, \phi, \nu)$ and $P_{\perp}(\theta, \phi, \nu)$, respectively. The detector is modeled as a polarizing grid with polarization leakage δ at an angle β and a total-power detector with a frequency passband F(ν).

to +Q) has a Mueller matrix given by

$$\begin{pmatrix} I' \\ Q' \\ U' \\ V' \end{pmatrix} = \begin{pmatrix} 1 & 0 & 0 & 0 \\ 0 & 1 & 0 & 0 \\ 0 & 0 & -1 & 0 \\ 0 & 0 & 0 & -1 \end{pmatrix} \begin{pmatrix} I_0 \\ Q_0 \\ U_0 \\ V_0 \end{pmatrix} \tag{2.9}$$

The detector array at the focal plane measures the intensity and polarization of light and transduces it to an electrical signal that can be sent to room-temperature electronics

and converted to a time-stream of digital data. An ABS detector can be parametrized as an imperfect polarizer followed by a total-power detector. The single detector picks out the first row of the Mueller matrix of the instrument. The detector sensitivity can be folded into a total calibration constant, s. Following [44], all of the effects described above are captured in the following equation:

$$d_i = n_i + \frac{s}{2}\int d\nu \frac{F(\nu)\lambda^2}{\Omega_b}\iint d\Omega \left[\left(P_\parallel + P_\perp\right) M_{II} I + \gamma\left(P_\parallel - P_\perp\right)\left(M_{IQ}Q + M_{IU}U\right)\right] \tag{2.10}$$

where functional dependences have been suppressed for concision. The parameters of the equation are defined as follows:

$$\begin{aligned}
d_i &= i^{th} \text{ data value taken at pixel } \mathbf{p} \\
n_i &= \text{noise for } i^{th} \text{ data value} \\
F(\nu) &= \text{detector passband} \\
\Omega_b(\nu) &= \text{beam solid angle} \\
P_\parallel(\theta,\phi,\nu) &= \text{copolar beam response} \\
P_\perp(\theta,\phi,\nu) &= \text{crosspolar beam response} \\
M_{II}(\theta,\phi,\nu,\chi) &= \text{Mueller-matrix element coupling intensity to intensity} \\
M_{IQ}(\theta,\phi,\nu,\chi) &= \text{Mueller-matrix element coupling intensity to Q Stokes parameter} \\
M_{IU}(\theta,\phi,\nu,\chi) &= \text{Mueller-matrix element coupling intensity to U Stokes parameter} \\
\gamma &= \text{detector polarization efficiency} \\
\mathrm{s} &= \text{overall calibration factor} \\
\theta &= \text{galactic latitude} \\
\phi &= \text{galactic longitude} \\
\chi &= \text{half-wave plate angle} \\
\psi &= \text{sky rotation angle} \\
\nu &= \text{frequency}
\end{aligned} \tag{2.11}$$

2.3 The HWP Model

2.3.1 Ideal HWP Mueller Matrix

The effect of the HWP on the incoming polarization of the light and the polarization sensitivity of the ABS detectors, can be represented as linear transformations between Stokes parameters. As noted above, these transformations can be represented in compact form using matrix manipulations if the Stokes parameters of the light being measured are collected into a four-element vector

$$\vec{S} = \begin{pmatrix} I \\ Q \\ U \\ V \end{pmatrix}. \tag{2.12}$$

Completely unpolarized light is represented as (I,0,0,0). For completely polarized light, horizontal linear polarization is represented by the vector (I,I,0,0), vertical polarization as (I,-I,0,0), linear polarization at $\pm 45^\circ$ as (I,0,$\pm$I,0), and circular polarization as (I,0,0,$\pm$I). The effect of an optical element can then be represented as a 4 x 4 matrix, called the Mueller matrix of the element. The Mueller matrix for an ideal HWP with fast axis vertical (in other words along the +Q direction) is given by

$$M_{\mathrm{HWP}} = \begin{pmatrix} 1 & 0 & 0 & 0 \\ 0 & 1 & 0 & 0 \\ 0 & 0 & -1 & 0 \\ 0 & 0 & 0 & -1 \end{pmatrix}. \tag{2.13}$$

Rotation of an optical element about the z axis is given by

$$M_{\rm rot}(\theta) = \begin{pmatrix} 1 & 0 & 0 & 0 \\ 0 & \cos 2\theta & \sin 2\theta & 0 \\ 0 & -\sin 2\theta & \cos 2\theta & 0 \\ 0 & 0 & 0 & 1 \end{pmatrix}. \tag{2.14}$$

An ideal HWP with its fast axis at an arbitrary angle, χ, to the x-axis in the x-y plane is given by

$$M_{\rm rot}(-\chi) M_{\rm HWP} M_{\rm rot}(\chi) = \begin{pmatrix} 1 & 0 & 0 & 0 \\ 0 & \cos 4\chi & \sin 4\chi & 0 \\ 0 & \sin 4\chi & -\cos 4\chi & 0 \\ 0 & 0 & 0 & 1 \end{pmatrix}. \tag{2.15}$$

The HWP used by ABS only introduces an exact 180° phase shift at a single frequency, chosen to be 145 GHz at the center of the band. At other frequencies, the phase difference introduced between two orthogonal linear polarizations differs from 180°, introducing some circular polarization to the beam. Additionally, the HWP is anti-reflection coated, which adds frequency and angle-dependent terms to the Mueller matrix for the realistic HWP. A realistic model of the HWP will need to have terms that depend explicitly on frequency and angle of incidence. These effects are treated in detail below.

2.3.2 Mueller matrix of the real HWP

We seek in this section to develop a method which allows the transmission, reflection, and absorption properties of the ABS sapphire HWP to be realistically modeled at arbitrary frequencies and angles of incidence. The final outputs will be Mueller matrix elements that can be used as inputs in the instrument model described earlier. The basic Mueller matrix for an ideal HWP, Equation 2.13, is only valid at a single frequency, at normal incidence, and for a HWP with no anti-reflection (AR) coatings. Matrix methods have been previously developed for analyzing stacks of anisotropic crystals at normal incidence [14, 83, 47, 60]. The full equations for reflection and refraction at the interface between a

uniaxial crystal and an isotropic dielectric have also been developed in [59], for instance, but these calculations were not developed into a matrix method. We extend these treatments to a matrix formalism for an arbitrary angle of incidence to a uniaxial crystal with its optical axis parallel to the surface of the HWP. To the best of our knowledge, this is the first time that this has been done.

Sapphire is a positively birefringent, uniaxial crystal. Among its three principle dielectric axes, two have the same refractive index at 150 GHz of 3.07, and the third has a higher refractive index of 3.40 at 150 GHz. These two refractive indices are called the "ordinary" and "extraordinary" indices. It is called uniaxial, because the crystal has a single preferred direction. We call this axis the optical axis of the crystal. It is positively birefringent because "extraordinary" rays with polarization parallel to this axis see a higher refractive index than do "ordinary" rays. The optical axis in this case is the "slow" axis because extraordinary rays travel more slowly than their ordinary counterparts.

The behavior of electromagnetic (EM) waves in anisotropic crystals such as sapphire is more complicated than in their isotropic counterparts. The consequences of this are well known and have been explored in detail in the literature. See chapter 15 of [13] for a thorough discussion. Interesting refractory effects, where an incoming plane wave is split into two separate beams or even a cone upon transmission into the medium, are possible within such materials. For our purposes, the fact that light traversing a uniaxial crystal travels at different speeds for two orthogonal polarizations allows the construction of a half-wave plate (HWP) in which a phase difference of 180° is created between two linear polarizations of light. This rotates linear polarization by an angle 2θ, where θ is the angle between the polarization of the ray and the slow axis of the crystal.

Electromagnetic waves in a uniaxial crystal

Anisotropic, non-magnetic, linear dielectrics can be characterized via their dielectric tensor $\overleftrightarrow{\varepsilon}$, which transforms the electric field vector in the material to the electric displacement. In the special case considered here of a uniaxial crystal with its optical axis tangential to the

surface of the sapphire and rotated at an arbitrary angle, χ, to the x-axis,

$$\begin{aligned}
\overleftrightarrow{\varepsilon}' &= \begin{pmatrix} \cos\chi & \sin\chi & 0 \\ -\sin\chi & \cos\chi & 0 \\ 0 & 0 & 1 \end{pmatrix} \begin{pmatrix} n_e^2 & 0 & 0 \\ 0 & n_o^2 & 0 \\ 0 & 0 & n_o^2 \end{pmatrix} \begin{pmatrix} \cos\chi & -\sin\chi & 0 \\ \sin\chi & \cos\chi & 0 \\ 0 & 0 & 1 \end{pmatrix} \\
&= \begin{pmatrix} n_e^2\cos^2\chi + n_o^2\sin^2\chi & \sin\chi\cos\chi(n_o^2 - n_e^2) & 0 \\ \sin\chi\cos\chi(n_o^2 - n_e^2) & n_e^2\sin^2\chi + n_o^2\cos^2\chi & 0 \\ 0 & 0 & n_o^2 \end{pmatrix} \\
&= \tfrac{1}{2}\begin{pmatrix} n_o^2 + n_e^2 + (n_e^2 - n_o^2)\cos 2\chi & (n_o^2 - n_e^2)\sin 2\chi & 0 \\ (n_o^2 - n_e^2)\sin 2\chi & n_o^2 + n_e^2 + (n_o^2 - n_e^2)\cos 2\chi & 0 \\ 0 & 0 & 2n_o^2 \end{pmatrix}
\end{aligned} \tag{2.16}$$

The above matrix holds for a slab of sapphire with its optical axis pointed in the direction of $\hat{\varepsilon}^e = (\cos\chi, \sin\chi, 0)$. The sapphire is assumed to have ordinary and extraordinary indices of refraction of n_o and n_e. The inverse to this matrix transforms $\vec{D}$ to $\vec{E}$, and is given by

$$\frac{1}{2n_o^2 n_e^2}\begin{pmatrix} n_o^2 + n_e^2 + (n_e^2 - n_o^2)\cos 2\chi & (n_e^2 - n_o^2)\sin 2\chi & 0 \\ (n_e^2 - n_o^2)\sin 2\chi & n_o^2 + n_e^2 + (n_o^2 - n_e^2)\cos 2\chi & 0 \\ 0 & 0 & 2n_e^2 \end{pmatrix} \tag{2.17}$$

One consequence of the anisotropy of the crystal is that the electric field vector, $\vec{E}$, and the electric displacement, $\vec{D} = \varepsilon_{ij}\vec{E}$, of an EM wave no longer point in the same direction. Both $\vec{E}$ and $\vec{D}$ remain perpendicular to the magnetic field, $\vec{H}$, and the direction of energy transport is still given by the Poynting Vector, $\vec{S} = \vec{E} \times \vec{H}$; however, the wave propagates in the direction of $\vec{D} \times \vec{H}$, given by the normal direction to planes of constant phase. It is therefore the triplet of vectors $\hat{k}$, $\vec{D}$, and $\vec{H}$ that are mutually orthogonal. This makes it useful to use boundary conditions on the components of $\vec{D}$ at the interface between a birefringent crystal and an isotropic dielectric. This is especially true since the magnitudes of $\vec{D}$, and $\vec{H}$ are related simply by

$$|\vec{H}| = \frac{1}{n}|\vec{D}|. \tag{2.18}$$

Given $\hat{k}$ and either $\vec{E}$ or $\vec{D}$, the other vectors for the wave can be calculated through Equations 2.16 and 2.17, as well as the fact that

$$\vec{H} = \frac{1}{n}\hat{k} \times \vec{D}. \tag{2.19}$$

Here n is a real-valued, angle-dependent refractive index which gives the speed of a ray as it traverses the medium, $\mathrm{v}_p = c/n$, that will be calculated below.

Another consequence of the anisotropy of the material is that a linearly-polarized plane wave at a dielectric boundary gets refracted into two separate plane waves polarized along preferred directions in the crystal unless the incoming plane wave happens to be polarized along one of the principle axes of the crystal. These two waves travel at different speeds. For a uniaxial crystal, one of these waves, the ordinary ray, always travels at the same speed, given by

$$v' = v_o = c/n_o, \tag{2.20}$$

while the extraordinary ray has a velocity which depends upon the angle ψ between the wave and the optical axis and is given by

$$v'' = \frac{c}{n''} = \sqrt{v_o^2 \cos^2\psi + v_e^2 \sin^2\psi} = c\sqrt{\frac{\cos^2\psi}{n_o^2} + \frac{\sin^2\psi}{n_e^2}}. \tag{2.21}$$

An EM wave which is incident at angle θ_i upon a surface of the uniaxial crystal from an isotropic dielectric of index n_1 will then refract by two separate angles, which are each individually given by the familiar Snell's Law

$$n_o \sin\theta' = n'' \sin\theta'' = n_1 \sin\theta_1. \tag{2.22}$$

The two rays remain in the plane of incidence. The ordinary ray is always at the same angle relative to the angle of incidence. The equation for the extraordinary ray is complicated

by the fact that the index of refraction depends on the angle through the material, which depends on the angle of incidence and the angle of the HWP, χ, in a nontrivial manner. Let the faces of the HWP lie in the x-y plane. The extraordinary ray that propagates through the material at angle θ'', yet to be determined, has unit propagation vector $\hat{k} = \sin\theta_e\hat{x} + \cos\theta''\hat{z}$. The angle ψ, defined in Equation 2.21, between these two is then $\cos\psi = \hat{k}\cdot\hat{\varepsilon}_e = \sin\theta''\cos\chi$. Thus Equation 2.21 becomes

$$\begin{aligned} n'' &= \left(\frac{\cos^2\psi}{n_o^2} + \frac{\sin^2\psi}{n_e^2}\right)^{-1/2} \\ &= n_o n_e \left((n_e^2 - n_o^2)\sin^2\theta''\cos^2\chi + n_o^2\right)^{-1/2}, \end{aligned} \tag{2.23}$$

and Equation 2.22 becomes

$$\sin\theta'' = \frac{n_1\sin\theta_1}{n_o n_e}\sqrt{(n_e^2 - n_o^2)\sin^2\theta''\cos^2\chi + n_o^2}. \tag{2.24}$$

Solving this equation for $\sin\theta''$ yields

$$\sin\theta'' = \frac{n_o n_e \sin\theta_1}{\sqrt{n_o^2 n_e^2 + n_1^2(n_o^2 - n_e^2)\sin^2\theta_1\cos^2\chi}}. \tag{2.25}$$

Equations 2.22 and 2.25 give the angles of the ordinary and extraordinary rays for a given angle of incidence and rotation of the HWP. These rays both travel in the x-z plane and have associated unit-normal vectors $\hat{k}'$ and $\hat{k}''$, which are

$$\hat{k}' = (\sin\theta', 0, \cos\theta'); \quad \hat{k}'' = (\sin\theta'', 0, \cos\theta'') \tag{2.26}$$

The directions of vibration of the electric displacement vector, or in other words the polarizations of the two refracted rays, can also be calculated. The ordinary ray, traveling through the material at angle θ', must have its electric displacement perpendicular to both the direction of propagation $\hat{k}'$ and the direction of the slow axis $\hat{\varepsilon}_e = (\cos\chi, \sin\chi, 0)$. Thus

$$\hat{D}' = \frac{\vec{D}'}{|\vec{D}'|} = \alpha'\hat{k}'\times\hat{\varepsilon}_e = \alpha'\begin{pmatrix} -\sin\chi\cos\theta' \\ \cos\chi\cos\theta' \\ \sin\chi\sin\theta' \end{pmatrix} \tag{2.27}$$

Similarly, the extraordinary ray must have an electric displacement that is perpendicular to its direction of propagation and to the direction of vibration of the ordinary ray. It is thus

$$\hat{D}'' = \frac{\vec{D}''}{|\vec{D}''|} = \alpha'' \hat{k}'' \times \hat{D}' = \alpha'' \begin{pmatrix} -\cos\chi\cos\theta'\cos\theta'' \\ -\sin\chi\left[\sin\theta'\sin\theta'' + \cos\theta'\cos\theta''\right] \\ \cos\chi\cos\theta'\sin\theta'' \end{pmatrix} \tag{2.28}$$

The constants α' and α'' normalize these vectors.

Boundary conditions

The geometry under consideration is shown in Figure 2.4. We need to derive relationships between $\vec{D}$ and $\vec{H}$ on both sides of the two interfaces (labeled I and II). In the absence of free charges on the boundary, the tangential components of both $\vec{D}$ and $\vec{H}$ are continuous. We will thus consider the relationship between the vector (D_x ,H_y, D_y, -H_x) on the two boundaries. In the calculations below, subscripts will denote incoming, transmitted, and reflected field amplitudes as lower-case i, t, and r, respectively, along with a roman-numeral I or II denoting the interface concerned. In the surrounding isotropic medium, subscripts s and p will denote waves with electric field vector perpendicular to the plane of incidence (s-polarized wave) and in the plane of incidence (p-polarized wave). In the uniaxial crystal $'$ or $''$ will denote the ordinary or extraordinary rays. As an example, E''_{tI} is the electric field amplitude of the extraordinary ray that is transmitted from interface I. A subscript of "r$'$II" denotes the ray reflected off interface II which has traversed the medium and is incident from below on interface I.

Rays that reflect off an interface have vector components in the x-z plane shifted in phase by 180°, which multiplies the x- and z-components of $\vec{D}$ and $\vec{H}$ by $e^{\pi} = -1$. Rays that traverse the uniaxial crystal develop a phase shift that depends on their angle, the thickness of the crystal, and the refractive index seen by that ray. The phase shifts differ for the ordinary and extraordinary rays, and are given by

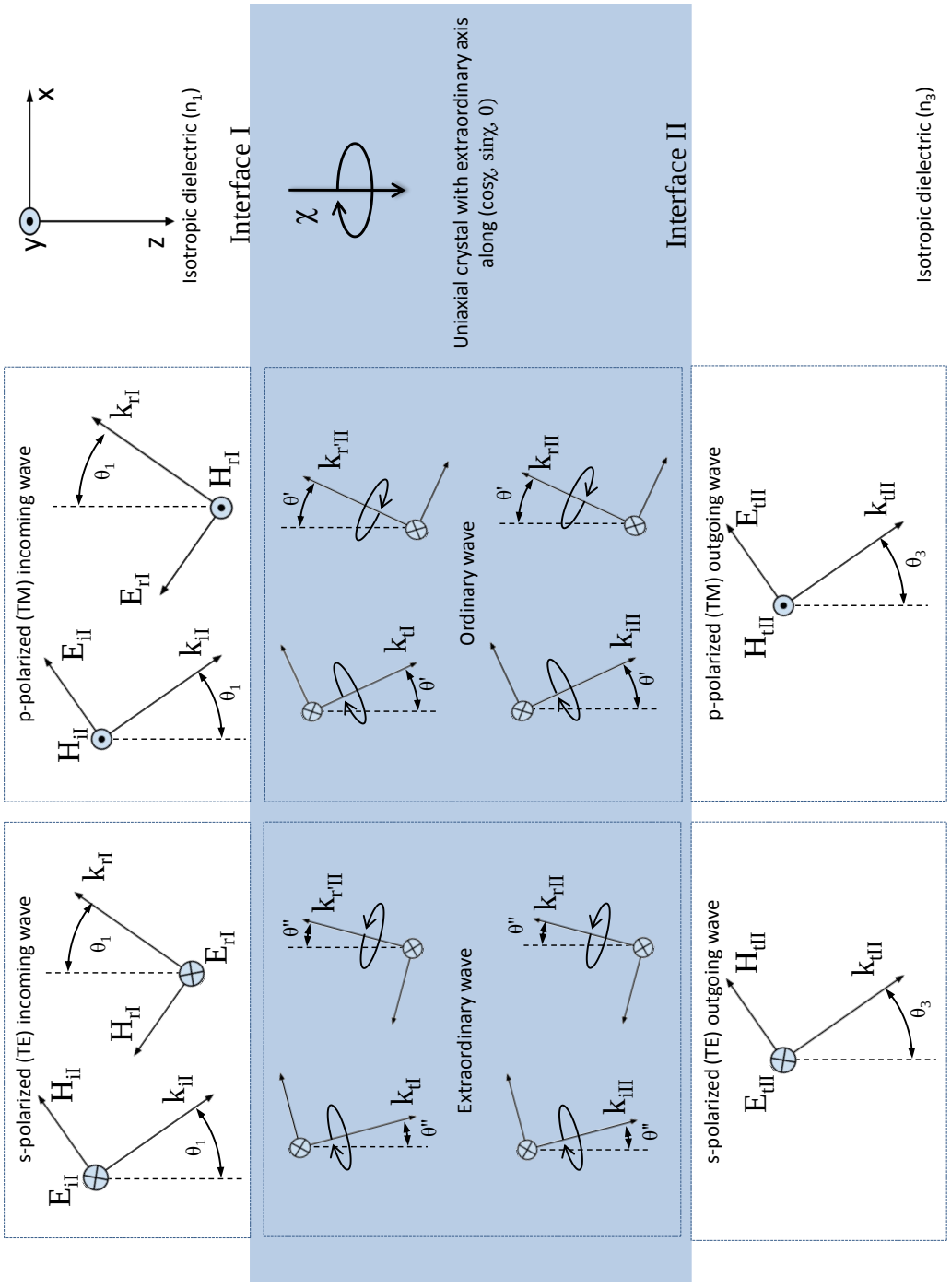

Figure 2.4: Geometry of the rays used to calculate the generalized characteristic matrix for the HWP. The two polarization states defined by the plane of incidence, the s- and p-waves, are mixed inside the uniaxial crystal into the ordinary and extraordinary waves.

$$\begin{aligned} \delta' &= \tilde{n}_o t \cos\theta' \\ \delta'' &= \tilde{n}'' t \cos\theta'' \end{aligned} , \tag{2.29}$$

where $\tilde{n} = n\sqrt{1 - \imath \tan\delta}$ is the complex refractive index, the imaginary part of which encodes dielectric loss in the material. The real part is the refractive index given above. Rays that are transmitted through Interface I are incident on Interface II with a phase shift. This relates D_{tI} and D_{iII} as

$$\begin{aligned} D'_{iII} &= D'_{tI} e^{\imath k_0 \delta'} \\ D''_{iII} &= D''_{tI} e^{\imath k_0 \delta''} \end{aligned} . \tag{2.30}$$

Likewise, the ray that reflects off interface II is phase shifted on its way to interface I, giving

$$\begin{aligned} D'_{rII} &= D'_{r'II} e^{-\imath k_0 \delta'} \\ D''_{rII} &= D''_{r'II} e^{-\imath k_0 \delta''} \end{aligned} . \tag{2.31}$$

In the above, k_0 is the wave number for the wave in vacuum, equal to $2\pi/\lambda_0$. For concision, we can break $\vec{D}$ and $\vec{H}$ into unknown total magnitudes multiplied by unit-vector directions that are known from Equations 2.27, 2.28, 2.19. The components of $\vec{D}$ and $\vec{H}$ transmitted from Interface I can be written out explicitly as

$$\begin{aligned} \vec{D}'_{tI} &= |\vec{D}'_{tI}|(\hat{D}'^{(\mathrm{x})}_{tI}, \hat{D}'^{(\mathrm{y})}_{tI}, \hat{D}'^{(\mathrm{z})}_{tI}) \\ \vec{D}''_{tI} &= |\vec{D}''_{tI}|(\hat{D}''^{(\mathrm{x})}_{tI}, \hat{D}''^{(\mathrm{y})}_{tI}, \hat{D}''^{(\mathrm{z})}_{tI}) \\ \vec{H}'_{tI} &= \tfrac{1}{n'}|\vec{D}'_{tI}|(\hat{H}'^{(\mathrm{x})}_{tI}, \hat{H}'^{(\mathrm{y})}_{tI}, \hat{H}'^{(\mathrm{z})}_{tI}) \\ \vec{H}''_{tI} &= \tfrac{1}{n''}|\vec{D}''_{tI}|(\hat{H}''^{(\mathrm{x})}_{tI}, \hat{H}''^{(\mathrm{y})}_{tI}, \hat{H}''^{(\mathrm{z})}_{tI}) \end{aligned} , \tag{2.32}$$

where use has been made of the relationship between the magnitudes of $\vec{D}$ and $\vec{H}$, Equation 2.18. The complex components of the field unit vectors, such as $D'^{(\mathrm{x})}_{tI}$, are known and given in explicit form in Equation 2.37 below. All other vectors at the two interfaces, shown in Figure 2.4, can be written in terms of the known transmitted field directions from interface I, as well as undetermined field amplitudes. The remaining field components at interface I can be written

$$\begin{aligned}
\vec{D}'_{\mathrm{r'II}} &= |\vec{D}'_{\mathrm{r'II}}|(-\hat{D}'^{(\mathrm{x})}_{tI}, \hat{D}'^{(\mathrm{y})}_{tI}, -\hat{D}'^{(\mathrm{z})}_{tI}) \\
\vec{D}''_{\mathrm{r'II}} &= |\vec{D}''_{\mathrm{r'II}}|(-\hat{D}''^{(\mathrm{x})}_{tI}, \hat{D}''^{(\mathrm{y})}_{tI}, -\hat{D}''^{(\mathrm{z})}_{tI}) \\
\vec{H}'_{\mathrm{r'II}} &= \tfrac{1}{n'}|\vec{D}'_{\mathrm{r'II}}|(-\hat{H}'^{(\mathrm{x})}_{tI}, \hat{H}'^{(\mathrm{y})}_{tI}, -\hat{H}'^{(\mathrm{z})}_{tI}) \\
\vec{H}''_{\mathrm{r'II}} &= \tfrac{1}{n''}|\vec{D}''_{\mathrm{r'II}}|(-\hat{H}''^{(\mathrm{x})}_{tI}, \hat{H}''^{(\mathrm{y})}_{tI}, -\hat{H}''^{(\mathrm{z})}_{tI})
\end{aligned} \tag{2.33}$$

A system of four equations relating the total-field x- and y-components at Interface I and the individual ray components (tI and r′II) can be written in matrix form as

$$\begin{pmatrix} D^x_I \\ H^y_I \\ D^y_I \\ -H^x_I \end{pmatrix} = \begin{pmatrix} \hat{D}'^{(\mathrm{x})}_{tI} & \hat{D}''^{(\mathrm{x})}_{tI} & -\hat{D}'^{(\mathrm{x})}_{tI} & -\hat{D}''^{(\mathrm{x})}_{tI} \\ \frac{1}{n'}\hat{H}'^{(\mathrm{y})}_{tI} & \frac{1}{n''}\hat{H}''^{(\mathrm{y})}_{tI} & \frac{1}{n'}\hat{H}'^{(\mathrm{y})}_{tI} & \frac{1}{n''}\hat{H}''^{(\mathrm{y})}_{tI} \\ \hat{D}'^{(\mathrm{y})}_{tI} & \hat{D}''^{(\mathrm{y})}_{tI} & \hat{D}'^{(\mathrm{y})}_{tI} & \hat{D}''^{(\mathrm{y})}_{tI} \\ -\frac{1}{n'}\hat{H}'^{(\mathrm{x})}_{tI} & -\frac{1}{n''}\hat{H}''^{(\mathrm{x})}_{tI} & \frac{1}{n'}\hat{H}'^{(\mathrm{x})}_{tI} & \frac{1}{n''}\hat{H}''^{(\mathrm{x})}_{tI} \end{pmatrix} \begin{pmatrix} |\vec{D}'_{tI}| \\ |\vec{D}''_{tI}| \\ |\vec{D}'_{\mathrm{r'II}}| \\ |\vec{D}''_{\mathrm{r'II}}| \end{pmatrix} \tag{2.34}$$

In matrix notation this can be written as $\Lambda_I = M_I X$. A similar relation holds for Interface II, where Equations 2.30 and 2.31 can be used to relate the fields on Interface II to those on Interface I. The vector $(D^x_{II}, H^y_{II}, D^y_{II}, -H^x_{II})$ is given by

$$\begin{pmatrix} \hat{D}'^{(\mathrm{x})}_{tI} e^{-\imath k_0 \delta'} & \hat{D}''^{(\mathrm{x})}_{tI} e^{-\imath k_0 \delta''} & -\hat{D}'^{(\mathrm{x})}_{tI} e^{\imath k_0 \delta'} & -\hat{D}''^{(\mathrm{x})}_{tI} e^{\imath k_0 \delta''} \\ \frac{1}{n'}\hat{H}'^{(\mathrm{y})}_{tI} e^{-\imath k_0 \delta'} & \frac{1}{n''}\hat{H}''^{(\mathrm{y})}_{tI} e^{-\imath k_0 \delta''} & \frac{1}{n'}\hat{H}'^{(\mathrm{y})}_{tI} e^{\imath k_0 \delta'} & \frac{1}{n''}\hat{H}''^{(\mathrm{y})}_{tI} e^{\imath k_0 \delta''} \\ \hat{D}'^{(\mathrm{y})}_{tI} e^{-\imath k_0 \delta'} & \hat{D}''^{(\mathrm{y})}_{tI} e^{-\imath k_0 \delta''} & \hat{D}'^{(\mathrm{y})}_{tI} e^{\imath k_0 \delta'} & \hat{D}''^{(\mathrm{y})}_{tI} e^{\imath k_0 \delta''} \\ -\frac{1}{n'}\hat{H}'^{(\mathrm{x})}_{tI} e^{-\imath k_0 \delta'} & -\frac{1}{n''}\hat{H}''^{(\mathrm{x})}_{tI} e^{-\imath k_0 \delta''} & \frac{1}{n'}\hat{H}'^{(\mathrm{x})}_{tI} e^{\imath k_0 \delta'} & \frac{1}{n''}\hat{H}''^{(\mathrm{x})}_{tI} e^{\imath k_0 \delta''} \end{pmatrix} \begin{pmatrix} |\vec{D}'_{tI}| \\ |\vec{D}''_{tI}| \\ |\vec{D}'_{\mathrm{r'II}}| \\ |\vec{D}''_{\mathrm{r'II}}| \end{pmatrix}, \tag{2.35}$$

where again this equation can be abbreviated as $\Lambda_{II} = M_{II} X$. These M matrices are unrelated to the Mueller matrix. We can find the relation we are seeking between Λ_I and Λ_{II} by solving for X in the above equations and setting these equal to one another. This yields

$$\Lambda_I = M_I M_{II}^{-1} \Lambda_{II}. \tag{2.36}$$

The matrix $M_I M_{II}^{-1}$ is the generalized characteristic matrix for a uniaxial crystal, such as the ABS sapphire HWP, with its optical axis at an angle χ to its planar surface. It should

be stressed that this matrix deals with *total* electric displacement and magnetic fields at the two boundaries of the crystal, which allows the matrix to take into account multiple reflections. Explicit formulas for the field components transmitted from Interface I are

$$\begin{aligned}
\hat{D}'^{(\mathrm{x})}_{tI} &= \frac{-\sin\chi\cos\theta'}{\sqrt{\cos^2\theta'+\sin^2\theta'\sin^2\chi}} \\
\hat{D}'^{(\mathrm{y})}_{tI} &= \frac{\cos\chi\cos\theta'}{\sqrt{\cos^2\theta'+\sin^2\theta'\sin^2\chi}} \\
\hat{D}'^{(\mathrm{z})}_{tI} &= \frac{\sin\chi\sin\theta'}{\sqrt{\cos^2\theta'+\sin^2\theta'\sin^2\chi}} \\
\hat{D}''^{(\mathrm{x})}_{tI} &= \frac{\cos\chi\cos\theta'\cos\theta''}{\sqrt{\cos^2\chi\cos^2\theta'+\sin^2\chi\cos^2(\theta'-\theta'')}} \\
\hat{D}''^{(\mathrm{y})}_{tI} &= \frac{\sin\chi(\sin\theta'\sin\theta''+\cos\theta'\cos\theta'')}{\sqrt{\cos^2\chi\cos^2\theta'+\sin^2\chi\cos^2(\theta'-\theta'')}} \\
\hat{D}''^{(\mathrm{z})}_{tI} &= \frac{-\cos\chi\cos\theta'\sin\theta''}{\sqrt{\cos^2\chi\cos^2\theta'+\sin^2\chi\cos^2(\theta'-\theta'')}} \\
\hat{H}'^{(\mathrm{x})}_{tI} &= \frac{-\cos^2\theta'\cos\chi}{\sqrt{\cos^2\theta'\cos^2\chi+\sin^2\chi}} \\
\hat{H}'^{(\mathrm{y})}_{tI} &= \frac{-\sin\chi}{\sqrt{\cos^2\theta'\cos^2\chi+\sin^2\chi}} \\
\hat{H}'^{(\mathrm{z})}_{tI} &= \frac{\cos\theta'\sin\theta'\cos\chi}{\sqrt{\cos^2\theta'\cos^2\chi+\sin^2\chi}} \\
\hat{H}''^{(\mathrm{x})}_{tI} &= \frac{-\cos(\theta'-\theta'')\cos\theta''\sin\chi}{\sqrt{\cos^2(\theta'-\theta'')\sin^2\chi+\cos^2\theta'\cos^2\chi}} \\
\hat{H}''^{(\mathrm{y})}_{tI} &= \frac{\cos\theta'\cos\chi}{\sqrt{\cos^2(\theta'-\theta'')\sin^2\chi+\cos^2\theta'\cos^2\chi}} \\
\hat{H}''^{(\mathrm{z})}_{tI} &= \frac{\cos(\theta'-\theta'')\sin\theta''\sin\chi}{\sqrt{\cos^2(\theta'-\theta'')\sin^2\chi+\cos^2\theta'\cos^2\chi}}
\end{aligned} \tag{2.37}$$

Matrix of an isotropic medium

Having in hand the matrix for an anisotropic medium as derived above, it is straightforward to compute the matrix for an isotropic medium, which has $\mathrm{n}' = \mathrm{n}'' = \mathrm{n}_2$. This implies that $\theta' = \theta'' = \sin^{-1}[\frac{n_1}{n_2}\sin\theta_1]$, and the "ordinary" and "extraordinary" rays have the same directions of vibration as the incoming s- and p-polarized waves. The much-simplified resulting matrix has no coupling between these two states, so the upper-right and lower-left blocks of the 4 x 4 matrix contain all zeroes. The matrix is

$$\begin{pmatrix} \cos k_0\delta & -\imath n_2 \cos\theta_1 \sin k_0\delta & 0 & 0 \\ -(\imath/n_2\cos\theta_1)\sin k_0\delta & \cos k_0\delta & 0 & 0 \\ 0 & 0 & \cos k_0\delta & -(\imath\cos\theta_1/n_2)\sin k_0\delta \\ 0 & 0 & -(\imath n_2/\cos\theta_1)\sin k_0\delta & \cos k_0\delta \end{pmatrix} \tag{2.38}$$

Any number of matrices corresponding to isotropic media can be cascaded in series to model the behavior of a stack of dielectrics. These could be anti-reflection coatings, for instance.

Transmission, reflection, and absorption coefficients

To calculate the amplitude transmission, reflection, and absorption coefficients for a stack of dielectrics, we need to consider coupling of the fields at the two interfaces to incoming and outgoing s- and p-polarized waves in isotropic media with refractive indices n_1 and n_3. If we assume there to be a wave incident on Interface I that has an associated reflected wave, and a transmitted wave leaving from Interface II, we can write the coupling between these fields in terms of the generalized characteristic matrix of the stack. We will switch back to relating components of $\vec{E} = \vec{D}/n^2$, as it will simplify the calculation of power amplitude ratios since it is $\vec{E}$, and not $\vec{D}$, which determines power flow.

$$\begin{pmatrix} (E_i^p - E_r^p)n_1^2\cos\theta_1 \\ n_1(E_i^p + E_r^p) \\ n_1^2(E_i^s + E_r^s) \\ (E_i^s - E_r^s)(n_1\cos\theta_1) \end{pmatrix} = \begin{pmatrix} m_{11} & m_{12} & m_{13} & m_{14} \\ m_{21} & m_{22} & m_{23} & m_{24} \\ m_{31} & m_{32} & m_{33} & m_{34} \\ m_{41} & m_{42} & m_{43} & m_{44} \end{pmatrix} \begin{pmatrix} E_t^p n_3^2\cos\theta_3 \\ n_3 E_t^p \\ n_3^2 E_t^s \\ E_t^s(n_3\cos\theta_3) \end{pmatrix}, \tag{2.39}$$

where use has been made of the convenient fact that in the isotropic media the p-polarized waves have no x-component to $\vec{D}$ and the s-polarized waves have no y-component to $\vec{D}$. The four conditions represented by the matrix equation above can be solved to give E_r^p, E_r^s, E_t^p, and E_t^s in terms of E_i^p and E_i^s. Our goal is to write these relations in the form of Jones

matrices for transmission and reflection, which can then be translated to Mueller matrices through the relation

$$M_{ij} = \frac{1}{2} Tr(\sigma_i J \sigma_j J^\dagger), \tag{2.40}$$

where σ_i are the Pauli matrices. To begin, the relations above can be written in a more concise form by introducing the constants

$$\begin{aligned}
\alpha &= (m_{11} n_3^2 \cos\theta_3 + m_{12} n_3)/(n_1^2 \cos\theta_1) \\
\beta &= (m_{13} n_3^2 + m_{14} n_3 \cos\theta_3)/(n_1^2 \cos\theta_1) \\
\gamma &= (m_{21} n_3^2 \cos\theta_3 + m_{22} n_3)/n_1 \\
\delta &= (m_{23} n_3^2 + m_{24} n_3 \cos\theta_3)/n_1 \\
\eta &= (m_{31} n_3^2 \cos\theta_3 + m_{32} n_3)/n_1^2 \\
\kappa &= (m_{33} n_3^2 + m_{34} n_3 \cos\theta_3)/n_1^2 \\
\rho &= (m_{41} n_3^2 \cos\theta_3 + m_{42} n_3)/(n_1 \cos\theta_1) \\
\sigma &= (m_{43} n_3^2 + m_{44} n_3 \cos\theta_3)/(n_1 \cos\theta_1)
\end{aligned} \quad . \tag{2.41}$$

In terms of these constants, the transmitted-wave amplitudes are

$$\begin{aligned}
\begin{pmatrix} E_t^p \\ E_t^s \end{pmatrix} &= \begin{pmatrix} J_{11}^t & J_{12}^t \\ J_{21}^t & J_{22}^t \end{pmatrix} \begin{pmatrix} E_i^p \\ E_i^s \end{pmatrix} \\
&= \frac{2}{(\alpha+\gamma)(\kappa+\sigma)-(\beta+\delta)(\eta+\rho)} \begin{pmatrix} \kappa+\sigma & -\beta-\delta \\ -\eta-\rho & \alpha+\gamma \end{pmatrix} \begin{pmatrix} E_i^p \\ E_i^s \end{pmatrix}
\end{aligned} \tag{2.42}$$

The reflected-wave amplitudes are

$$\begin{pmatrix} E_r^p \\ E_r^s \end{pmatrix} = \begin{pmatrix} J_{11}^r & J_{12}^r \\ J_{21}^r & J_{22}^r \end{pmatrix} \begin{pmatrix} E_i^p \\ E_i^s \end{pmatrix} = \frac{1}{(\alpha+\gamma)(\kappa+\sigma)-(\beta+\delta)(\eta+\rho)} \times$$
$$\begin{pmatrix} (\gamma-\alpha)(\kappa+\sigma)-(\delta-\beta)(\eta+\rho) & 2(\alpha\delta-\gamma\beta) \\ 2(\eta\sigma-\rho\kappa) & (\alpha+\gamma)(\kappa-\sigma)-(\beta+\delta)(\eta-\rho) \end{pmatrix} \begin{pmatrix} E_i^p \\ E_i^s \end{pmatrix} \tag{2.43}$$

The Jones matrices for the reflected and transmitted waves can then be transformed into Mueller matrices using Equation 2.40. Given an incoming plane wave described by a Stokes vector (I_0, Q_0, U_0, V_0), these matrices give reflected and transmitted Stokes vectors. A python script is being developed to calculate the reflected and transmitted Mueller matrices in this way.

2.4 Detector Mueller Matrix

Bolometric polarimeters such as the ones used in ABS can be characterized as partial polarizers followed by total-power detectors [44]. The Jones matrix for an imperfect horizontal polarizer is

$$\begin{pmatrix} \eta & 0 \\ 0 & \delta \end{pmatrix}, \tag{2.44}$$

where η is the transmission efficiency of the polarizer and δ is the cross-polar leakage, $\eta \gg \delta$. From Equation 2.40, this yields a Mueller matrix for the polarizer of

$$\frac{1}{2}\begin{pmatrix} \eta^2+\delta^2 & \eta^2-\delta^2 & 0 & 0 \\ \eta^2-\delta^2 & \eta^2+\delta^2 & 0 & 0 \\ 0 & 0 & 2\eta\delta & 0 \\ 0 & 0 & 0 & 2\eta\delta \end{pmatrix}. \tag{2.45}$$

These equations hold for one of the detectors in a polarimeter, while the matrices for the orthogonal detector are given by exchanging $\eta \leftrightarrow \delta$ in the above. The bolometer of the TES then picks out the total power incident on it, which involves summing the first row of the Mueller matrix multiplied by the Stokes parameters, as $M_{II}I + M_{IQ}Q + M_{IU}U + M_{IV}V$.

2.5 Conclusion

A matrix method has been developed which allows the calculation of reflection and transmission Mueller matrices for an arbitrary stack of dielectrics with uniaxial crystals as part of

the stack. The method can treat stacks with multiple uniaxial crystals in series along with any number of isotropic media. From these matrices, the sensitivity of the ABS instrument to polarization on the sky can be calculated versus HWP angle for each detector in the focal plane. Sum and difference time-streams can also be investigated with this formalism.

Chapter 3

The ABS Instrument

3.1 Receiver Overview

The receiver for the Atacama B-Mode Search (ABS) was designed to measure the polarization of the CMB. This required careful consideration of all design parameters in order to maximize detector sensitivity and reduce contamination of the signal by the atmosphere, optical elements, and the ground. This is achieved through a combination of 4 K reflective optics and cold aperture stop; warm, continuously-rotating half-wave plate (HWP); and, state-of-the-art, feedhorn-coupled, transition-edge-sensor (TES) polarimeters developed by the Quantum Sensors Group at the National Institute of Standards and Technology (NIST). ABS will provide the first field test of this new detector technology, which is scheduled to be used for a number of upcoming experiments, including ACTPol, SPTPol, and CLASS. An overview of the telescope receiver is shown in Figure 3.1. This chapter deals with all aspects of the instrument except the free-space filters, which are discussed in Chapter 4.

3.1.1 Cryogenics

Reducing the intrinsic noise of bolometric detectors like those used on ABS requires that one maintain the lowest-possible base temperature for the focal plane. The ABS polarimeter chips are designed to operate from a base temperature of 300 mK, which was chosen because

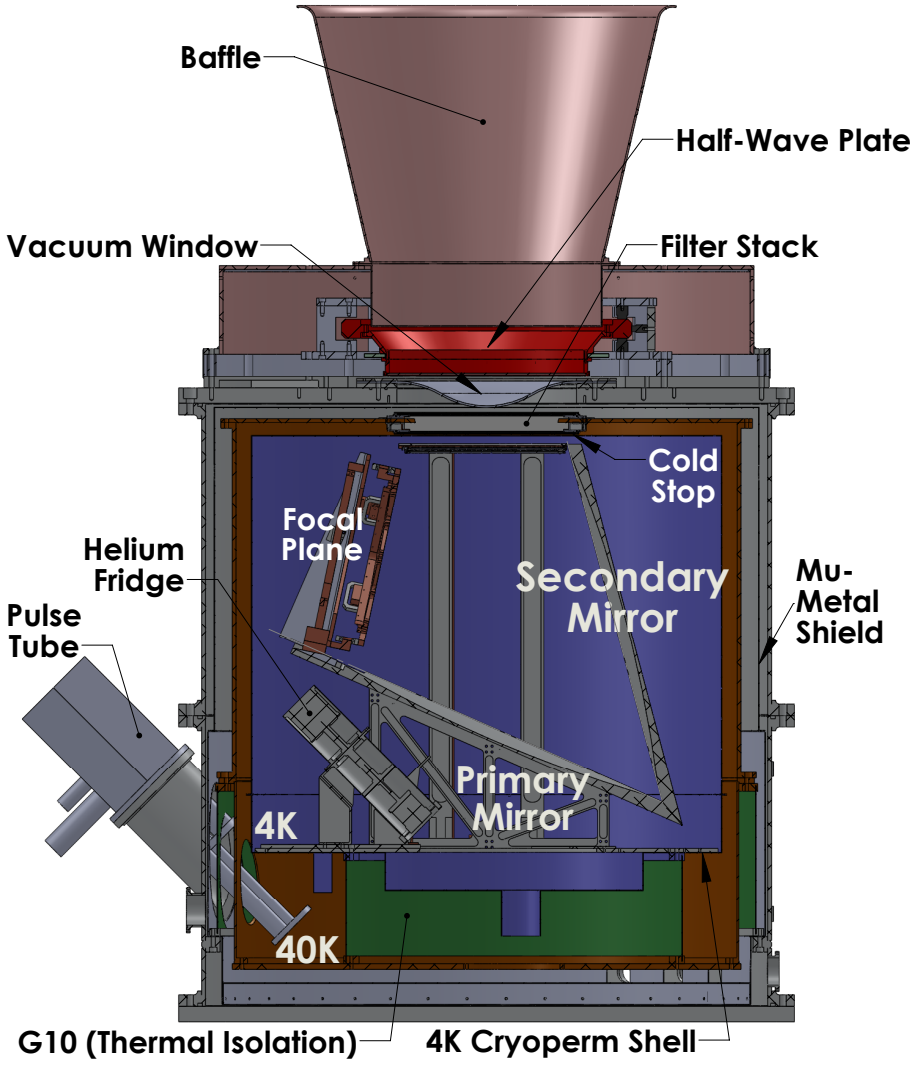

Figure 3.1: Diagram of the ABS receiver, with major components indicated. The 4 K volume is shown in blue and the 40 K volume in brown. G10 supports, which provide thermal isolation, are shown in green. The primary and secondary mirrors, which are approximately 60 cm in diameter each, lie entirely within the 4 K volume. Pulse tube refrigerators provide cooling to approximately 4 K and 40 K. A ^{3}He/^{4}He adsorption system is then used to cool the focal plane to below 300 mK. Magnetic shielding for the sensitive SQUID amplifiers is provided by a mu-metal shield at 300 K, a cryoperm shield at 4 K, and niobium sheets at 300 mK that are not shown in this figure. Metal-mesh and absorptive filters provide thermal load mitigation and some band definition.

a legacy helium adsorption system was available. The system is capable of producing temperatures as low as 220 mK. Achieving such low temperatures requires careful control of all sources of thermal loading, from mechanical supports, radiation, and electrical wiring. As will be seen below, the need for cryogenic bolometers also drives many other aspects of the ABS design, from the detector readout cables to the design of free-space filters in the optical aperture.

The ABS cryogenics system was designed by Lucas Parker and modeled after the successful Column CAMera (CCAM) and Millimeter Bolometer Array Camera (MBAC) designs that were installed on the Atacama Cosmology Telescope, and in fact the helium adsorption system used by ABS is directly from the CCAM instrument. The ABS cryostat uses two pulse-tube refrigerators.[1] These combine to provide 1.7 W and 55 W of cooling power at their 4 K and 40 K stages, respectively. G10 tubes with 3.2-mm wall thickness provide thermal isolation between 300 K, 40 K, and 4 K. Thirty layers of "super insulation" reduce radiative loading to a minimum. This super-insulation consists of Mylar that is coated on one side with aluminum. The entire system is kept in vacuum at a pressure of no more than 10^{-6} Torr to eliminate any conductive or convective thermal transport from residual gas in the cryostat.

A ^{3}He / ^{4}He adsorption refrigerator system is then used to maintain the focal plane at around 300 mK. This system was initially designed by Mark Devlin's group at the University of Pennsylvania [21], and then constructed and optimized at Princeton for use in the CCAM instrument [55, 57]. The 4 K base temperature provided by the pulse tubes is sufficient to liquify a quantity of ^{4}He. The refrigerator then has a charcoal adsorption pump, which is initially kept at an elevated temperature of 40 K. By connecting the charcoal to the 4 K base plate through a heat switch, the charcoal begins to adsorb helium, reducing the pressure above the pot of liquid ^{4}He and evaporatively cooling it to a temperature of around 800 mK.

This process is repeated with a ^{3}He system to achieve temperatures below 300 mK. The

[1] ABS uses one PT407 and one PT410 from Cryomech, Inc., 113 Falso Drive, Syracuse, New York, 13211

cold plate of one ^{4}He refrigerator is used to liquify a volume of ^{3}He, which is then pumped on to evaporatively cool it. With no loading, the cold plate of the ^{3}He refrigerator has been maintained at 217 mK. With the thermal loading of ~ 10 μW it experiences in the cryostat under operating conditions, its cold plate typically reaches 250 mK.

3.2 Optical Design

ABS uses a crossed-Dragone optical configuration, which was chosen for its compactness, large focal plane for a given reflector size, and low cross-polarization leakage[22, 23, 94]. Crossed Dragonian configurations have been chosen by other CMB experiments for these same reasons, most notably C$_\ell$over [77] and QUIET [72]. Such an all-reflector design would also simplify the transition to a multi-frequency device, as the HWP is the only optical element that would need to be significantly changed. Our design is unique in that the primary and secondary reflectors are kept at 4 K within the cryostat to reduce loading from the reflectors on the detectors and maintain the reflectors at a constant, well-known temperature. The ability to place an aperture stop at 4 K drove much of the ABS optical design and is to the best of our knowledge unique to our design. This ensures that any beam spillover lands on only cold optical elements. It also allows the placement of the ABS HWP skyward of all other optical elements, meaning that any instrumental polarization is not modulated along with the sky polarization.

A crossed-Dragone telescope consists of a concave parabolic primary reflector which shares its focus with one of the focal points of a concave hyperbolic secondary reflector. The second focus of the secondary hyperboloid is at the focal plane. Optimization of crossed-Dragone imaging systems to yield near-zero cross-polarization is described in the literature [15]. With this as a starting point, Silviu Pufu, along with Princeton undergraduate student Cary Malkiewich, further optimized the design using the ray-tracing software CodeV [79, 28]. His final design, shown in Figure 3.2, is compact enough to fit within the ABS cryostat while giving good optical quality over a focal plane large enough to accommodate 240 detectors. The primary and secondary reflectors are 57.1 cm and 58.5 cm in diameter,

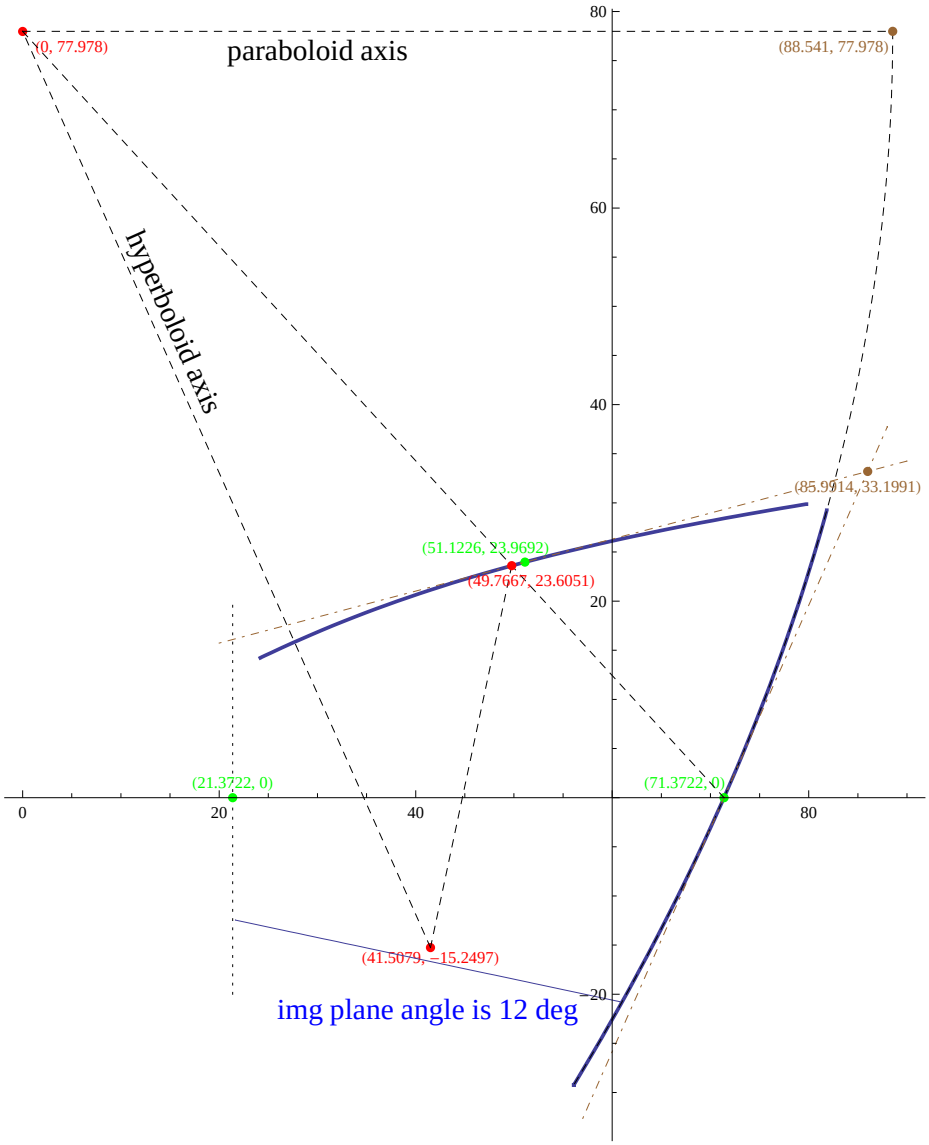

Figure 3.2: Layout of the primary reflector paraboloid, secondary reflector hyperboloid, focal plane, and aperture stop. All units are in centimeters. The sky is to the left. The optical axis of the telescope is the x axis. The primary reflector was machined out to a diameter of 58.5 cm (the figure shows it extending further down than this). The secondary reflector was machined out to a diameter of 57.1 cm. Both reflector diameters are measured in a plane tangent to the mirror surfaces at their centers. The green point at (51.1226, 23.9692) is the center of the secondary, whereas the red point at (49.7667 cm, 23.6051 cm) is where a ray following the optical axis and striking the primary at its center strikes the secondary. The center of the focal plane is the place where this ray intersects the focal plane. Figure courtesy of Silviu Pufu.

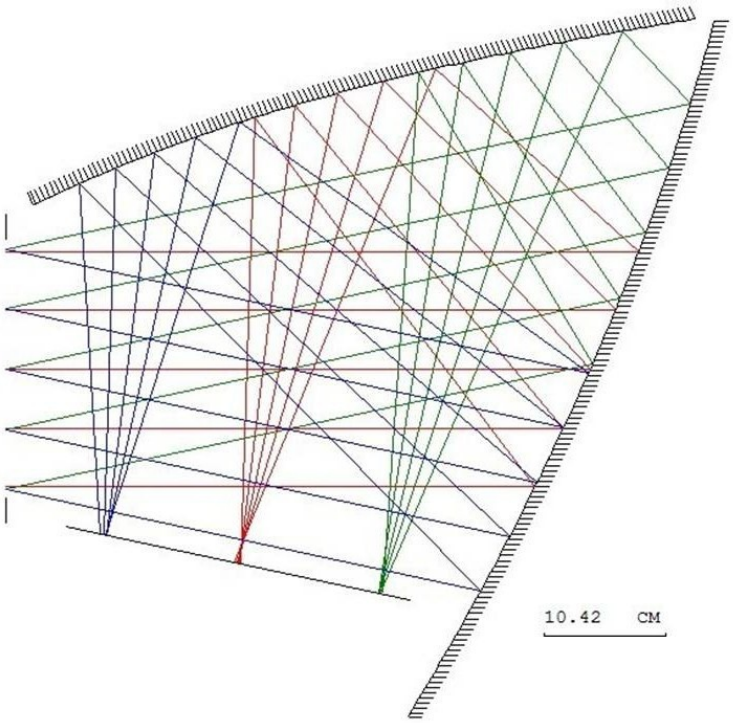

Figure 3.3: CodeV ray tracing diagram for the final ABS reflector design. The sky is to the left in the figure. The focal plane is at the bottom, primary reflector at right, and secondary reflector at the top. All rays of the same color correspond to rays coming in at the same angle from the sky and converge on approximately the same point in the focal plane. Figure courtesy of Silviu Pufu.

respectively. CodeV outputs for the final optical design are shown in Figures 3.3 and 3.4.

3.2.1 Physical Optics Simulations with DADRA

Once the optical design had been optimized using the CodeV ray-tracing software, it was further verified using the DADRA program[2] . This code performs a physical optics analysis of the feedhorn, primary reflector, and secondary reflector system of ABS. The radiation pattern from the feedhorns was simulated using CCORHRN and then input into DADRA along with the shapes of the primary and secondary reflectors. DADRA generates complex three-dimensional, electric-field data in the plane of the 4 K aperture stop. With a separate

[2]Diffraction Analysis of a Dual Reflector Antenna, Rahmat-Samii, Y., Imbriale, W., & Galindo-Israel, V., YRS Associates

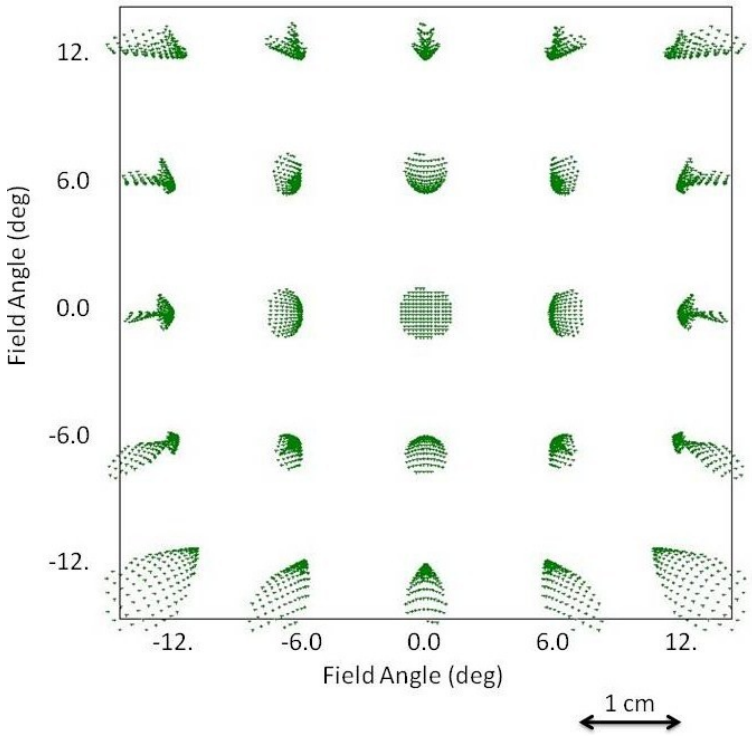

Figure 3.4: CodeV spot diagram for the final ABS optical design. Each group of spots represents rays entering the cryostat at the same angle. The x- and y-axis show this angle away from the center of the array on the sky. Each spot diagram then shows the spread of the rays in centimeters in the focal plane, with the plate scale shown in the bottom right of the figure. For reference the feedhorn physical aperture is 1 cm. Figure courtesy of Silviu Pufu

program, these data were then truncated and set to zero outside of the 25-cm aperture for ABS. A Fast Fourier Transform (FFT) was performed to simulate the beam on the sky. The resulting copolar beams for one probe of all 240 feedhorns of ABS are shown in Figure 3.5.

Determination of Feedhorn Angles

The angle of each feedhorn in the ABS focal plane was a free parameter. The electromechanical design of the focal plane would have been simplified by arranging the feedhorns either all at the same angle or at one of a few angles; however, it was found that the integrated copolar beam difference, defined as the point-by-point integral of the difference

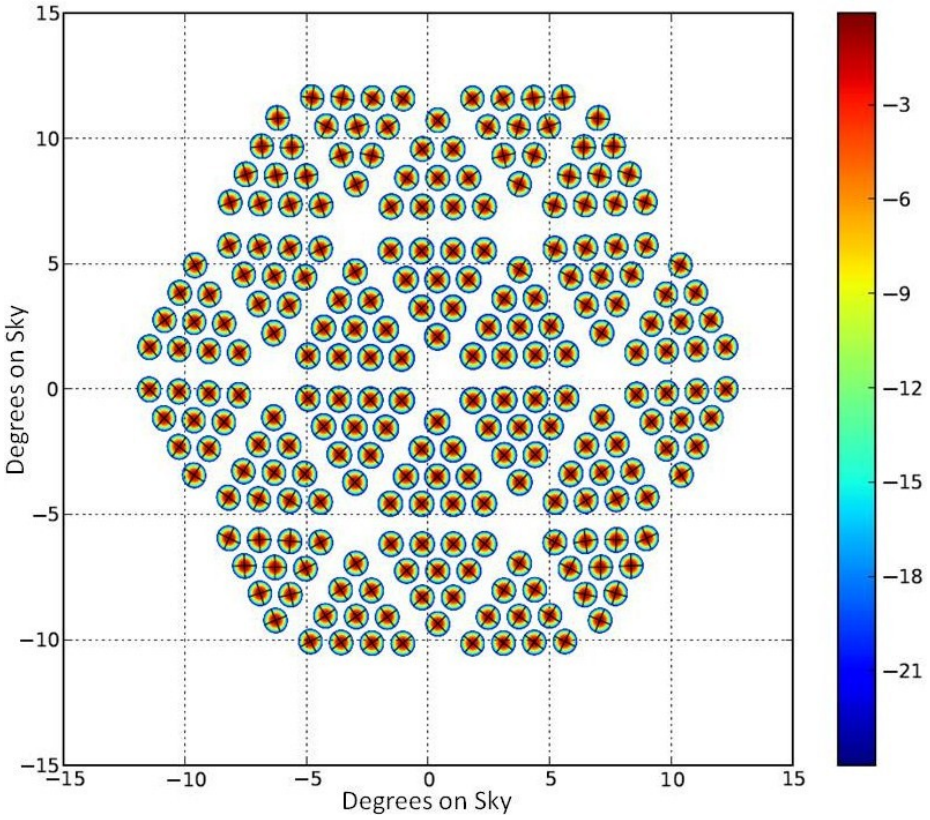

Figure 3.5: Copolar beams (in dB on right colorbar) of one probe of each of the 240 ABS feedhorns, with polarization angles for the two probes shown as solid black lines. Each triangular group of ten beams comprises a "pod" in the focal plane. There are 24 pods.

between the two beams from detectors in the same feedhorn,

$$\Delta B = \int\int d\Omega \, |B_A^{co}(\theta,\phi) - B_B^{co}(\theta,\phi)| \tag{3.1}$$

could vary considerably depending upon feedhorn orientation. If the two beams from a given feedhorn are subtracted to eliminate common-mode noise, from the atmosphere for example, a difference in the shape of the two beams on the sky can lead to temperature-to-polarization leakage. To reduce the level at which temperature is leaked into polarization, an optimization was performed for each feedhorn, in which ΔB was calculated at 1° increments. The angle for each feedhorn in the focal plane was then chosen to minimize the beam difference calculated in this way. The pod interface plates, described in Section 3.3.3,

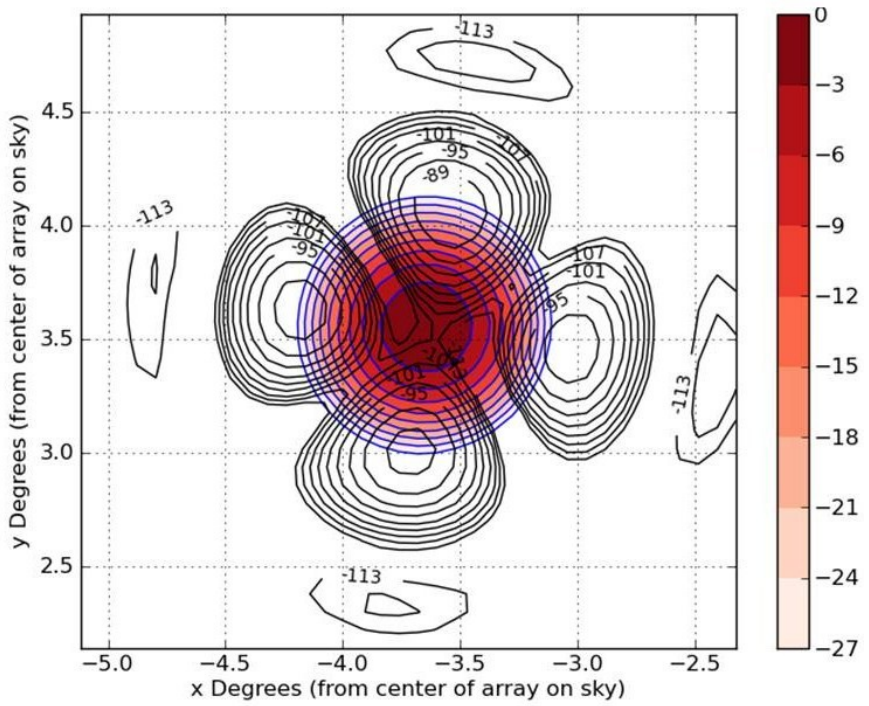

Figure 3.6: Simulated co- and crosspolar beams in dB for a feedhorn near the center of the array from DADRA. The copolar beam magnitude as a function of position on the sky is shown as red fill corresponding to the color scale on the right. Blue lines demarcate the borders between the colorbar cutoffs. Crosspolar contours show dB relative to the copolar maximum.

set the feedhorn orientations in each pod. The pod interface plates were made with bolt patterns peculiar to each of the 24 pods in the focal plane.

DADRA Estimates of Beam Systematics

The DADRA program outputs were also used to estimate the edge taper on the cold aperture stop, beam centers, beam widths, and polarization angles for ABS detectors. A number of other systematic effects were explored with DADRA as well. Estimates for all 240 ABS feedhorns were made of the level of crosspolar contamination, beam ellipticity, differential beam, and beam squint. Sample copolar and crosspolar beams for a horn at 145 GHz toward the center of the array are shown in Figure 3.6.

For each copolar beam, a least-squares fit was performed to an elliptical Airy function

of the form

$$\begin{aligned} B(\theta_x, \theta_y) &= (\tfrac{2J_1(r)}{r})^2 \\ r &= \sqrt{\left(\tfrac{(\theta_x \cos\alpha - \theta_y \sin\alpha) - x_0}{\Delta x}\right)^2 + \left(\tfrac{(\theta_x \sin\alpha + \theta_y \cos\alpha) - y_0}{\Delta y}\right)^2} \end{aligned}, \tag{3.2}$$

where θ_x and θ_y are angular positions on the sky; α is the rotation angle of the beam ellipse; Δx and Δy are beam widths; x_0 and y_0 are beam centers; and, $J_1(r)$ is the first-order Bessel function. For each beam the ellipticity was calculated as

$$\epsilon = \left|\frac{\Delta x - \Delta y}{\Delta x + \Delta y}\right| \times 100\%. \tag{3.3}$$

The average beam width is $\theta_{\mathrm{FWHM}} = (\theta_x + \theta_y)/2$. The beam squint, ξ, is the distance between the beam centers for the two copolar beams from a given feedhorn.

In addition to the quantities derived from the elliptical Airy disk fit, the differential copolar beam response was calculated according to Equation 3.1; the integrated crosspolar response, relative to the copolar response, was calculated; and, the average polarization angle for each copolar beam was calculated. The polarization angle for each copolar beam was calculated point-by-point as

$$\tan^{-1} |E_x|/|E_y|, \tag{3.4}$$

and these angles were averaged within the -9 dB contour of the beam. This was done to eliminate noise caused by random polarization angle fluctuations for points far from the beam center that have little contribution to the beam response. A number of different cutoffs, in dB, were investigated for a small number of beams, and negligible difference was found between the polarization angle derived from cutoffs of -3, -6, -9, or -12 dB. The value of $\Delta\phi_{\pi/2}$ quoted in Table 3.1 is the deviation from 90° of the difference between the polarization angles of the two beams from the same feedhorn. The edge taper on the cold aperture stop was estimated from DADRA using the electric-field magnitudes in the aperture plane. The value of $\mathrm{P}_{\mathrm{stop}}$ quoted in Table 3.1 is the intensity, in dB down from the maximum, at the rim of the aperture stop.

θ_{FWHM} [deg]	ϵ [%]	$\Delta\phi_{\pi/2}$ [deg]	χ [dB]	ΔB [dB]	ξ [arcsec]	$\mathrm{P_{stop}}$ [dB]
0.682 ± 0.007	2.72 ± 1.1	−1.4± 0.68	-72.4 ± 4.7	-46.1 ± 15.8	0.22 ± 0.31	-10.4 ± 0.9

Table 3.1: DADRA estimates of the beam width, W_B; ellipticity, ϵ; deviation of the polarization angles from 90°, $\Delta\phi_{\pi/2}$; crosspolar response, χ; beam difference, ΔB; and, beam squint, ξ, across the focal plane at 145 GHz. The mean and standard deviation of the quantities as estimated by DADRA for all feedhorns is also shown.

Plots showing the variation of these quantities across the focal plane at the lower edge, center, and upper edge of the ABS frequency band at 127, 145, and 163 GHz are collected in Appendix A. All beam quantities estimated by DADRA are also tabulated there. The average values of these quantities across the focal plane are shown in Table 3.1.

3.2.2 4 K Optics Mechanical Design

The primary and secondary reflectors were machined using a computer-numerical-control (CNC) milling machine at Princeton. The reflectors were machined out of 1.9-cm-thick aluminum to a surface RMS of 23 μm. The reflectors were larger than the horizontal throw of the milling machine, so the reflector surfaces were machined in two halves. The back side of each reflector had ribs machined in it with the CNC mill to reduce thermal mass and weight. The milling machine was programmed to cut to within 3.2 mm of front mirror surface. The code written to program the CNC mill to cut the primary and secondary reflector surfaces, along with mechanical drawings of the outer dimensions of the reflector pieces, are shown in an appendix, Section B.3.

The primary and secondary reflectors weigh 7.8 and 5.9 kg, respectively. At 4K, the specific heat of aluminum is approximately 0.3 J kg^{-1} K^{-13} . The primary and secondary reflectors thus have heat capacities of approximately 2.3 and 1.7 J/K, respectively. The overall mechanical design is shown in Figure 3.7. Two angled mirror supports, only one of which is visible in the figure, attach the primary reflector to the 4 K baseplate and ensure that the primary reflector is at the correct angle with regard to the optical axis. The

[3]NIST Cryogenic Material Properties, cryogenics.nist.gov/MPropsMAY/material%20properties.htm

secondary reflector bolts to the primary reflector at the bottom and is held at the proper angle by two cross braces. Only one brace is visible in the figure. Brass pins 3.2 mm in diameter precisely align the primary and secondary reflectors with the cross brace. All of these parts are machined out of aluminum and lightweighted where possible.

Two aluminum brackets bolt into the primary reflector and hold the focal plane assembly at the proper angle relative to the reflectors. The brackets are aligned with the primary reflector and the focal plane with the brackets using 3.2-mm brass pins fit into holes. Tight mechanical tolerances were maintained in the machining of the entire assembly, such that the reflectors and focal plane are held at the proper angles relative to each other to within 0.25°. All dimensions were also scaled to take into account the thermal contraction of aluminum from room temperature to 4 K, which is approximately 0.4% [78].

3.3 Focal Plane Design

3.3.1 Focal Plane Support

The focal plane support, hereafter FPS, holds the 24 pods of ABS and provides thermal contact with the 300 mK stage of the cryogenics. Due to the compact design of the reflectors, the maximum aperture that could be fit without beams being clipped by the secondary reflector was 25 cm. As described in Table 3.1, this leads to edge tapers at the exit to the cryostat of -10.4 dB on average. Assuming a Gaussion beam profile at the aperture stop, which is at least approximately valid, this means that 9.2% of the power contained in the beam of the feedhorn (looking at the optics in the time-reversed sense) spills onto the cold stop. This also means that the optical efficiency through the aperture stop is only 90.8%.

To ensure good optical efficiency and reduce unnecessary loading and beam clipping from the 4 K aperture stop, the FPS was designed to place each pod at a unique angle which sent a ray from the central feedhorn of each pod, as modeled in CodeV software, through the center of the aperture stop. These angles are small at the center of the array and increase to as much as 4° toward the edge of the array. The FPS is a spider-web copper

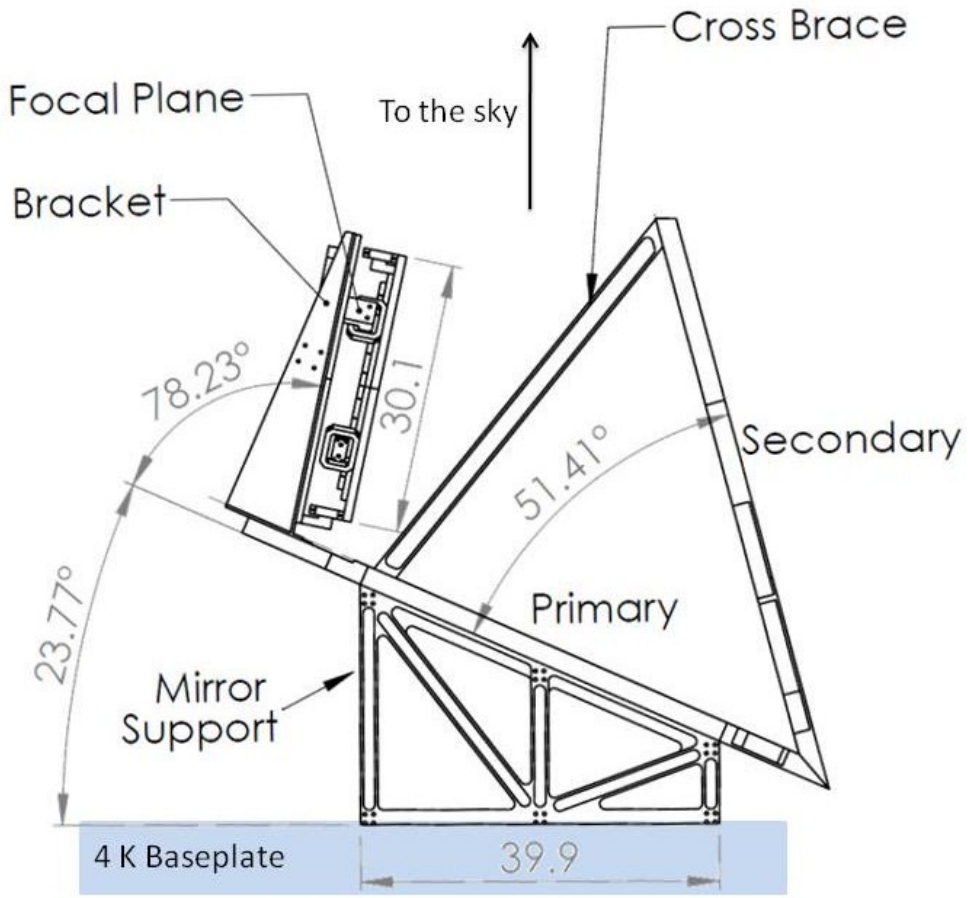

Figure 3.7: Angles of reflectors, focal plane, and supporting structures in ABS. Dimensions are in centimeters.

structure, shown in Figure 3.8 mounted in the focal plane. The web supports between pods are 3.2 mm wide and 5.9-8.5 cm thick, being thicker at the edges of the FPS and thinner in the middle. Each pod bolts into the FPS in three places with 4-40 screws fitted with belleville spring washers to maintain bolting force, which is tied strongly to thermal conductivity across the joint, as the pieces contract relative to one another as they cool from room temperature to 300 mK. After machining, the piece was electroplated with gold to increase thermal conduction at the pod-FPS interfaces. Copper can form an oxide layer that reduces thermal conductivity bolted joints. Gold does not form such an oxide.

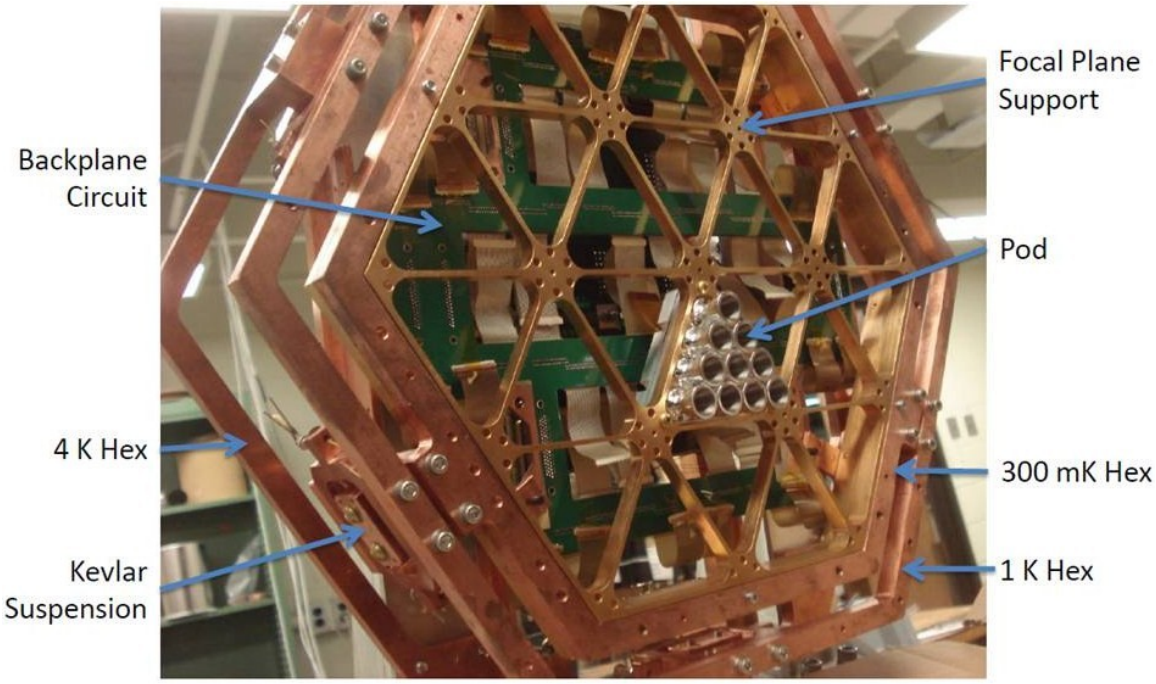

Figure 3.8: Photograph of the focal plane with major one pod installed, making the backplane circuit visible.

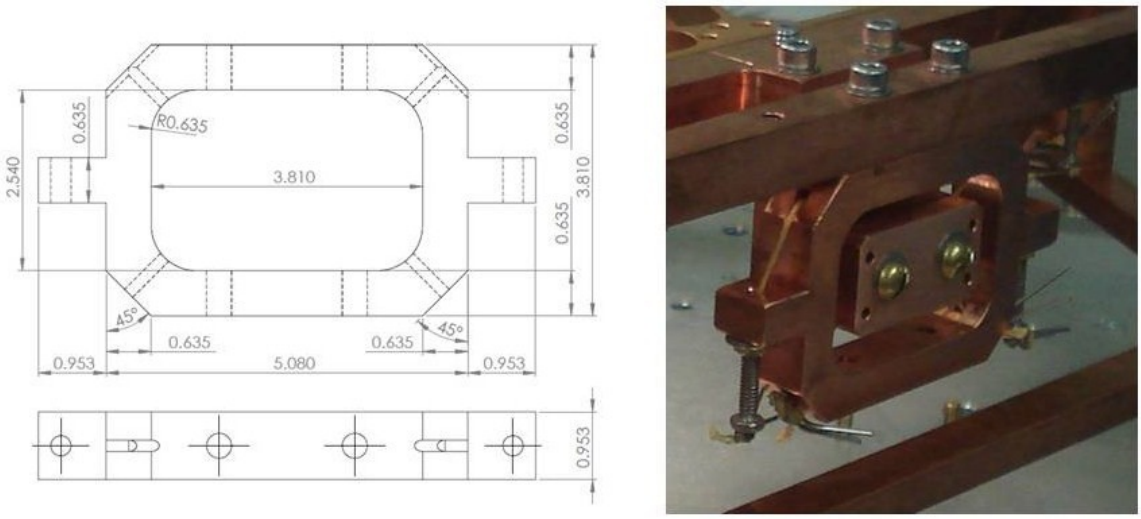

Figure 3.9: *Left:* Drawing of the Kevlar tensioning frame. Kevlar threads go through the four 45° holes in the frame and around pins on a mating L-bracket piece. *Right:* Photograph of a tensioned Kevlar suspension.

The FPS was machined by an outside shop[4] with a five-axis milling machine. This allowed the machine tool to be placed at any orientation so that flats could be machined for each pod at its own angle. The part was first machined out of aluminum as a test piece before attempting the more difficult, softer copper. The machining was done in multiple stages to allow internal stresses in the copper to work themselves out before the final high-precision cuts were made. After machining, the part was brought back to Princeton and its tolerances tested on a milling machine by bringing a ball mill that was not being turned close to the piece. The X, Y, and Z positions of all bolt holes for holding the pods was determined in this way to be within 75 μm of their ideal positions.

3.3.2 Kevlar Thermal Isolation Suspension

The 300 mK stage of the cryogenic system needs to have all sources of thermal loading reduced to below 10 μW if it is to maintain a low base temperature and long hold times. This requires that the mechanical support for the FPS place no more than a few μW of thermal loading on the 300 mK stage, while holding the FPS against accelerations of up to a few times the acceleration of gravity. The system chosen for ABS was a set of tensioned-Kevlar supports, shown in Figure 3.8. Three supports hold the 300 mK focal plane to the 1 K hexagon, and three more hold the 1 K hexagon to the 4 K hexagon.

Kevlar is a polymer with good mechanical strength and low thermal conductivity that can be spun into threads. Kevlar thread is readily available in a variety of thicknesses. The thread used for the ABS focal-plane suspension is 635 μm thick. This has an approximate tensile strength of 270 N, and a thermal conductivity of 3.9×10^{-5} $T^{1.71}$ W cm^{-1} K^{-1} [78]. If the Kevlar thread were solid, which it is not, the cross-sectional area would be 4×10^{-3} cm^2. The threads travel a minimum of 0.75 cm between the 300 mK and 1 K stages. This implies that the thermal load on the 300 mK stage of each thread is no more than 150 nW. The twelve threads holding the 300 mK to the 1 K stage combined then load the 300 mK stage by no more than 1.8 μW.

[4]RJD Machine Products Inc., 1424 Heath Avenue, Trenton, NJ 08638. (609) 392-1098. www.rjdmachineproducts.com

Kevlar thread is known to relax slowly under tension, so the thread used for the suspension was left tensioned with a 11.3 kg weight for two weeks before being tensioned in the support. The Kevlar lengthened in that time by as much as 2.5%. After the length stopped changing, the Kevlar was cut to length in preparation for tensioning. A small cotter pin was bent around one end of each Kevlar thread and epoxied in place using Stycast 2865.

The focal plane, 1 K hexagon, and 4 K hexagon were placed in a jig designed to hold the three elements in the correct position relative to one another while being tensioned. The jig had 3.2 mm brass pins which located the three parts precisely relative to the jig. The six Kevlar tensioning frames that the Kevlar threads through, shown in Figure 3.9, were bolted in place. There are two Kevlar threads per tensioning frame. Each thread goes through one of the bottom holes in the frame, wraps around two brass pins on the L bracket, and then up through the corresponding upper hole in the frame. The cotter pin on each Kevlar thread keeps the thread from coming through the bottom hole.

The Kevlar thread runs from the top hole of the tensioning frame through a vented 4-40 screw. Before assembly, these screws were carefully inspected under a microscope and any burrs were removed with a file to reduce the risk of wear on the Kevlar thread. The screws thread through holes in the tensioning frame. These screws also had a nut and two back-to-back belleville spring washers installed on their end A cotter pin was bent onto the end near the cap of the screw. Epoxy was applied to the thread on the cotter pin to hold it firmly in place. While all pieces were firmly held in place by the tensioning jig, each Kevlar thread was tensioned by slowly turning the screw. As the screw threaded out of the hole, it pulled the Kevlar taut. Each Kevlar thread was pulled just barely taut, then a second round of tensioning was performed on each thread to make it fully taut. The entire assembly was left to sit overnight, to allow the Kevlar to lengthen if it were going to. This procedure was repeated for two more days until the Kevlar no longer relaxed overnight.

3.3.3 Pod Design

The feedhorn-coupled TES polarimeters described in the previous section are arranged in "pods" of ten feedhorns each, with twenty-four pods comprising the entire focal plane. The pods and their supporting structure were designed with a number of mechanical, thermal, and electromagnetic constraints, including (1) proper position and angle of the horns relative to the secondary reflector; (2) compact design allowing close-packed detectors; (3) firm mechanical support free of strong resonances with the pulse-tube frequency; (4) good thermal contact of all components with the ^{3}He/^{4}He sorption fridge cold head at a nominal temperature of 300 mK; (5) thermal isolation from the 4K bath; (6) low impedance in the TES readout loop; (6) magnetic shielding, especially of the multiplexing SQUID chip; and lastly, (7) ease of assembly and robustness.

Individual detector chips, with backshorts attached as described in Section 3.3.6 below, are glued onto the bottom of each feedhorn. The feedhorn detector package has a boss machined into the bottom of it to allow alignment of the detector chip to the waveguide of the feedhorn. Figure 3.10 shows the geometry of this boss.

Ten feedhorns are assembled into a triangular pod. The pod interface plate holds each feedhorn at a unique angle, chosen to minimize beam mismatch between the two orthogonal polarizations from a given detector. The TES and heater lines from each detector are connected to a specialized aluminum circuit board by aluminum wirebonds. The wirebonding for ABS was performed by Bert Harrop. Aluminum was chosen for the circuit-board material because it goes superconducting at around 1.2 K, and thus introduces no additional resistance to the TES loop. The board is split into two rigidized areas, with a flexible bridge between them. One side of the board carries detector signals from each detector chip. The other side of the board holds the interface chip with the shunt resistors and Nyquist inductors, as well as the MUX chip. The flexible bridge between them allows the MUX side of the board to fold over, placing all of the readout circuitry in a compact configuration directly behind the detector feedhorns.

The pod assembly has been perfected by John Appel and Emily Grace. It proceeds

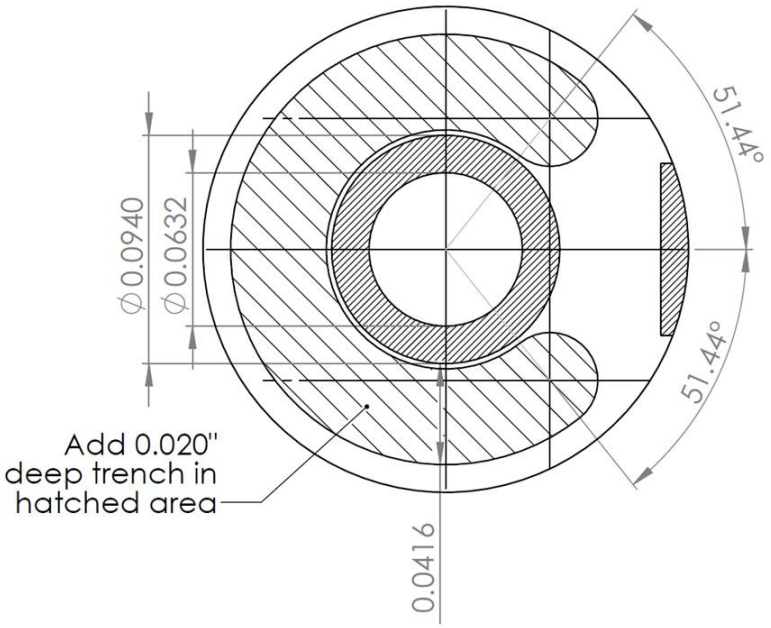

Figure 3.10: Geometry of bottom of feedhorn where detector chips are glued, showing crescent-shaped trench (widely-spaced hatches) that is blackened to dampen reflected radiation and raised bosses (finely-hatched area) for detector chip alignment and $\lambda/4$ cavity creation. Dimensions are in inches. The detector bondpads that are at the bottom of Figure 3.16 point toward the small raised boss on right. A flat on the detector chip abuts this boss for alignment.

as follows. First feedhorns are assembled and their beams are mapped. Those feedhorns with beam maps that show unwanted asymmetry or overly-wide beams had their top and bottom pieces shuffled until combinations were found with good beam maps. In most cases, shuffling produced the desired improvements in beam quality. After feedhorns were tested, they were mounted to the pod interface plate. The detector chips with backshorts were then epoxied in place. All epoxy used in the ABS pods was Scotch-Weld$^{\text{TM}}$2216 two-part adhesive. Separately, the top niobium sheet was glued to the back of the MUX side of the pod-readout board. The pod-readout board was then glued to the pod interface plate. The MUX and shunt chips, described below, were glued to the top niobium sheet, and wirebonds were laid down between the readout board and the MUX, shunt, and detector chips. The bottom niobium sheet was placed on spacers above the detector chips, and the MUX side

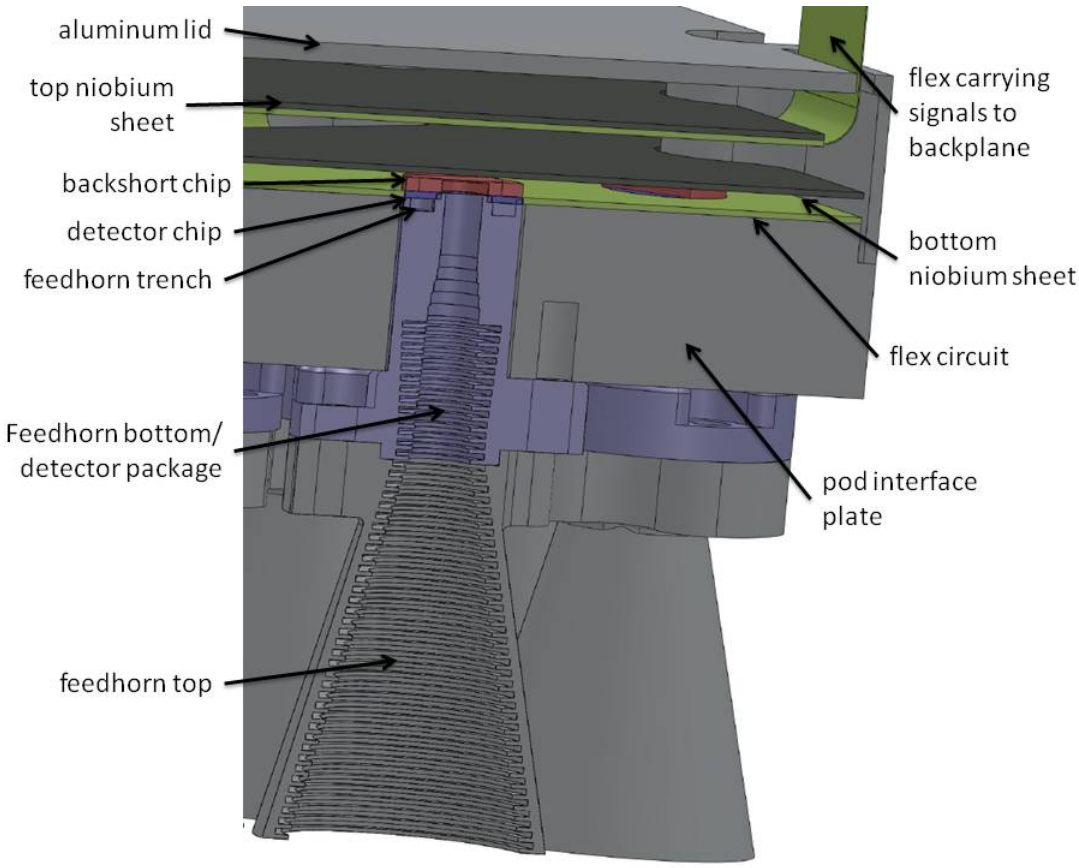

Figure 3.11: Section view of a pod, with major components indicated.

of the readout board, with the top niobium sheet glued to it, was folded over and secured with nuts. A 2-56 rod threads into the pod interface plate and passes through the readout board and niobium sheets. This allows washers to be placed as spacers at the three corners of each board, and a nut to clamp down the entire stack. The flex that carries signals to the backplane circuit is then threaded through a slot in the aluminum lid of the pod, and the lid is fastened at six points with 2-56 screws.

Superconducting Aluminum Flexible Circuitry

The hybrid pod readout circuit board used in ABS is a central component of the overall pod design. It incorporates superconducting aluminum traces between the shunt chip and detector chips. To the best of our knowledge, ABS will be the first instrument to deploy

superconducting aluminum flex circuits in a millimeter-wave telescope receiver. We worked closely with the circuit board company[5] to determine the fabrication limitations for these boards, including minimum pitch (250 μm pitch was the minimum pitch found to produce reliable results) and minimum bend radius (the ABS boards bend at 5-mm radius between the detector and MUX sides of the board). The minimum pitch could be reduced further, possibly to 6 μm, if one is not going to have the boards bend with a small radius.

Because of issues in getting aluminum traces to reliably connect with the zero-insertion-force (ZIF) connectors used in ABS, the traces from the MUX chip out of the pod are gold-plated copper. While the company making the detector readout circuits has the capability to produce boards with different metalization on different parts of the board, this would have represented an additional engineering challenge with the possibility of delays. As such, the ABS boards were made in two parts: (1) an aluminum circuit board that bolts to the pod interface plate and carries signals from the detectors to the shunt chip, and (2) a gold-plated copper circuit that carries signals from the MUX chip through a flexible bridge to the ZIF connectors on the backplane circuit.

As detailed in Figure 3.12, the circuit board is rigidized in two portions with flexible bridges between the rigid sections. This allows the MUX and shunt chips to be placed directly behind the feedhorns and facing the detector chips, which is critical in keeping the pods compact and close-packed across the focal plane. This also facilitates the placement of sheets of niobium, a superconductor with a transition temperature of 9.3 K, above and below the MUX chip to shield the SQUIDs from magnetic fields. A thin flexible kapton bridge runs from the rigidized portion of the Au/Cu circuit board, out through a thin hole in the aluminum lid of the pod, and out to a ZIF connector on the backplane circuit.

The technology to make aluminum circuit boards is at present not as mature as the industry-standard copper circuit-board technology. Aluminum circuit boards have begun to be made by a small set of companies for niche markets in which either the rising price of copper allows aluminum circuits to be cheaper when produced in bulk or when the

[5]Tech-Etch, Incorporated, 45 Aldrin Road, Plymouth, MA 02360. www.tech-etch.com

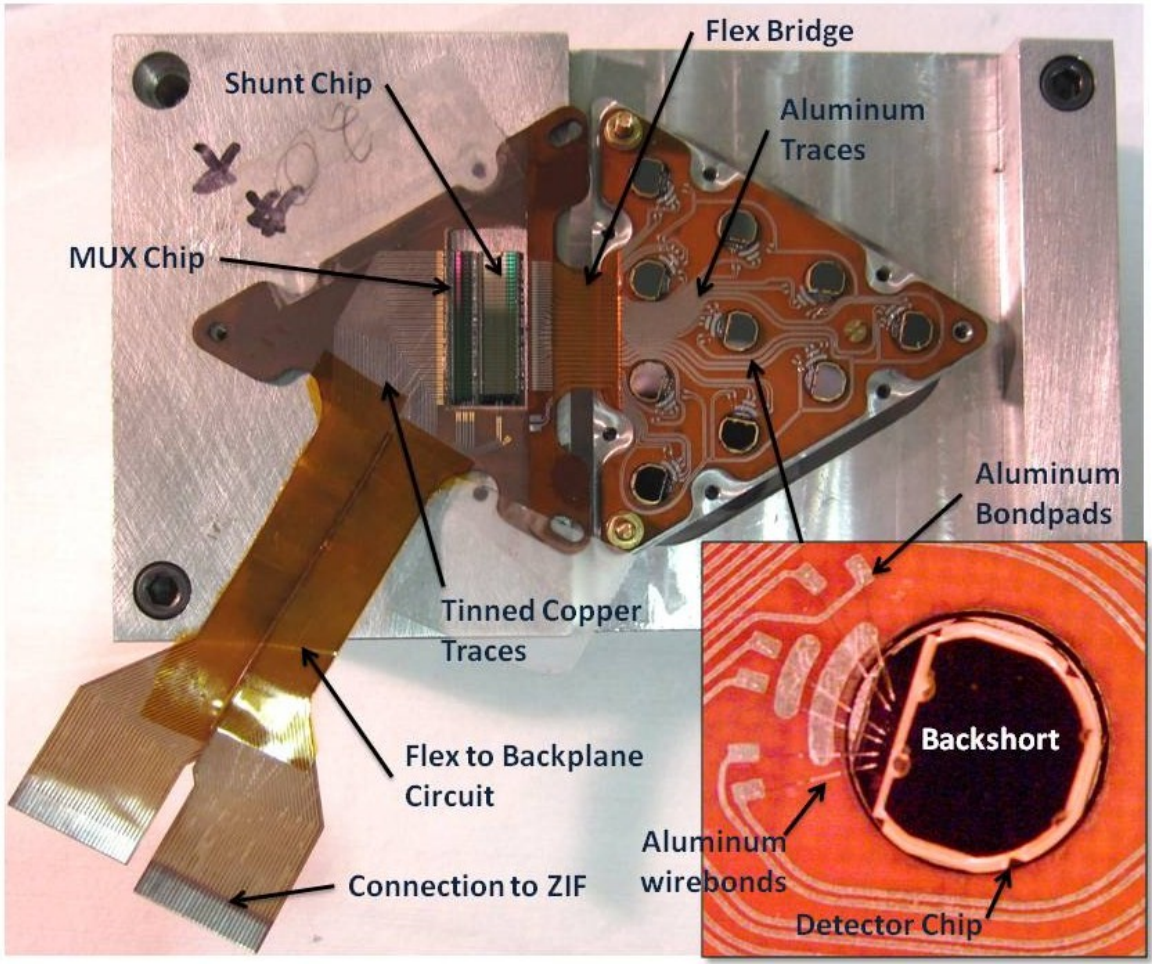

Figure 3.12: Photograph of an ABS pod unfolded in the wirebonding jig. Major components are indicated. The detector side of the circuit board, on the right, has aluminum traces. The circuit board on the left, which carries signals from the MUX chip to the backplane circuit, is tinned copper with gold plating where wirebonds are made to the MUX chip. The left triangular section folds over the right circuit board. A rectangular hole is cut in the circuit boards, and the MUX and shunt chips are directly glued onto the top niobium sheet.

aluminum provides certain performance advantages, as in very low-temperature applications where aluminum traces are superconducting. The aluminum wire-bonding machine used to connect the detector chips to the readout circuit are also made more reliable when bonding to aluminum bond pads.

The aluminum circuits for ABS were made by first bonding 25-μm aluminum 5052

sheets to a 25-μm flexible polyimide base layer with 25 μm of a proprietary adhesive. The aluminum is then patterned using standard photolithography processes. The rigidized sections are made by bonding 250-μm thick FR4 to the back (non-patterned) side of the polyimide with 50 μm of adhesive.

A combination of the material properties of aluminum and the presence of non-rigid adhesive between the aluminum traces and the polyimide base layer place limits on how thin traces can be made. The circuit boards were originally designed with 150-μm pitch, but this was found to lead to too many defects. Defects seemed to form particularly where flexible bridges met with rigid sections. The pitch was eventually increased to a minimum of 250-μm, and up to 500 μm where possible. This meant that only one dark TES could be read out per pod, but this seemed to be a good trade-off for increased reliability.

The adhesive under the aluminum traces also created difficulties in wirebonding if the bond pads were made too small. Because the feedhorn angles are optimized pod by pod, semicircular bond pads 178 μm wide were originally chosen, to give easy bonding regardless of feedhorn, and hence detector bondpad, orientation. These bondpads, while much wider than normally needed for aluminum bondpads, were found to be insufficient. The wirebonding machine had to be set to maximum power to get bonds to adhere, and even when adhered, the pull strength of the bonds was low. The final design incorporates 508 μm by 508 μm bondpads, with greater bond lengths needed to get from the circuit board bondpads to those on the detector chips. This has increased bond reliability and strength.

3.3.4 Feedhorn Design

The feedhorns for ABS were optimized using CCORHRN, a finite-element simulation that solves Maxwell's equations in a set of rings. The optimization was done by Jennifer Lin, a Princeton undergraduate. The feedhorns were designed to give high transmission and single-moded performance across the ABS bandpass. The voltage standing-wave ratio (VSWR) and gain of the feedhorns versus frequency is given in Figure 3.13. The VSWR is the ratio between the voltage at a node and a voltage at an antinode of standing waves set up

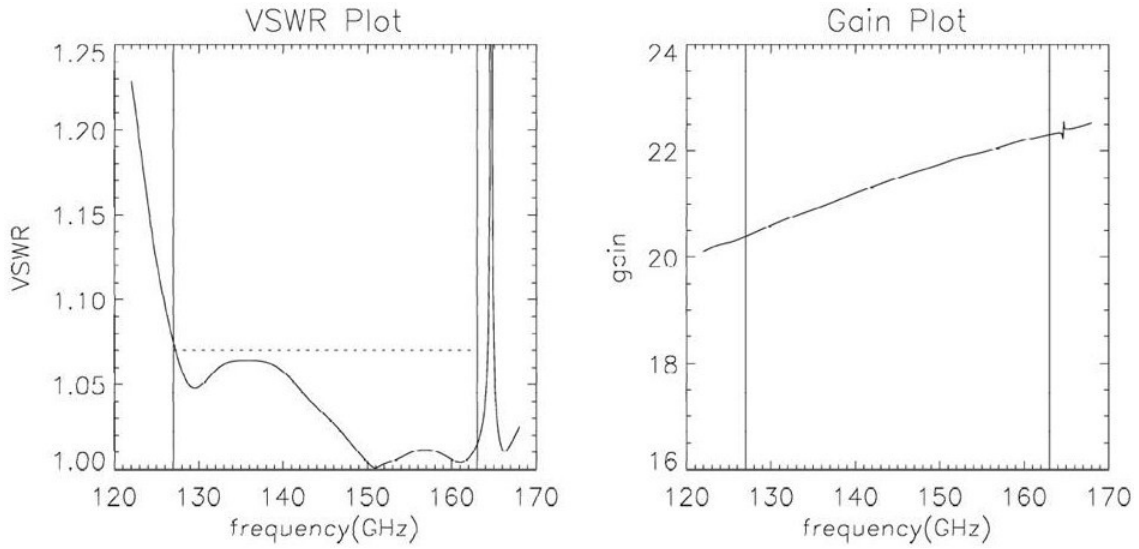

Figure 3.13: Simulated voltage standing-wave ratio (VSWR) and gain (in dB), as defined in the text, versus frequency over the instrument passband for the ABS horns. Figure courtesy of Jennifer Lin.

in the feedhorn. A ratio of unity indicates a lack of standing waves in the feedhorn and correspondingly maximum power transmission. VSWR is intimately tied to the reflection coefficient via the formula

$$R = \frac{VSWR - 1}{VSWR + 1} \tag{3.5}$$

The VSWR for the ABS horns is expected from CCORHRN simulations to be smaller than 1.12 across the instrument passband (127-163 GHz), indicating a reflectance of no more than 5.7%. The gain of the feedhorn is the efficiency of the feedhorn multiplied by its directivity, the ratio of the power radiated in a particular direction to that radiated in all directions. The value plotted versus frequency in Figure 3.13 is the maximum gain achieved in all directions, and is a measure of the beam solid angle. This is given by G= $4\pi/\Omega_b$.

The corrugated design of the feed draws the fields away from the metallic walls, giving generally lower crosspolar response and resistive loss than smooth-walled feedhorns. A beam-mapping range was built by Katerina Visnjic to individually test the ABS feedhorns before being placed in the focal plane. This consisted of a narrow-band source centered at

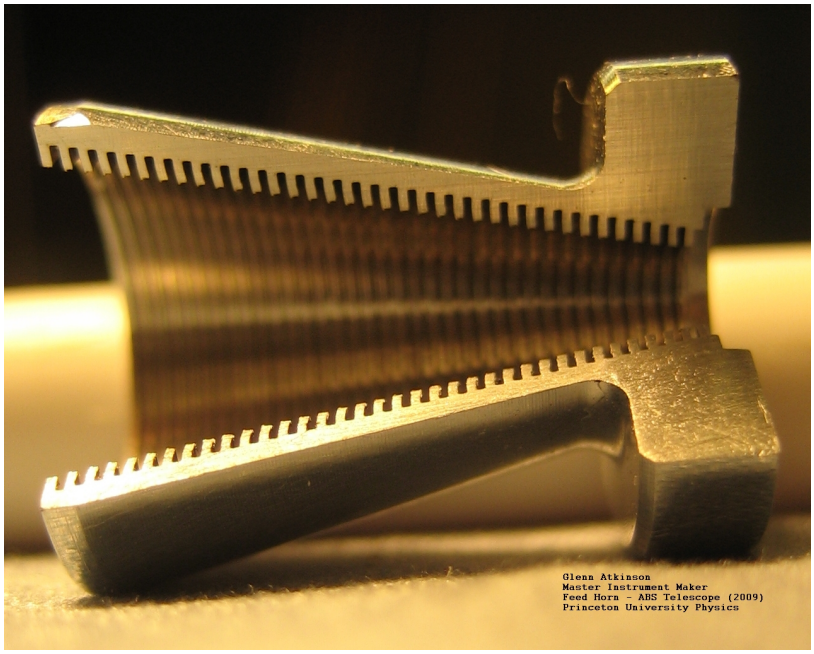

Figure 3.14: Photograph of the top portion of a feedhorn with one quarter cut out so that the corrugations are visible.

145 GHz placed approximately in the far field 0.5 meters from the feedhorn being measured. The feedhorn was placed on a rotating stage, and a broadband receiver at the base of the feedhorn measured the response of the feedhorn versus angle relative to the source. This range allowed the copolar beam of the feedhorn to be measured at the central frequency in our band.

A representative copolar beam map is shown in Figure 3.15. The range was built to ensure that feedhorns had no anomalies in the main lobe and no excessive sidelobes. The noise in the maps, generally at a level of -30 dB from the copolar maximum, was too high to get far-sidelobe structure in the copolar beams above 30 degrees from center or to see crosspolar response. This does place an upper limit on the crosspolar response of the feedhorn at -30 dB down from the copolar maximum.

The feedhorns were directly machined at Princeton by Glenn Atkinson using a custom-made 90° steel tool on a computer numerical control (CNC) lathe. The feedhorn corrugations, are only 250 μm wide and up to 984 μm deep. The extremely narrow tool needed

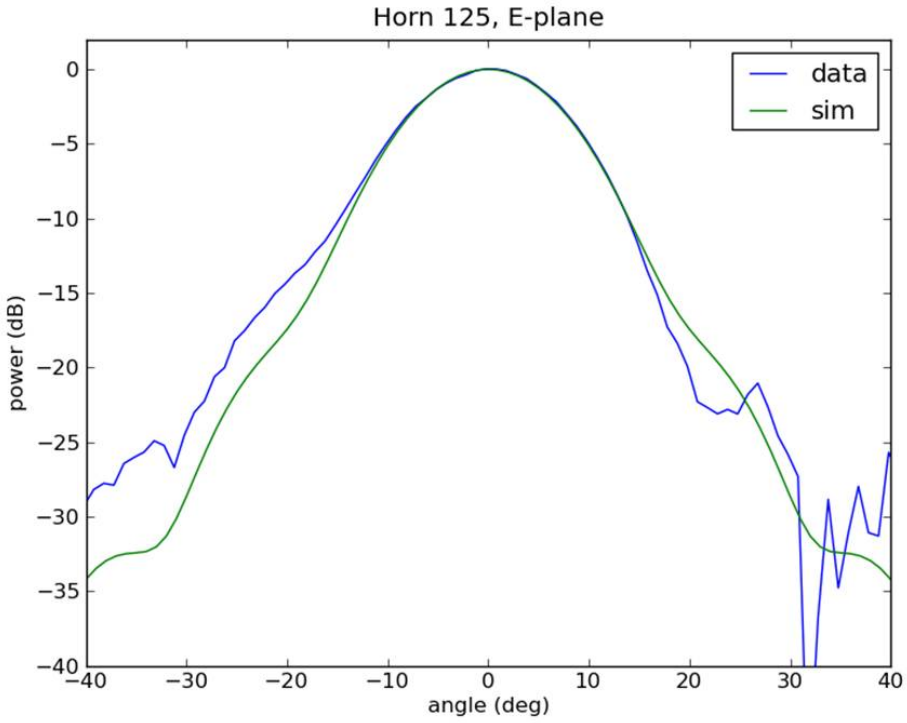

Figure 3.15: Copolar E-plane beam map for an ABS feed, as taken in the mapping range. This map is representative of beam maps taken in the range, including a left-right asymmetry due to the presence of a wall on one side of the range and not the other. The noise floor appears at around -30 dB. Figure courtesy of Katerina Visnjic.

for this work could not be made the 2.5 cm long that it needed to be for machining the feedhorn in one piece. Thus, the feedhorn was broken into top and bottom pieces which are bolted together before being bolted into the detector pods. This can be seen in Figure 3.11. A photograph of the top portion of a feedhorn with one quarter cut out so that you can see the corrugations is shown in Figure 3.14.

3.3.5 Feedhorn-Coupled Transition-Edge-Sensor Polarimeters

ABS will be the first field test of feedhorn-coupled, transition-edge-sensor (TES) polarimeters initially developed by a collaboration between the Quantum Sensors Group at the National Institute of Standards and Technology (NIST), Princeton University, and the Uni-

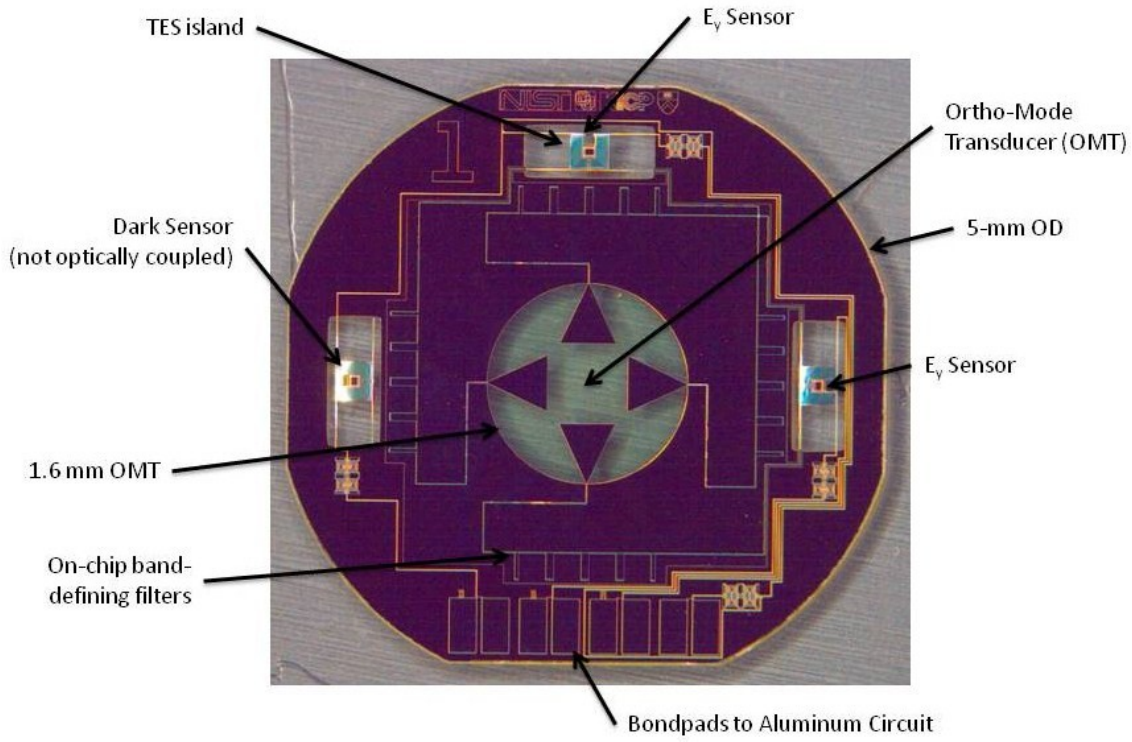

Figure 3.16: Photograph of a detector chip for ABS made at NIST, with major components indicated, including the on-chip, band-defining filters and the bond-pads used for interfacing with the electronic readout circuit. The clear circular membrane in the center of the chip is made of silicon nitride and coincides with the 1.6-mm circular waveguide at the end of the feedhorn. The triangular fins are made of niobium. The top and bottom fins carry signals to the "E_y" TES bolometer, and the left and right fins carry signals to the "E_x" TES bolometer. There is additionally a "dark" TES bolometer which is not optically coupled.

versity of Chicago. The detector chips are fabricated in groups of around 100 on 10-cm diameter silicon wafers. These detectors are designed to couple the two linear polarizations coming down a circular waveguide to separate TES bolometers on the detector chip using a planar ortho-mode transducer (OMT).

A photograph of a detector chip is shown in Figure 3.16. Each detector chip is designed to be glued to the bottom of a feedhorn, which couples light from the secondary reflector onto the OMT. The OMT has two pairs of triangular niobium fins, which couple the two orthogonal linear polarizations coming through the circular waveguide at the bottom of the feedhorn onto first co-planar waveguide and then microstrip lines. Band-defining stub filters

are placed on each microstrip line, which pass frequencies between 127 and 160 GHz.

The TES bolometers consist of "islands" of silicon suspended via thin legs, which provide mechanical support and a weak thermal link to the rest of the detector chip. Power that comes down the microstrip lines is deposited on the TES islands when they reach a lossy, resistive, meandering gold line. The bolometer measures incoming changes in optical power as a change in temperature of the island. In the simplest model of the bolometer performance, the bolometer has a heat-capacity C which is linked to the thermal bath of the detector chip with a conductance G. Diagrams of the electrical and thermal circuits are shown in Figure 3.17. A change in incoming power results in a change in temperature given by

$$C\frac{dT}{dt} = P_\gamma + P_{\text{bias}} - P_G, \tag{3.6}$$

where P_γ is the photon loading coming down the microstrip line and P_{bias} is the power dissipated by the current running through the TES. P_G is the power that flows to the bath through the thermal link with conductance G, which is given by

$$P_G = \int_{T_{\text{bath}}}^{T} G(T)dT. \tag{3.7}$$

The TES is a thin molybdenum-copper bilayer with a superconducting transition temperature around 500 mK. This transition temperature can be tuned by changing the thicknesses of the two metals. The target bath temperature for ABS is 300 mK. The TES is used as a thermometer. It is operated at its transition temperature so that a small change in temperature leads to a large change in resistance. A shunt resistance is placed in parallel with the TES, effectively biasing the TES at constant voltage. The equation governing the current, I_{TES}, through the TES is given by:

$$L\frac{dI_{\text{TES}}}{dt} + I_{\text{TES}}R_{\text{TES}} = \left(I_B - I_{\text{TES}}\right)R_s, \tag{3.8}$$

where L, R_s, and I_B

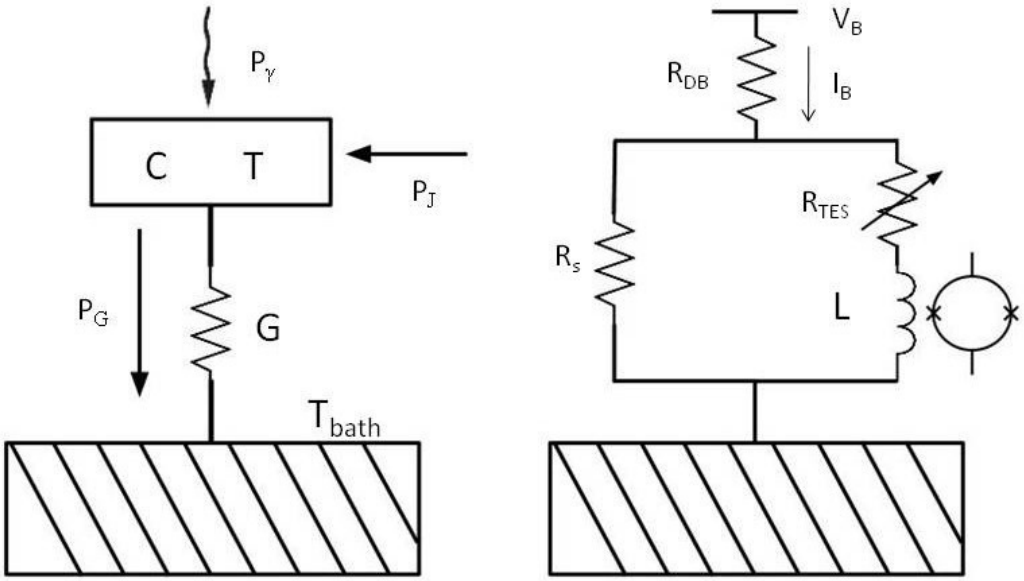

Figure 3.17: TES bolometer thermal and electric circuits.

Negative electrothermal feedback stabilizes the TES on its transition despite changes in external loading. An increase in incoming optical power raises the temperature of the TES island, correspondingly increasing the resistance of the TES. The power dissipated on the TES by the voltage bias, given by V^2/R, is then decreased. This decrease in bias power compensates the increased optical power. The current running through the TES loop is inductively coupled to a Superconducting Quantum Interference Device (SQUID), which provides the first stage of amplification for the signal on its way out to room temperature electronics.

3.3.6 Detector Backshorts

Each detector chip has a $\lambda/4$ backshort cavity created behind it by a silicon chip designed and fabricated at NIST. A photograph of one of the backshort chips is shown in Figure 3.18. The backshort chips are made of two pieces of silicon – one silicon wafer that is 600-μm thick has a circular hole 1.6 mm in diameter etched through it using the Bosch process of deep reactive-ion etching. A thin silicon wafer cap is then glued on to the backshort, and

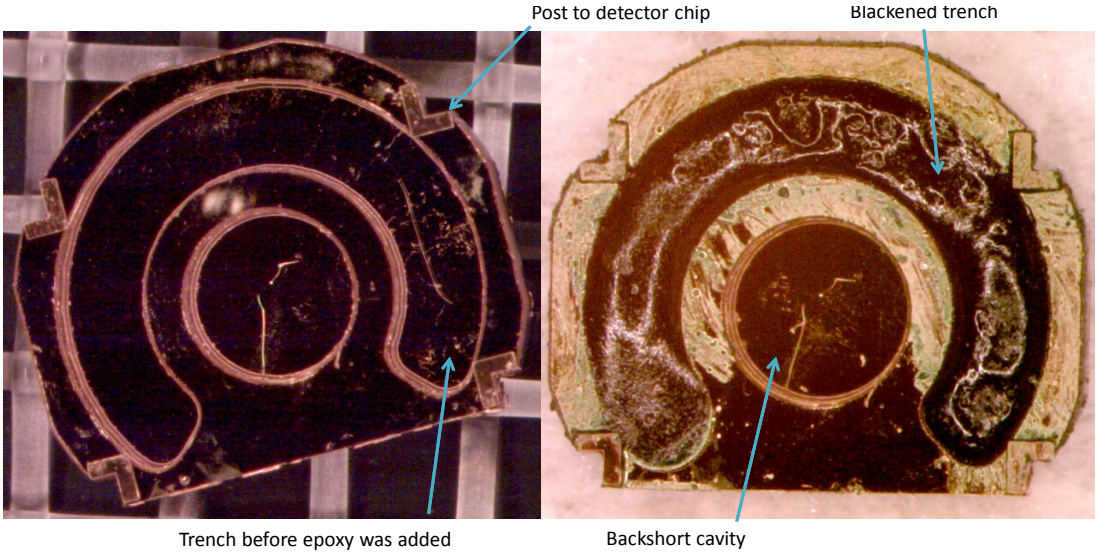

Figure 3.18: *Left:* Photograph of a backshort chip made by NIST before the trench was blackened. The L-shaped SU8 posts that glue to the detector chip are indicated, along with the horsheshoe trench. *Right:* Photograph of a detector chip after the trench was blackened. The backshort cavity that sits behind the detector OMT and the blackened trench are indicated.

both pieces are electroplated with gold. Small posts made of SU8, visible in Figure 3.18, space the backshort chip off of the detector chip. A small amount of glue is placed on each post to fasten the backshort to the detector chip.

3.3.7 Detector Passband

The detectors for ABS have a designed passband which extends from 127 to 160 GHz. Measurements with an FTS at Princeton suggest that the band is actually shifted low by 3-5 GHz. Additionally, the ABS detectors have sensitivity to frequencies well above this band, a phenomenon which has been dubbed the "blue leak." Measurements of total power incident on an ABS detector with a cold thermal load coupled through rectangular waveguide in a test dewar at Princeton suggest that there is power coupling onto all TESs on chip, including the dark TES that is not coupled to the OMT. These measurements were carried out by John Appel. FTS measurements carried out at the University of Chicago

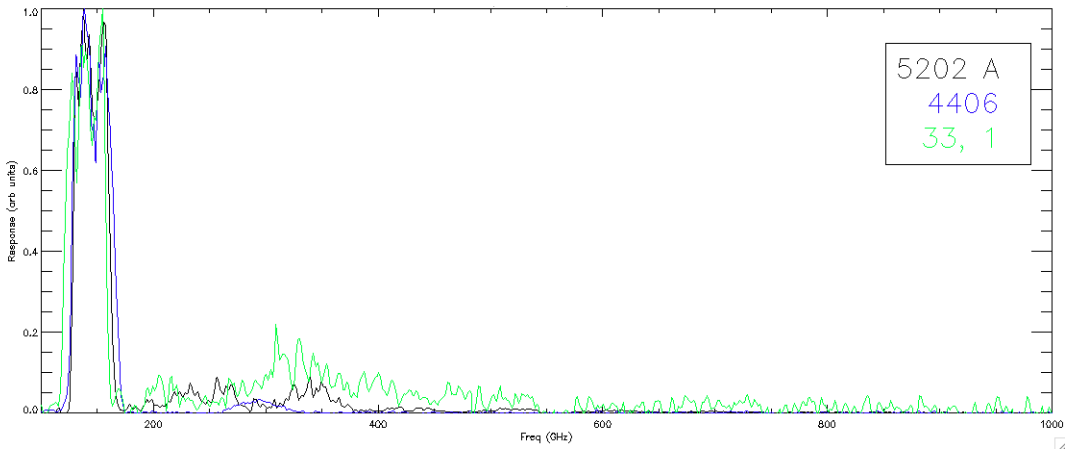

Figure 3.19: Measured bandpasses for detector chips with identical on-chip bandpass filters to ABS, as measured by an FTS at the University of Chicago. The spectrum is normalized to be unity at the maximum. Figure courtesy of Lindsey Bleem.

(a representative spectrum is shown in Figure 3.19) show that much of this power is from radiation far outside the designed passband. To mitigate this problem, the cavity that the TES islands sit in, formed by the bottom of the feedhorn and the backshort chip, has been dampened as much as possible, by adding blackened trenches to both the feedhorn bottom and the backshort chip, as described above.

Time-Division Multiplexing

Because the wiring that would be necessary to read out more than 480 TES bolometers individually would strain the cryogenic system and complicate the cryostat design, the ABS detectors are multiplexed with a time-division scheme. Readout chips were developed by the Quantum Sensors Group at NIST and specialized multiplexing hardware, the multi-channel electronics (MCE), were developed by the University of British Columbia. The MCE has been used by a number of experiments to date, including the Atacama Cosmology Telescope (ACT)[90].

In time-division multiplexing, the detector array is broken into smaller groups. The detectors within each group are read out one at a time in sequence via the same wire. In the case of ABS, there are 24 detectors in each group, which cuts the number of wires needed

to address the detector array by a factor of ten, once you factor in additional lines needed for SQUID biasing in the multiplexing scheme. The 21 TES bolometers (10 polarimeters with one TES for each of two polarizations, plus one dark TES) in each pod are read out with a NIST SQUID multiplexing (MUX) chip. The MUX chip couples all first-stage SQUIDs in a given pod to a single second-stage SQUID. The 24 second-stage SQUIDS, one for each pod in the focal plane, are biased sequentially one at a time. A given addressing line, which couples to one detector SQUID loop in each of the 24 pods, is at any time reading out only one detector time sample. The MUX chip has been carefully designed to reduce pickup to external magnetic fields as much as possible.

3.4 UHMWPE Vacuum Window

The vacuum window for ABS is made of ultra-high-molecular-weight polyethylene (UHMWPE) 3.2 mm thick. UHMWPE is attractive because of its low loss tangent of 2×10^{-4} and mechanical strength. A prototype window was tested under vacuum and found to sag up to 4 cm when heated to 45°C, which was at a level which could be accommodated into the optical design. This prototype window was subsequently kept under vacuum for three months with no signs of degradation or wear.

The ABS window is anti-reflection (AR) coated with 0.43 mm of porous PTFE on both sides. The porous PTFE material was acquired from Porex. It has an open-pore structure with approximately 50% porosity, leading to an index of refraction of approximately 1.22. The AR coating was heat-pressed onto the UHMWPE window using low-density polyethylene (LDPE), which has a melting temperature of 120°C. The heat pressing was performed at a temperature of approximately 135°C for a minimum of four hours, with 15 kg of metal weights stacked on top. The two sides of the window were AR coated in two separate steps to ensure that the porous PTFE was centered on the window in each case. The process was similar to that used by BICEP for its PTFE filters [103].

The mounting ring for the window is bevelled on the bottom to allow the window to bow without being pressed into a sharp edge. A photograph of the window in its mounting

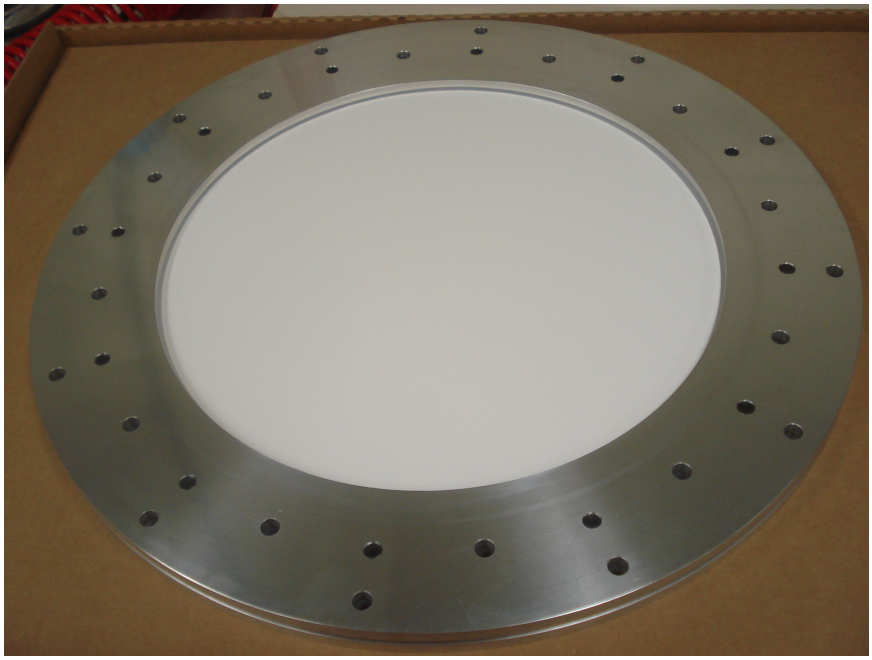

Figure 3.20: Photograph of an UHMWPE window for ABS in its mounting ring.

ring is shown in Figure 3.20. The transmission of the window has been demonstrated to be greater than 98 ± 1.5% by measurement in a feedhorn range with a broadband diode detector and a broadband source centered at 127 GHz with a FWHM of 30 GHz. This matches with expectations at the level of uncertainty allowed.

3.5 Half-Wave Plate Air Bearing System

The half-wave plate (HWP) for ABS is designed to be continuously rotated directly above the vacuum window at a speed of up to 3 Hz. This would yield a modulation of the detector signals at four times that frequency, or 12 Hz. This modulation frequency is high enough to modulate the signal faster than the scan speed, but low enough not to be cut off by the time constants of the detectors, which can range from 4 to 100 Hz. Rotating a sapphire plate weighing approximately 1 kg with a diameter of 330 mm this quickly with low vibration, so as not to couple HWP rotation microphonically onto the detectors, and with low magnetic noise from a motor is a challenge. The HWP system for ABS employs air bearings that

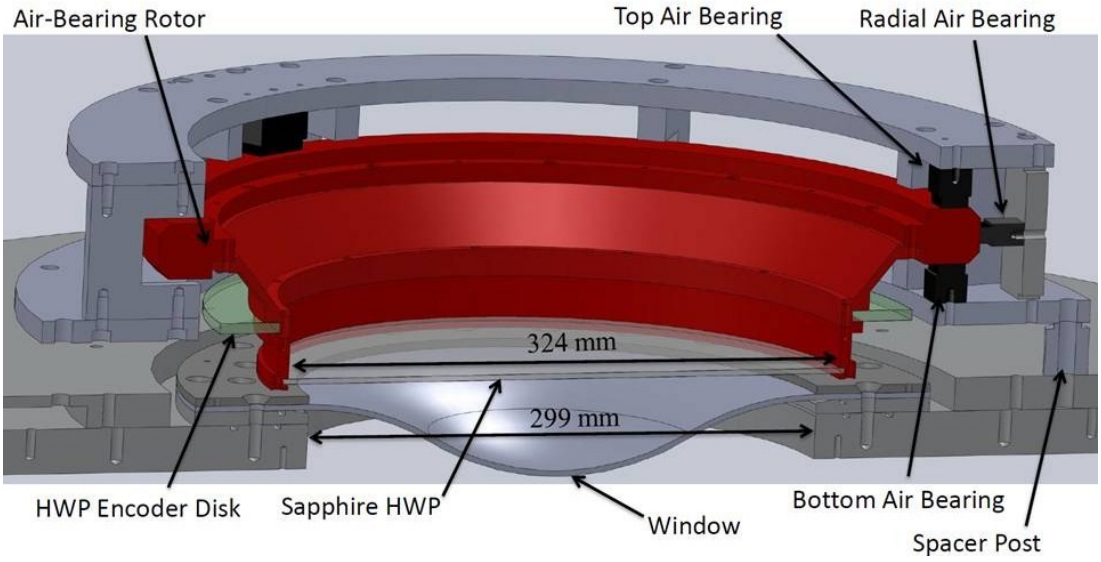

Figure 3.21: Diagram of the HWP air-bearing assembly, with major components indicated.

provide firm mechanical support with negligible friction. Typical coefficients of friction for the air bearings 1×10^{-5}. This system was designed by Norm Jarosik.

The air bearings for ABS were produced by New Way Air Bearings[6] . The overall system layout can be seen in Figure 3.21. The air bearings consist of porous rectangular graphite pads that are 25 × 50 mm. At three places evenly distributed around the circumference of the rotor, three graphite bearings stabilize the rotor from top, bottom, and radial directions. This makes for nine air bearings in total. The air bearings are designed to be conformal with the rotor and approximately 125 μm away. For the top and bottom bearings, this requires that they be flat to within 25 μm, while for the three radial bearings this requires that the bearing have a radius that is very carefully matched to be 125 μm greater than the radius of the rotor. For this reason, the rotor was machined out of aluminum and anodized to produce a hard, stable surface before the radial bearings were produced.

[6]50 McDonald Boulevard, Aston, PA 19014, (610) 494-6700, www.newwayairbearings.com

HWP Encoder

The angular position of the HWP needs to be known to within a tenth of a degree to avoid E to B mixing dominating the B-mode signal in the final maps made by ABS. To achieve this an optical encoder is mounted to the outside of the HWP rotor. This encoder, produce by Gurley Precision Instruments[7] , is a glass disk with a photolithographed pattern of 9000 lines etched in aluminum around its circumference. An optical readhead consisting of a light-emitting diode on one side of the disk and a set of photo-sensitive diodes on the other side of the disk count the number of lines that have gone by the readhead. This allows for relative angular position to be known to within 2.4 arcmin. An additional reference mark at one point around the circumference allows the absolute position to be determined after no more than one full rotation.

An interpolator circuit, also available from the company, produces a quadrature-square-wave output from the photodiode signals. This signal consists of two square waves that pass through a full period every time a line passes the readhead. The two square waves are $\pm 180^\circ$ out of phase; the sign of the phase difference encodes the direction of travel of the disk. The signals (quadrature square wave plus once-per-revolution index signal) from the interpolator circuit travel to the analog breakout box (ABOB) along twisted-pair wires with RS422 differential signal protocol. In the ABOB, the quadrature square wave is interpreted by a Sensoray 2620 card[8] , which counts the number of lines and reference marks that have gone by. This count is passed to the Sensoray main module 2601 unit and from there is read into the main housekeeping time stream.

The encoder disk is mounted onto the outside of the air-bearing rotor as shown in Figure 3.21. The encoder pattern is not concentric with the encoder disk. A simple centering procedure was employed in which the air-bearing rotor was spun by hand with the encoder disk attached loosely. The encoder disk was tapped lightly to move it until the pattern no longer seemed to shift relative to the readhead. The encoder readhead is mounted onto the air-bearing bottom support ring, and needs to be mounted within 500 μm of the encoder

[7] 514 Fulton Street, Troy, NY 12180, (800) 759-1844, www.gurley.com
[8] Sensoray Inc., 7313 SW Tech Center Drive, Tigard, OR 97223, (503) 684-8005, www.sensoray.com

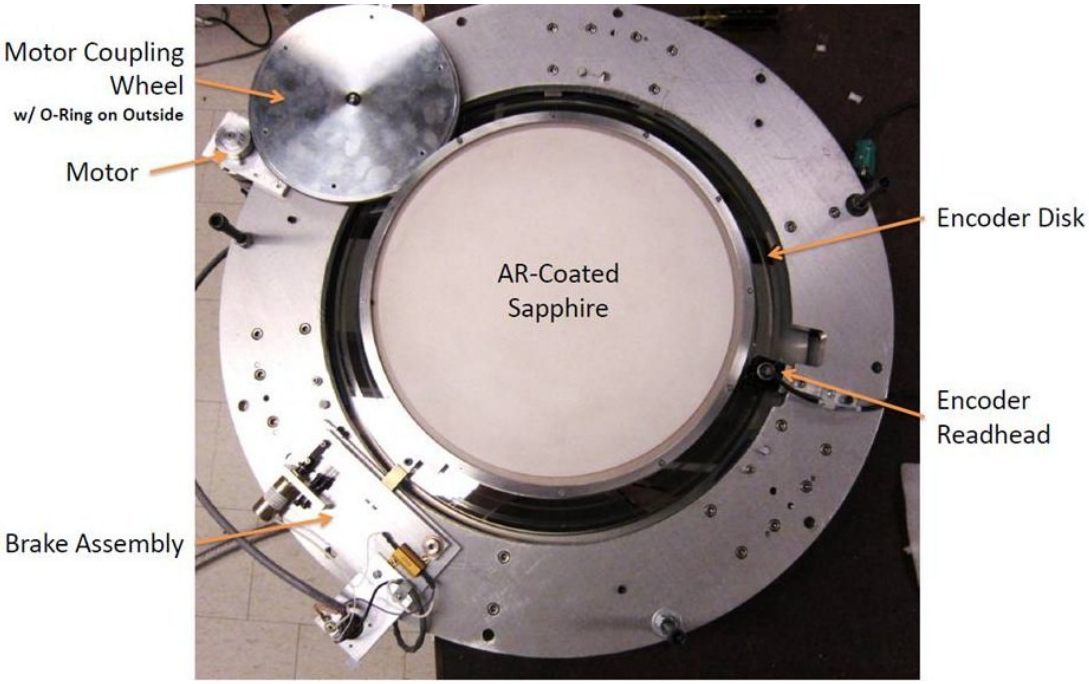

Figure 3.22: Photograph of the HWP assembly with components indicated.

disk for optimal performance. Adjustment screws were built into the assembly to allow for final adjustment to this tight tolerance.

Motor and Brake

The HWP rotor is turned at constant speed by a brushless DC motor with built-in speed control[9] . A proportional-integral feedback control circuit that uses the encoder output to precisely measure rotor speed changes the 0-5 V speed input voltage to the motor to keep the rotor spinning at a constant speed. This speed is set by a turn-dial potentiometer on the front panel of the servo circuit box. The motor axis is coupled to a 3.34-cm diameter disk. This spins a 10 cm diameter wheel with an 3.2-mm O-ring on its outside. The O-ring serves to provide enough friction between the disk and the wheel to spin it. This wheel then contacts the air-bearing rotor. A set of springs keeps the wheel O-ring firmly in contact with both the motor disk and the air-bearing rotor. The layout is shown in Figure 3.22.

[9] Anaheim Automation, Model BLWR23MD3S-36V-4000, 910 East Orangefair Lane, Anaheim, CA 92801, (714) 992-6990.

A brake made of cork is kept in contact with the HWP rotor by a solenoid valve unless the pressure in the ballast tank is above a minimum value. A pressure switch on the ballast tank energizes the solenoid valve when this minimum pressure is achieved, removing the brake from the rotor and allowing the motor to start turning the rotor. The motor itself is simultaneously switched on only when the pressure switch closes the solenoid valve relay.

Compressed-Air System

The rotor assembly with the HWP weighs approximately 7.8 kg. The open-celled graphite pads are provided with 414 kPa (60 PSI) of compressed air, which provides 156 Newtons of force from each bearing. The air flow through each bearing is 0.06 standard cubic feet per minute (SCFM), meaning that the total usage air usage of the air bearing system is approximately 0.5 SCFM. The compressed air for the system is provided by an electric air compressor which can output five standard cubic feet per minute (SCFM) at 621 kPa (90 PSI) at sea level. The maximum pressure that the system can achieve is 1.38 MPa (200 PSI) at sea level. This air compressor has an 80-liter storage tank, which allows the compressor motor not to run continuously. The maximum allowable duty cycle of the air compressor is 60% on and 40% off.

The air coming from the compressor is filtered first with a condensate filter and then with a course 5-μm filter to remove the bulk of the oil, water, and particulates. A commercial dessicator system[10] placed directly after these filters switches between two dessicator cartridges approximately every three minutes, providing continuous dry air to the air bearings at a dewpoint of -40°C. This system vents each cartridge to atmospheric pressure in order to recharge it and uses approximately one SCFM at 621 kPa (90 PSI) when allowed to operate at its default setting. Due to the dry conditions at the site in Chile, the duty cycle of the dessicator is planned to be reduced when there by putting the dessicator into a dormant state when the compressor motor is turned off. This is achieved by the use of a relay tied to the compressor pressure switch that opens or closes pins on the control circuit

[10]Parker Domnick Hunter, Model DAS1, Dukesway, Team Valley Trading Estate, Gateshead, Tyne, and Wear, NE11 OPZ England.

of the dessicator system.

The operation of the system at the site in Chile at 5200 meters altitude, where the pressure is roughly half that at sea level, can be assumed to both reduce the maximum pressure of the compressor by half and reduce the output in SCFM at a given pressure by half. This is due to the fact that the compressor motor cycle produces a fixed compression ratio regardless of altitude, which means that reducing the ambient pressure by half will reduce the maximum final pressure by half. Additionally, in each stroke of the compressor motor, a certain volume of gas is moved, which goes directly with pressure, meaning that for a given number of strokes per second, half the number of moles of gas (or equivalently standard cubic feet) is moved. The system can be assumed to provide up to 689 kPa (100 PSI) of pressure at the Chilean site, which is well above the 414 kPa (60 PSI) needed by the air bearings.

The 5 SCFM at 621 kPa (90 PSI) output of the compressor motor is its rating while continuously operating. At a maximum, the motor can be on only 60% of the time, meaning that the actual output of the system is reduced to 3 SCFM at 621 kPa (90 PSI). This value will be reduced by half when operating in Chile, meaning that the system will provide only 1.5 SCFM at 90 PSI at the site. With the dessicator system at its factory default settings using 1.0 SCFM and the air bearings using 0.5 SCFM, the compressor system would be pushed to its limits. To avoid this the dessicator system is switched on and off with the compressor motor, reducing its duty cycle and compressed-air usage.

One further modification needed to be made to accommodate operation in Chile. A pressure switch built into the air compressor is designed to switch the compressor motor on when the pressure in the tank reaches approximately 1.07 MPa (155 PSI) and switches it back off when the pressure in the tank reaches approximately 1.34 MPa (195 PSI). As the compressor motor will have its maximum output pressure reduced to 689 kPa (100 PSI) or a little above, the air compressor would be running continously. This would operate the motor above its rated duty cycle, and likely burn it out over time. To avoid this, an additional pressure switch was added to the system after the factory-installed pressure

switch and before the regulator. This additional pressure switch turns the compressor motor on at one set pressure and off at another. The pressure at which the motor is turned off can be adjusted between 414 and 758 kPa (60 and 110 PSI), and the pressure difference between the high and low pressures is adjustable in the range 103-172 kPa (15-25 PSI). These levels can be adjusted as needed for operation in Chile. For tests in Princeton, the pressure switch was set to turn the motor on when the tank pressure reached 586 kPa (85 PSI) and off when the tank pressure reached 655 kPa (95 PSI). With these settings, the motor runs for 25 seconds out of every 210 seconds, a 12% duty cycle. At the site, the motor would operate 50-60 seconds out of every 210 seconds, a 25-30% duty cycle, well within the operating range of the compressor.

A 19-liter (five-gallon) ballast tank mounted on the side of the receiver provides a safeguard in case compressed air is suddenly cut off from the air-bearing system. In such an eventuality, the ballast tank provides compressed air to the air bearings for enough time for the brake to stop the rotor from spinning before the air bearings lose pressure. This reduces the possibility of wear on the bearings. A regulator on the output of the ballast tank provides the steady 60 PSI of compressed air needed by the bearings. One final stage of particulate filters and a dessicator cartridge ensure that only clean, dry air reaches the bearings. A pressure switch monitors the pressure in the ballast tank. If the pressure in the tank drops below an adjustable level, which has been set at 83 PSI for tests in Princeton, the pressure switch closes a relay to the HWP motor that turns it off and switches off the solenoid valve, deploying the brake.

3.6 Inner Baffle and HWP Enclosure

As described in detail in Section 3.8, an inner baffle and ground screen are employed by ABS to reduce spurious signals from the ground and other structures near the telescope. The inner baffle is incorporated into an overall enclosure around the window and HWP that serves to keep dust and moisture away from these elements. The window is cooler than ambient temperature due to its proximity to cryogenic elements in the optical chain.

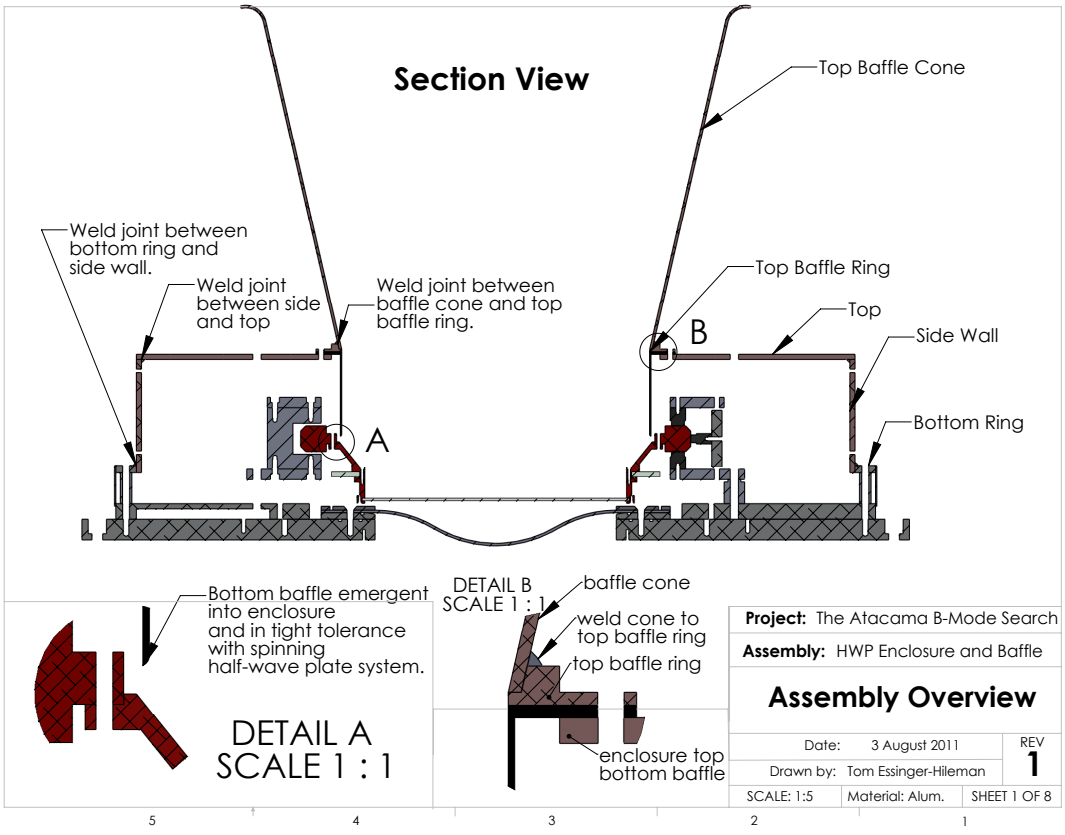

Figure 3.23: Overview of the inner baffle and enclosure around the HWP and window.

This causes the window to condense moisture onto it. In the lab in Princeton, which is more humid than the telescope site will be, this can create large build-ups of accumulated moisture. This accumulated moisture would absorb and re-emit in our observing band, and also possibly degrade the window AR coating or O-ring seals over time. The telescope site is also dusty, and dust accumulating on the window or HWP over time could degrade telescope performance as well. Cleaning the window would require the removal of the HWP system, which is both time-consuming and carries the risk of damage to the HWP.

For these reasons, the HWP and window are placed inside an approximately air-tight and light-tight enclosure. The layout of the enclosure is shown in Figure 3.23. The enclosure incorporates the inner baffle, which has a cylindrical piece in close proximity with the air-

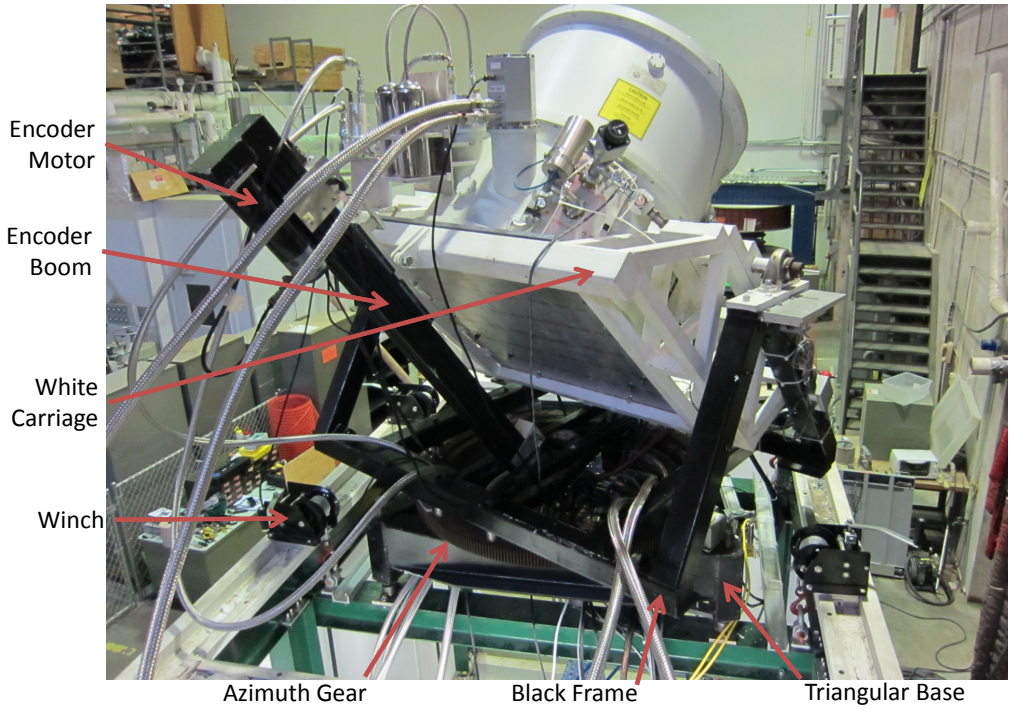

Figure 3.24: Photograph of the ABS receiver on its base on top of the container. Major components of the bawe are indicated. Everything from the black frame upward rotates in azimuth. The white carriage and receiver are tilted by the encoder motor moving on the encoder boom. Two of the four winches used to raise the base and receiver out of the container are visible. The green I beams of the base support and jack system are visible at the bottom of the photograph.

bearing rotor, as well as a conical baffle that extends 45 cm above the rest of the enclosure. Small openings are allowed in the enclosure for compressed-air and electrical feedthroughs for the HWP system. The large opening at the top of the baffle will be sealed with a taut, thin sheet of polyethylene. The dry air that flows through the air-bearing system will provide enough positive pressure in the enclosure to exclude dust and moisture.

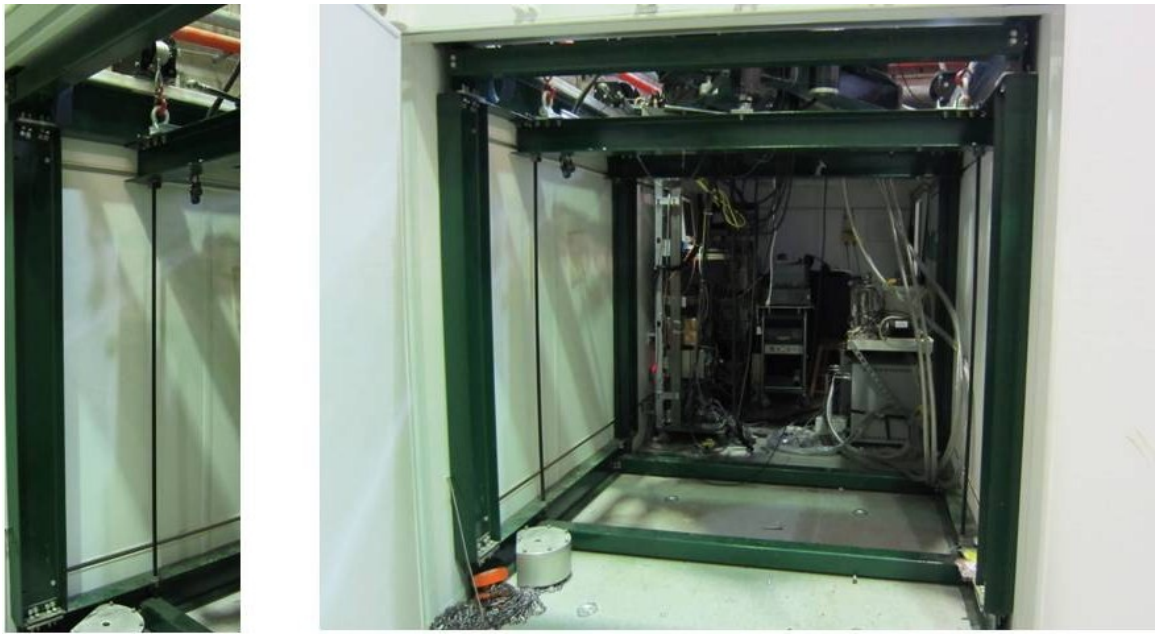

Figure 3.25: *Left:* Closeup photograph of one of the four winch systems that raise the ABS base and cryostat out of the container. The threaded rod that guides the base as it is raised is visible. The winch is at the top mounted to the top of the container. *Right:* Photograph of the jack system and I-beam support system with the base raised out of the container.

3.7 Telescope Base and Lifting Jack

An azimuth-elevation telescope base points the ABS receiver on the sky. This base is a legacy from the MINT experiment [31] that was modified to accommodate the ABS receiver. A triangular frame with three adjustment rods allows leveling of the base. A large crane bearing allows the telescope to turn 360° in azimuth. The azimuth motion is controlled by a Dynaserv motor and drive. The receiver sits on a carriage that can rotate in elevation relative to the rest of the base. Motion in elevation is driven with a Cleveland Motor Controls servo motor, which is attached to a boom as shown in Figure 3.24. Additionally, a linear motor allows quick back-and-forth scanning of the telescope in azimuth. A clutch allows the linear motor to disengage when large movements in azimuth are required and re-engage when scanning is needed.

The base and receiver are designed to be raised and lowered through an opening in the

roof of a custom-built 2.4 m × 2.4 m × 6.1 m (8' × 8' × 20') shipping container. This jack system, built by Princeton undergraduate Alicia Kollar, uses four winches to raise and lower the base using steel cable. Four threaded rods guide I-beam supports under the base while it is being raised and lowered. Ball screws can be raised up the threaded rods to provide additional support to the base when it is raised for observations. The I beams can also be bolted into top support beams with 1/2"-28 screws. A photograph of the jack system is shown in Figure 3.25.

3.8 Ground Pickup Reduction: Baffle and Ground Screen

Stray radiation from the warm ground, especially highly-polarized radiation from emission or reflection at steep angles, must be minimized in order to reduce overall detector loading and spurious scan-synchronous signals. A conical baffle mounted on top of the cryostat directly above the rotating half-wave plate system provides a first level of ground-pickup reduction. A ground shield constructed of 19-mm aluminum honeycomb paneling mounted to the cryostat carriage on the telescope base provides a second level. The baffle and ground screen together ensure that any radiation from the ground must diffract twice at steep angles to enter the cryostat.

To get a rough idea of the power diffracted by the ground screen and baffle from the ground to the detectors, one may treat the diffracting edge as a semi-infinite conducting plane. This is a good approximation for the conical baffle only when the radius of curvature, $R \sim 60$ cm, at the top of the baffle is much larger than $\lambda = 2$ mm. This is only approximately true in our case. Additionally, the top of the baffle is curved at a radius of 12 mm, which should reduce the diffracted power [46]. Diffraction around a conducting half plane was solved in closed form by Sommerfeld in 1896 [88]. Well into the shadow of the diffracting plane, and at a distance of many wavelengths, the amplitude of a diffracted plane wave for the E- and H-polarized waves is given by [13]:

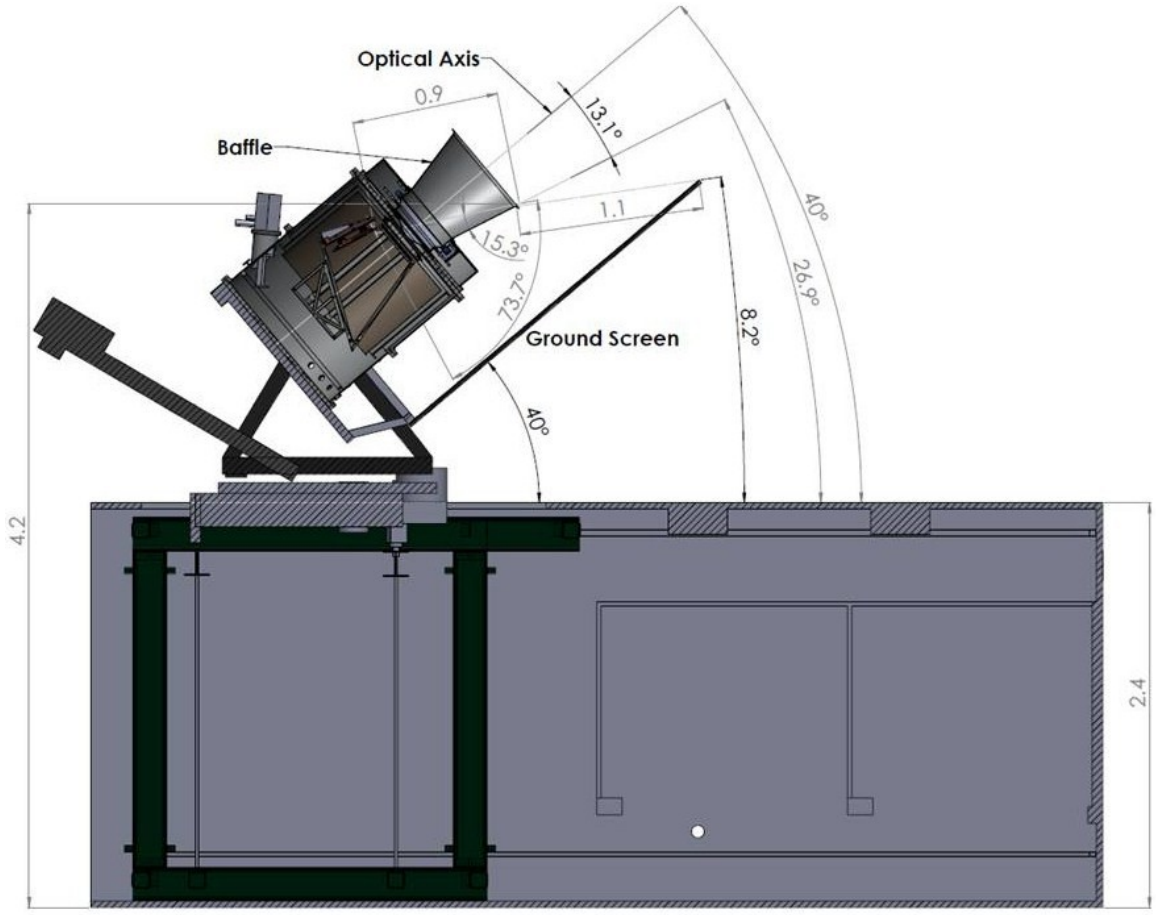

Figure 3.26: Section view of the ABS container with telescope base and cryostat mounted on top. The cryostat is shown tilted to its lowest elevation of 40°. Relevant angles and distances are shown.

$$E_z = \sqrt{\frac{2}{\pi}} e^{\imath\pi/4} \frac{\sin(\alpha/2)\sin(\theta/2)}{\cos\alpha + \cos\theta} \frac{e^{\imath kr}}{\sqrt{kr}} \tag{3.9}$$

$$H_z = -\sqrt{\frac{2}{\pi}} e^{\imath\pi/4} \frac{\cos(\alpha/2)\cos(\theta/2)}{\cos\alpha + \cos\theta} \frac{e^{\imath kr}}{\sqrt{kr}} \tag{3.10}$$

Unpolarized light will be polarized at a level given by the ratio of these two equations, or

$$\frac{E_z}{H_z} = -\tan(\alpha/2)\tan(\theta/2) \tag{3.11}$$

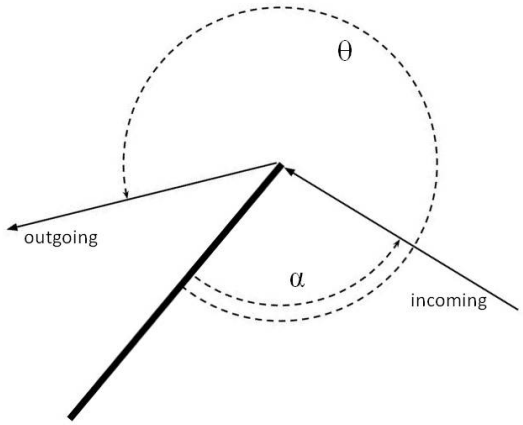

Figure 3.27: Angle definitions for diffraction around a semi-infinite conducting plane.

In the above equations, α is the angle of incidence of the plane wave, and θ is the angle of the propagating wave. The definitions of these two angles are shown in Figure 3.27. Ground pickup will be most severe when the telescope is tilted to its lowest elevation angle of 40°. A diagram showing the cryostat at this angle on top of the ABS container, with baffle and ground shield, is shown in Figure 3.26. The primary concern is that diffracted radiation from the ground can directly strike the feedhorns near the top of the focal plane, albeit at a steep angle. The relevant angles, α and θ, for diffraction around the ground screen and the subsequently around the conical baffle, are shown in Figure 3.26, and are tabulated in Table 3.2.

	α	θ	d (m)	Diffracted Intensity	Diffracted Polarization
Ground screen	140°	312°	1.1 m	-46.4 dB	-60.4 dB
Inner baffle	161°	344°	0.9 m	-27.7 dB	-42.9 dB
Feedhorn pickup	74°			-30.0 dB	-30.0 dB
Total				-104 dB	-133 dB

Table 3.2: Compiled maximum diffracted powers around the ground screen and inner baffle, and then picked up by feedhorn. The pickup quoted for the feedhorn is the noise floor seen in the beam mapping setup. This estimate is pessimistic as this noise is electronic in nature. The feedhorn pickup at steep angles is as much as -20 dB below the noise.

Chapter 4

Filter Development for ABS

Free-space filters are critical elements of millimeter-wave telescopes, providing thermal load mitigation for the cryogenic system and often also band-definition. The bolometers used by the majority of contemporary CMB experiments, including ABS, are intrinsically broad-band and low-temperature devices. The detector passband needs to be defined by filters elsewhere. Free-space metal-mesh filters often define the experiment passband. In ABS, the detector passband is set by on-chip microstrip stub filters; however, ABS still uses a metal-mesh lowpass filter at 4 K to reduce the blue leak discussed in Section 3.3.7.

TES bolometers also place stringent requirements on cryogenic systems, which only become more exacting as telescope apertures increase. The two pulse tubes used by ABS are rated to have a combined cooling power of 1.7 W at 4.2 K, and only 0.9 W at our preferred operating temperature of 3.5 K. In contrast, the 300 K radiation entering the telescope aperture, if not attenuated, would place 30 W on the 4K stage. Thermal filtering on the entrance aperture to the telescope is essential to mitigate this loading.

ABS uses a combination of absorptive and reflective filters to cut thermal loading on the cryogenic stages and reduce blue-leak power picked up by the detectors. The three filter types and what cryogenic stage they are placed on are:

PTFE absorptive filter (40 K) A 2.5 cm slab of PTFE absorbs significantly in the infrared while allowing millimeter-wave radiation to pass. This filter is additionally

Filter Number	g	a	ν_0	Cryogenic Stage & Position
1	150 μm	25 μm	1.75 THz	300 K
2	125 μm	17.5 μm	2 THz	40 K above PTFE
3	110 μm	15 μm	3 GHz	40 K above PTFE
4	125 μm	17.5 μm	2 THz	40 K above PTFE
5	110 μm	15 μm	3 GHz	40 K above PTFE
6	150 μm	25 μm	1.75 THz	40 K above PTFE
7	150 μm	25 μm	1.75 THz	40 K below PTFE
8	125 μm	17.5 μm	2 THz	40 K below PTFE
9	110 μm	15 μm	3 GHz	40 K below PTFE
10	125 μm	17.5 μm	2 THz	40 K below PTFE
11	110 μm	15 μm	3 GHz	40 K below PTFE
12	150 μm	25 μm	1.75 THz	4 K above LP Filter

Table 4.1: Grid g and a defined as in Figure 4.5, and transmission minima, ν_0, along with position in the stack of the IR blockers used in ABS. A scale drawing of the filter layout is shown in Figure 4.1.

AR-coated with a porous PTFE membrane[1] .

Single-layer reflective IR blockers (4 K, 40 K, 300 K) Grids of aluminum squares patterned on 6-μm-thick Mylar substrates are nearly purely reflective lowpass filters with cutoffs of 2.0, 2.4, and 3.2 THz.

Multilayer reflective lowpass filter (4 K) Six metal-mesh filter layers, similar to those used for the IR blockers, separated by polypropylene, which provides further IR blocking and cuts off the blue leak.

4.1 Absorptive Filters

Filters made of materials that are highly absorptive in the infrared but transmissive at millimeter wavelengths can strongly reduce thermal loading, are easy to fabricate and anti-reflection coat, and are mechanically robust. Their primary disadvantage when compared with the metal-mesh filters described in Section 4.2 is their inability to have tunable fre-

[1] Zitex® G-115, Saint-Gobain Performance Plastics

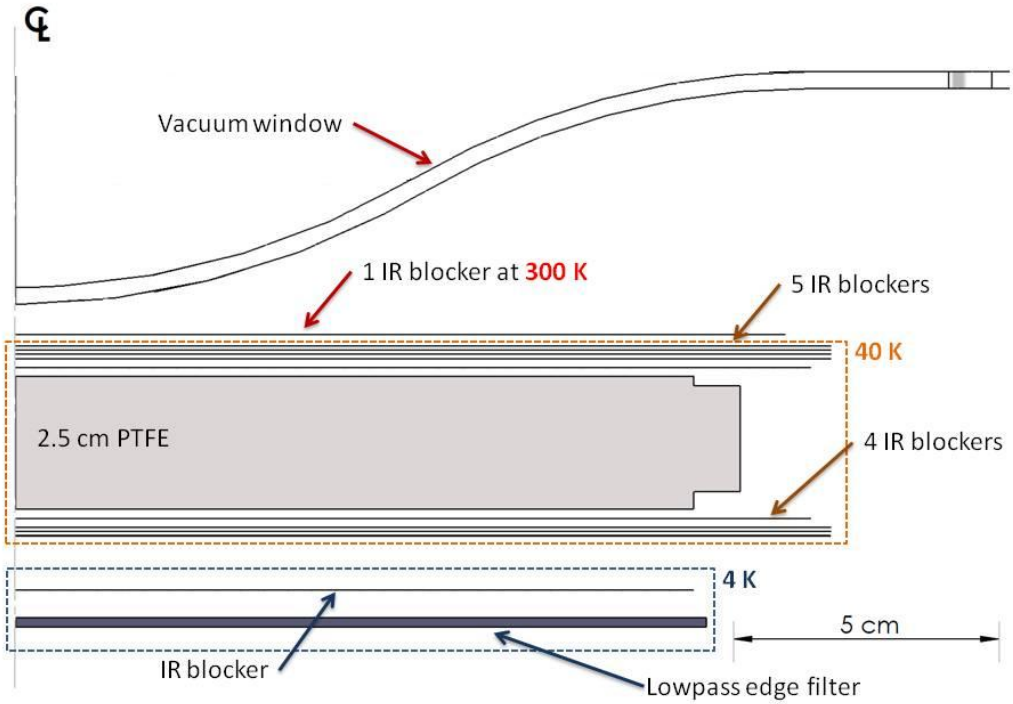

Figure 4.1: Layout of the ABS filter stack (drawing to scale). The IR blockers are single-layer square grids of aluminum on 6-μm Mylar, with one of three cutoff frequencies of 67, 80, and 125 cm^{-1} (2, 2.4, and 3.75 THz). The absorptive PTFE filter is 2.5 cm thick and is AR coated with a Zitex® G115 porous PTFE membrane. The lowpass edge filter is composed of six square grid layers spaced by polypropylene and glued together with Stycast 1266 epoxy.

quency characteristics. The material used entirely determines the frequency spectrum of the filter.

Polytetrafluoroethylene (PTFE) was chosen for the ABS 40 K filter because it has a low loss tangent of 3×10^{-4} at 150 GHz [52], strong absorption in the IR above 6 THz [3], and good thermal conductivity [17]. PTFE also has a relatively low index of refraction of 1.44 [52], reducing reflective losses. Absorptive PTFE filters also have heritage in CMB experiments, having been used by previous projects to good effect [103]. Fluorogold, a loaded PTFE material, had been the standard for millimeter-wave absorptive filters for some

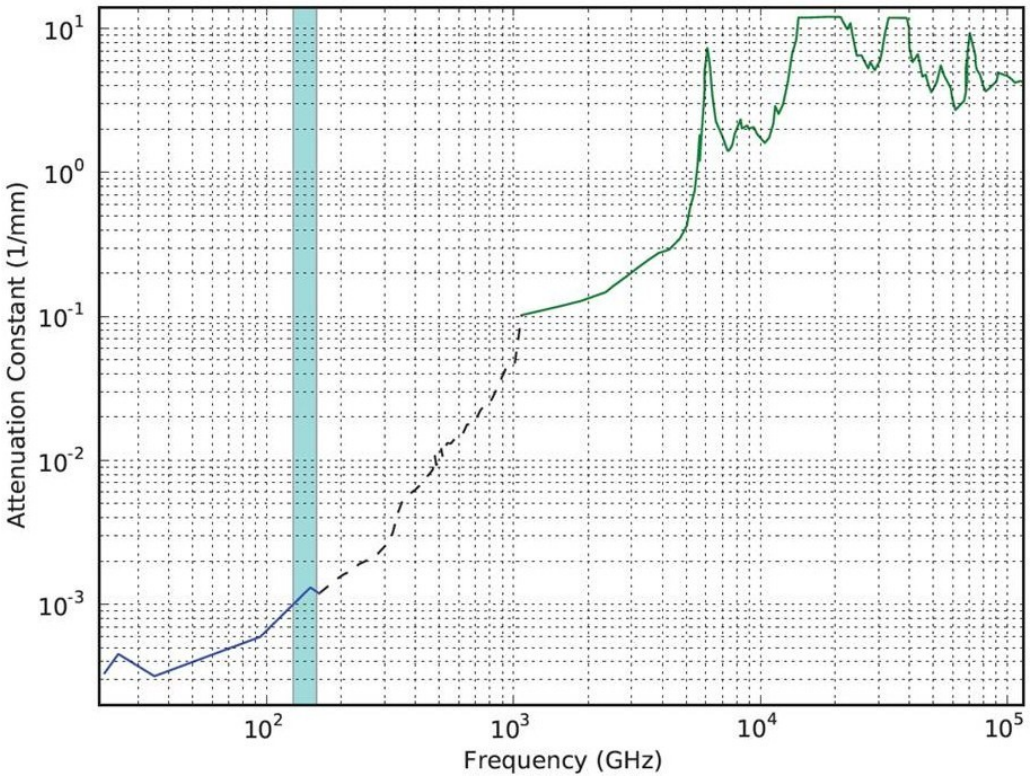

Figure 4.2: Composite attenuation constant of PTFE. Data for frequencies below 162 GHz (blue line) were compiled by [53]. The attenuation from 162 GHz to 1 THz (dashed black line) was measured by [9]. At infrared frequencies (green line), 1-116 THz, the attenuation was measured by [3]. The ABS passband of 127-160 GHz is shown in cyan.

time; however, fluorogold absorption and emission are polarized [37], making it impractical for ABS.

The attenuation constant per mm of PTFE from 100 GHz to 116 THz is shown in Figure 4.2. Data from 1 THz to 116 THz were taken from published spectra measured in a Fourier Transform Spectrometer by [3]. Low-frequency absorptivities were linearly interpolated from this data to the value quoted by Lamb at 150 GHz [52].

4.1.1 Porous PTFE Anti-Reflection Coating

The PTFE filter is AR coated with a Zitex® G-115 porous PTFE membrane. In addition to reducing in-band reflection from the two surfaces of the filter, the Zitex membrane has

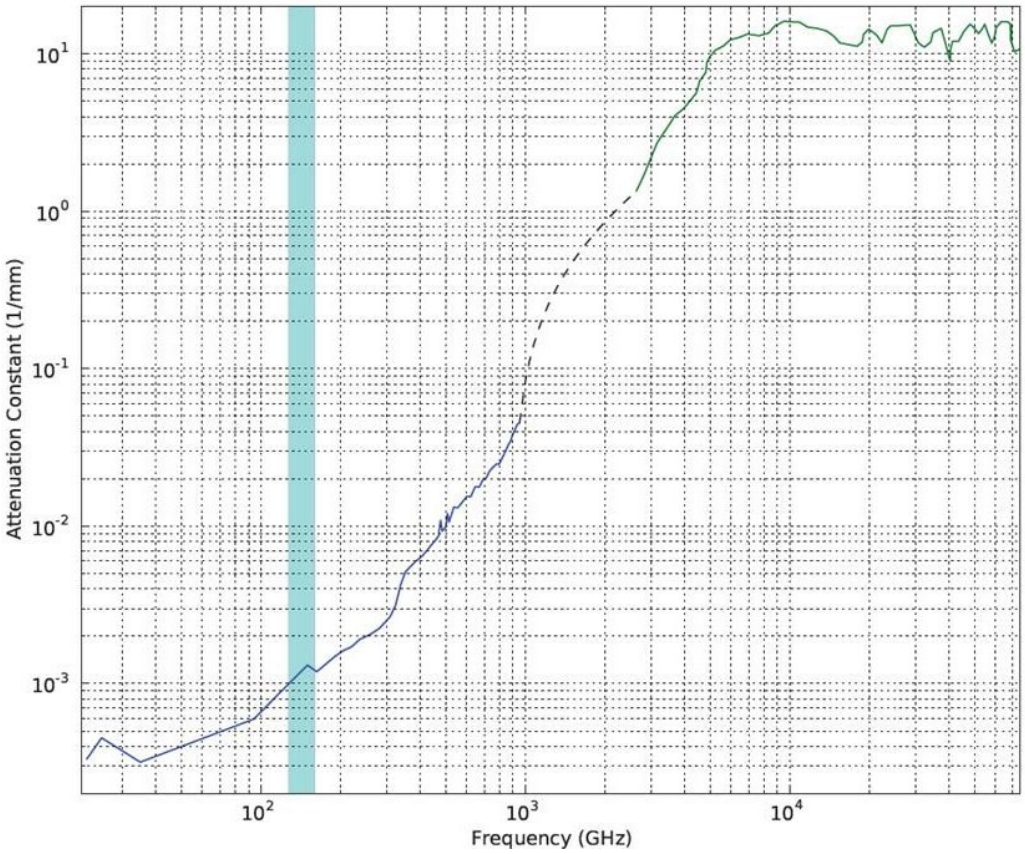

Figure 4.3: Composite attenuation constant of Zitex. At frequencies up to 952 GHz the value quoted is that for PTFE multiplied by 60% due to the porosity of Zitex (blue line). At infrared frequencies (green line) in the range 2.46-74 THz the value was measured by [3]. The dashed black line is a linear interpolation from 952 GHz to 2.46 THz. The ABS passband of 127-160 GHz is shown in cyan.

been shown to scatter IR radiation [3], adding an additional layer of IR blocking to the ABS filter stack. The G-115 membrane has a porosity of 40%, which places its index of refraction at around the 1.2 needed for AR coating PTFE (n = 1.44). Its thickness is 380 ± 50 μm. A composite plot of attenuation constant versus frequency for Zitex G-115 is shown in figure 4.3.

The Zitex membrane was heat-pressed onto the PTFE filter using low-density polyethylene (LDPE) as a sacrificial layer. Before heat pressing, the surfaces of the PTFE were roughened with 400-grit sandpaper. LDPE sheets 25-μm thick were placed between the

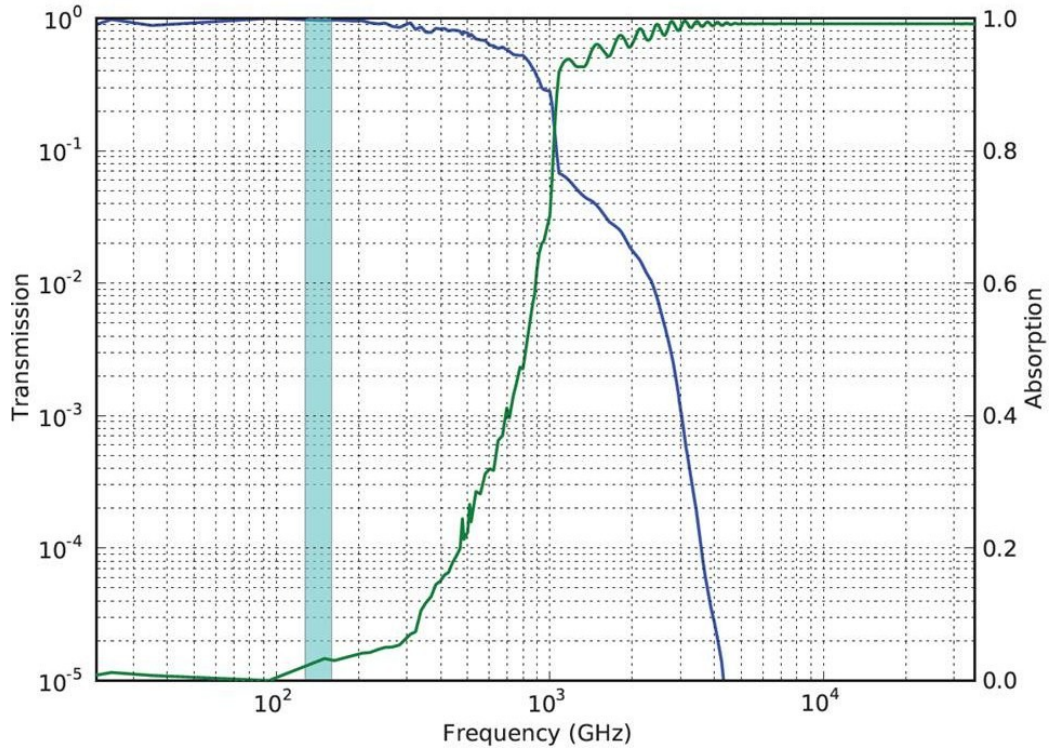

Figure 4.4: Modeled transmission (on a logarithmic scale) and absorption (on a linear scale) of the PTFE filter with Zitex anti-reflection coating used in ABS. The transmission-line model of Section 4.2.1 was used, with an attenuation constant versus frequency for PTFE and Zitex as plotted in the previous figures. The ABS passband is shown in cyan for reference. The band-averaged absorption for the filter is 3.5%.

Zitex and PTFE on each side of the filter. The entire stack was then placed under weight in an oven at 135° for a minimum of 6 hours. The oven was then turned off and the entire stack allowed to cool slowly overnight to room temperature. Slowly cooling the stack after heat-pressing was found to create a more robust bond between the PTFE and LDPE.

4.1.2 Modeling of PTFE Filter

Using values of attenuation versus frequency, as in Figures 4.2 and 4.3, and an index of refraction of 1.44 from the literature, matrix methods, such as the characteristic-matrix method or the transmission-line matrix method described in Section 4.2.1 can be used to model the transmission, reflection, and absorption spectra of the entire stack. The

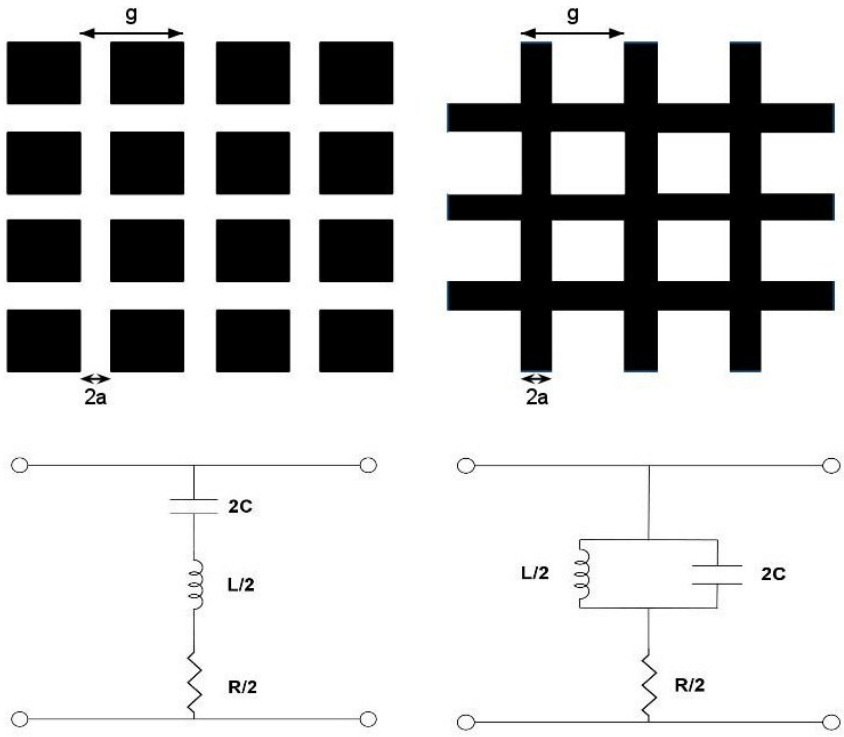

Figure 4.5: *Left:* Lowpass filter composed of a grid of metallic squares, with the corresponding equivalent circuit also shown. The frequency response of the filter depends on the grid parameters g and a, shown in the diagram. *Right:* Complementary highpass wire grid, with equivalent circuit.

transmission and absorption spectra of the complete AR-coated filter are shown in Figure 4.4. The absorption of the filter is 90% above 800 GHz, and is greater than 99% for frequencies above 3 THz.

4.2 Quasi-Optical Filters Using Frequency-Selective Surfaces

The remainder of the ABS filters use frequency-selective surfaces (FSS) to produce filters with the desired frequency characteristics. A frequency-selective surface is a thin metallic layer patterned in such a way as to reflect and transmit incoming plane waves with useful frequency spectra. For millimeter and sub-millimeter astronomy, an FSS is usually implemented by patterning metal on thin plastic substrates. For a recent review of the use of

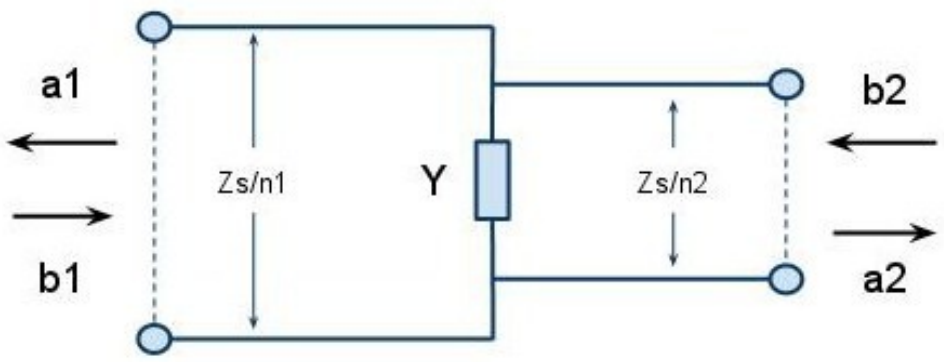

Figure 4.6: Coefficients used in the transmission-line model of filter performance. b_1 and b_2 are incoming wave amplitudes from the left and right, respectively, whereas a_1 and a_2 are the corresponding outgoing wave amplitudes. An interface between dielectrics is modeled as a change in impedance in the transmission line, with an FSS modeled as a shunt impedance.

FSS-based, quasi-optical filters for millimeter-wave astronomy, see [1].

4.2.1 Transmission-Line Model of Filter Behavior

An extensive literature has arisen around understanding FSS behavior [69, 35]. To accurately capture the frequency response of a given filter design at all frequencies, full electromagnetic simulations are needed; however, the behavior of simple designs for wavelengths above the diffraction region ($\lambda > g$, where g is the grid spacing) can be modeled using equivalent circuits of passive components shorting a transmission line. Figure 4.5 shows simple patterns which give lowpass and highpass behavior, along with their representations in terms of inductors, capacitors, and resistors. A grid of metal squares acts as a primarily capacitive impedance leading to a lowpass filter, whereas its complement, a wire grid, acts as an inductive impedance and gives highpass behavior. Bandpass behavior can be achieved through hybrid shapes such as grids of crosses.

Particular choices of L, R, and C that accurately capture the spectrum of a given FSS can be motivated by theory; however, empirical determinations of the filter parameters are ultimately needed to verify the theory. In 1967, Ulrich determined relations between the frequency responses and grid parameters of simple wire meshes and square grids [98,

Resonance Frequency	ω_0	$\sim$	λ/g
Characteristic Impedance	Z_0	$=$	$1/(2\omega_0 \ln \csc(\pi a/g))$
Generalized Frequency	Ω	$=$	$\omega/\omega_0 - \omega_0/\omega$
Normalized Admittance	Y	$=$	$1/\left(R + jZ_0\Omega\right)$

Table 4.2: Parameter definitions used to model capacitive square grids using the transmission-line model.

97]. Whitbourne and Compton corrected a numerical error in Ulrich's paper and extended the transmission-line model to include the dielectrics on which the grids are deposited [99]. Matrix methods can be developed which allow for quick calculation of the effect of cascading a number of filter elements in series. Cascading elements in filter stacks allows one to increase bandwidth, decrease in-band ripple, or increase cutoff sharpness to suit one's needs. These methods have been used to guide filter design for a number of millimeter-wave applications. A few examples are found in [2, 43, 92].

Figure 4.6 graphically shows the relation between the quantities of interest for the transmission-line model. Outgoing complex amplitudes a_1 and a_2 can be related to incoming amplitudes b_1 and b_2 via:

$$b_1 = m_{11}a_2 + m_{12}b_2 \tag{4.1}$$

$$a_1 = m_{21}a_2 + m_{22}b_2 \tag{4.2}$$

Assuming that there is an incoming wave from the left and none from the right, such that $a_2 = 0$, the reflection and transmission coefficients of interest are then:

$$\begin{aligned} R &= |b_1/a_1|^2 = |m_{12}/m_{22}|^2 \\ T &= |b_2/a_1|^2 = |1/m_{22}|^2 \end{aligned} \tag{4.3}$$

As described in [92], the matrix for the interface between two materials of index n_1 and n_2, with an FSS that has characteristic admittance Y, is then given by:

$$M = \frac{1}{2n_1}\begin{bmatrix} -Y + (n_1 + n_2) & -Y + (n_1 - n_2) \\ Y + (n_1 - n_2) & Y + (n_1 + n_2) \end{bmatrix} \tag{4.4}$$

As shown in Figure 4.5, the square-grid patterns used by ABS have characteristic admittances that can be related to their grid periods, g, and spacing between squares, $2a$. One would expect the resonance frequency for such a square grid to occur around a wavelength $\lambda \sim g$, making it convenient to work in normalized frequency units of $\omega \equiv g/\lambda$. Empirically, it has been found [98, 99] that the resonance frequency for such a grid between dielectrics occurs at

$$\omega_0 = \sqrt{\frac{2}{n_1^2 + n_2^2}} \left(1 - 0.27\frac{a}{g}\right). \tag{4.5}$$

The characteristic admittance of a grid can be expressed as

$$\Omega = \left(\frac{\omega}{\omega_0} - \frac{\omega_0}{\omega}\right) \tag{4.6}$$

$$Z_0 = R + iX\Omega \tag{4.7}$$

$$X = \frac{2}{n_1^2 + n_2^2}\left(4\omega_0 \ln \csc \frac{\pi a}{g}\right) \tag{4.8}$$

$$R \simeq \sqrt{\frac{4\pi\epsilon_0 c}{\lambda\sigma}}\frac{\eta}{4}, \tag{4.9}$$

where σ is the bulk conductivity of the metal in the mesh, λ is the free-space wavelength, and ϵ_0 is the permittivity of free space. Here $\eta = 1/(1 - 2a/g)$ is a form factor that accounts for grid geometry. The characteristic resistance of the grid, R, which represents the loss in the system, was determined empirically [98].

One key advantage of this simple transmission-line model is that a multi-layer system can easily be modeled by cascading the matrices of each of the layers. A dielectric boundary without an FSS has a matrix given by Equation 4.4 with Y = 0. A dielectric with thickness t and complex dielectric constant $\tilde{\epsilon} = \epsilon_{real}(1 - i\tan\delta)$ (refractive index is $\sqrt{\epsilon_{real}}$.) multiplies the wave amplitudes by a phase factor. This can be represented in matrix form as

$$M_{dielectric} = \begin{pmatrix} e^{-i\gamma} & 0 \\ 0 & e^{i\gamma} \end{pmatrix} \tag{4.10}$$

,

with $\gamma = 2\pi\tilde{n}t/\lambda$ and $\tilde{n} = \sqrt{\tilde{\epsilon}}$. The optical properties of a stack of materials can be calculated by multiplying together the matrices from individual elements,

$$M_{tot} = M_1 M_2 ... M_N \tag{4.11}$$

4.2.2 Finite-Element Electromagnetic Simulations

For an understanding of the behavior of quasioptical filters at all frequencies and for non-normal incidence, the transmission-line model falls short and full electromagnetic simulations are needed. A finite-element analysis of a filter design can be run using the HFSS software package.[2] The geometry in question can be modeled in three dimensions, with infinite periodic boundary conditions assumed in two directions.

HFSS is limited to modeling single-layer filters. The random angles placed between layers in multi-layer filters would require the model to be run many times with many different combinations of angles for each layer. The computation time required for a multi-layer model rises dramatically with each layer added, and becomes prohibitive for the 6-8 layers typically used for lowpass edge filters. However, as a verification of a single-layer design, HFSS is extremely useful. A comparison between the HFSS model, transmission-line model, and FTS measurements of a single-layer with a grid spacing of 150 μm is shown in Figure 4.7. As that figure shows, the HFSS model successfully captures both the frequency at which the first minimum occurs, as well as the position of the resonance peak directly afterwards. Probably due to insufficient grid refinement, the height of this peak is not accurately captured, and there are ripples in the transition which are not seen in the measured data.

4.3 Large-Format Quasi-Optical Filters for ABS

Physical implementation of quasioptical filters requires choosing a substrate material, metallic conductor, and, for filter stacks, a choice of dielectric or vacuum spacing. A large number

[2] Ansys, Inc. www.ansys.com

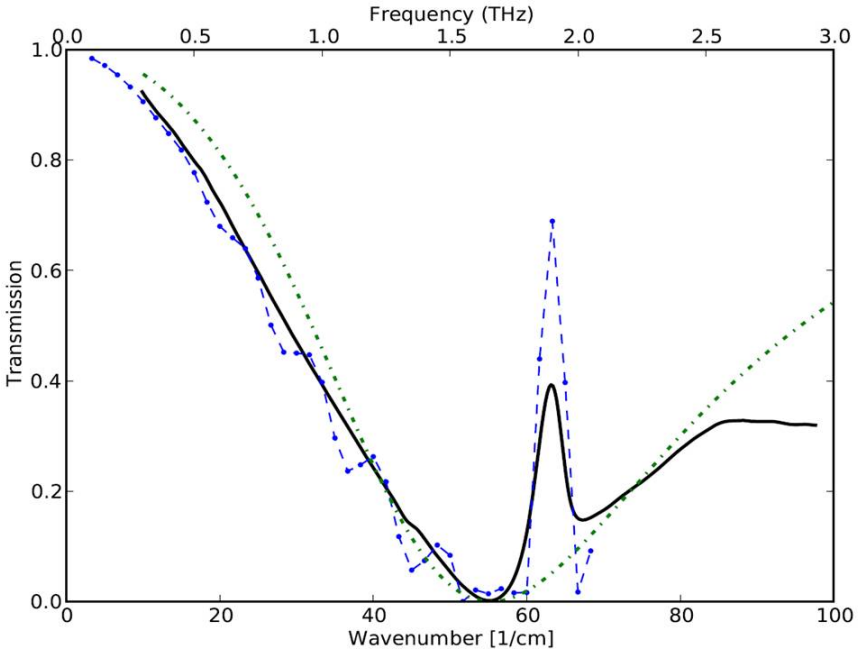

Figure 4.7: Measured transmission spectrum (solid black line) measured by Ed Wollack using a high-frequency Fourier Transform Spectrometer at Goddard Space Flight Center of a single-layer capacitive grid with grid spacing of 150 μm, compared with equivalent-circuit (dot-dash green line) and numerical HFSS models (dashed blue line). The equivalent-circuit model clearly deviates from the measurement above the resonance and does not capture the transmission peak at 67 cm^{-1}. The resonance frequency for the equivalent-circuit model was placed at $\nu \sim 0.83/g$, consistent with measurements by others [92].

of substrate and conductor combinations, as well as fabrication techniques, were considered for the ABS filters. Metal deposition and photolithography facilities available to us in Princeton could produce high-quality filters on a number of substrate materials, but were limited to 12.5 cm diameter patches, whereas the filters for ABS need to be a minimum of 25 cm in diameter.

A commercial solution was eventually found in which aluminized Mylar, which is readily available in rolls many feet wide with Mylar substrates as thin as 6 μm, was patterned by Tech-Etch, Incorporated[3] . Circuit-board fabrication companies routinely pattern substrates far larger than 300 mm in diameter, and Tech-Etch specializes in patterning metals other than copper. Tech-Etch was one of three vendors who attempted to pattern metals on

[3]Tech-Etch, Inc., 45 Aldrin Road, Plymouth, MA 02360 USA, tel: (508) 746-0300

Material	n	$\tan\delta$ ($\times 10^4$)	κ W /(cm K)
Polypropylene	1.5	5-7	0.001-0.002
Mylar	1.8	100	0.001
PTFE	1.40-1.45	3-6	0.002-0.003
Zitex G115	1.22	1.5-3	Unknown
Stycast 1266	1.68	0.023	Unknown

Table 4.3: Index of refraction, n; loss tangent, $\tan\delta$; and thermal conductivity, κ, for selected materials at 150 GHz considered for filter design. Refractive indices and loss tangents are taken from [53] and are typical reported values for millimeter wavelengths and at room temperature. Thermal conductivities are reported at 50K from [78, 73, 33, 48]. The Stycast 1266 data are from [56].

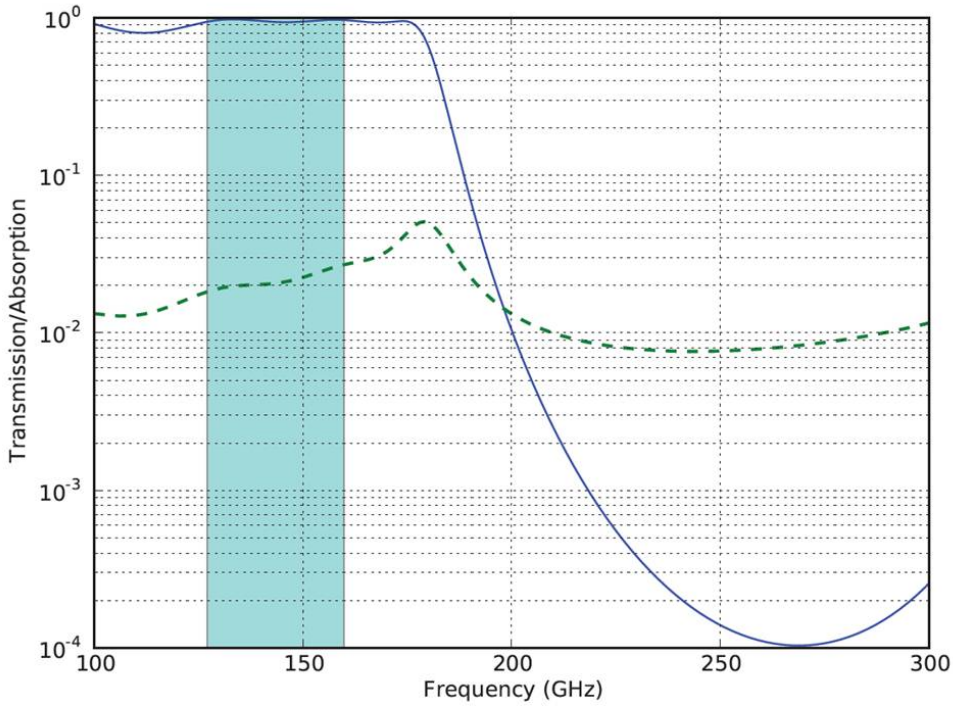

Figure 4.8: Expected transmission and absorption for the 4 K lowpass filter as computed from the transmission-line model. The solid blue line is the power transmission coefficient. The dashed green line is the expected absorption. The ABS passband is shown in cyan for reference.

6 μm Mylar, and was the only one that successfully produced a usable product. Tech-Etch can now produce filters with feature sizes down to 50 μm at sizes of 400 mm by 400 mm.

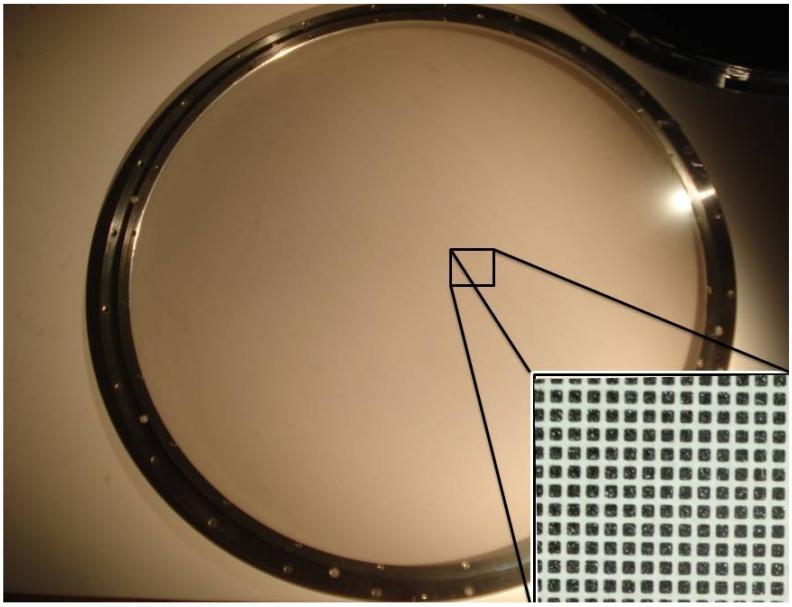

Figure 4.9: Photograph of a commercial IR blocker (∼300 mm in diameter) produced by Tech-Etch, Inc., mounted and ready to deploy on the ABS. The inset shows the square grid of the IR blocker, which has a grid spacing of 150 μm, at 25 times magnification.

Tech-Etch takes this material and photolithographically patterns the Mylar to produce a quasioptical filter.

Validation of single layers of metal-mesh filter at high frequencies was done through Fourier Transform Spectrometer (FTS) measurements at the Goddard Space Flight Center. One pattern ($g = 150\mu$m, $a = 25\mu$m, $f_0 \simeq 1.9$ THz) has had its frequency spectrum measured in the range 10-650 cm^{-1}. This spectrum is compared with results from transmission-line and HFSS models in Figure 4.7, where it can be seen that the transmission-line model agrees well at low frequencies but does not capture the resonance peak around 63 cm^{-1}.

4.3.1 Single-Layer IR Blockers

Single layers of metal mesh on 6-μm Mylar substrates are used in ABS to provide reflective IR-blocking filters. As can be seen from Figure 4.1, these IR blockers are used at the 40 K aperture of the cryogenic system to reduce the load on the absorptive PTFE filter as well

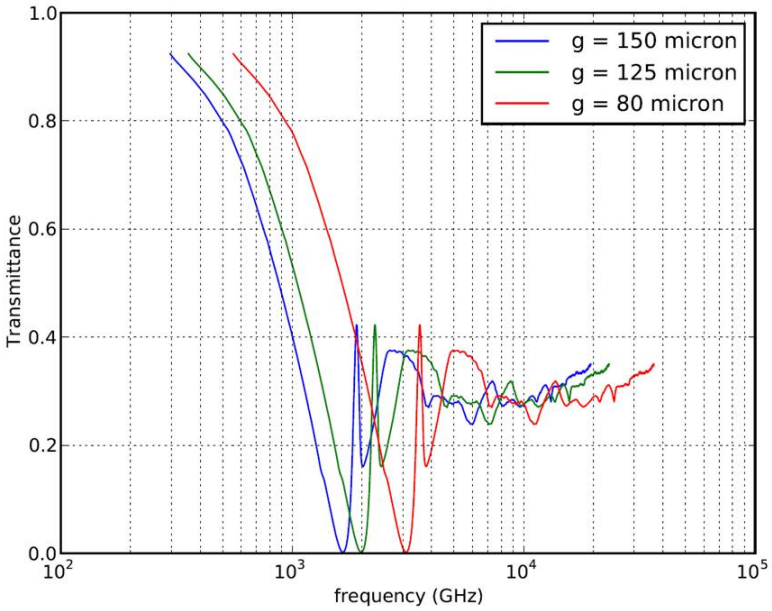

Figure 4.10: Transmission spectra of the IR blockers used by ABS. The spectrum of the 150 μm-grid-spacing filter (blue curve) was measured in an FTS, while the spectra of the other two filters are derived by shifting this spectrum in frequency.

as to reduce the IR emission of the PTFE filter to the 4 K cryogenic stage.

As shown in Figure 4.10, a single layer of metal mesh has a cutoff at a frequency of approximately $0.83\lambda/g$. Three different IR blocker patterns, with grid spacings of 80, 125, and 150 μm are employed in ABS, which have transmission minima of approximately 3.1, 2.0 and 1.6 THz, respectively. While only the pattern with 150 μm grid spacing was measured in an FTS, the scale-invariance of electrodynamics allows one to infer frequency spectra for the other two patterns simply by multiplying the transmission spectrum of the g = 150 μm pattern by 150 μm $/g'$, where g$'$ is the grid spacing of the pattern in question. The assumption of scale-invariance assumes that everything in the system scales according to this same factor, which is not strictly true for the three IR blockers used in ABS, because the substrate material and aluminum thicknesses are the same for all three patterns. However, their thickness is much smaller than the wavelengths we are concerned with, and can be neglected to first approximation.

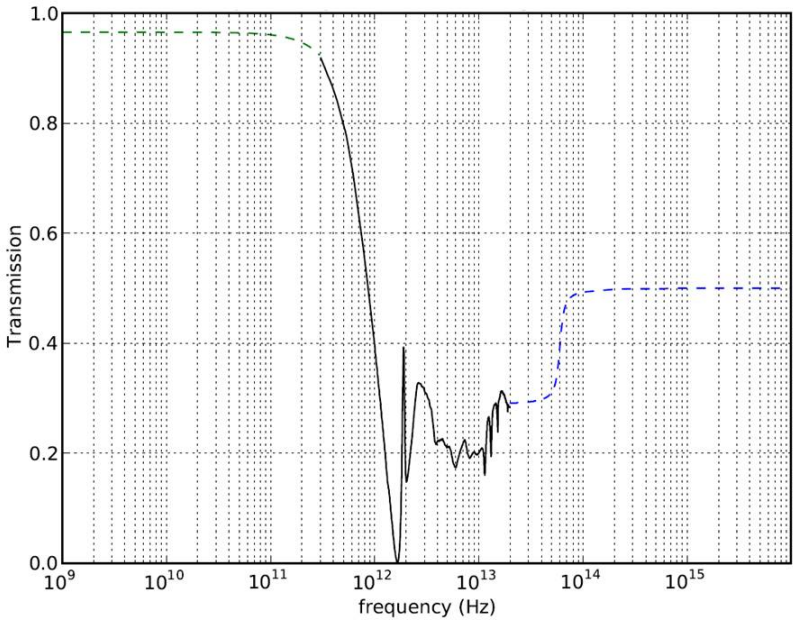

Figure 4.11: Composite transmission spectrum for a single (g = 150 μm) IR blocker. Measured data from an FTS (black line) cover the range 300 GHz - 20 THz. The transmission-line model (dashed green line) extrapolates the data on the low-frequency side. An arctangent function is used to extrapolate the high-frequency data to 50% by 100 THz.

The transmission spectra of the three IR blockers used in ABS, measured or inferred as described above, are shown in Figure 4.10. By creating stacks of IR blockers of varying cutoffs, one can stagger their frequency minima and resonance peaks to block a broader range of frequencies. The FTS at GSFC could only measure optical properties in the range 300 GHz to 20 THz. At higher frequencies, the transmission of the filter is assumed to approach 50% (the approximate filling fraction of metal in the square-grid pattern). At low frequencies, the transmission-line model could be used to extend these measurements. Measurements of the transmission of a broadband (127 $\pm$ 8 GHz) source through IR blockers in a simple feedhorn-coupled range show transmission above 97% at the lower end of the ABS passband and validate the transmission-line model at low frequencies. The extended spectrum assumed for the IR blockers in the filter-stack modeling below is shown in Figure 4.11.

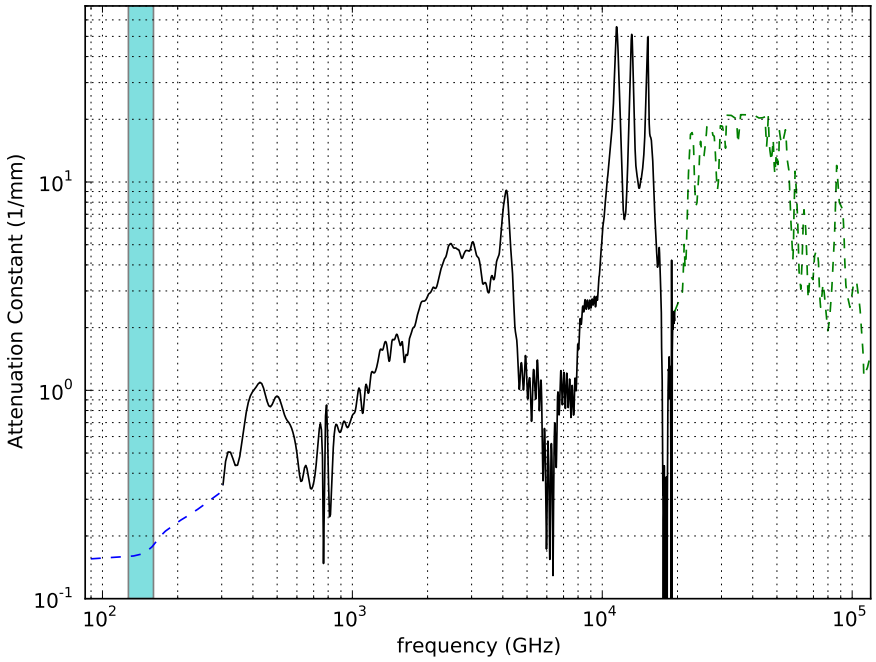

Figure 4.12: Composite absorptivity of Mylar from millimeter to mid-IR wavelengths. At frequencies from 90-304 GHz the data (blue dashed line) are taken from [43]. At intermediate frequencies from 304 GHz to 20 THz, the absorptivity is inferred from spectra taken by Ed Wollack of an ABS IR blocker at Goddard Space Flight Center. The high-frequency data in the range 20-118 THz are taken from [95]. The ABS passband is shown in cyan for reference.

Analysis of a stack of IR blockers

Analyzing the thermal mitigation provided by a stack of multiple IR blockers in series is complicated by a number of factors. The IR blockers are thin membranes stretched in metal rings. Some wrinkling, at the level of 10 microns, is present at room temperature, and differential contraction between the Mylar membrane and aluminum mounting ring will induce further wrinkling upon cooling. The transmission-line model describes stratified media where all variation in optical properties occurs in one dimension. Additionally, the transmission-line model is only valid for wavelengths below the grid spacing of the metal mesh. Most of the power from blackbody emission from the warm optics occurs at frequencies above the cutoff frequencies of the IR blockers. This failure of the transmission-line

model requires the use of measured transmission data from an FTS at high frequencies, along with a model that can incorporate the effects of multiple reflections from a stack of filters.

One cannot use the equivalent-circuit parameters for metal mesh for frequencies above the resonance frequency $\nu \sim 1/g$ of the grids. Yet, given the transmission data for a single IR blocker, as from the FTS measurements done at Goddard Space Flight Center, and an estimate of the attenuation constant of Mylar at all frequencies, one can invert the transmission-line model to calculate the admittance of the grid at a discrete set of frequencies. The matrix for a single grid on a dielectric substrate of thickness t and complex index of refraction $\tilde{n} = n\sqrt{1 - \imath \tan\delta}$ surrounded by vacuum is

$$\frac{1}{4n}\begin{pmatrix} -Y+(1+n) & -Y+(1-n) \\ Y+(1-n) & Y+(1+n) \end{pmatrix}\begin{pmatrix} e^{-\imath 2\pi\tilde{n}t/\lambda} & 0 \\ 0 & e^{\imath 2\pi\tilde{n}t/\lambda} \end{pmatrix}\begin{pmatrix} n+1 & n-1 \\ n-1 & n+1 \end{pmatrix}, \tag{4.12}$$

where λ is the free-space wavelength of the electromagnetic wave. The transmission is then the squared modulus of the lower-right element of the resulting matrix. This equation can then be inverted to get the admittance given a transmission and attenuation constant at a given frequency. This was done using the compiled transmission spectrum shown in Figure 4.11 and the composite attenuation constant plotted in Figure 4.12. The matrices of the three IR blocker patterns obtained in this way could then be cascaded to model the transmission of a stack of IR blockers, and the transmission calculated from this. The transmission calculated in this way for stacks of two through six IR blockers for the filter cutoffs of the top stack in ABS are shown in Figure 4.13.

To take into account the effect of thermal emission of Mylar in the stack, it was assumed that the temperatures of the filters in the stack varied linearly. For the stack of 6 IR blockers above the PTFE filter, it was assumed that the top filter was at 300 K, and that the filters went down linearly to approach the 120 K PTFE filter. For the stack below the PTFE filter, it was assumed that the filter temperatures went down linearly from the 120 K PTFE filter temperature to 10 K. The emissivity of the IR blocker was modeled using the transmission-

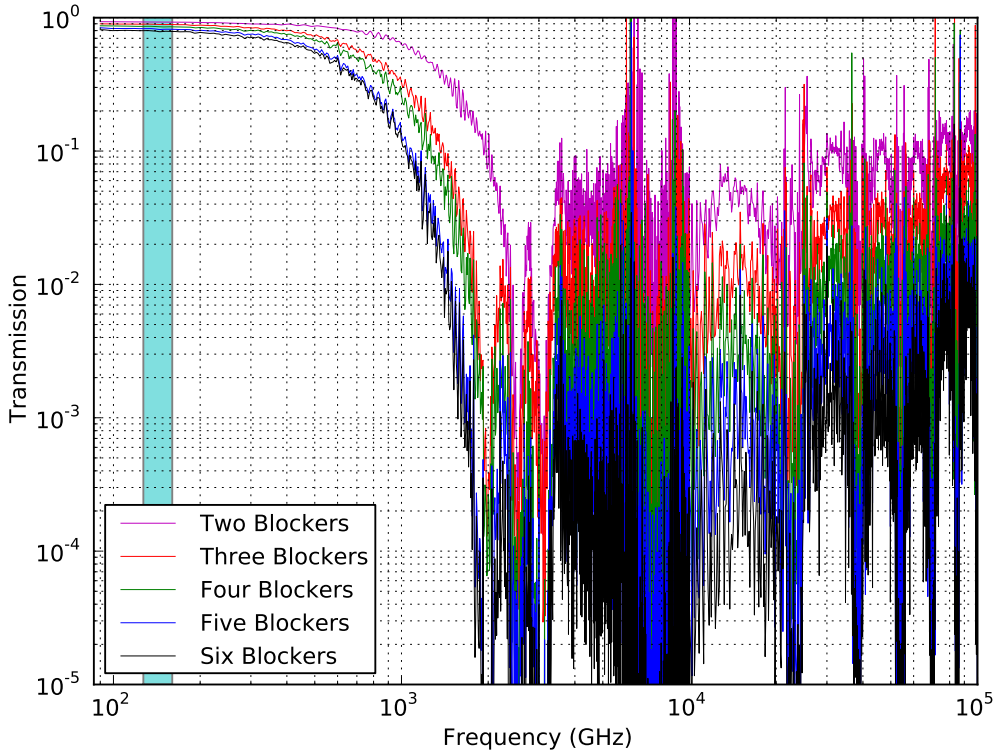

Figure 4.13: Modeled transmission spectra for stacks of two through six IR blockers. The diminishing returns of adding additional blockers can be seen. The stack of six IR blockers cuts transmitted power in the IR down to a level of 10^{-2}-10^{-3}, less than the value that would be inferred by simply multiplying single IR blocker spectra together, due to Mylar thermal emission.

line model with the composite attenuation constant of Figure 4.12. Each filter emission was then cut by the stack of filters below it and added to the total. This neglects to take into account thermal emission that is reflected back up the stack, but as a first pass calculation this should be accurate at the level of a few percent.

Additionally, to take into account the wrinkles that form in the IR blockers when cooled, which change the distances between filters, each stack was analyzed five times with spacings changed at random by up to one millimeter. The spectra for the five cases were then averaged together to get the form shown in the figure. The shapes of the transmission curves was essentially unchanged, and the spread in transmission was approximately ±5%.

4.3.2 Lowpass Edge Filter Construction

The lowpass edge filter for ABS uses six layers of square grid separated by polypropylene. The patterns used and their spacing were determined through trial and error using the transmission-line model described in Section 4.2.1. A number of patterns were available with grid spacings from 600 μm down to 70 μm. Combinations of these patterns were investigated until one was found with high transmission in band and a cutoff below the blue leak, which has structure starting at 180 GHz. The thickness of the polypropylene layers between pattern layers was also tuned by trial and error. Placing an additional polypropylene layer of approximately $\lambda/4$ thickness was found to make transmission in band much flatter. The lowpass edge filter that was chosen has two outer layers with g = 150 μm and a = 25 μm; the inner four layers have g = 260 μm and a = 55 μm. The details of the layers used in the lowpass filter are summarized in Table 4.4. The expected spectrum from the transmission-line model is shown in Figure 4.8.

Heat-pressing Mylar to polypropylene was investigated in detail. Adhesion was achieved by raising the temperature of the filter stack above the melting point of polypropylene but below that of Mylar. Higher temperatures produced better adhesion, with temperatures of 175-180 °C best. Pressing at these high temperatures requires specialized jigs in order to get the desired thickness of polypropyelene between each Mylar layer, as the polypropylene becomes fully liquid and flows under pressure. This makes it impossible to put any significant pressure on the stack without thinning the polypropylene.

The heat pressing was performed under vacuum, so that the polypropylene did not oxidize. Adhesion was greatly enhanced when a metal pattern was present on the Mylar, likely because the metal pattern gave the polypropylene features to melt around. Even with metal patterns and high oven temperatures, filter stacks made by heat pressing never performed well under thermal cycling. Heat-pressed stacks always delaminated over time.

Because of the lack of success in heat pressing Mylar and polypropylene together, epoxy was used to adhere the two instead. Stycast 1266 was chosen because its properties were known [56]. It is a low-viscosity epoxy, which allows very thin (0.25-0.5-mil) layers to be

Layer Number	Material	Thickness	Pattern	g	a
1	polypropylene	107 μm	No	—	—
2	mylar	6 μm	Yes	150 μm	25 μm
3	polypropylene	279 μm	No	—	—
4	mylar	6 μm	Yes	260 μm	55 μm
5	polypropylene	279 μm	No	—	—
6	mylar	6 μm	Yes	260 μm	55 μm
7	polypropylene	279 μm	No	—	—
8	mylar	6 μm	Yes	260 μm	55 μm
9	polypropylene	279 μm	No	—	—
10	mylar	6 μm	Yes	260 μm	55 μm
11	polypropylene	279 μm	No	—	—
12	mylar	6 μm	Yes	150 μm	25 μm
13	polypropylene	107 μm	No	—	—

Table 4.4: Material types, thicknesses, and grid parameters, if applicable, of the layers that comprise the ABS lowpass filter.

used for adhesion. Its optical properties have been measured in a reflectometer at Princeton. Its relatively high absorption at 2 mm wavelengths increases the overall absorption of the filter, but stacks produced with epoxy stayed intact after many thermal cycles. Final gluing of the ABS lowpass filter was performed by Katerina Visnjic.

4.3.3 Analysis of Total Filter Stack

A blackbody in thermal equilibrium at a temperature T radiates power with a frequency spectrum given by the Planck formula

$$B(\nu, T) = \frac{2h\nu^3}{c^2} \frac{1}{e^{\frac{h\nu}{kT}} - 1}, \tag{4.13}$$

where h is the Planck constant, k is the Boltzmann constant, and c is the speed of light. $B(\nu, T)$ gives the power radiated in W m^{-2} sr^{-1} Hz^{-1}. The total power incident on a planar aperture of total area A can be calculated by evaluating the integral

$$\begin{aligned} P &= A \int_0^{2\pi} d\phi \int_0^{\pi/2} d\theta \sin\theta \cos\theta \int_0^{\infty} d\nu B(\nu, T) \\ &= \pi A \int_0^{\infty} d\nu B(\nu, T) \end{aligned} . \tag{4.14}$$

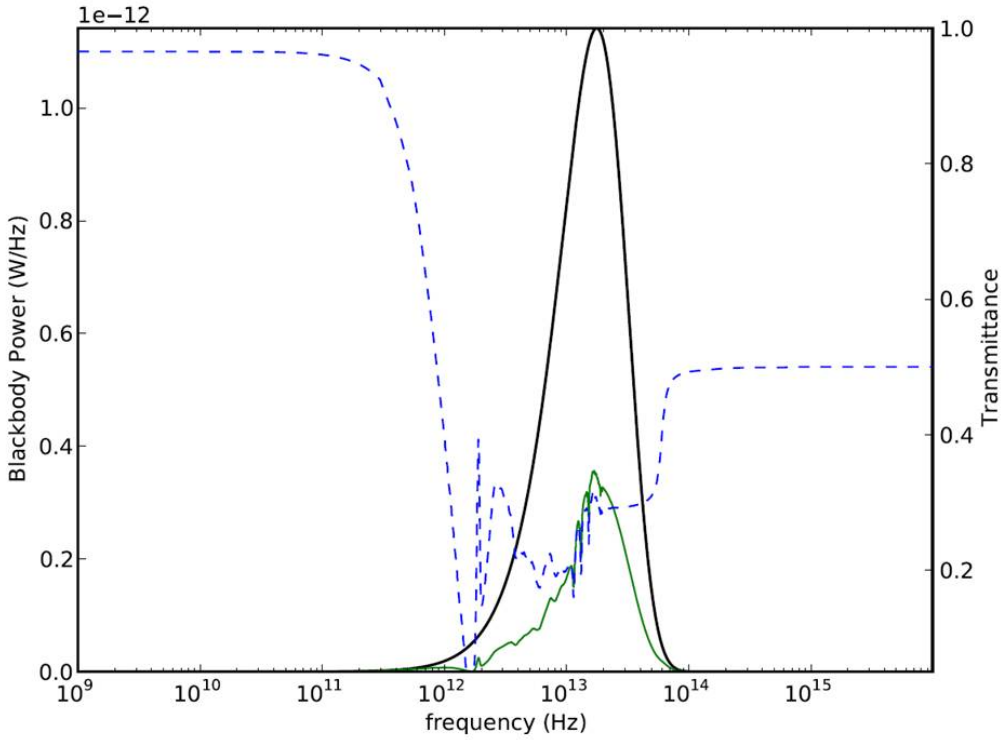

Figure 4.14: A 300 K blackbody spectrum (solid black line) is shown versus the transmission spectrum from the IR blocker at the 300 K stage (dashed blue line). The resultant power transmitted to the 40 K filter stack (solid green line). The power is reduced from 32.62 W to 9.13 W, a reduction by 72%.

The $\cos\theta$ factor comes from the reduction in effective aperture area for radiation coming in at oblique angles. The angular integral evaluates to π. The evaluation of the integral over all frequencies leads to the Stefan-Boltzmann law with a factor relating to the area

$$P = A\sigma T^4, \tag{4.15}$$

where σ, the Stefan-Boltzmann constant, is 5.67×10^8 W / (m^2 K^4).

300 K stage

The 300 K stage for ABS has an optical aperture of 300-mm diameter. This gives an area of 0.071 m^2. Using Equation 4.15, this implies that the power incident on the 40 K aperture

is approximately 32.6 W. This power is cut by an IR blocker with a grid spacing of 150 μm and a frequency cutoff around 2 THz. This initial filter should cut power going to the 40K filter stack by approximately 70%. Figure 4.14 shows the IR blocker transmission versus frequency, along with a 300 K blackbody spectrum. A 300 K blackbody spectrum entering the telescope aperture will be reduced in power by approximately 70% by this first stage of thermal filtering. Additional filters added at the 300 K stage were found to mitigate little thermal load at the 40 K and 4 K stages. This is most likely due to radiation leaking through the 40 K aperture from the cavity between the 300 K and 40 K stages of the cryostat.

40 K stage

The bulk of the thermal filtering occurs at the 40 K stage. There are five IR blockers above, and four IR blockers below, the 2.5-cm PTFE filter at 40 K. The five filters above have grid spacings of 125, 80, 125, 80, and 150 μm, in that order from the sky to the PTFE filter. The four IR blockers below have cutoffs of 150, 80, 125, and 125 μm, in that order from the PTFE filter toward the 4 K stage. It was found through multiple cooldowns in the ABS cryostat, that this relatively large number of IR blockers was necessary to reduce the loading on the PTFE filter (subsequently lowering the temperature of the PTFE and reducing its re-emission to 4 K) and the eventual loading on the 4 K stage.

The modeled transmitted power through the top stack of IR blockers, including the one at 300 K, that reaches the PTFE filter is shown in Figure 4.15. The model used for this is described in greater detail in Section 4.3.1. The modeled power transmitted down to the lowpass filter at 4 K is shown in Figure 4.16. The emissivity of the PTFE filter was taken from the model of Figure 4.4, which was multiplied by a blackbody spectrum at 120 K, and then input into the model of the bottom stack of 5 IR blockers, including the one at 4 K.

The model is only accurate to within a factor of three, as can be seen from the mismatch between modeled incident power on the PTFE to the modeled emitted power. The 237 mW of incident power on the PTFE filter cannot produce the 825 mW of emitted power. This points to an underestimation of the power that transmits through the IR blocker stacks

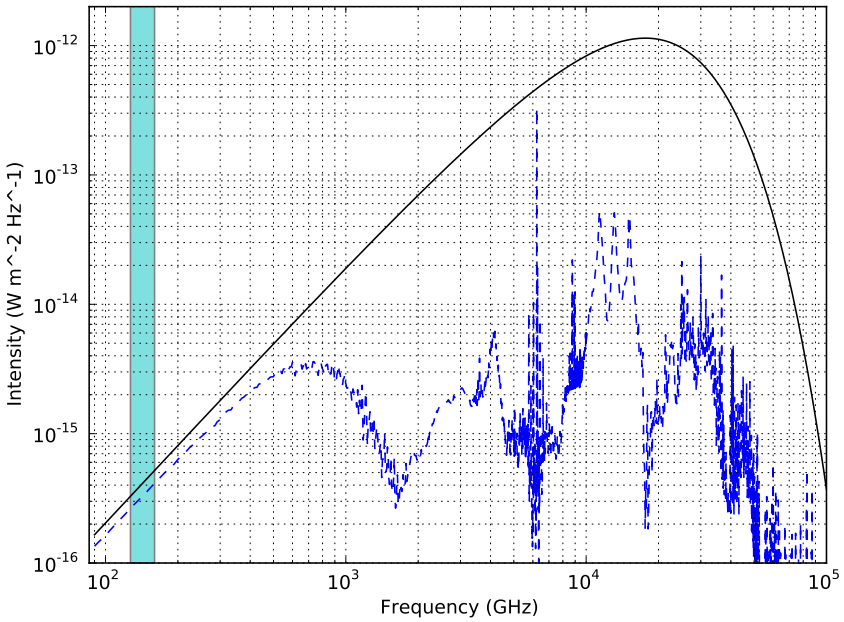

Figure 4.15: Modeled spectrum of radiation incident on the absorptive PTFE filter from above. The solid black curve is a 300 K blackbody spectrum. The dashed blue curve shows this spectrum after passing through the set of IR blockers. Total integrated power is cut from 32.6 W to 237 mW, a reduction of nearly 99.3%.

or an overestimation of the temperature of the PTFE filter. A test filter 2 cm thick with no AR coating was cooled in the ABS cryostat with a diode thermometer at its center. In that test it reached 129 K at its center. The filter actually used in ABS is 2.2 cm thick and has an additional level of IR blocking due to the pores of the Zitex coating, so a reduced temperature is likely. The value of 120 K for the model above was chosen somewhat arbitrarily. If the PTFE filter actually reaches a temperature of 110 K instead of 120 K the emitted power is cut to 582 mW and the mismatch is reduced significantly. To reach an emitted power of 237 mW, the temperature of the filter would have to be reduced significantly further to 88 K.

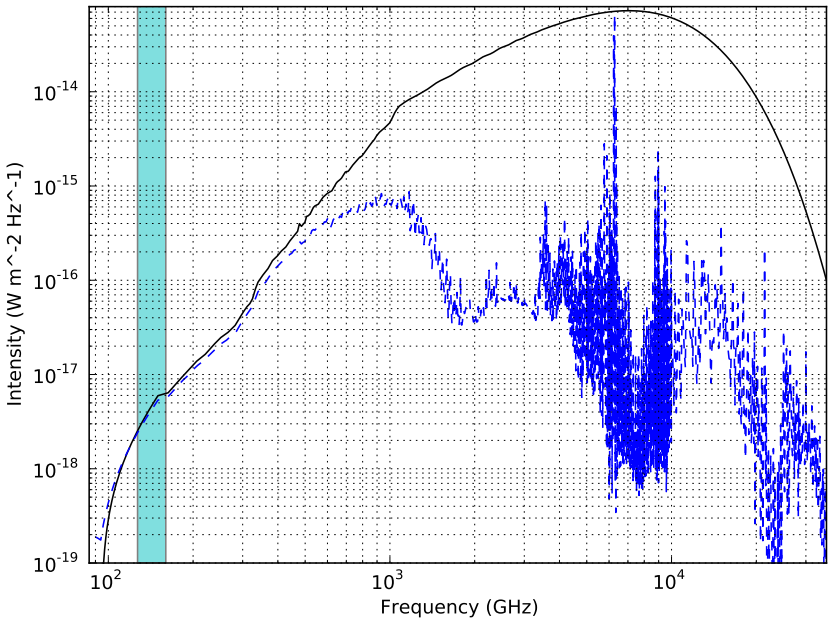

Figure 4.16: Modeled spectrum of radiation emitted by the PTFE filter (solid black line) and then cut by the bottom IR blocker stack, including the IR blocker at 4 K. The spectrum of radiation transmitted down to the 4 K lowpass filter is shown (dashed blue line). Almost no power is expected to transmit through the PTFE filter at IR frequencies. The PTFE filter emits 825 mW of power at a temperature of 120 K. This power is cut to 3 mW by the filter stack, a 99.6% reduction.

4 K Stage

The lowpass filter at the 4 K stage affords one final layer of IR blocking. Figure 4.17 shows the effect of the lowpass filter on radiation entering the 4 K volume. The model cannot be trusted at frequencies much above the 180 GHz cutoff of the filter, so the power reduction afforded by the lowpass filter cannot be inferred. The 3 mW of power that are incident upon the lowpass filter according to the model would cause a negligible rise in the 4 K base temperature. A rise in 4 K base temperature by 100-200 mK is observed when the cryostat is open to light; however, suggesting that the ABS filter stack actually transmits 60-100 mW. This additional load could be caused by additional radiation loading on the outside of the 4 K shell or it could be caused by more than 3 mW passing through the filter stack.

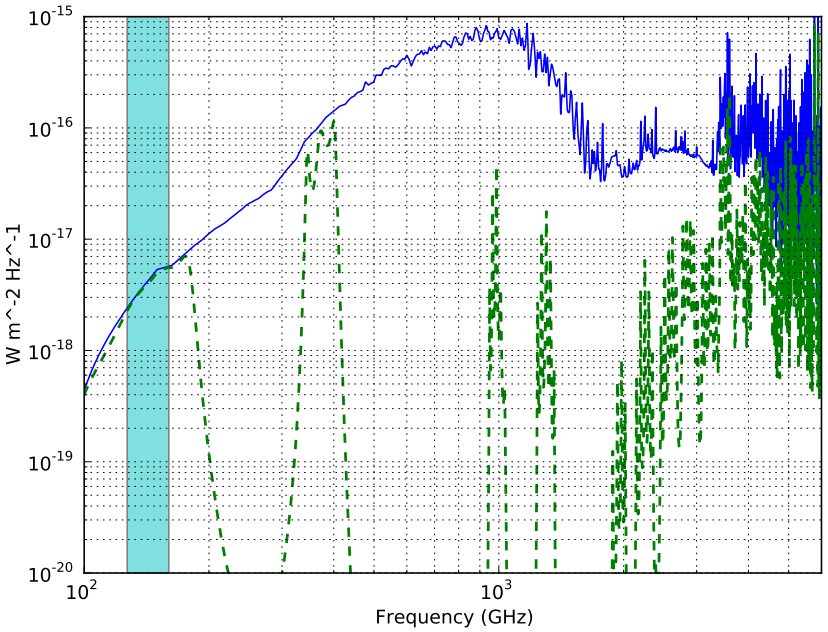

Figure 4.17: Modeled power incident upon (solid blue curve) and transmitted through (dashed green curve) the 4 K lowpass filter. The model cannot be trusted for high frequencies, so the level of power reduction cannot be evaluated accurately.

4.4 Summary

Free-space filters for ABS were designed and constructed to reduce the thermal load on the cryogenic system from radiation entering the telescope aperture. We worked closely with a circuit-board manufacturer, Tech-Etch, Inc., to develop commercial capabilities for producing quasi-optical filters made by patterning aluminum on 6μm Mylar substrates up to 40-cm in diameter. These quasi-optical filters were made into single-layer IR blockers as well as a six-layer lowpass filter stack with a cutoff around 180 GHz. This lowpass stack was produced by epoxying pattern layers to polypropylene layers that act as dielectric spacers. Transmission-line matrix models were used to model the quasi-optical filters using equivalent circuits of passive electrical components. The filter stack has been tested with the ABS cryostat open to the lab in Princeton, and reduces the total additional load at 4 K, compared to when the cryogenic stages were capped off, to a level of 100-200 mW.

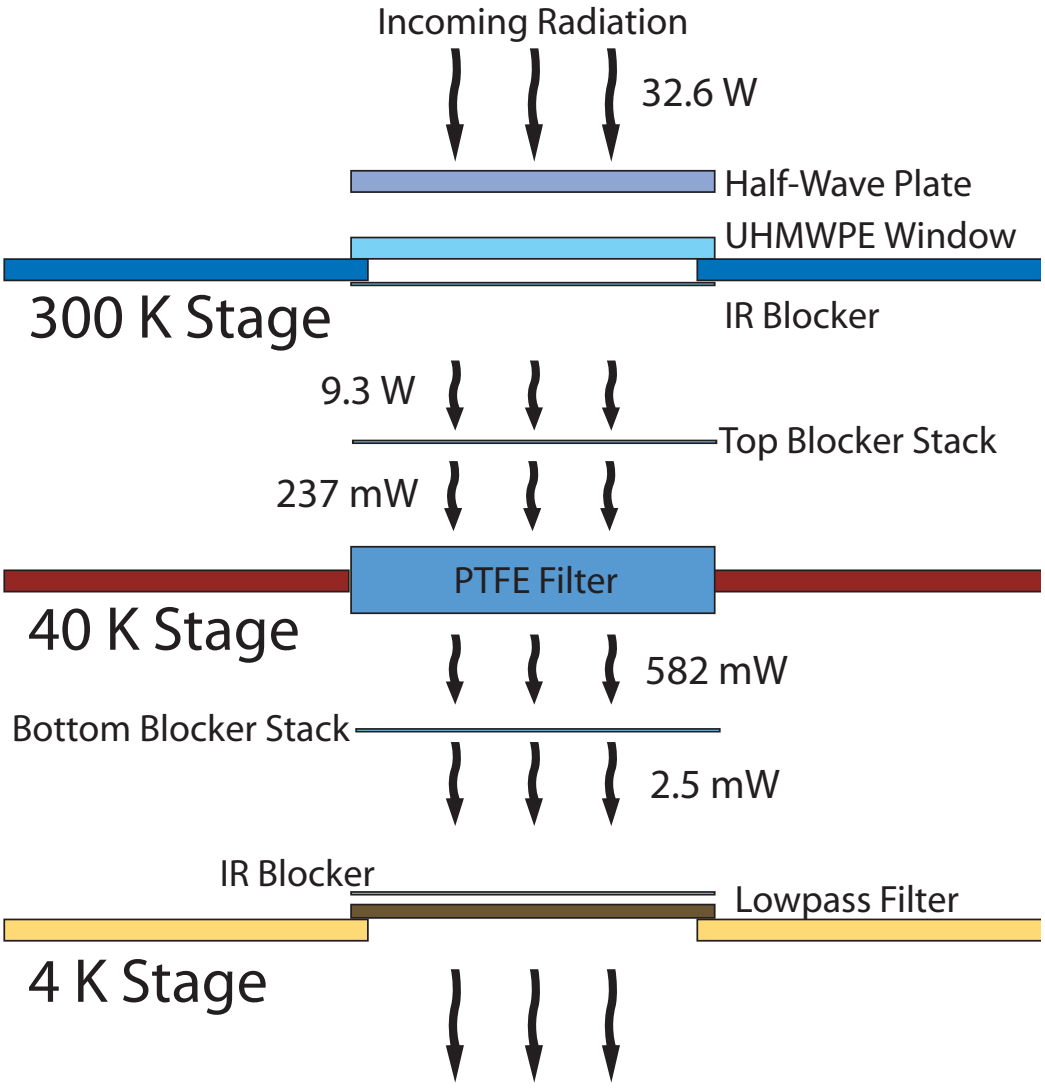

Figure 4.18: Summary of modeled powers transmitted by the ABS filter stack. A power of 32.6 W from a blackbody spectrum at 300 K is incident on the telescope. This power is cut successively by IR blockers, the PTFE filter at the 40 K, and the final lowpass filter at 4 K. The PTFE filter is assumed to be at 110 K. The incident and emitted powers for the PTFE filter do not match due to underestimating the power that transmits through a stack of IR blockers or the PTFE filter being colder than 110 K. Ultimate power to the 4 K stage through the filter stack is not well understood.

Chapter 5

Current Status

ABS has been designed and built over the last three years, and is currently being prepared for deployment to Chile. All subsystems of the telescope have been tested individually in Princeton, and final integration of the receiver, telescope base, shipping container, and associated electronics, which began in the summer of 2011, is now nearly complete. A photograph of the instrument on top of the shipping container is shown in Figure 5.3. A photograph of the inside of the ABS container is shown in Figure 5.4.

The receiver currently contains a focal plane with 12 of the 24 pods installed. The detector chips to fill out the remainder of the focal plane are currently being fabricated at NIST and will be installed at the site in Chile. The receiver cryogenic system is operating at a base temperature of 3.0-3.2 K and achieving cycles of its adsorption refrigerators down to 270 mK with hold times of up to 48 hours. Of the 240 TES bolometers (120 polarimeter chips) installed in the focal plane, 218 are able to be operated on their transition temperatures. The HWP air-bearing system has been run at rotational frequencies of up to 2.5 Hz for days at a time.

Recent measurements with the cryostat in the high bay looking at the warm room through a wire-grid polarizer with the HWP rotating have shown modulation of the detector signal at four times the rotation frequency. Time streams from a single pod, Figure 5.1, show clear modulation in two groups of detectors that are out of phase by 90°, as one would

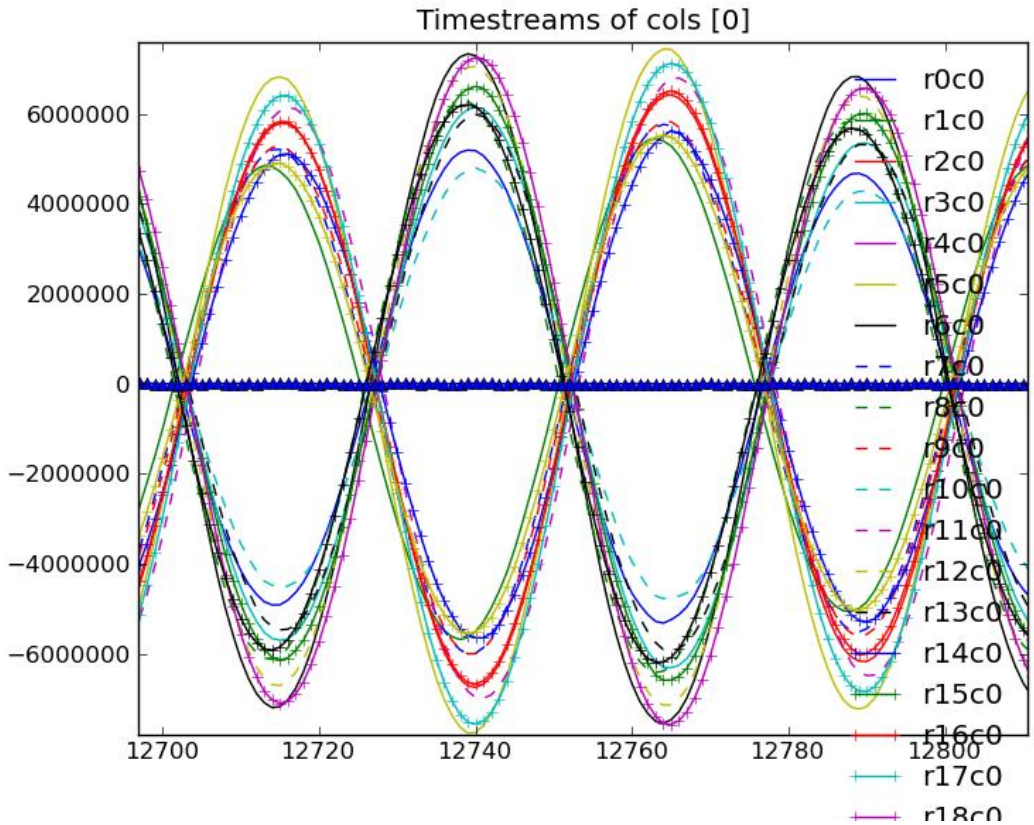

Figure 5.1: Timestream of detector data from all working detectors within a pod as the cryostat look out at the room-temperature high bay through a polarizing wire grid, showing modulation of the signal at four times the HWP rotation frequency. The x and y axes are in arbitrary units. The x axis is time, with approximately 400 units corresponding to one second. The HWP was rotating at around 2 Hz. The two families of curves that are out of phase by 90° correspond to the two sets of orthogonal probes. In this pod, most of the feedhorns had their orthomode transducers in the same orientation.

expect. Figure 5.2 shows stacked frequency spectra from all working detectors for this data stream. The 8 Hz line is clearly visible in nearly all detectors, along with weaker 2 and 4 Hz lines.

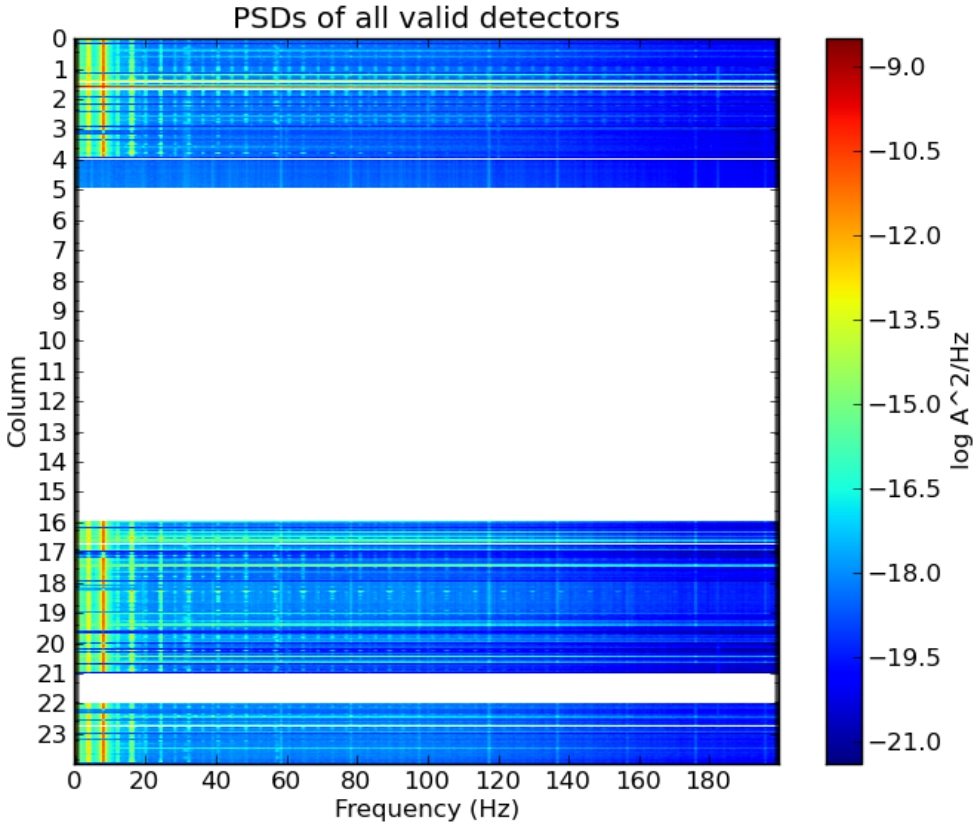

Figure 5.2: Waterfall plot showing stacked detector frequency spectra from a two-minute time stream taken while the cryostat looked out at the warm high bay with a polarizing wire grid and the HWP rotating at 2 Hz. Column number, corresponding to different pods, is shown on the y axis. Frequency in Hz is shown on the x axis. Only half of the pods are in the focal plane, and the detectors in column 21 become unlocked when the HWP motor is running. However, in the remainder of the detectors, a clear 8 Hz line is visible in nearly all detectors, as are weaker 2 Hz and 4 Hz signals. The colorbar on the right shows the scale in A^2/Hz.

Figure 5.3: Photograph of the ABS experiment from the side. The base and receiver are raised to the roof as they will be for observations in Chile.

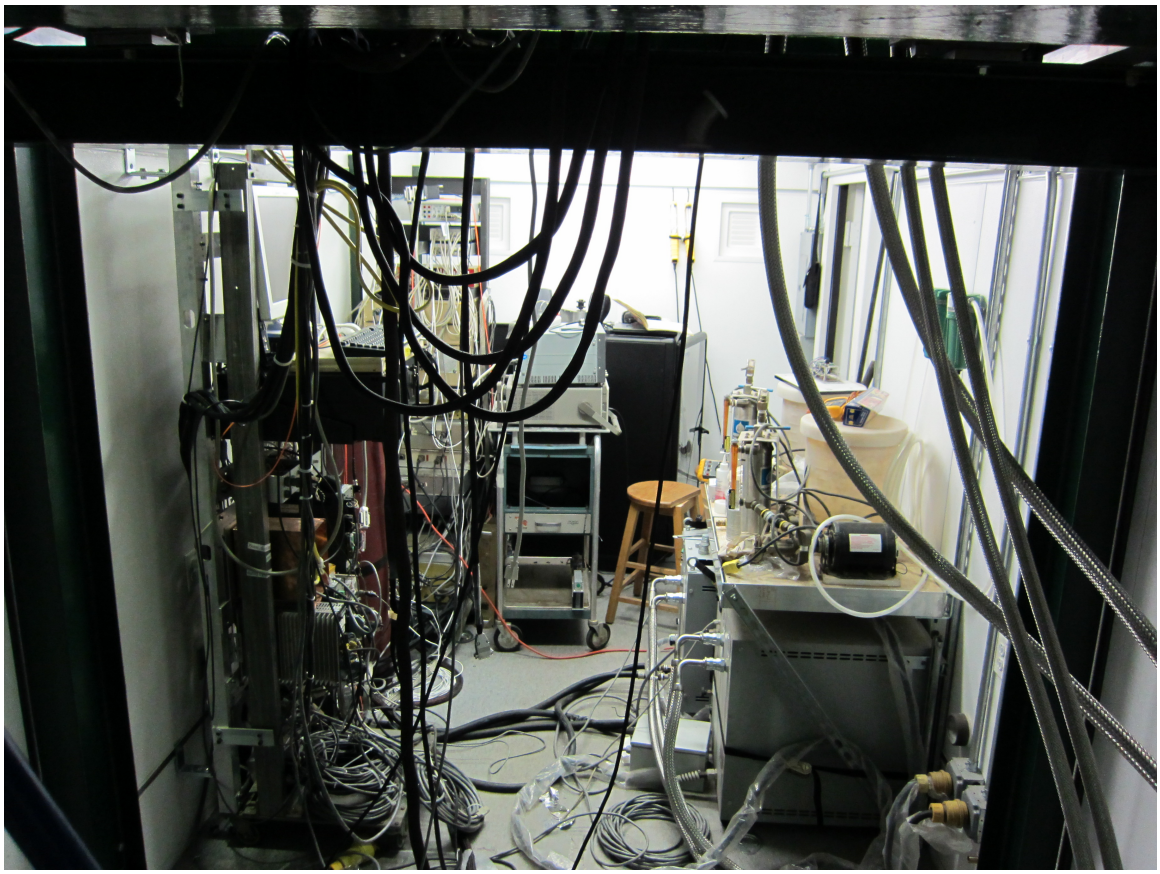

Figure 5.4: Photograph of the inside of the ABS container with the base and receiver raised to the roof. The pulse-tube compressors are on the floor on the right. Above the compressors are the water-cooling pump stations for them. Readout electronics racks are along the left wall.

Appendix A

Compiled Outputs from DADRA Simulation of Optics

This appendix compiles estimates of beam parameters from the DADRA physical-optics code as described in Section 3.2.1. Figure A.1 shows the numbering of the pods and feeds versus position on the sky. Figures A.2 A.3 A.4 A.5 A.9 A.10 A.11 A.12 A.13 A.14 A.15 A.16 A.17 show the distribution of estimated beam parameters across the focal plane, in coordinates on the sky.

Note that the differential beam plotted in Figures A.9 A.10 A.11 is much more uniform across the focal plane than other beam parameters. This is due to the fact that each feedhorn angle was individually varied in order to minimize this quantity, leaving other beam parameters to fluctuate.

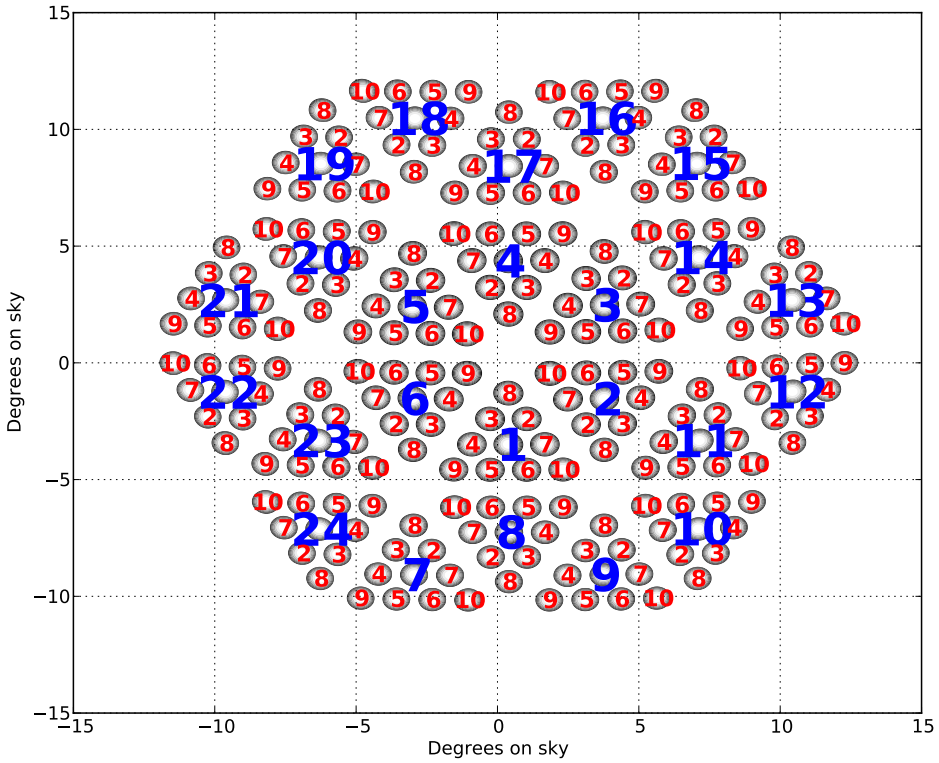

Figure A.1: Layout of the ABS copolar beams on the sky, numbered by pod (large blue numbers) and feed (small red numbers). Outer dark contours are at -24 dB. Feed number one in each pod is the central feed.

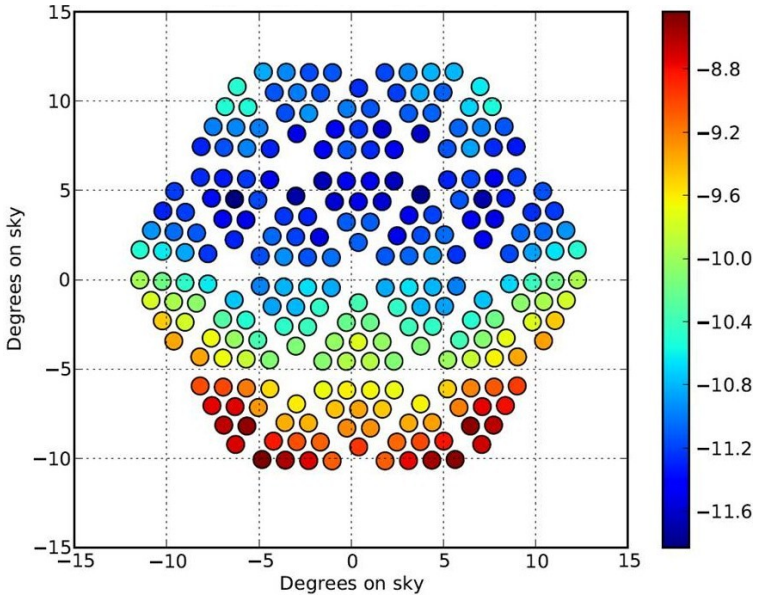

Figure A.2: Edge taper at 145 GHz averaged over the edge of the cold aperture stop at 4 K in dB down from maximum response across the ABS focal plane. The value for each feedhorn is shown at its position on the sky relative to the center of the array.

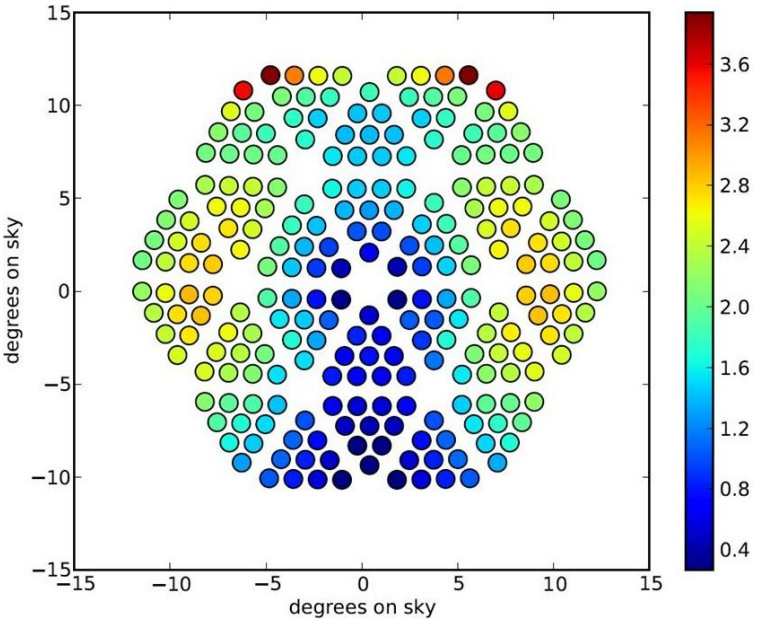

Figure A.3: Beam ellipticity as a percentage of beam width for one of the probes on each feedhorn at 127 GHz.

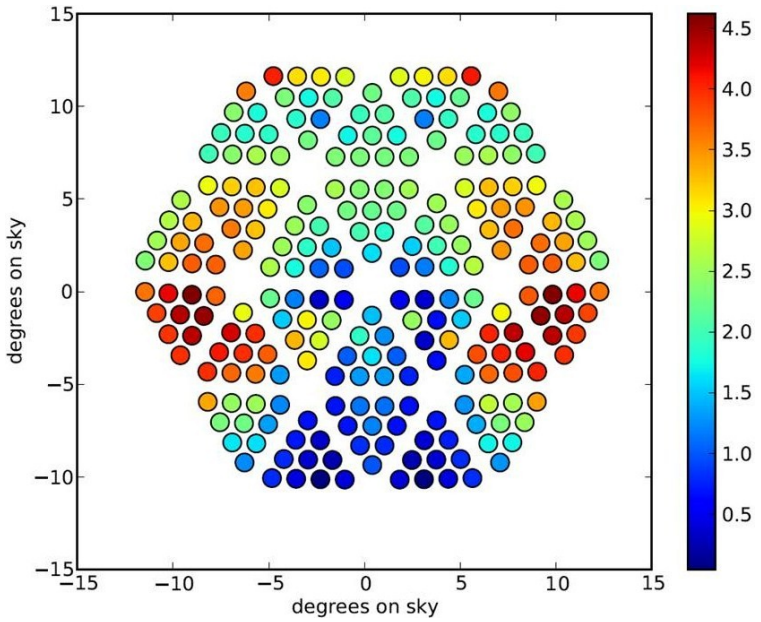

Figure A.4: Beam ellipticity as a percentage of beam width for one of the probes on each feedhorn at 145 GHz.

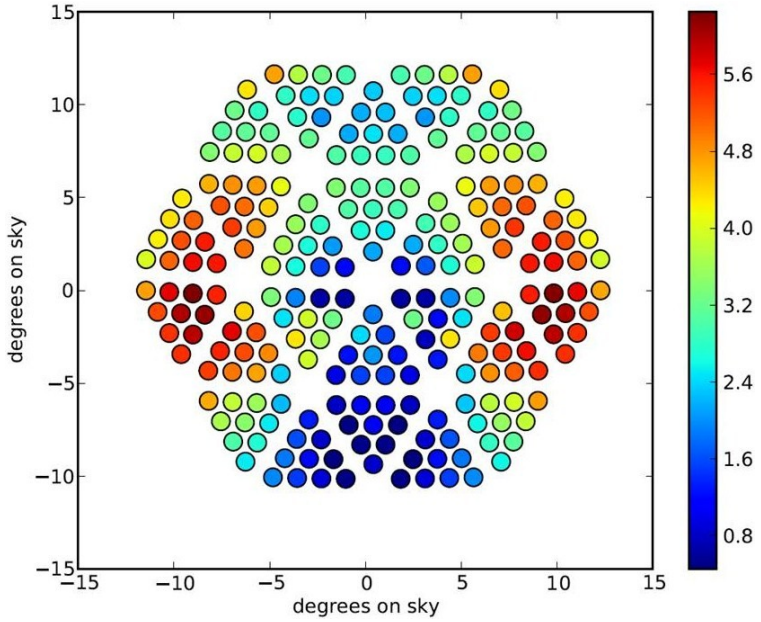

Figure A.5: Beam ellipticity as a percentage of beam width for one of the probes on each feedhorn at 163 GHz.

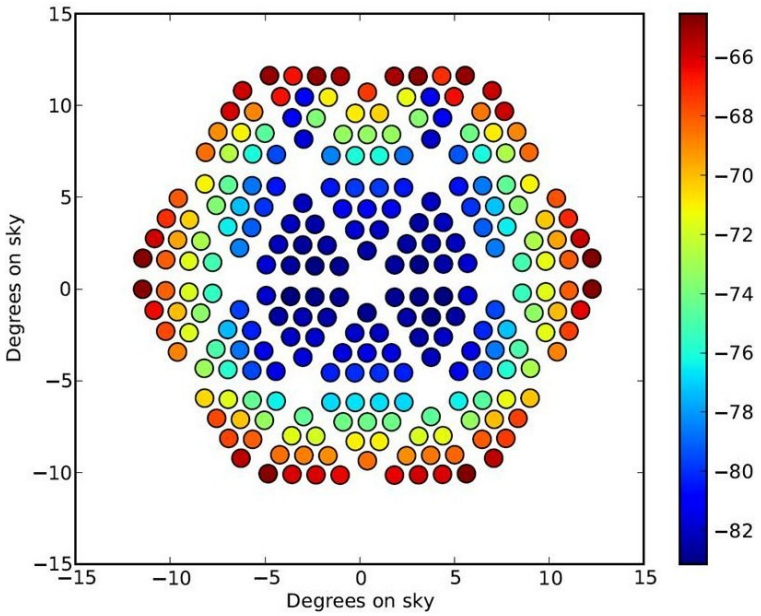

Figure A.6: Crosspolar response at 127 GHz in dB down from copolar response, integrated over the beam, for each feedhorn in ABS, shown versus the position of the feedhorn beam on the sky.

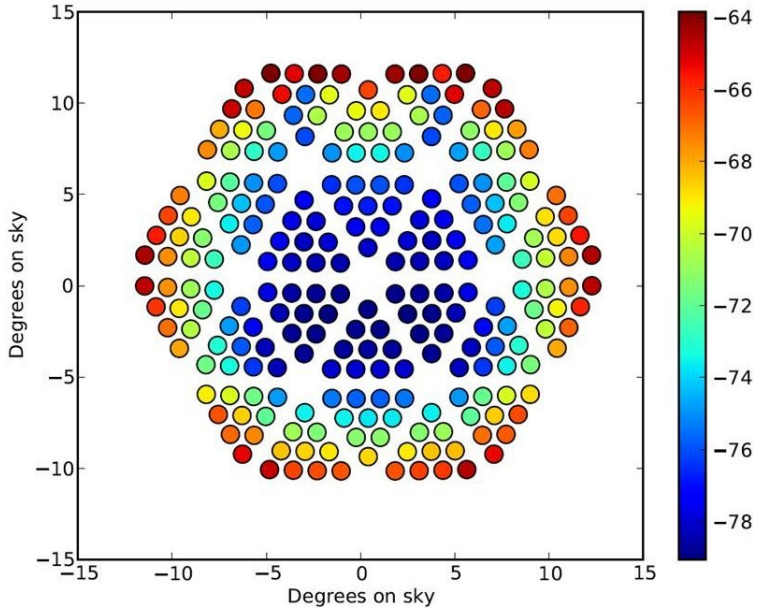

Figure A.7: Crosspolar response at 145 GHz in dB down from copolar response, integrated over the beam, for each feedhorn in ABS, shown versus the position of the feedhorn beam on the sky.

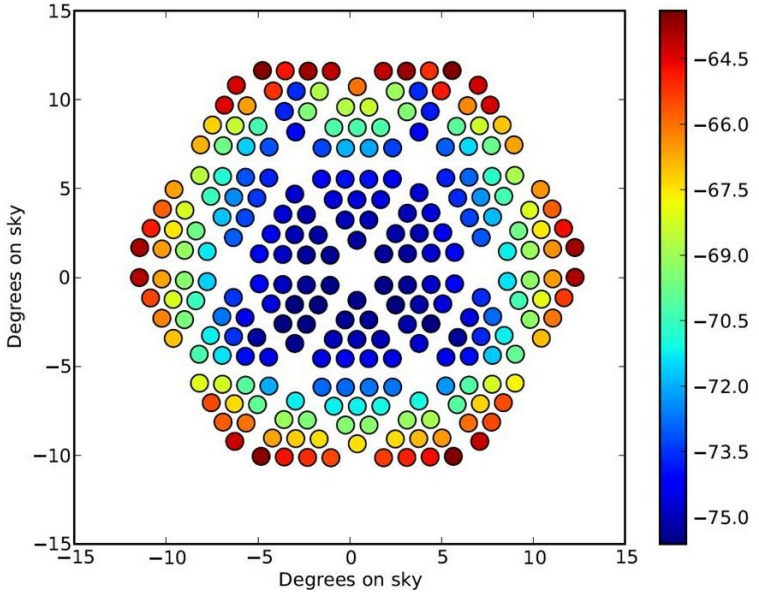

Figure A.8: Crosspolar response at 163 GHz in dB down from copolar response, integrated over the beam, for each feedhorn in ABS, shown versus the position of the feedhorn beam on the sky.

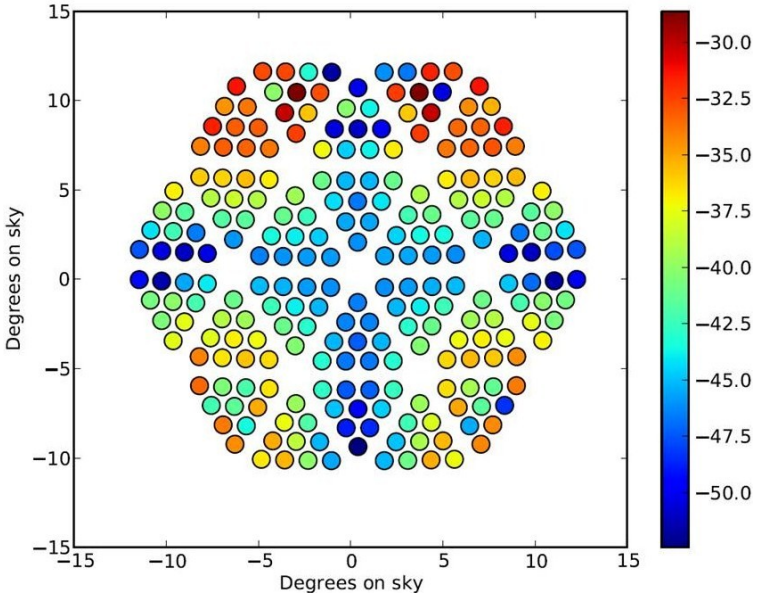

Figure A.9: Differential beam response at 127 GHz integrated over the sky in dB down from the copolar response integrated over the sky. This is the copolar beam of probe A minus the copolar beam of probe B evaluated point by point.

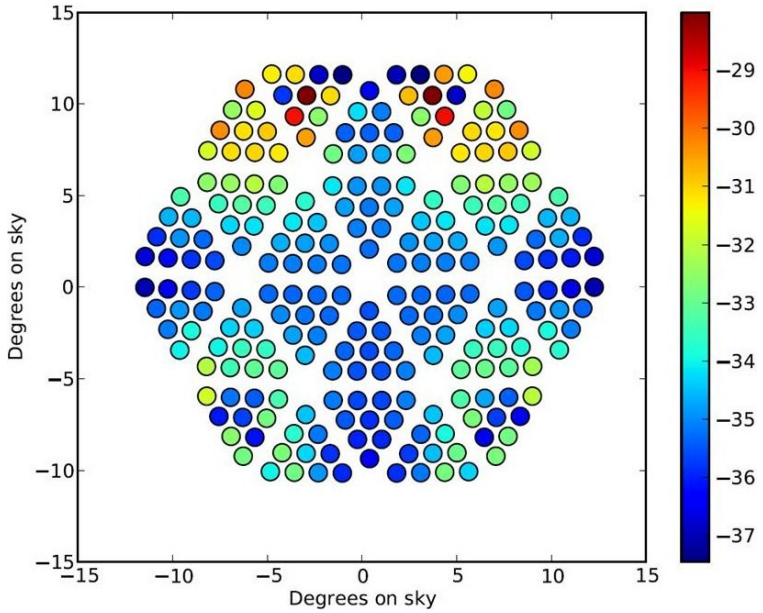

Figure A.10: Differential beam response at 145 GHz integrated over the sky in dB down from the copolar response integrated over the sky. This is the copolar beam of probe A minus the copolar beam of probe B evaluated point by point.

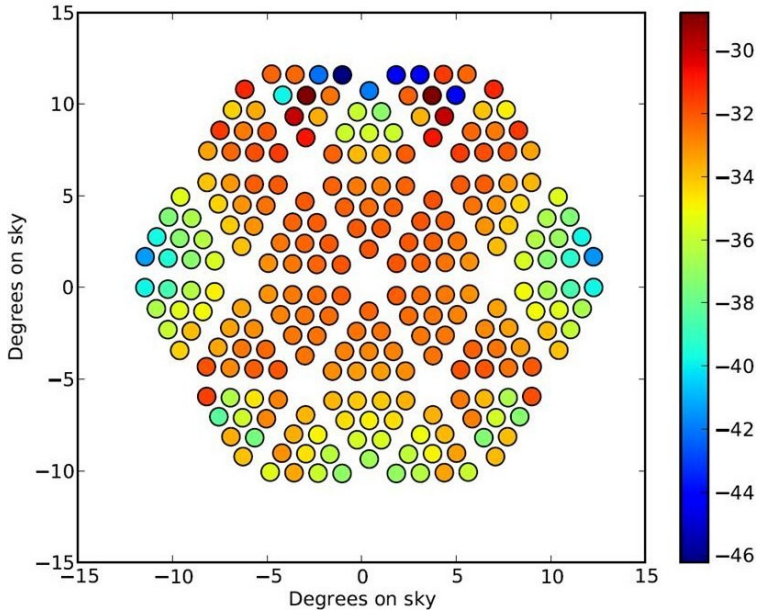

Figure A.11: Differential beam response at 163 GHz integrated over the sky in dB down from the copolar response integrated over the sky. This is the copolar beam of probe A minus the copolar beam of probe B evaluated point by point.

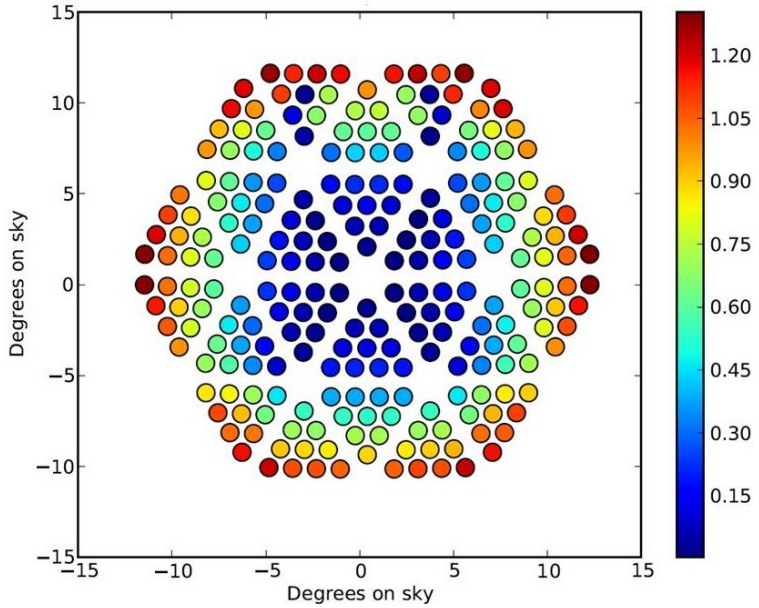

Figure A.12: Difference (in degrees) from 90° of the polarization angle of the two probes from a given feedhorn at 127 GHz.

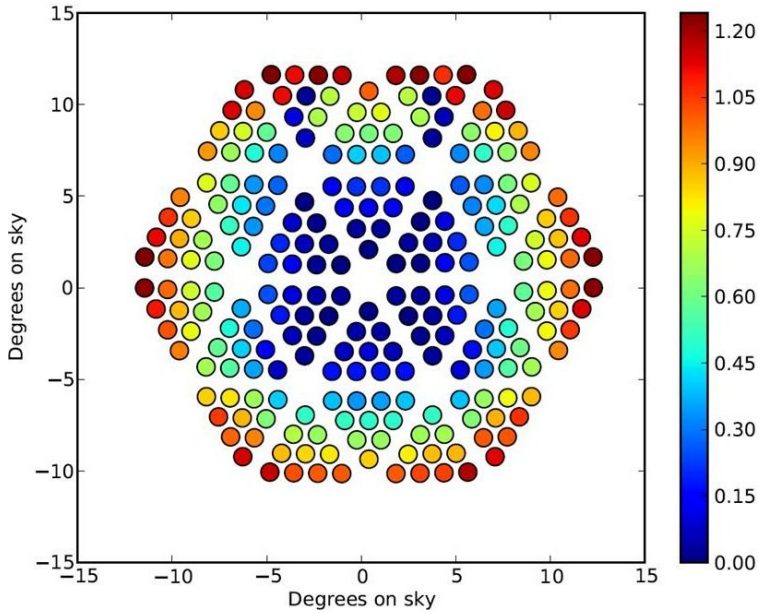

Figure A.13: Difference (in degrees) from 90° of the polarization angle of the two probes from a given feedhorn at 145 GHz.

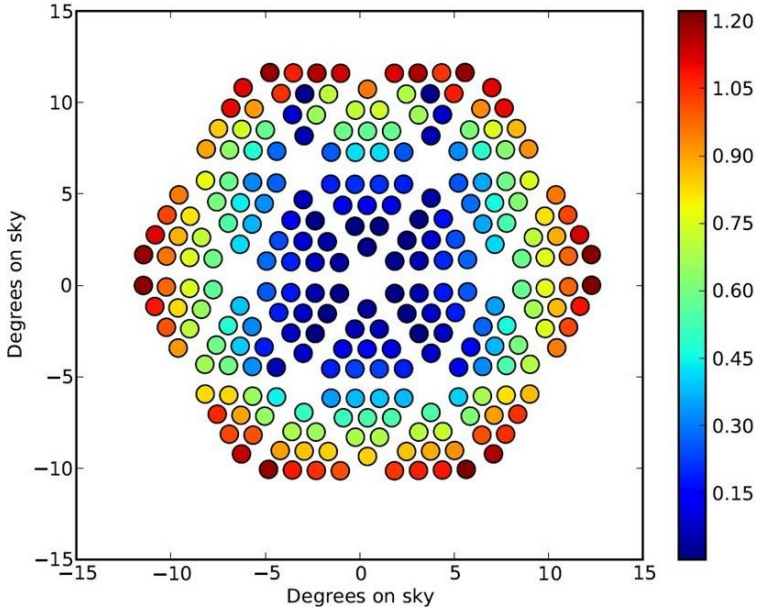

Figure A.14: Difference (in degrees) from 90° of the polarization angle of the two probes from a given feedhorn at 163 GHz.

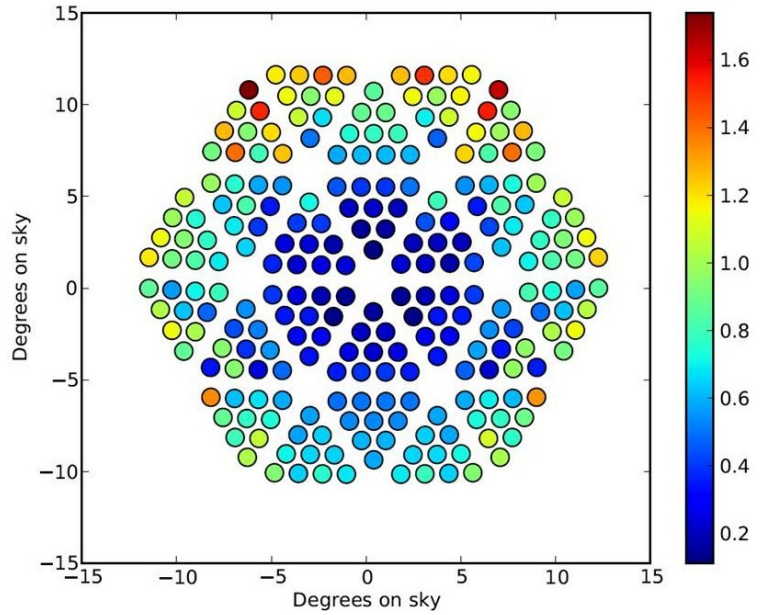

Figure A.15: Beam squint, the distance between beam centers for the two probes from a given feedhorn, in arcseconds at 127 GHz for each feedhorn in the focal plane plotted at the beam position of the feedhorn on the sky.

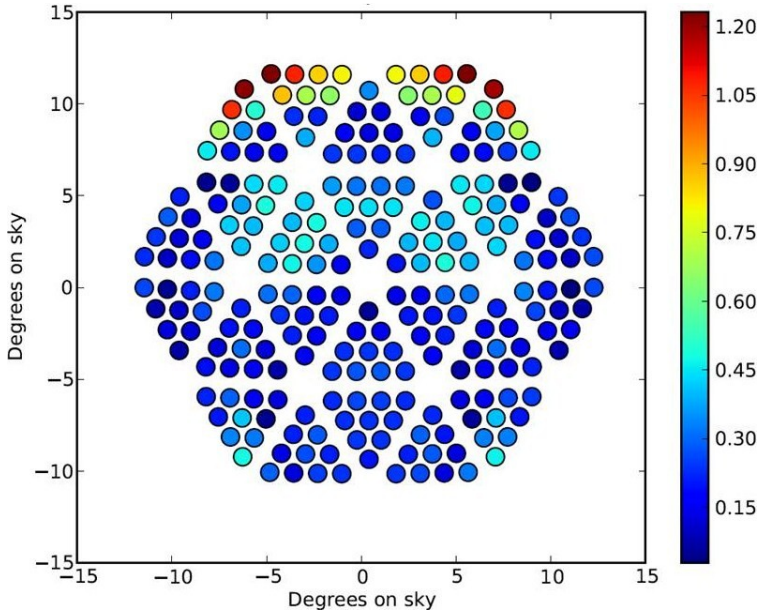

Figure A.16: Beam squint, the distance between beam centers for the two probes from a given feedhorn, in arcseconds at 145 GHz for each feedhorn in the focal plane plotted at the beam position of the feedhorn on the sky.

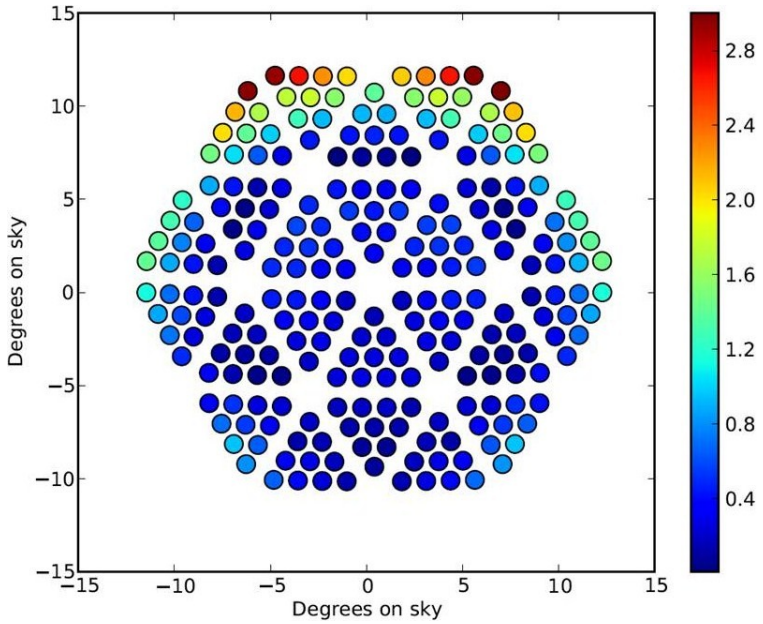

Figure A.17: Beam squint, the distance between beam centers for the two probes from a given feedhorn, in arcseconds at 163 GHz for each feedhorn in the focal plane plotted at the beam position of the feedhorn on the sky.

Appendix B

Compiled Mechanical Drawings for ABS

This appendix compiles a number of mechanical drawings of parts of the ABS instrument, particularly those parts in the optical chain. This includes drawings of the inner baffle and HWP enclosure, the vacuum window, the reflectors, and the focal plane.

B.1 HWP Enclosure and Baffle Assembly

Drawings of the HWP enclosure and inner baffle are shown in Figures B.2, B.3, B.4, B.5, B.6, B.7, B.8, and B.9.

B.2 Window Assembly

The vacuum window assembly consists of a top ring, shown in Figure B.13, and a bottom ring, shown in Figures B.11 and B.12, that clamp the 3.2-mm thick ultra-high molecular weight polyethylene window. This assembly interfaces with a bolt circle and O-ring in the top of the cryostat. The details of the cryostat top plate are shown in Figure B.10.

B.3 Reflector Assembly

Figures B.14, B.15, B.16, B.17, and B.18 show the mechanical specifications of the ABS primary reflector. Figures B.19, B.20, B.21, B.22, B.23, and B.24 show the mechanical specifications of the ABS secondary reflector. The CNC machine code to mill the reflector paraboloid and secondary hyperboloid is reprinted in Section B.3.1.

Figures B.25, B.26, B.27, and B.28 detail the angled support under the reflector assembly, which connects the reflectors to the 4 K baseplate of the cryostat. The angled bracket that the 4 K hex of the focal plane bolts to is shown in Figures B.29 and B.30. The cross brace that maintains the primary and secondary reflectors at a fixed angle is detailed in Figures B.31 and B.32.

B.3.1 CNC G code for milling of reflector surfaces

A specialized computing language, known as G code, is used by many CNC mills and lathes. This section shows the code used to machine the primary and secondary reflector surfaces. The horizontal throw of the milling machine was not sufficient to cut the 60-cm diameter of the reflectors in one pass. A jig was made to flip the mirror by 180° while keeping it centered on the same point. There are thus two codes for each of the primary and secondary reflectors.

Primary reflector side one

;The only difference between the two codes is that the

;formula for the paraboloid, when the mirror is flipped,

;sends x → -x in the formula for Z1.

G0G90X0Y0T6M6

S2000M3; Spindle speed.

J1=0.01; Distance between mill passes.

R1=11.75; Radius of mirror with an extra quarter inch.

A1=469.031; Constants in paraboloid's equation.

A2=2.27092

A3=6.15709

A4=5802.99

A5=0.162414

A6=56.1929

F1=0.99569; Factor by which the aluminum will contract from 300K to 4K.

Z7=1.00433; Factor by which the aluminum will expand from 4K to 300K.

Z8=0.911646; Shift in z-direction to place zero at highest mirror point.

G0X0.Y0.Z0.25; Move to home position above mirror.

Y1=(-1)*2*J1; Set y to -2J.

L2; Increment y up and calculate x on circle given y.

Y1=Y1+J1

X2=(-1.0)*SQR(R1*R1-Y1*Y1)

X1=J1

L3; Increment x down just below calculated value x2.

X1=X1-J1

?X1<GT>X2

=L3!

X2=X2*(-1)

G0Y1X1Z0.25; Move to correct x and y position.

L4; Increment x up and check if x has reached its maximum for this pass.

X1=X1+J1

?X1<GT>X2; If x has reached maximum, go back, increment y, and begin next pass.

=L2!

;Calculate z for the paraboloid given x and y. This is corrected for thermal contraction

;from 300K to 4K as well as the size of the ball mill.

Z1=(A1+A2*X1*F1-A3*SQR(A4-A5*Y1*Y1*F1*F1+A6*X1*F1)-Z8)*Z7

G1Y1X1Z1F10.0; Feed mill to new position.

?Y1<LT>R1; If y is inside circle, continue machining.

=L4!; Otherwise end program.

G0X0.Y0.Z0.25; Back to home position at end of program.

Primary reflector side two

;The only difference between the two codes is that the

;formula for the paraboloid, when the mirror is flipped,

;sends x → -x in the formula for Z1.

G0G90X0Y0T6M6

S2000M3; Set spindle speed.

J1=0.01; Distance between mill passes.

```
R1=11.75; Radius of mirror with an extra quarter inch.
A1=469.031; Constants in paraboloid's equation.
A2=2.27092
A3=6.15709
A4=5802.99
A5=0.162414
A6=56.1929
F1=0.99569; Factor by which the aluminum will contract from 300K to 4K.
Z7=1.00433; Factor by which the aluminum will expand from 4K to 300K.
Z8=0.911646; Shift in z-direction to place zero at highest mirror point.
G0X0.Y0.Z0.25; Move to home position above mirror.
Y1=(-1)*2*J1; Set y to -2J.
L2; Increment y up and calculate x on circle given y.
Y1=Y1+J1
X2=(-1.0)*SQR(R1*R1-Y1*Y1)
X1=J1
L3; Increment x down just below calculated value x2.
X1=X1-J1
?X1<GT>X2
=L3!
X2=X2*(-1)
G0Y1X1Z0.25; Move to correct x and y position.
L4; Increment x up and check if x has reached its maximum for this pass.
X1=X1+J1
?X1<GT>X2; If x has reached maximum, go back, increment y, and begin next pass.
=L2!
;Calculate z for the paraboloid given x and y. This is corrected for thermal contraction
;from 300K to 4K as well as the size of the ball mill.
```

Z1=(A1-A2*X1*F1-A3*SQR(A4-A5*Y1*Y1*F1*F1-A6*X1*F1)-Z8)*Z7

G1Y1X1Z1F10.0; Feed mill to new position.

?Y1<LT>R1; If y is inside circle, continue machining. =L4!; Otherwise end program.

G0X0.Y0.Z0.25; Back to home position at end of program.

Secondary Reflector Side One

;The only difference between the two codes is that the

;formula for the hyperboloid, when the mirror is flipped,

;sends x → -x in the formula for Z1.

G0G90X0Y0T6M6

S2000M3; Spindle speed.

J1=0.01; Distance between mill passes.

R1=11.5; Radius of mirror with an extra quarter inch.

A1=7.84437; Constants in hyperboloid's equation.

A2=0.182233

A3=0.222359

A4=1244.54

A5=2.59735

A6=57.8236

A7=2.67379

F1=0.99569; Factor by which the aluminum will shrink from 300K to 4K.

Z7=1.00433; Factor by which the aluminum will expand from 4K to 300K.

Z8=1.09231; Shift in z-direction to place zero at highest mirror point.

G0X0.Y0.Z0.25; Move to home position above mirror.

Y1=(-1)*2*J1; Set y to -2J.

L2; Increment y up and calculate x on circle given y.

Y1=Y1+J1

X2=(-1.0)*SQR(R1*R1-Y1*Y1)

X1=J1

L3; Increment x down just below calculated value x2.

X1=X1-J1

?X1<GT>X2

=L3!

X2=X2*(-1)

G0Y1X1Z0.25; Move to correct x and y position.

L4; Increment x up and check if x has reached its maximum for this pass.

X1=X1+J1

?X1<GT>X2; If x has reached maximum, go back, increment y, and begin next pass.

=L2!

;Calculate z for hyperboloid given x and y. This is corrected for thermal contraction from

;300K to 4K and for the size of the end mill.

Z1=(-A1-A2*X1*F1+A3*SQR(A4+A5*Y1*Y1*F1*F1+A6*X1*F1+A7*X1*X1*F1*F1)-Z8)*Z7

G1Y1X1Z1F10.0; Feed mill to new position.

?Y1<LT>R1; If y is inside circle, continue machining.

=L4!; Otherwise end program.

G0X0.Y0.Z0.25; Back to home position at end of program.

Secondary Reflector Side Two

;The only difference between the two codes is that the

;formula for the hyperboloid, when the mirror is flipped,

;sends x → -x in the formula for Z1.

G0G90X0Y0T6M6

S2000M3; Spindle speed.

J1=0.01; Distance between mill passes.

R1=11.5; Radius of mirror with an extra quarter inch.

A1=7.84437; Constants in hyperboloid's equation.

A2=0.182233

A3=0.222359

A4=1244.54

A5=2.59735

A6=57.8236

A7=2.67379

F1=0.99569; Factor by which the aluminum will contract from 4K to 300K.

Z7=1.00433; Factor by which the aluminum will expand from 4K to 300K.

Z8=1.09231; Shift in z-direction to place zero at highest mirror point.

G0X0.Y0.Z0.25; Move to home position above mirror.

Y1=(-1)*2*J1; Set y to -2J.

L2; Increment y up and calculate x on circle given y.

Y1=Y1+J1

X2=(-1.0)*SQR(R1*R1-Y1*Y1)

X1=J1

L3; Increment x down just below calculated value x2.

X1=X1-J1

?X1<GT>X2

=L3!

X2=X2*(-1)

G0Y1X1Z0.25; Move to correct x and y position.

L4; Increment x up and check if x has reached its maximum for this pass.

X1=X1+J1

?X1<GT>X2; If x has reached maximum, go back, increment y, and begin next pass.

=L2!

;Calculate z for hyperboloid given x and y. This is corrected for thermal contraction from

;300K to 4K and for the size of the end mill.

Z1=(-A1+A2*X1*F1+A3*SQR(A4+A5*Y1*Y1*F1*F1-A6*X1*F1+A7*X1*X1*F1*F1)-Z8)*Z7

Pod	x [cm]	y [cm]	θ	ϕ
1	-0.635	3.849	0.817	99.917
2	3.033	2.487	0.865	35.761
3	3.688	-1.372	1.088	-27.559
4	0.673	-3.867	1.316	-81.674
5	-2.995	-2.505	1.176	-133.706
6	-3.649	1.354	0.907	164.888
7	-3.322	9.637	1.598	111.676
8	0.019	7.708	1.344	89.844
9	3.352	9.637	1.599	68.141
10	6.702	7.708	1.728	43.139
11	6.702	3.849	1.582	23.431
12	10.043	1.920	2.255	0.673
13	10.043	-1.938	2.735	-21.650
14	6.702	-3.867	2.360	-38.410
15	6.702	-7.726	3.693	-56.696
16	3.361	-9.655	4.090	-74.713
17	0.019	-7.726	2.946	-89.884
18	-3.322	-9.655	4.086	-105.126
19	-6.664	-7.726	3.686	-123.175
20	-6.664	-3.867	2.351	-141.474
21	-10.005	-1.938	2.726	-158.338
22	-10.005	1.929	2.247	179.200
23	-6.664	3.849	1.575	156.389
24	-6.664	7.708	1.724	136.660

Figure B.1: Center positions (in centimeters) and angles (in degrees) of each of the ABS pods. In a coordinate system where the z-axis runs from the center of the focal plane to the center of the secondary and the y-axis points toward the primary mirror, if one drew a unit vector normal to the surface of the pod interface plate for each pod, this vector would be given by $(\sin\theta\cos\phi, \sin\theta\sin\phi, \cos\theta)$.

G1Y1X1Z1F10.0; Feed mill to new position.

?Y1<LT>R1; If y is inside circle, continue machining.

=L4!; Otherwise end program.

G0X0.Y0.Z0.25; Back to home position at end of program.

B.4 Focal Plane Support

Drawings for the focal plane support (FPS) are shown in Figures B.33, B.34, B.35, B.36, and B.37. The mounting surface for each pod was cut at an angle given in Table B.1.

B.5 Series Array Mount

A set of copper brackets mechanically support and thermally heatsink the series arrays and their readout circuits at 4 K. An overview of the assembly and its relation to the focal plane and reflector assemblies is shown in Figure B.38. An aluminum wedge holds the series array parallel to the focal plane. A drawing of the wedge is shown in Figure B.40. The main copper bracket for the series array is shown in Figure B.39. This interfaces with the aluminum wedge through two bottom brackets, detailed in Figure B.41. Aluminum side brackets, detailed in Figures B.42 and B.43, stabilize the series array main bracket to focal plane angled support.

B.6 Pod Design

The pod assembly was described in section Drawings for the pod interface plates are shown in Figures B.44, B.45, and B.46. Figure B.47 shows a drawing for the niobium sheets in the pods. The specifications of the pod aluminum lids are shown in Figures B.48 and B.49.

B.7 Feedhorn Design

Drawings of the overall dimensions of the feedhorn top are shown in Figure B.50 and of the feedhorn bottom and detector package in Figures B.51, B.52, and B.53. A feedhorn assembly overview is shown in Figure B.54. The dimensions of the feedhorn corrugations are shown in Figures B.55 and B.56.

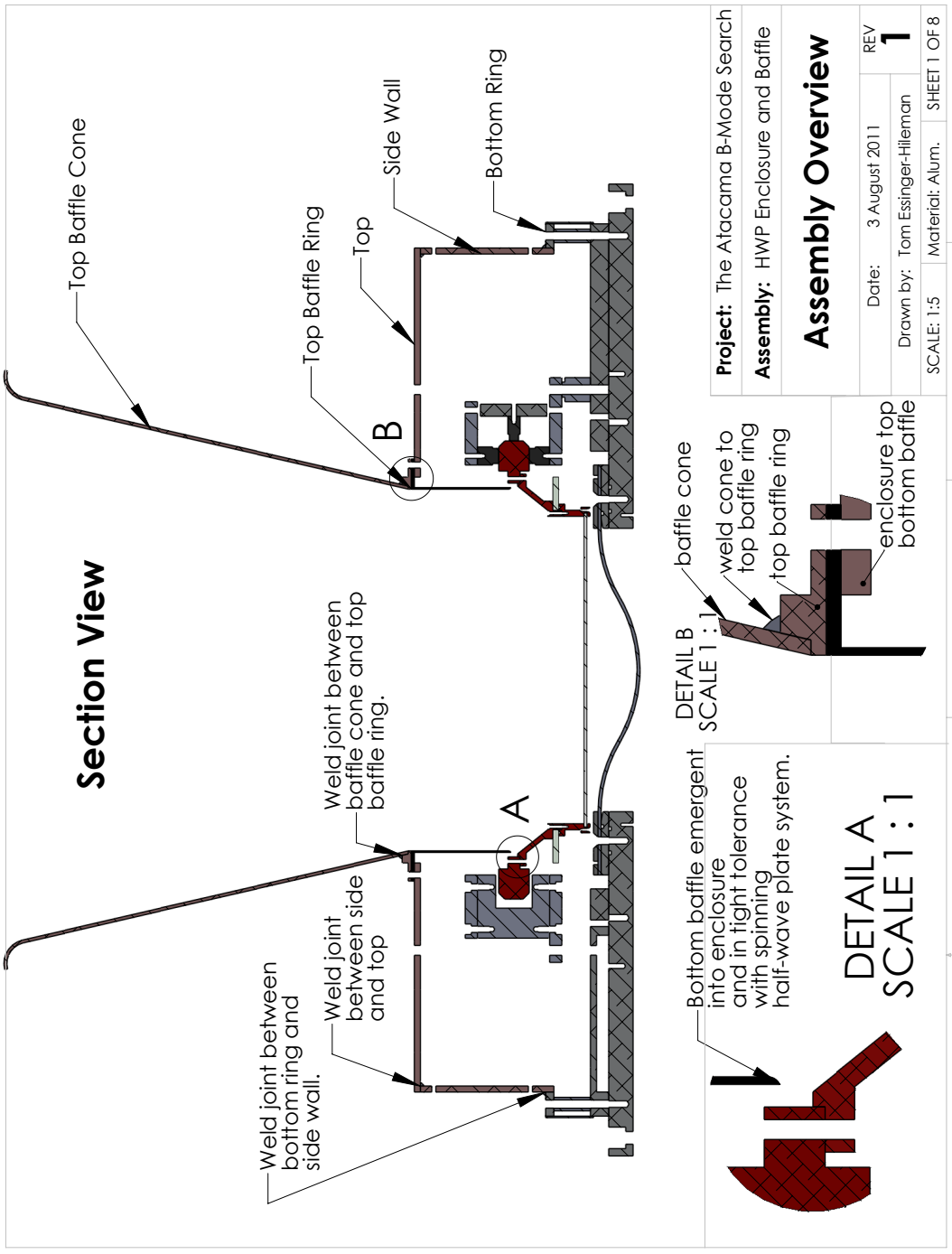
Section View
Top Baffle Cone
Top Baffle Ring
Top
Side Wall
Bottom Ring
B
A
Weld joint between baffle cone and top baffle ring.
Weld joint between side and top
Weld joint between bottom ring and side wall.
DETAIL B
SCALE 1 : 1
baffle cone
weld cone to top baffle ring
top baffle ring
enclosure top bottom baffle
Bottom baffle emergent into enclosure and in tight tolerance with spinning half-wave plate system.
DETAIL A
SCALE 1 : 1
Project: The Atacama B-Mode Search
Assembly: HWP Enclosure and Baffle
Assembly Overview
Date: 3 August 2011
REV 1
Drawn by: Tom Essinger-Hileman
SCALE: 1:5
Material: Alum.
SHEET 1 OF 8

Figure B.2:

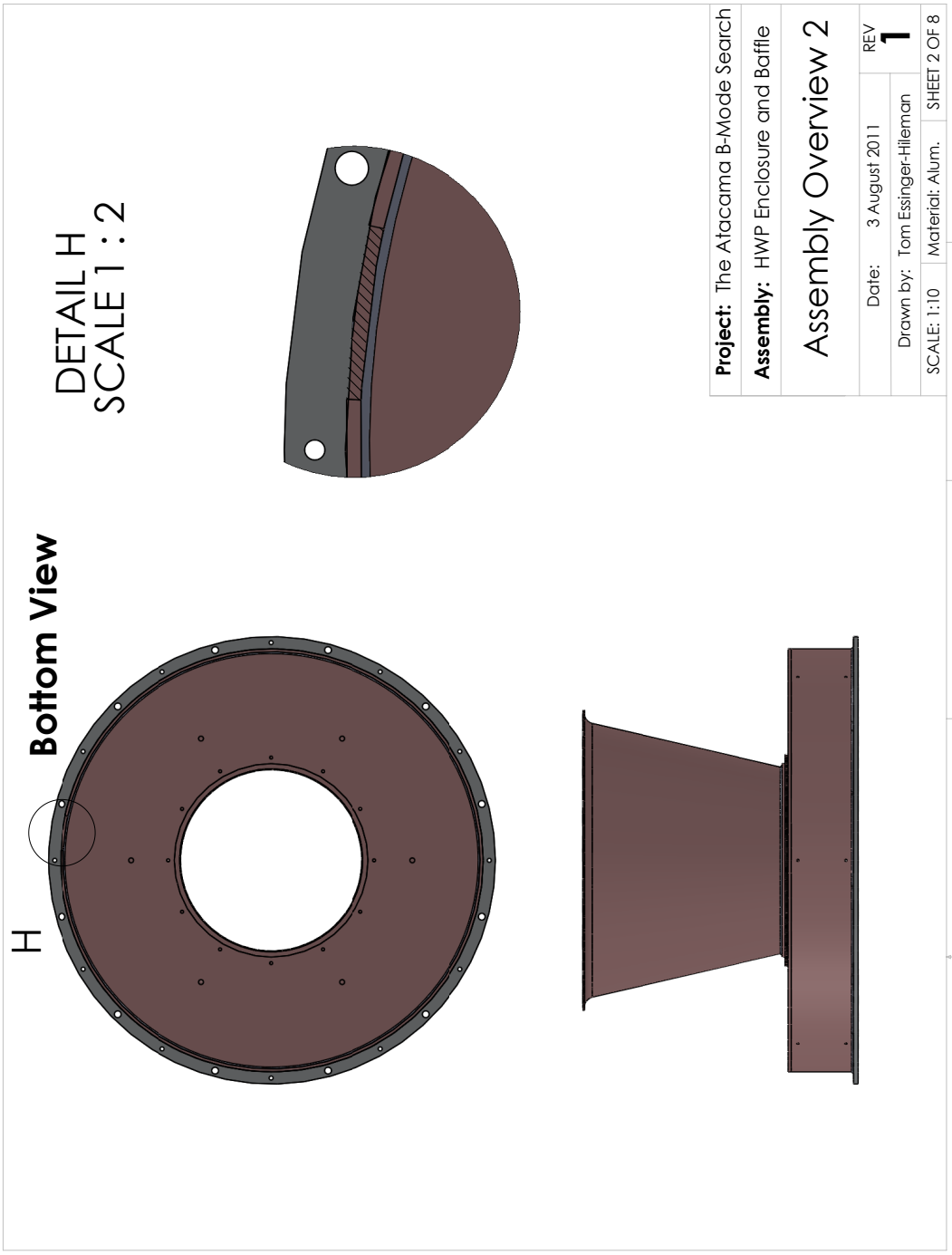
H
Bottom View
DETAIL H
SCALE 1 : 2
Project: The Atacama B-Mode Search
Assembly: HWP Enclosure and Baffle
Assembly Overview 2
Date: 3 August 2011
REV 1
Drawn by: Tom Essinger-Hileman
SCALE: 1:10
Material: Alum.
SHEET 2 OF 8

Figure B.3:

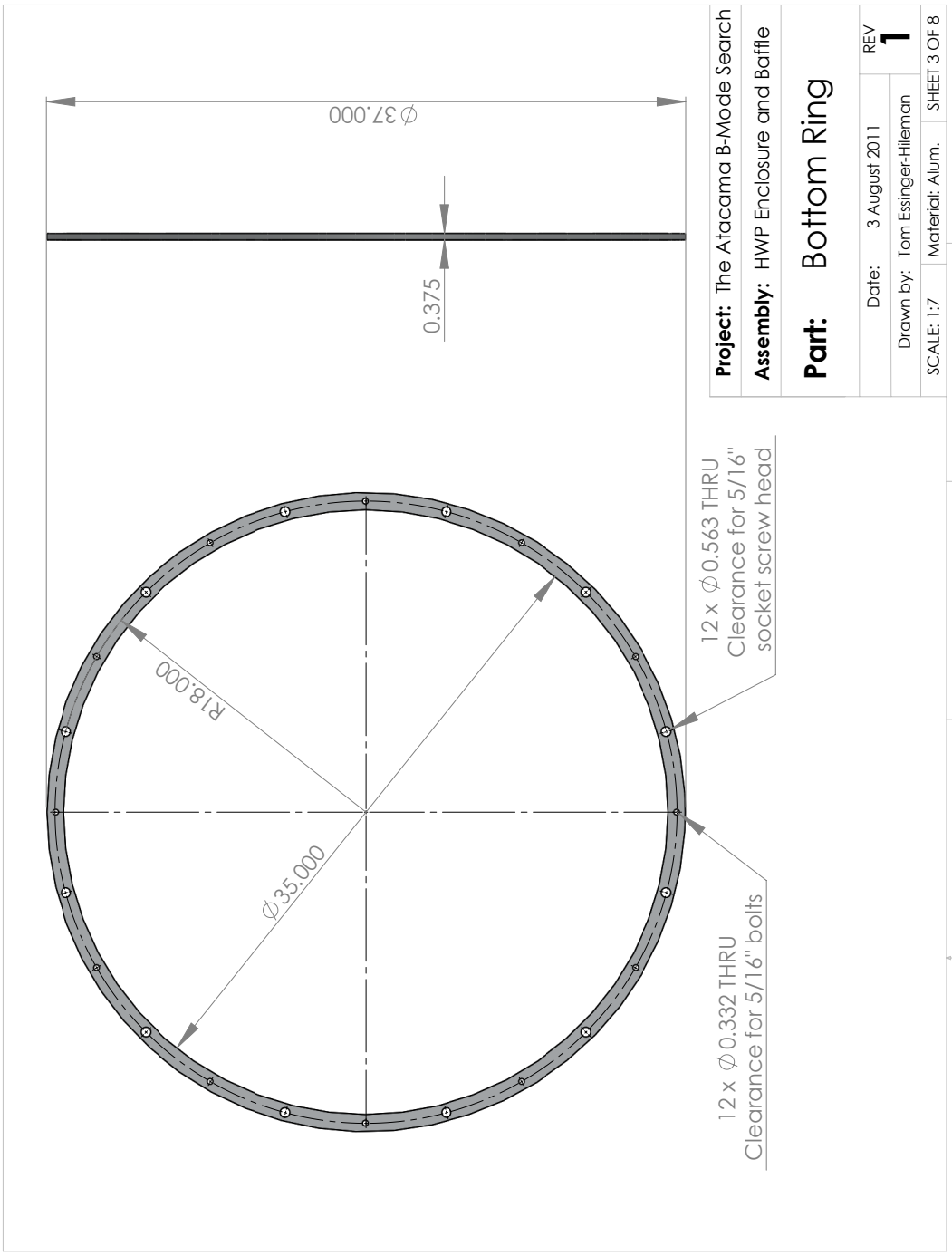
Project: The Atacama B-Mode Search
Assembly: HWP Enclosure and Baffle
Part: Bottom Ring
Date: 3 August 2011
REV 1
Drawn by: Tom Essinger-Hileman
SCALE: 1:7
Material: Alum.
SHEET 3 OF 8
∅37.000
0.375
R18.000
∅35.000
12 x ∅0.563 THRU
Clearance for 5/16"
socket screw head
12 x ∅0.332 THRU
Clearance for 5/16" bolts

Figure B.4:

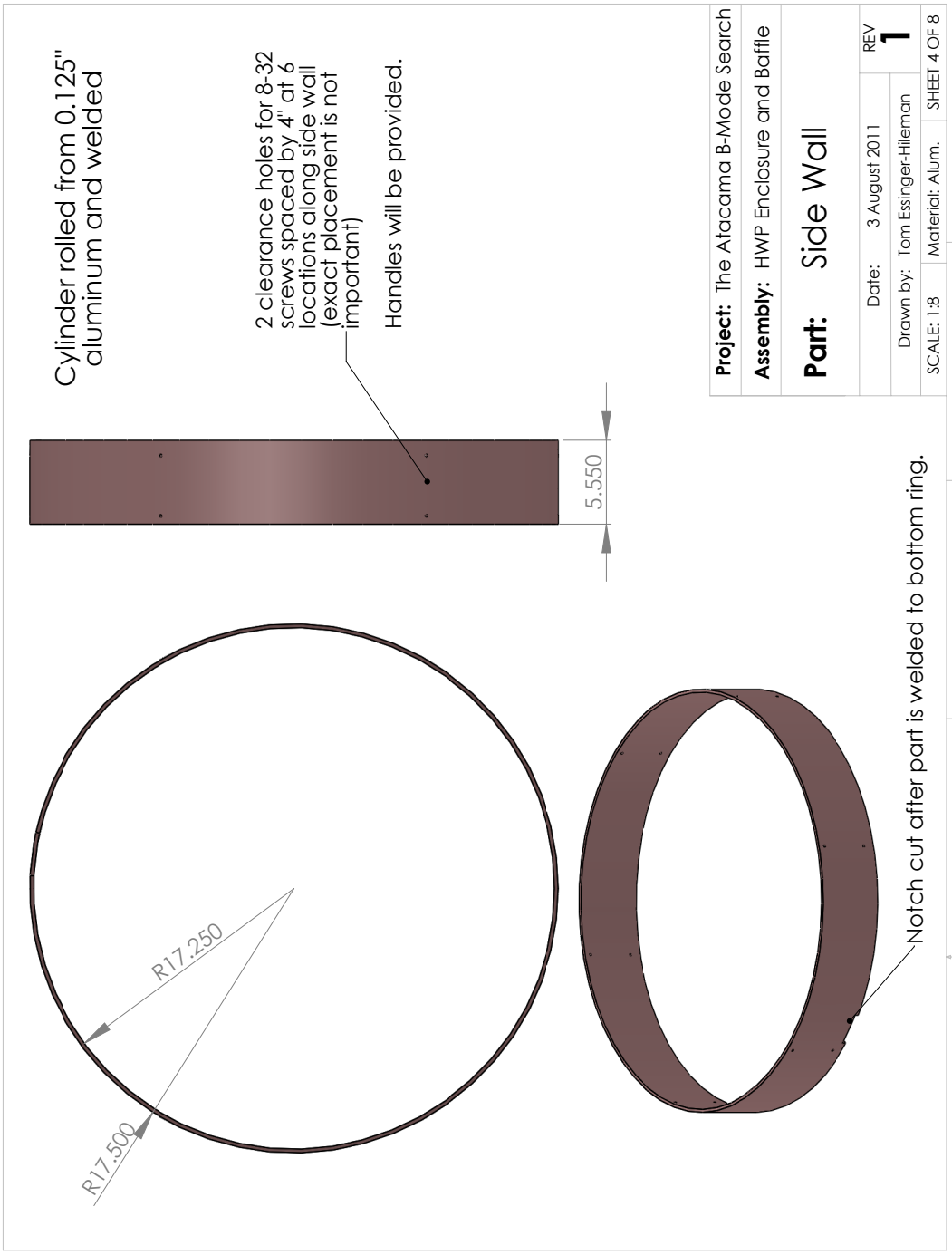
Cylinder rolled from 0.125" aluminum and welded
2 clearance holes for 8-32 screws spaced by 4" at 6 locations along side wall (exact placement is not important)
Handles will be provided.
5.550
R17.250
R17.500
Notch cut after part is welded to bottom ring.
Project: The Atacama B-Mode Search
Assembly: HWP Enclosure and Baffle
Part: Side Wall
Date: 3 August 2011
REV 1
Drawn by: Tom Essinger-Hileman
SCALE: 1:8
Material: Alum.
SHEET 4 OF 8

Figure B.5:

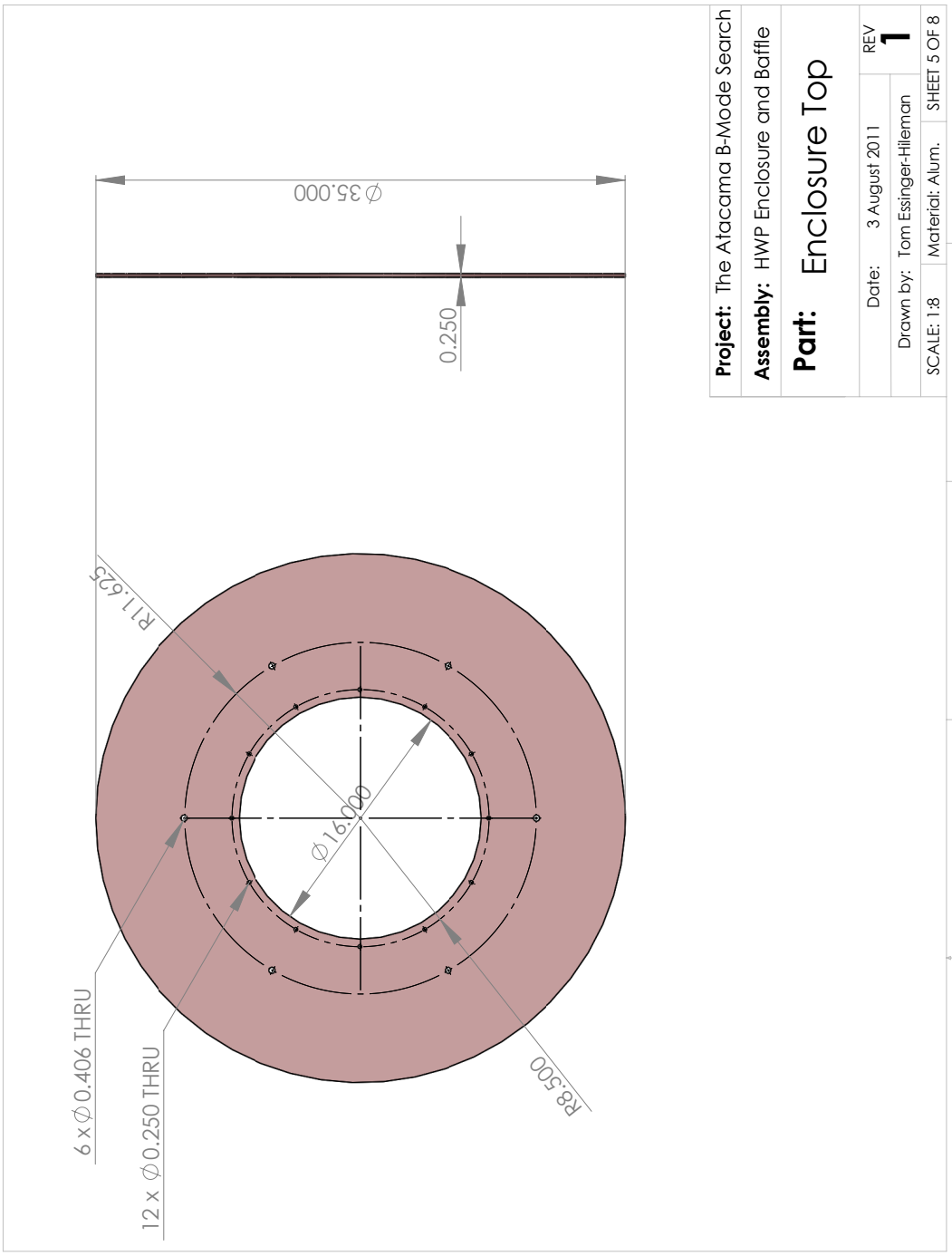
Project: The Atacama B-Mode Search
Assembly: HWP Enclosure and Baffle
Part: Enclosure Top
Date: 3 August 2011
REV 1
Drawn by: Tom Essinger-Hileman
SCALE: 1:8
Material: Alum.
SHEET 5 OF 8
∅35.000
0.250
R11.625
∅16.000
R8.500
6 x ∅0.406 THRU
12 x ∅0.250 THRU

Figure B.6:

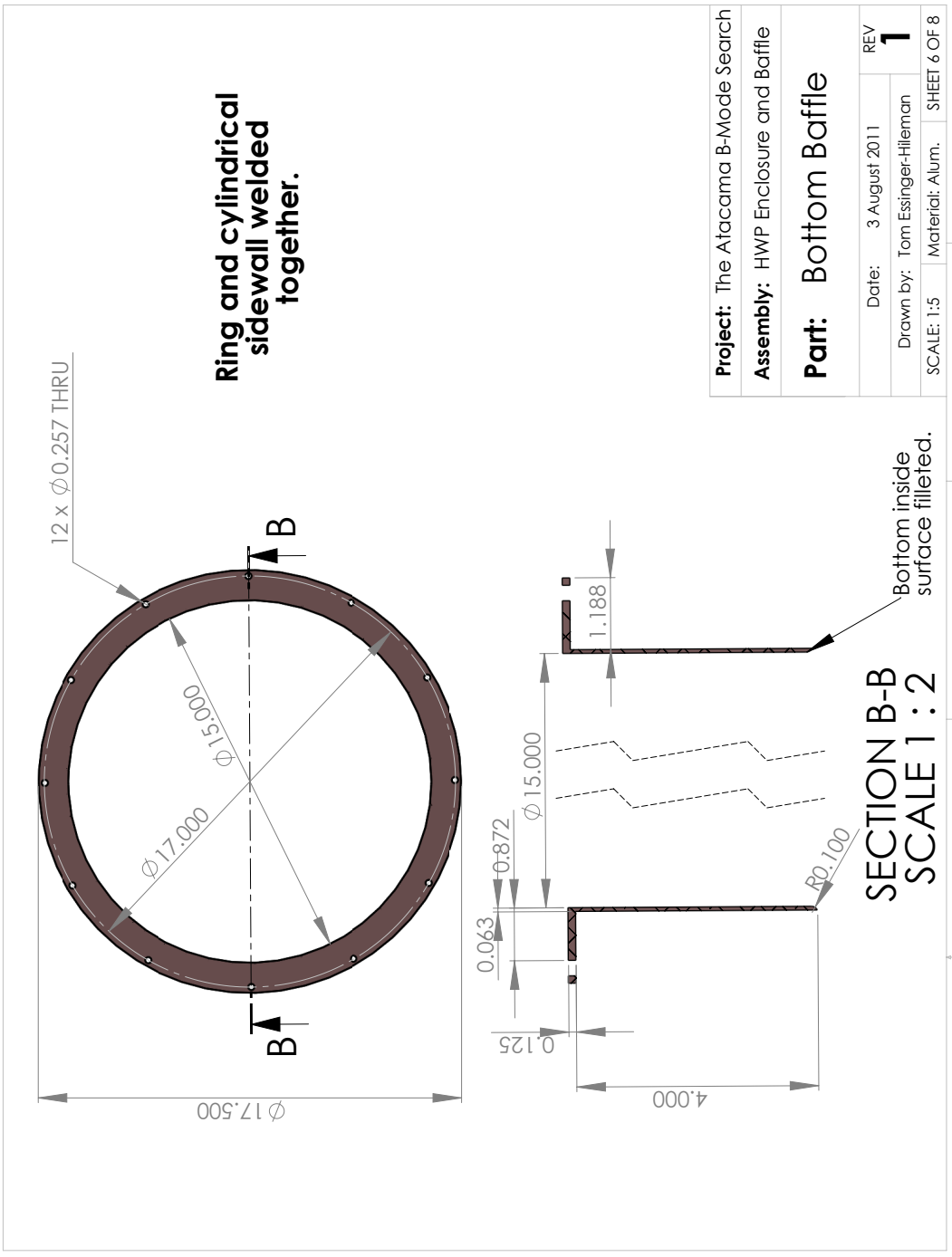
Ring and cylindrical sidewall welded together.
12 x ⌀0.257 THRU
⌀15.000
⌀17.000
⌀17.500
B
B
SECTION B-B
SCALE 1 : 2
1.188
⌀15.000
0.872
0.063
0.125
4.000
R0.100
Bottom inside surface filleted.
Project: The Atacama B-Mode Search
Assembly: HWP Enclosure and Baffle
Part: Bottom Baffle
Date: 3 August 2011
Drawn by: Tom Essinger-Hileman
REV 1
SCALE: 1:5
Material: Alum.
SHEET 6 OF 8

Figure B.7:

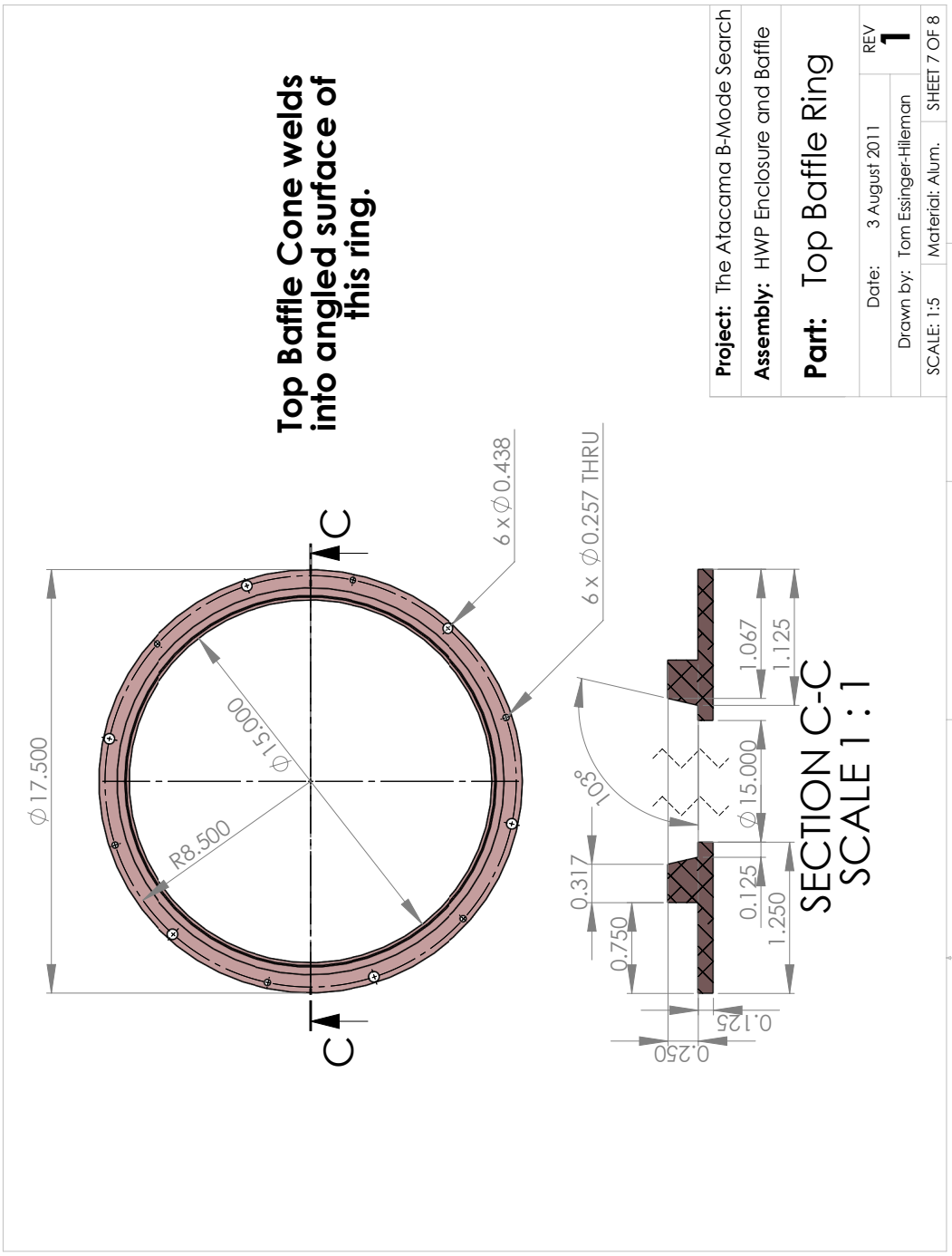
Top Baffle Cone welds into angled surface of this ring.
Project: The Atacama B-Mode Search
Assembly: HWP Enclosure and Baffle
Part: Top Baffle Ring
Date: 3 August 2011
REV 1
Drawn by: Tom Essinger-Hileman
SCALE: 1:5
Material: Alum.
SHEET 7 OF 8
⌀17.500
⌀15.000
R8.500
6 x ⌀0.438
6 x ⌀0.257 THRU
C
C
SECTION C-C
SCALE 1 : 1
10°
0.317
0.750
0.125
1.250
⌀15.000
1.067
1.125
0.125
0.250

Figure B.8:

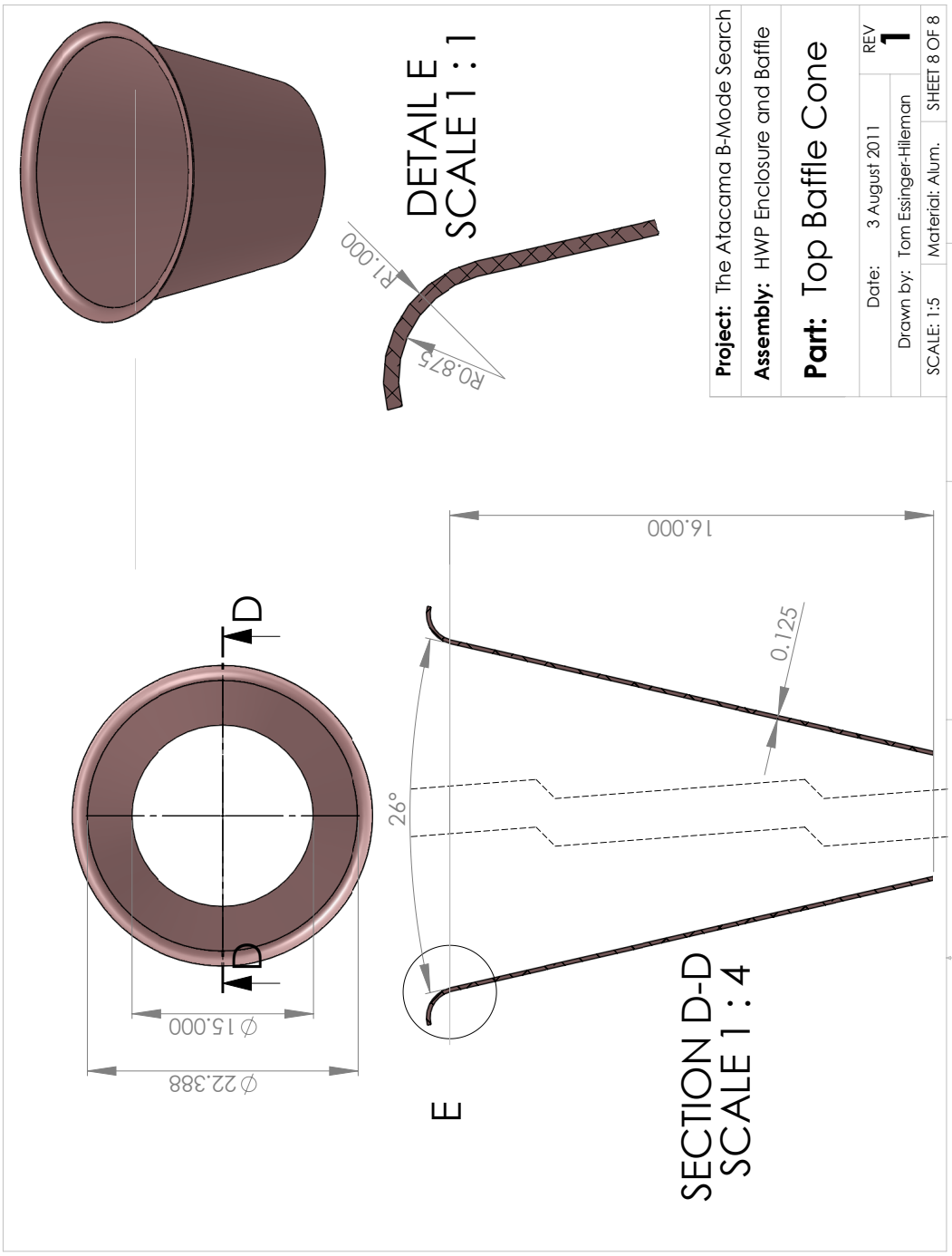
DETAIL E
SCALE 1 : 1
R1.000
R0.875
Project: The Atacama B-Mode Search
Assembly: HWP Enclosure and Baffle
Part: Top Baffle Cone
Date: 3 August 2011
REV 1
Drawn by: Tom Essinger-Hileman
SCALE: 1:5
Material: Alum.
SHEET 8 OF 8
D
D
∅15.000
∅22.388
E
16.000
0.125
26°
SECTION D-D
SCALE 1 : 4

Figure B.9:

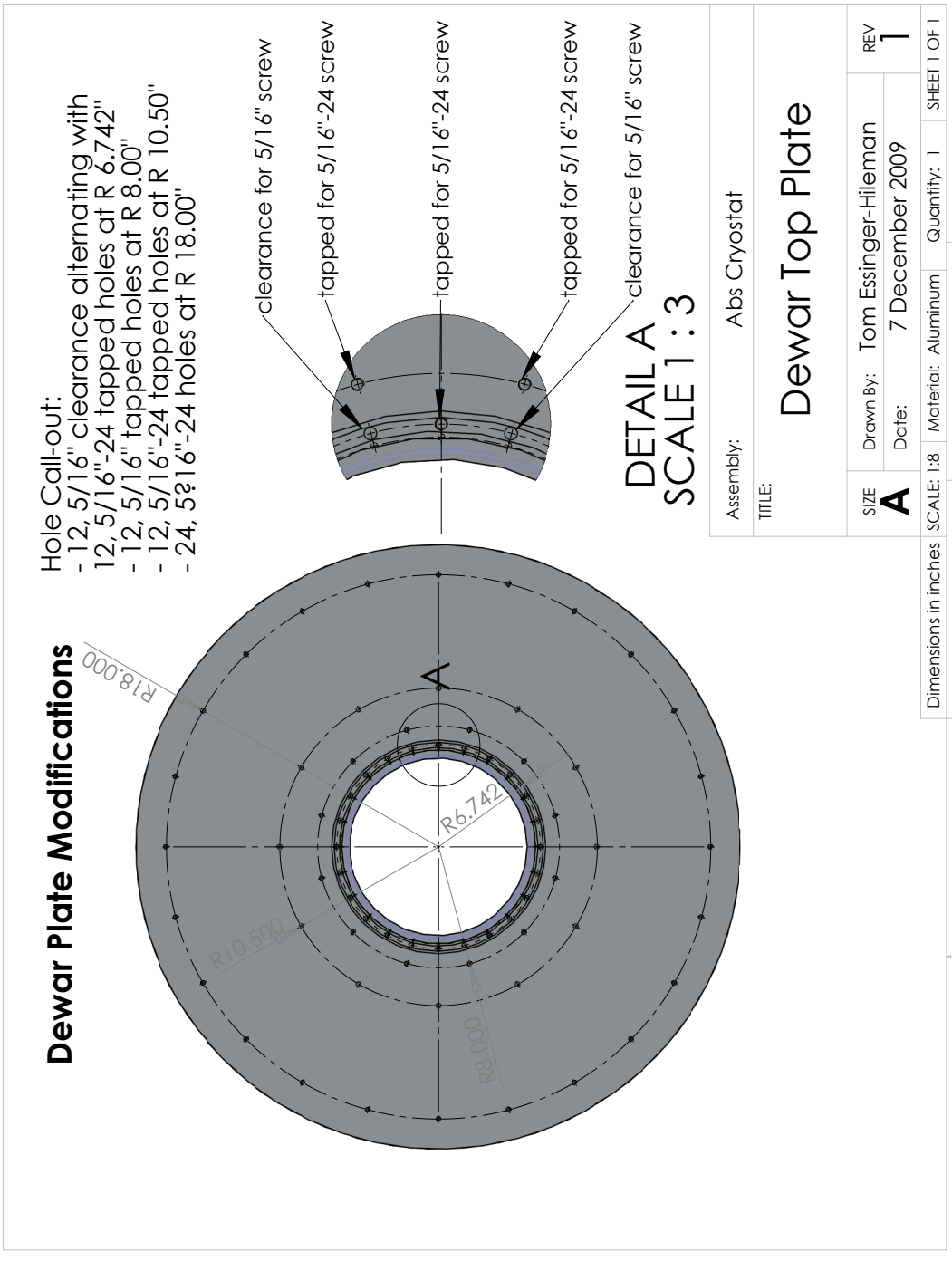
Dewar Plate Modifications
Hole Call-out:
- 12, 5/16" clearance alternating with 12, 5/16"-24 tapped holes at R 6.742"
- 12, 5/16" tapped holes at R 8.00"
- 12, 5/16"-24 tapped holes at R 10.50"
- 24, 5?16"-24 holes at R 18.00"
R18.000
R10.500
R8.000
R6.742
A
clearance for 5/16" screw
tapped for 5/16"-24 screw
tapped for 5/16"-24 screw
tapped for 5/16"-24 screw
clearance for 5/16" screw
DETAIL A
SCALE 1 : 3
Assembly: Abs Cryostat
TITLE: Dewar Top Plate
SIZE A
Drawn By: Tom Essinger-Hileman
Date: 7 December 2009
REV 1
Dimensions in inches
SCALE: 1:8
Material: Aluminum
Quantity: 1
SHEET 1 OF 1

Figure B.10:

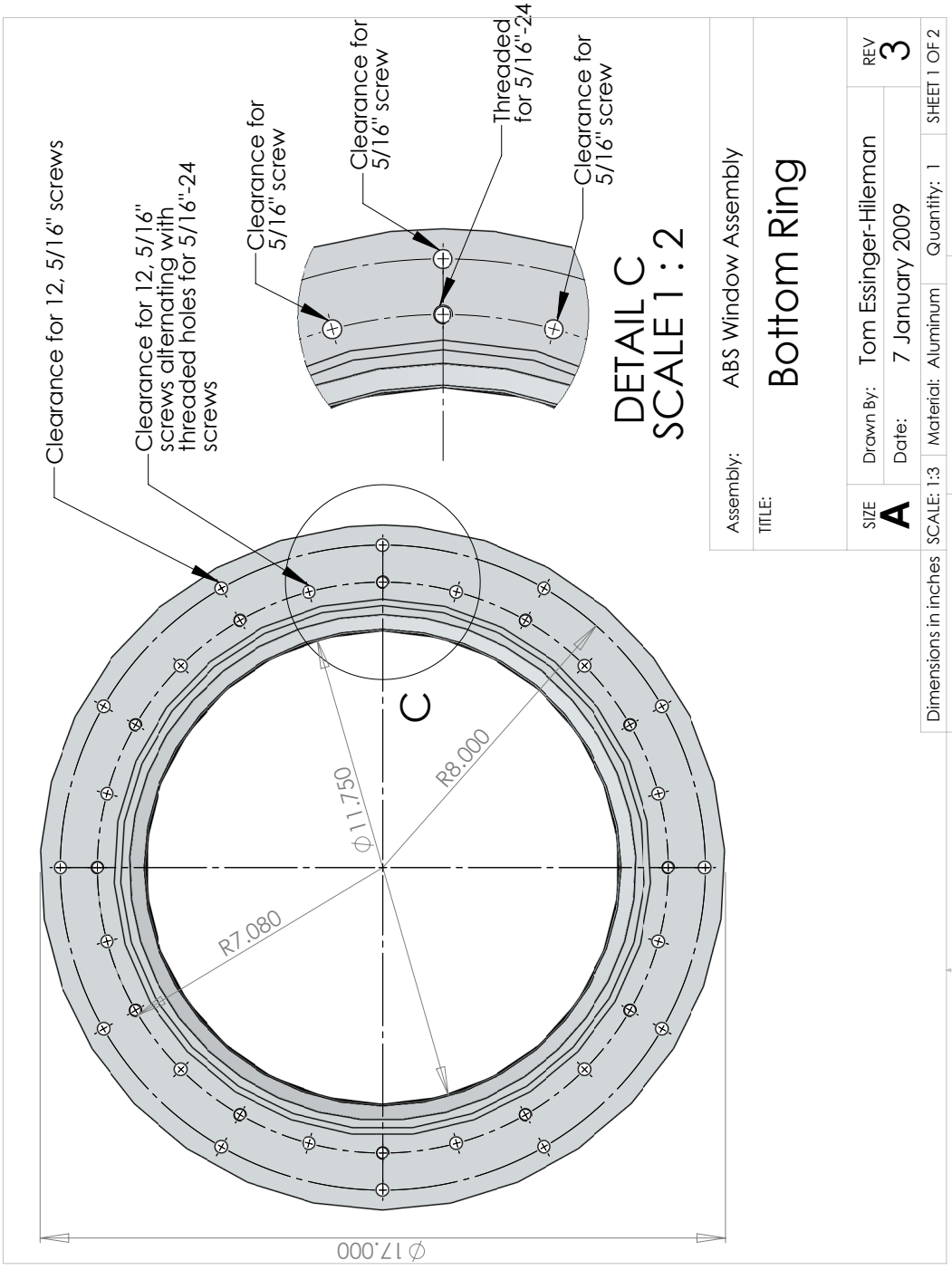
Clearance for 12, 5/16" screws
Clearance for 12, 5/16" screws alternating with threaded holes for 5/16"-24 screws
Clearance for 5/16" screw
Clearance for 5/16" screw
Threaded for 5/16"-24
Clearance for 5/16" screw
DETAIL C
SCALE 1 : 2
C
R8.000
⌀11.750
R7.080
⌀17.000
Assembly: ABS Window Assembly
TITLE: Bottom Ring
SIZE A
Drawn By: Tom Essinger-Hileman
Date: 7 January 2009
REV 3
Dimensions in inches
SCALE: 1:3
Material: Aluminum
Quantity: 1
SHEET 1 OF 2

Figure B.11:

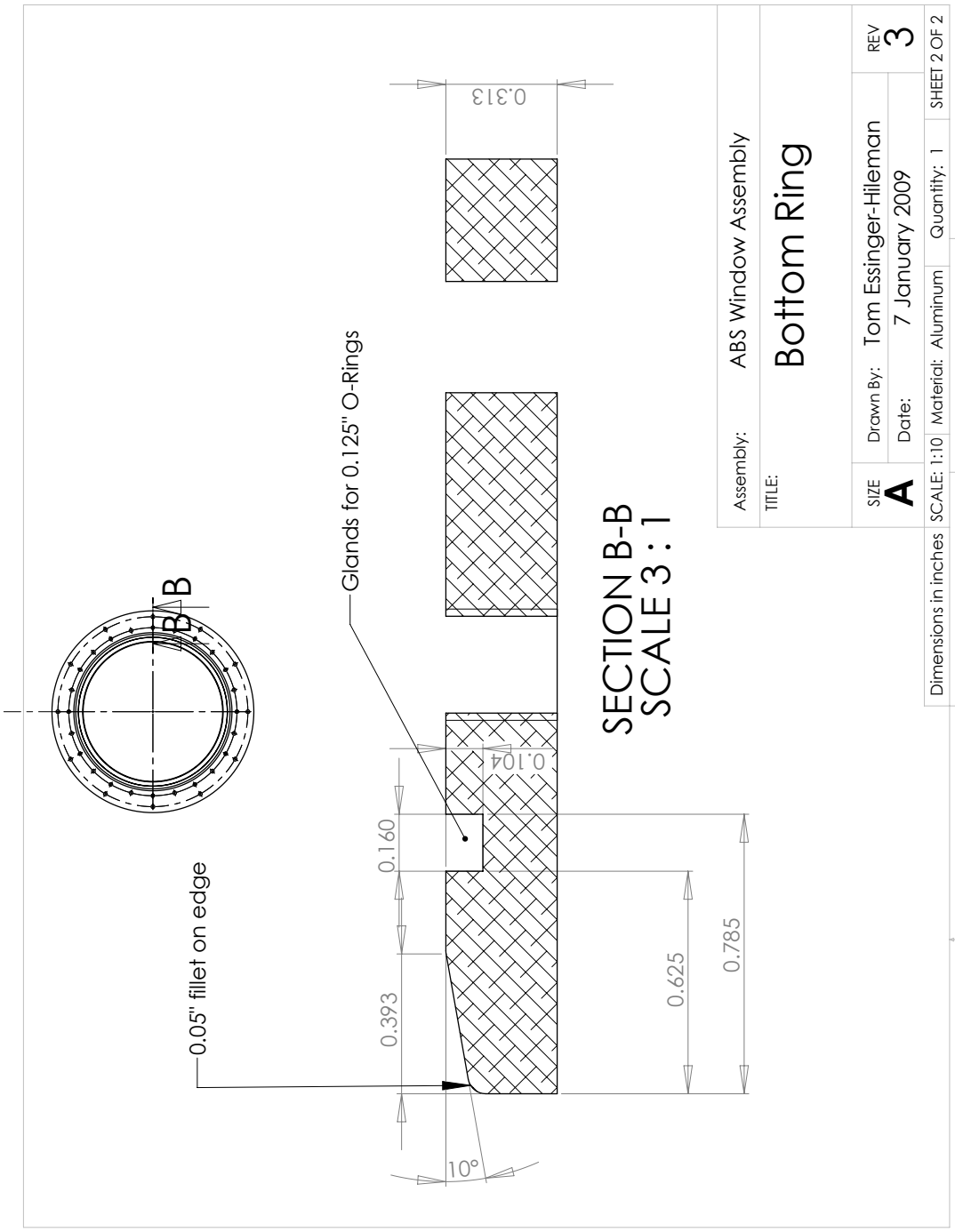
B
B
Glands for 0.125" O-Rings
0.313
0.104
0.160
0.393
0.625
0.785
10°
0.05" fillet on edge
SECTION B-B
SCALE 3 : 1
Assembly: ABS Window Assembly
TITLE: Bottom Ring
SIZE A
Drawn By: Tom Essinger-Hileman
Date: 7 January 2009
REV 3
Dimensions in inches
SCALE: 1:10
Material: Aluminum
Quantity: 1
SHEET 2 OF 2

Figure B.12:

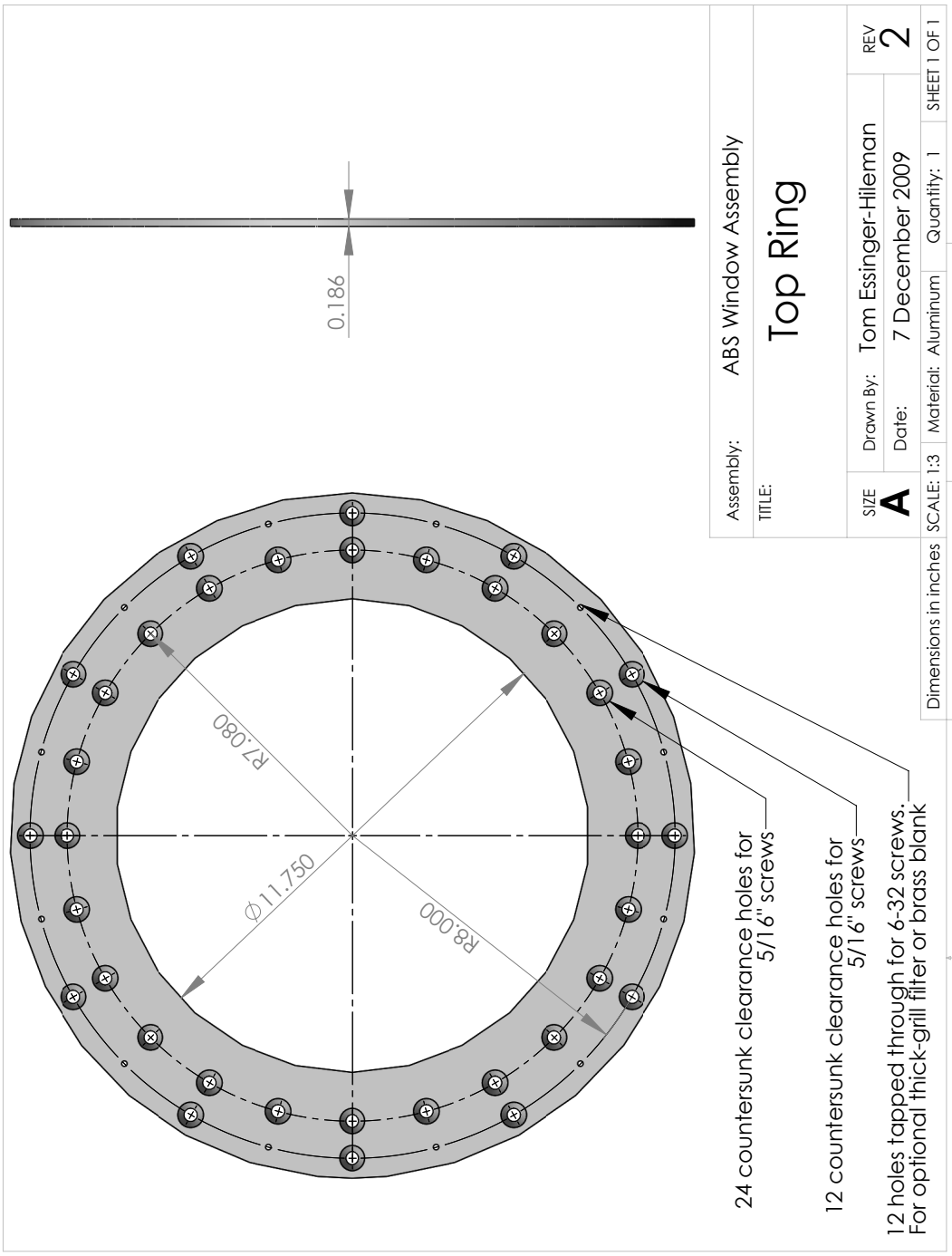
0.186
R7.080
∅11.750
R8.000
24 countersunk clearance holes for 5/16" screws
12 countersunk clearance holes for 5/16" screws
12 holes tapped through for 6-32 screws. For optional thick-grill filter or brass blank
Assembly: ABS Window Assembly
TITLE: Top Ring
SIZE A
Drawn By: Tom Essinger-Hileman
Date: 7 December 2009
REV 2
Dimensions in inches
SCALE: 1:3
Material: Aluminum
Quantity: 1
SHEET 1 OF 1

Figure B.13:

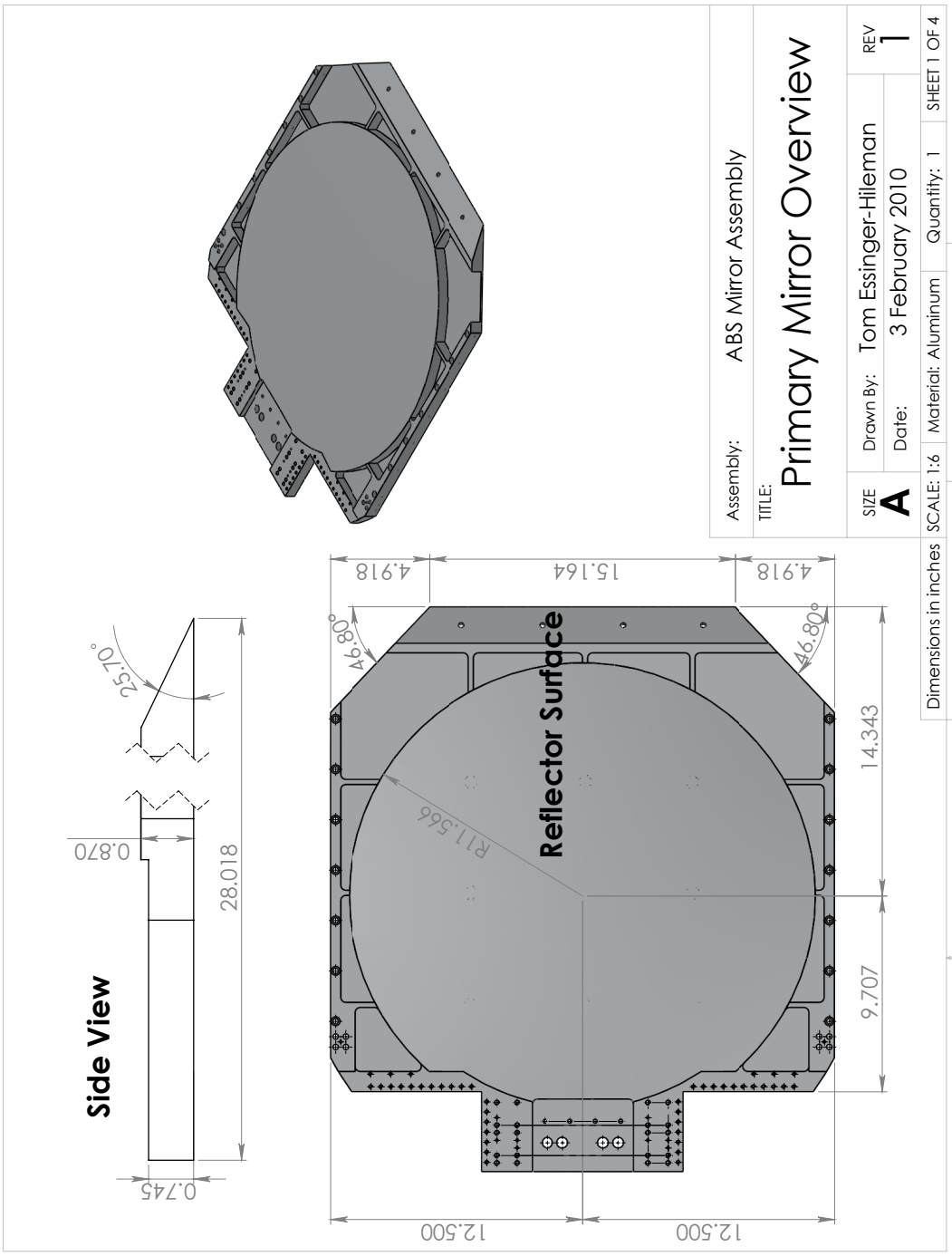
Assembly:
ABS Mirror Assembly
TITLE:
Primary Mirror Overview
SIZE
A
Drawn By:
Tom Essinger-Hileman
Date:
3 February 2010
REV
1
Dimensions in inches
SCALE: 1:6
Material: Aluminum
Quantity: 1
SHEET 1 OF 4
Reflector Surface
Side View
4.918
15.164
4.918
49.80°
46.80°
R11.566
14.343
9.707
12.500
12.500
0.870
28.018
0.745
25.70°

Figure B.14:

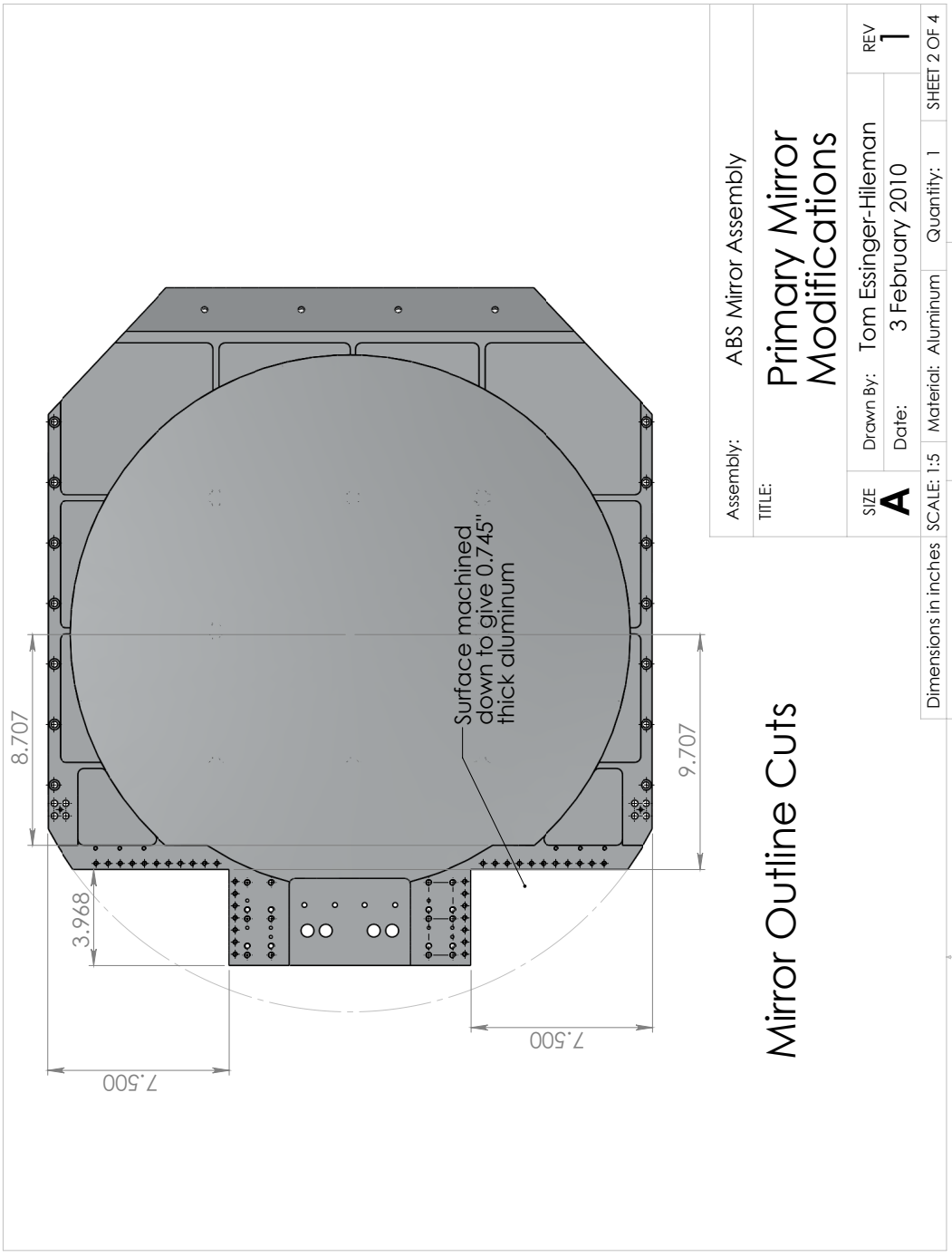
Mirror Outline Cuts
Surface machined down to give 0.745" thick aluminum
8.707
9.707
3.968
7.500
7.500
Assembly: ABS Mirror Assembly
TITLE: Primary Mirror Modifications
SIZE A
Drawn By: Tom Essinger-Hileman
Date: 3 February 2010
REV 1
Dimensions in inches
SCALE: 1:5
Material: Aluminum
Quantity: 1
SHEET 2 OF 4

Figure B.15:

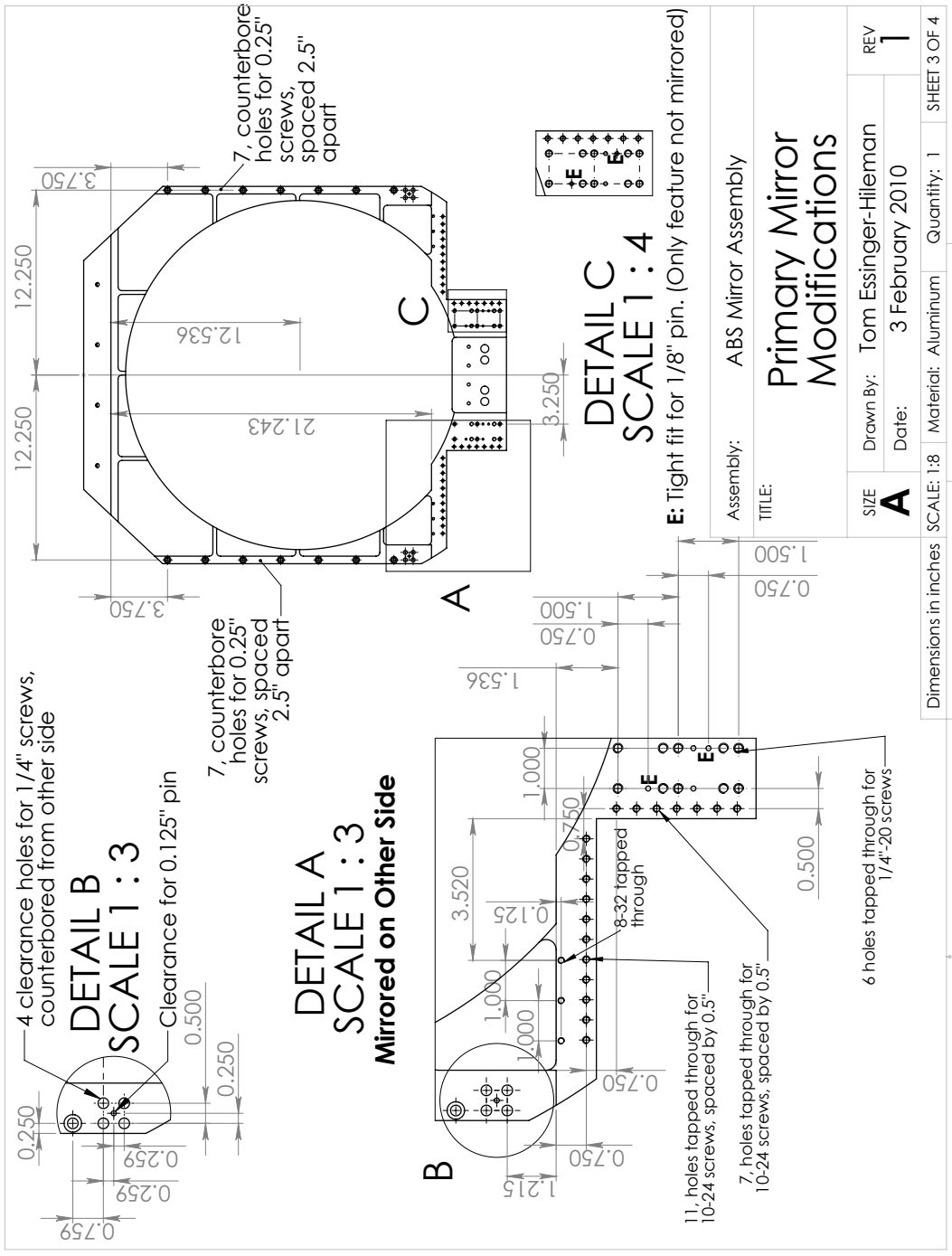
DETAIL B
SCALE 1 : 3
4 clearance holes for 1/4" screws, counterbored from other side
Clearance for 0.125" pin
DETAIL A
SCALE 1 : 3
Mirrored on Other Side
7, counterbore holes for 0.25" screws, spaced 2.5" apart
11, holes tapped through for 10-24 screws, spaced by 0.5"
7, holes tapped through for 10-24 screws, spaced by 0.5"
8-32 tapped through
6 holes tapped through for 1/4"-20 screws
DETAIL C
SCALE 1 : 4
E: Tight fit for 1/8" pin. (Only feature not mirrored)
Assembly: ABS Mirror Assembly
TITLE: Primary Mirror Modifications
SIZE A
Drawn By: Tom Essinger-Hileman
Date: 3 February 2010
REV 1
Dimensions in inches
SCALE: 1:8
Material: Aluminum
Quantity: 1
SHEET 3 OF 4

Figure B.16:

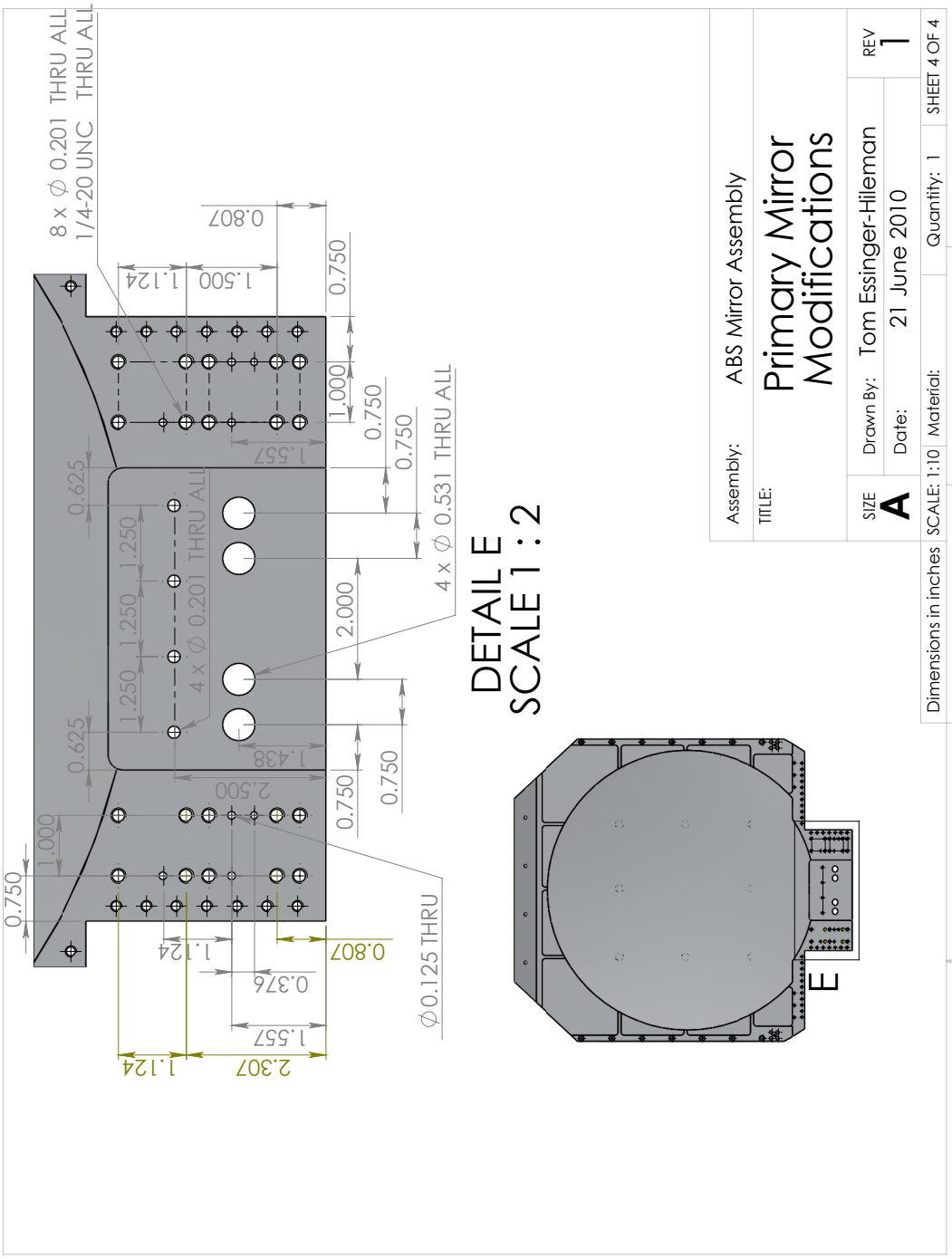
8 x ∅ 0.201 THRU ALL
1/4-20 UNC THRU ALL
0.807
1.500
1.124
0.750
1.000
0.750
0.750
1.557
4 x ∅ 0.531 THRU ALL
0.625
1.250
1.250
1.250
4 x ∅ 0.201 THRU ALL
2.000
0.625
1.438
2.500
0.750
0.750
1.000
0.750
1.124
0.807
0.376
1.557
2.307
1.124
∅0.125 THRU
DETAIL E
SCALE 1 : 2
E
Assembly: ABS Mirror Assembly
TITLE: Primary Mirror Modifications
SIZE A
Drawn By: Tom Essinger-Hileman
Date: 21 June 2010
REV 1
Dimensions in inches
SCALE: 1:10
Material:
Quantity: 1
SHEET 4 OF 4

Figure B.17:

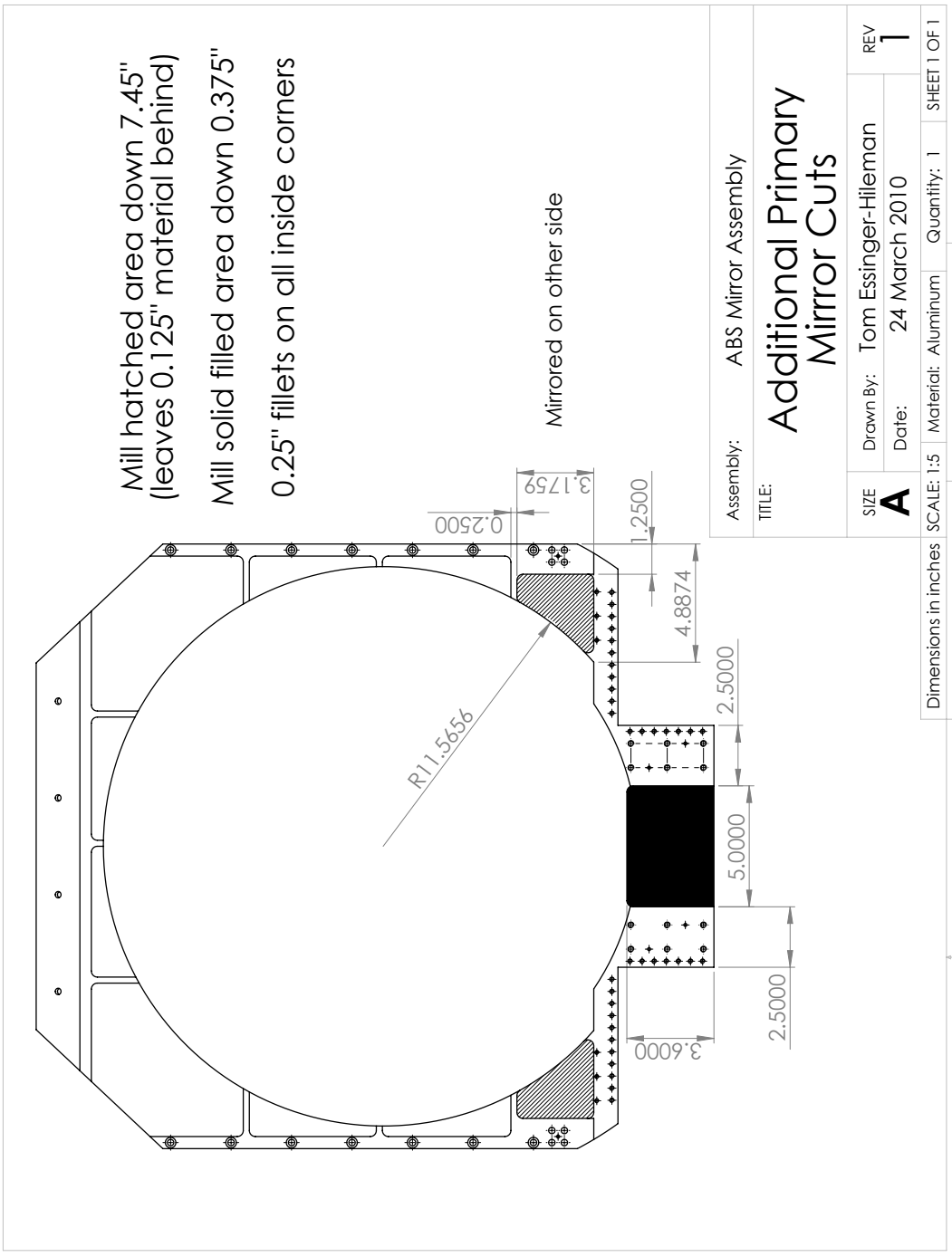
Mill hatched area down 7.45"
(leaves 0.125" material behind)
Mill solid filled area down 0.375"
0.25" fillets on all inside corners
Mirrored on other side
R11.5656
0.2500
3.1759
1.2500
4.8874
2.5000
5.0000
2.5000
3.6000
Assembly: ABS Mirror Assembly
TITLE: Additional Primary Mirrror Cuts
SIZE A
Drawn By: Tom Essinger-Hileman
Date: 24 March 2010
REV 1
Dimensions in inches
SCALE: 1:5
Material: Aluminum
Quantity: 1
SHEET 1 OF 1

Figure B.18:

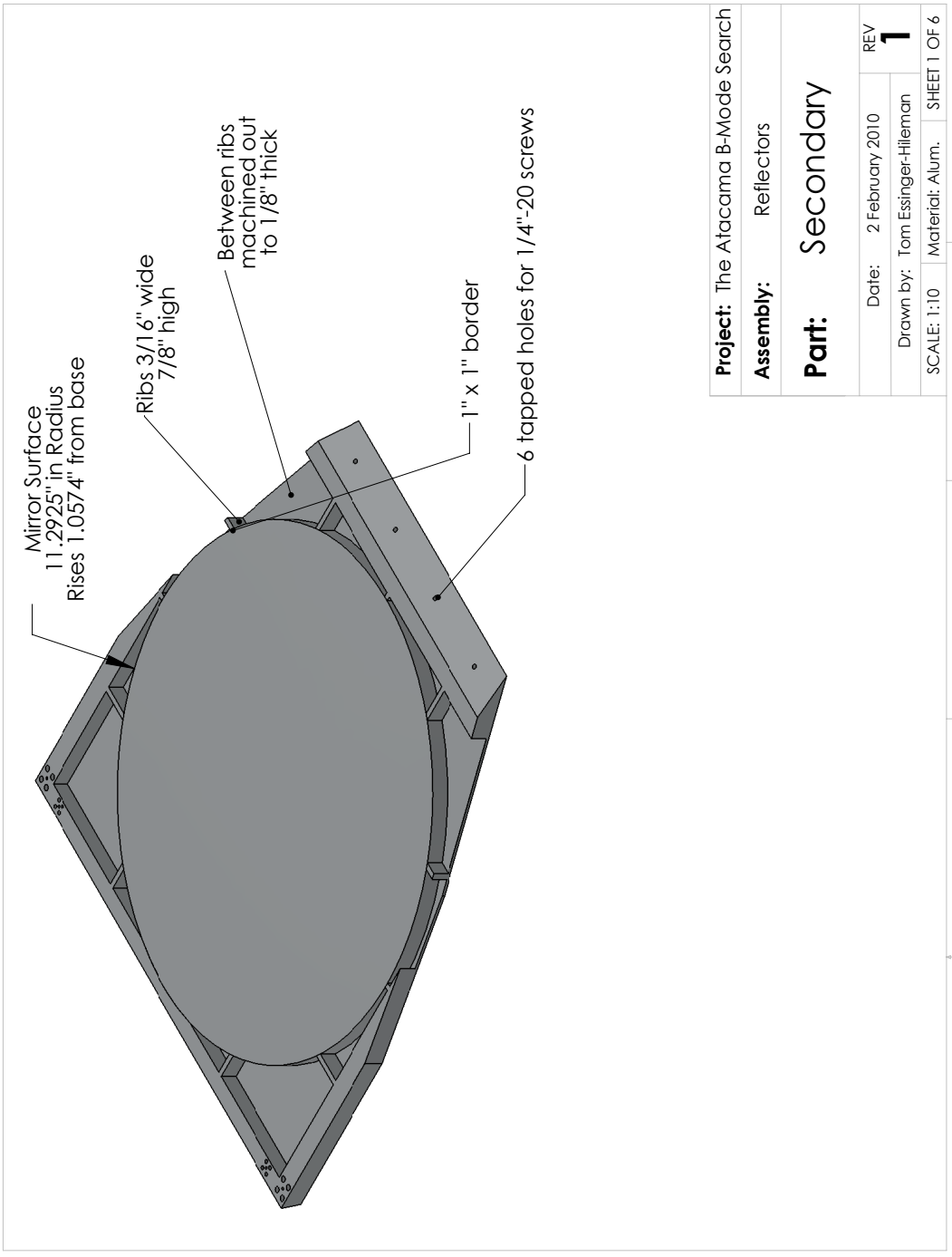
Mirror Surface
11.2925" in Radius
Rises 1.0574" from base
Ribs 3/16" wide
7/8" high
Between ribs
machined out
to 1/8" thick
1" x 1" border
6 tapped holes for 1/4"-20 screws
Project: The Atacama B-Mode Search
Assembly: Reflectors
Part: Secondary
Date: 2 February 2010
REV 1
Drawn by: Tom Essinger-Hileman
SCALE: 1:10
Material: Alum.
SHEET 1 OF 6

Figure B.19:

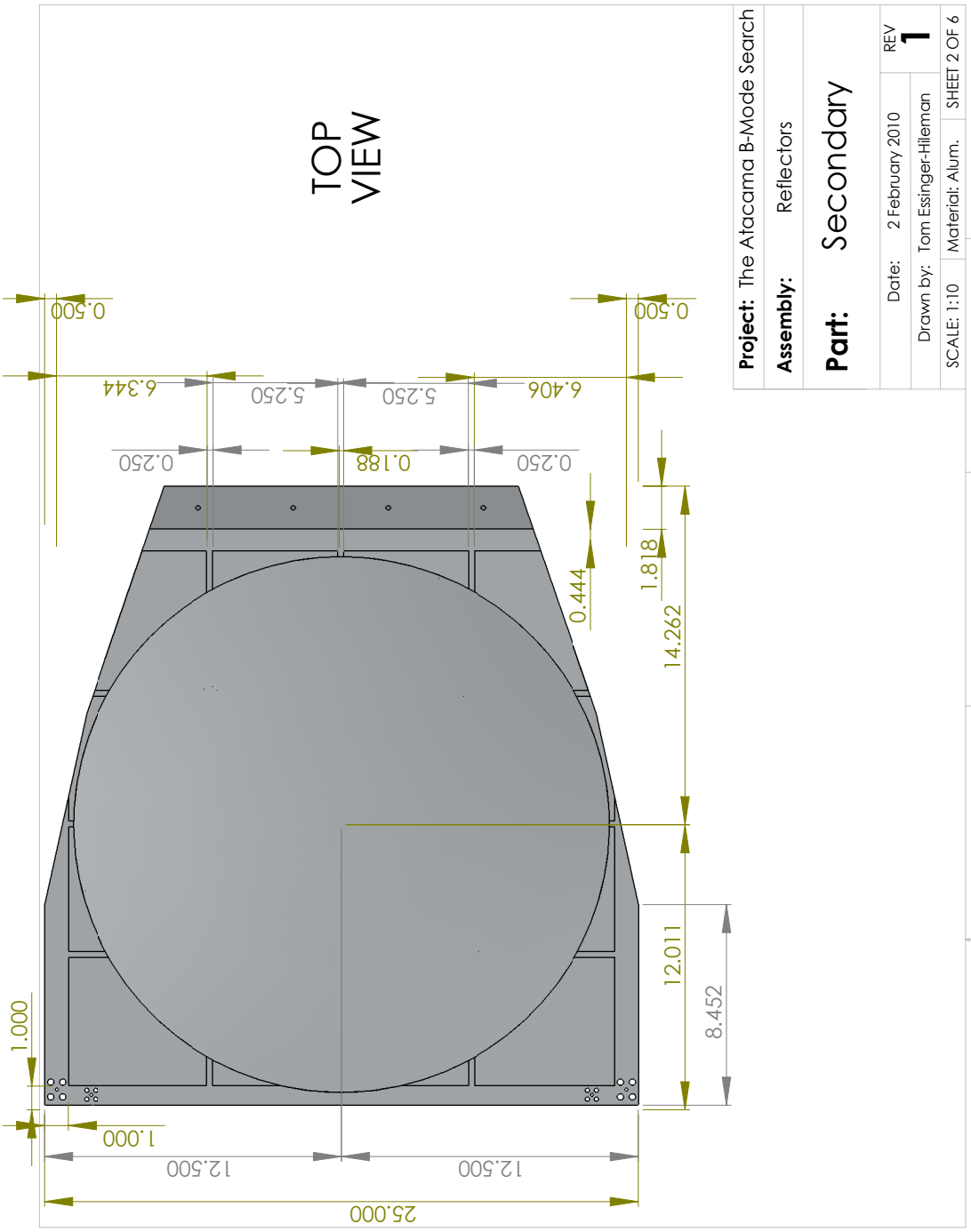
TOP
VIEW
0.500
6.344
5.250
6.406
0.500
0.250
0.188
0.250
0.444
1.818
14.262
12.011
8.452
1.000
1.000
12.500
12.500
25.000
Project: The Atacama B-Mode Search
Assembly: Reflectors
Part: Secondary
Date: 2 February 2010
Drawn by: Tom Essinger-Hileman
REV 1
SCALE: 1:10
Material: Alum.
SHEET 2 OF 6

Figure B.20:

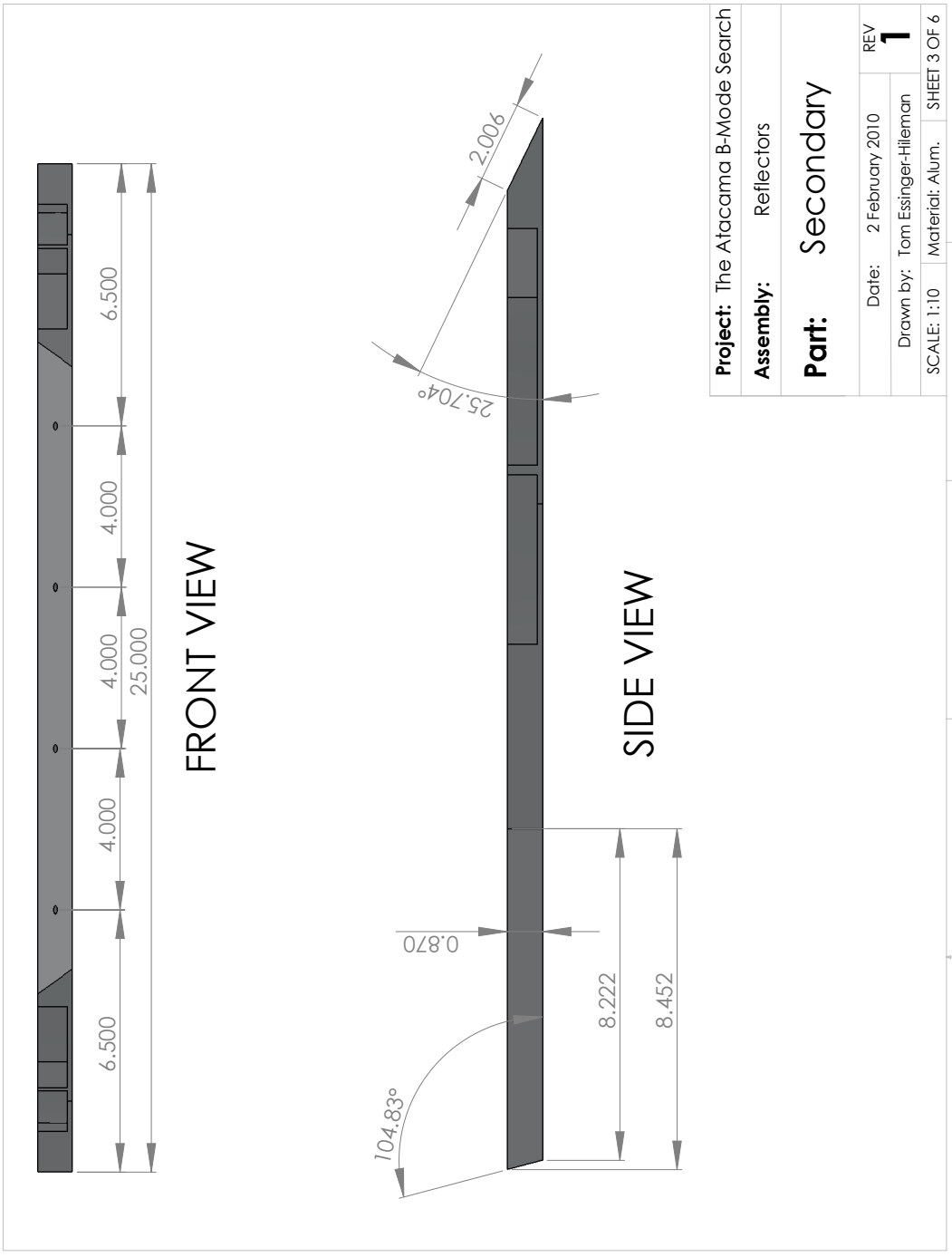
FRONT VIEW
6.500
4.000
4.000
4.000
25.000
6.500
SIDE VIEW
2.006
25.704°
0.870
8.222
8.452
104.83°
Project: The Atacama B-Mode Search
Assembly: Reflectors
Part: Secondary
Date: 2 February 2010
REV 1
Drawn by: Tom Essinger-Hileman
SCALE: 1:10
Material: Alum.
SHEET 3 OF 6

Figure B.21:

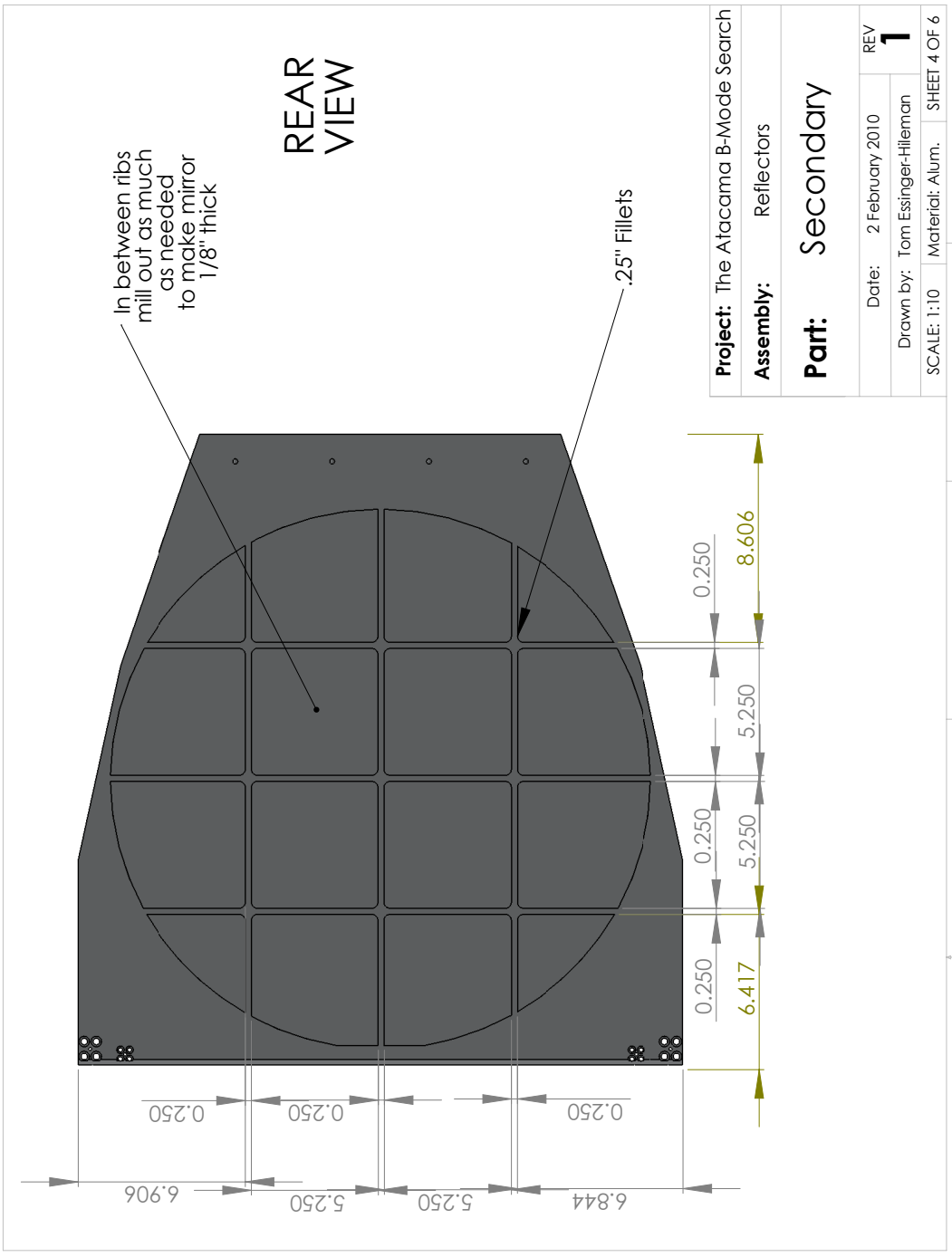
REAR
VIEW
In between ribs
mill out as much
as needed
to make mirror
1/8" thick
.25" Fillets
Project: The Atacama B-Mode Search
Assembly: Reflectors
Part: Secondary
Date: 2 February 2010
Drawn by: Tom Essinger-Hileman
SCALE: 1:10
Material: Alum.
SHEET 4 OF 6
REV
1
8.606
0.250
5.250
0.250
5.250
0.250
6.417
0.250
0.250
0.250
6.906
5.250
5.250
6.844

Figure B.22:

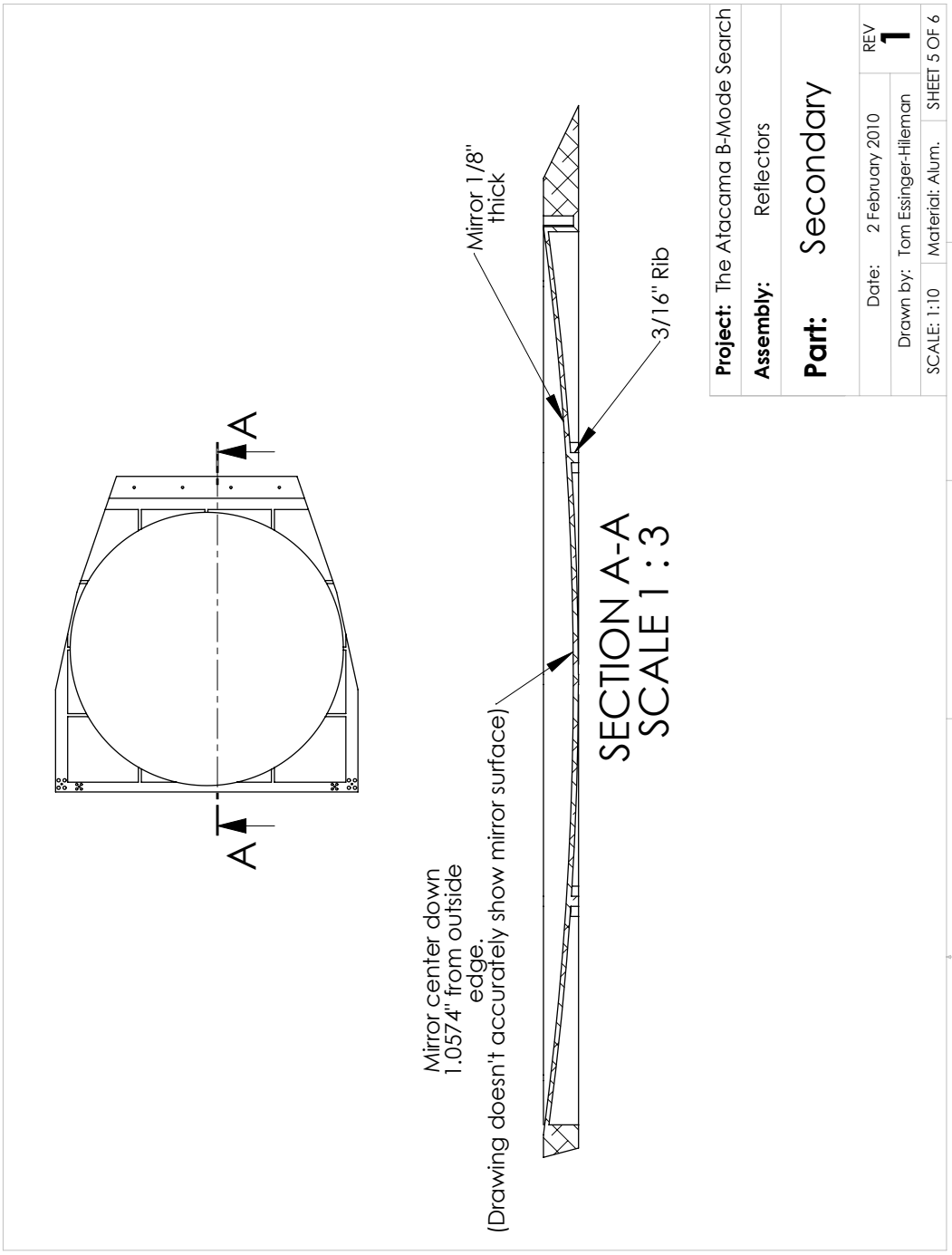
A
A
SECTION A-A
SCALE 1 : 3
Mirror 1/8" thick
3/16" Rib
Mirror center down 1.0574" from outside edge.
(Drawing doesn't accurately show mirror surface)
Project: The Atacama B-Mode Search
Assembly: Reflectors
Part: Secondary
Date: 2 February 2010
Drawn by: Tom Essinger-Hileman
REV 1
SCALE: 1:10
Material: Alum.
SHEET 5 OF 6

Figure B.23:

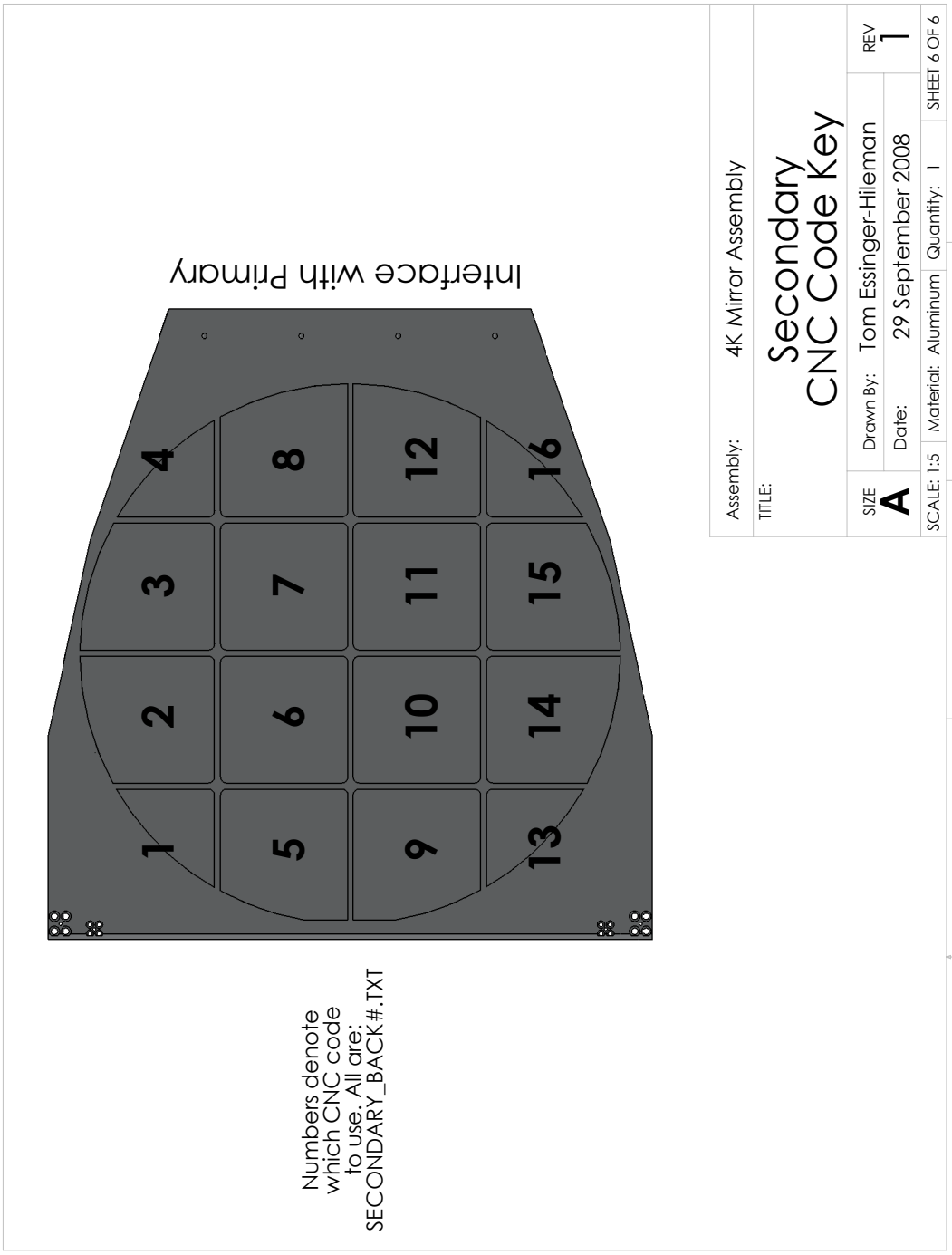
Interface with Primary
1
2
3
4
5
6
7
8
9
10
11
12
13
14
15
16
Numbers denote
which CNC code
to use. All are:
SECONDARY_BACK#.TXT
Assembly: 4K Mirror Assembly
TITLE:
Secondary
CNC Code Key
SIZE A
Drawn By: Tom Essinger-Hileman
Date: 29 September 2008
REV 1
SCALE: 1:5
Material: Aluminum
Quantity: 1
SHEET 6 OF 6

Figure B.24:

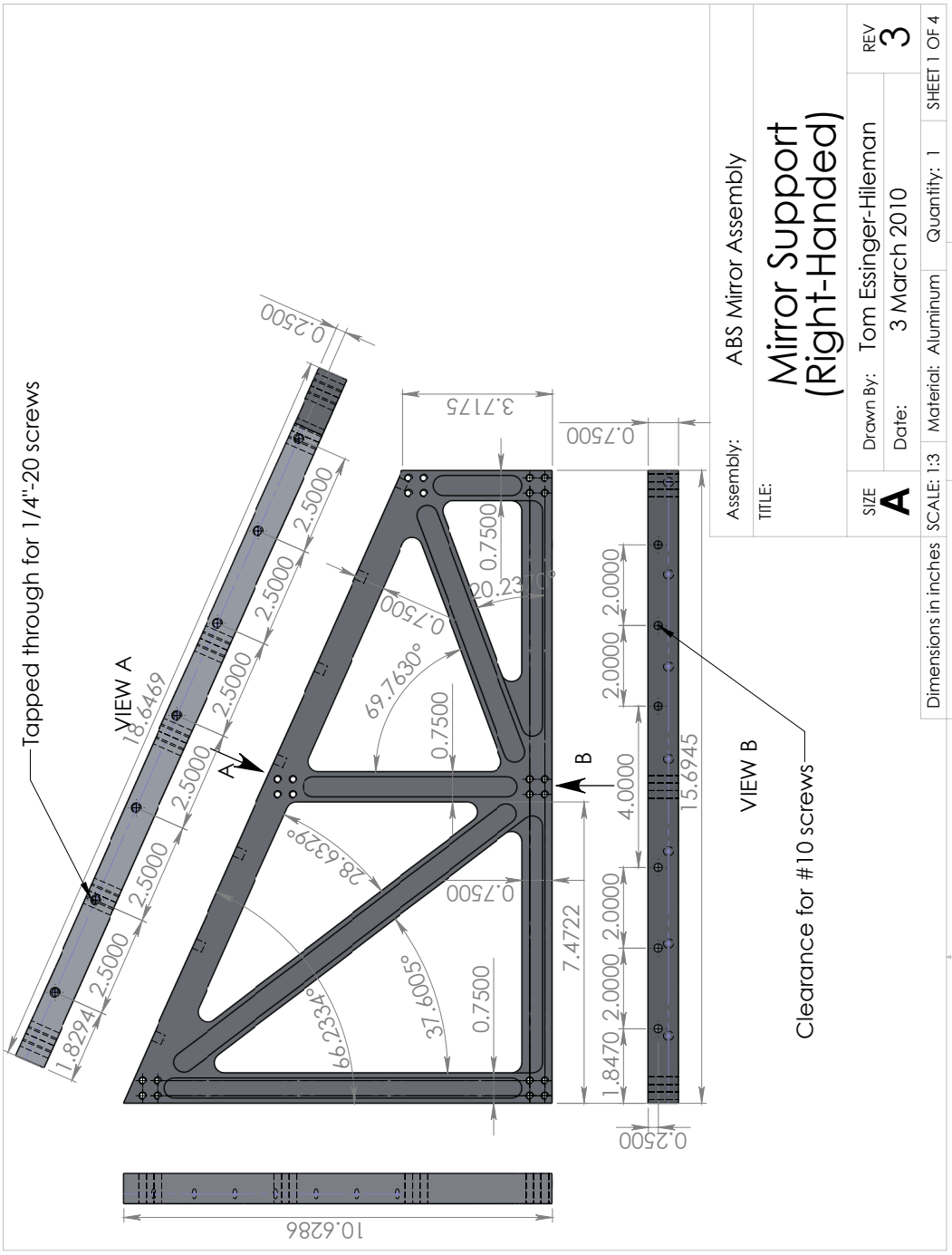
Tapped through for 1/4"-20 screws
VIEW A
18.6469
1.8294
2.5000
2.5000
2.5000
2.5000
2.5000
2.5000
0.2500
A
B
3.7175
0.7500
0.7500
20.2310°
0.7500
69.7630°
0.7500
28.6329°
0.7500
37.6005°
0.7500
66.2334°
7.4722
1.8470
2.0000
2.0000
2.0000
4.0000
2.0000
2.0000
15.6945
VIEW B
Clearance for #10 screws
0.2500
10.6286
Assembly:
ABS Mirror Assembly
TITLE:
Mirror Support
(Right-Handed)
SIZE
A
Drawn By:
Tom Essinger-Hileman
Date:
3 March 2010
REV
3
Dimensions in inches
SCALE: 1:3
Material: Aluminum
Quantity: 1
SHEET 1 OF 4

Figure B.25:

TAG	X LOC	Y LOC
A1	0.1875	0.1875
A2	0.1875	0.5625
A3	0.1875	9.7875
A4	0.1875	10.1625
A5	0.5625	0.1875
A6	0.5625	0.5625
A7	0.5625	9.7875
A8	0.5625	10.1625
A9	7.6595	0.1875
A10	7.6595	0.5625
A11	7.6595	6.4375
A12	7.6595	6.8125
A13	8.0345	0.1875
A14	8.0345	0.5625
A15	8.0345	6.4375
A16	8.0345	6.8125
A17	15.1315	0.1875
A18	15.1315	0.5625
A19	15.1315	3.1875
A20	15.1315	3.5625
A21	15.5065	0.1875
A22	15.5065	0.5625
A23	15.5065	3.1875
A24	15.5065	3.5625

Hole Callout

All holes tapped through for 10-24 screws

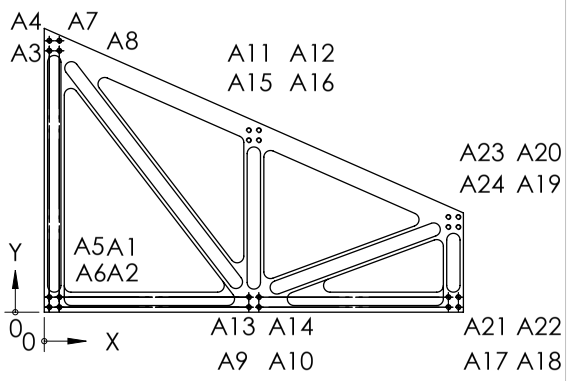

Assembly:	ABS Mirror Assembly		
TITLE:	Mirror Support (Right-Handed)		
SIZE A	Drawn By: Tom Essinger-Hileman		REV 3
	Date: 3 March 2010		
Dimensions in inches	SCALE: 1:3	Material: Aluminum	Quantity: 1
			SHEET 2 OF 4

5 4 3 2 1

Figure B.26:

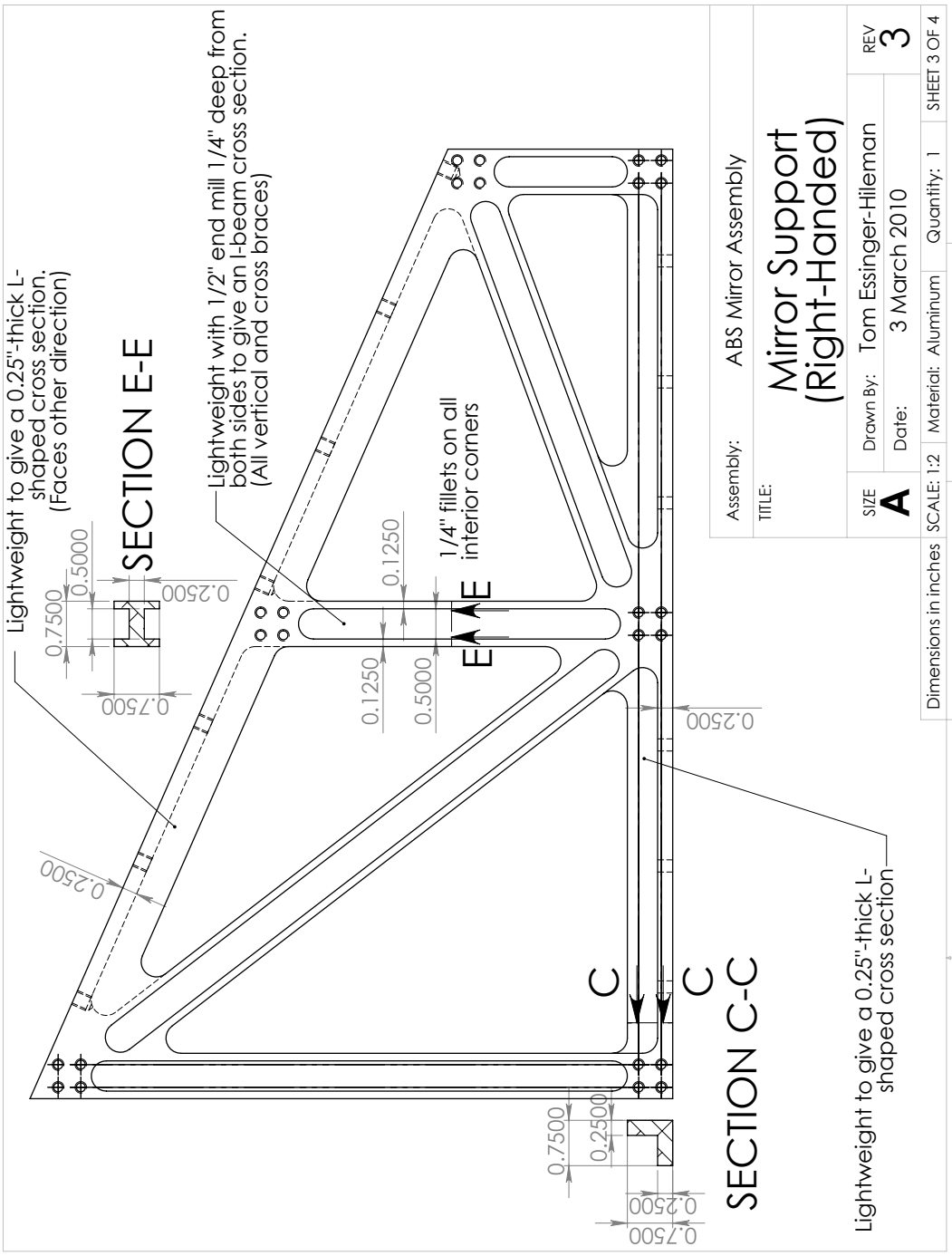
Lightweight to give a 0.25"-thick L-shaped cross section. (Faces other direction)
SECTION E-E
0.7500
0.5000
0.2500
0.7500
Lightweight with 1/2" end mill 1/4" deep from both sides to give an I-beam cross section. (All vertical and cross braces)
1/4" fillets on all interior corners
0.1250
0.1250
0.5000
E
E
0.2500
0.2500
C
C
SECTION C-C
0.7500
0.2500
0.2500
0.7500
Lightweight to give a 0.25"-thick L-shaped cross section
Assembly: ABS Mirror Assembly
TITLE: Mirror Support (Right-Handed)
SIZE A
Drawn By: Tom Essinger-Hileman
Date: 3 March 2010
REV 3
Dimensions in inches
SCALE: 1:2
Material: Aluminum
Quantity: 1
SHEET 3 OF 4

Figure B.27:

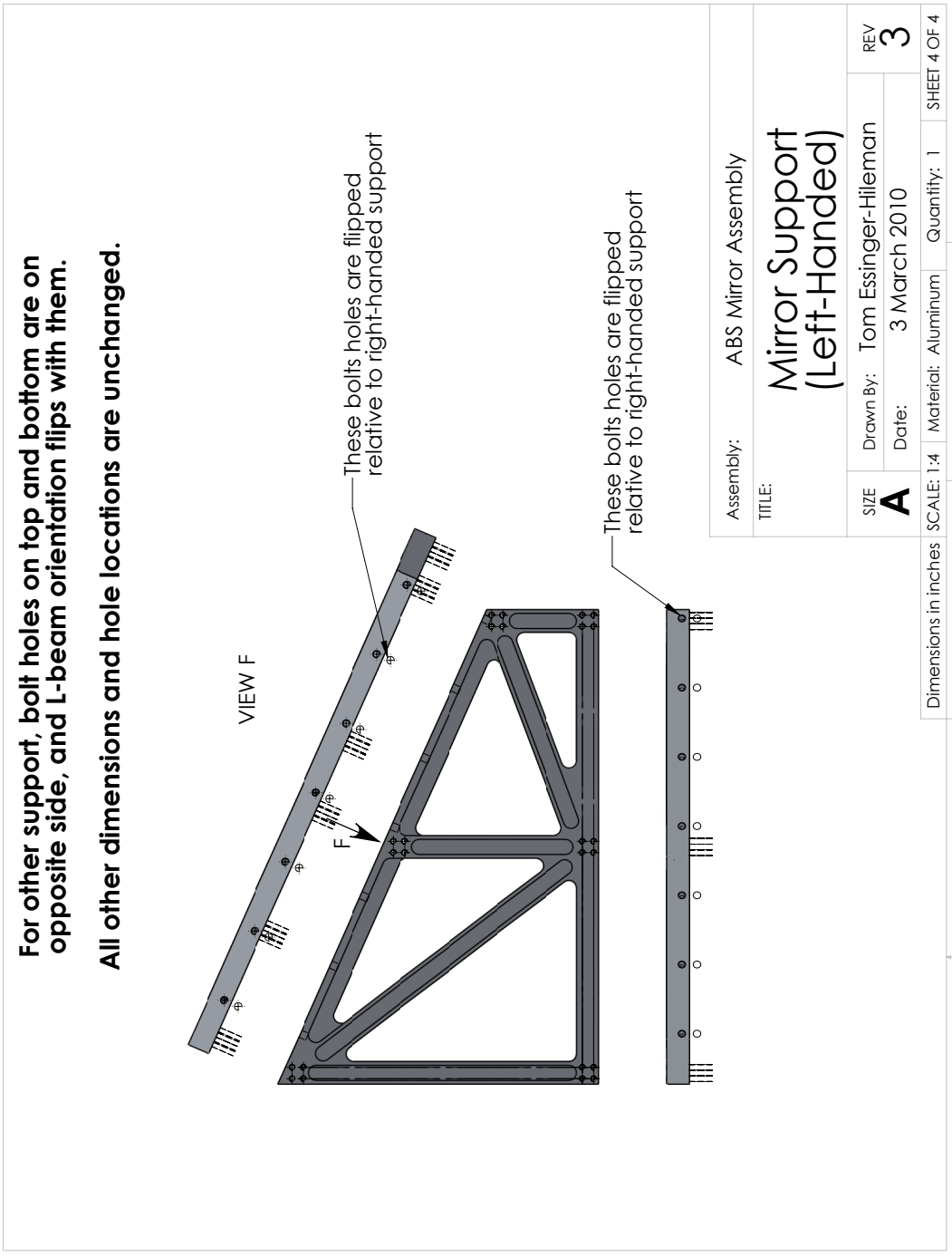
For other support, bolt holes on top and bottom are on opposite side, and L-beam orientation flips with them.
All other dimensions and hole locations are unchanged.
VIEW F
F
These bolts holes are flipped relative to right-handed support
These bolts holes are flipped relative to right-handed support
Assembly: ABS Mirror Assembly
TITLE: Mirror Support (Left-Handed)
SIZE A
Drawn By: Tom Essinger-Hileman
Date: 3 March 2010
REV 3
Dimensions in inches
SCALE: 1:4
Material: Aluminum
Quantity: 1
SHEET 4 OF 4

Figure B.28:

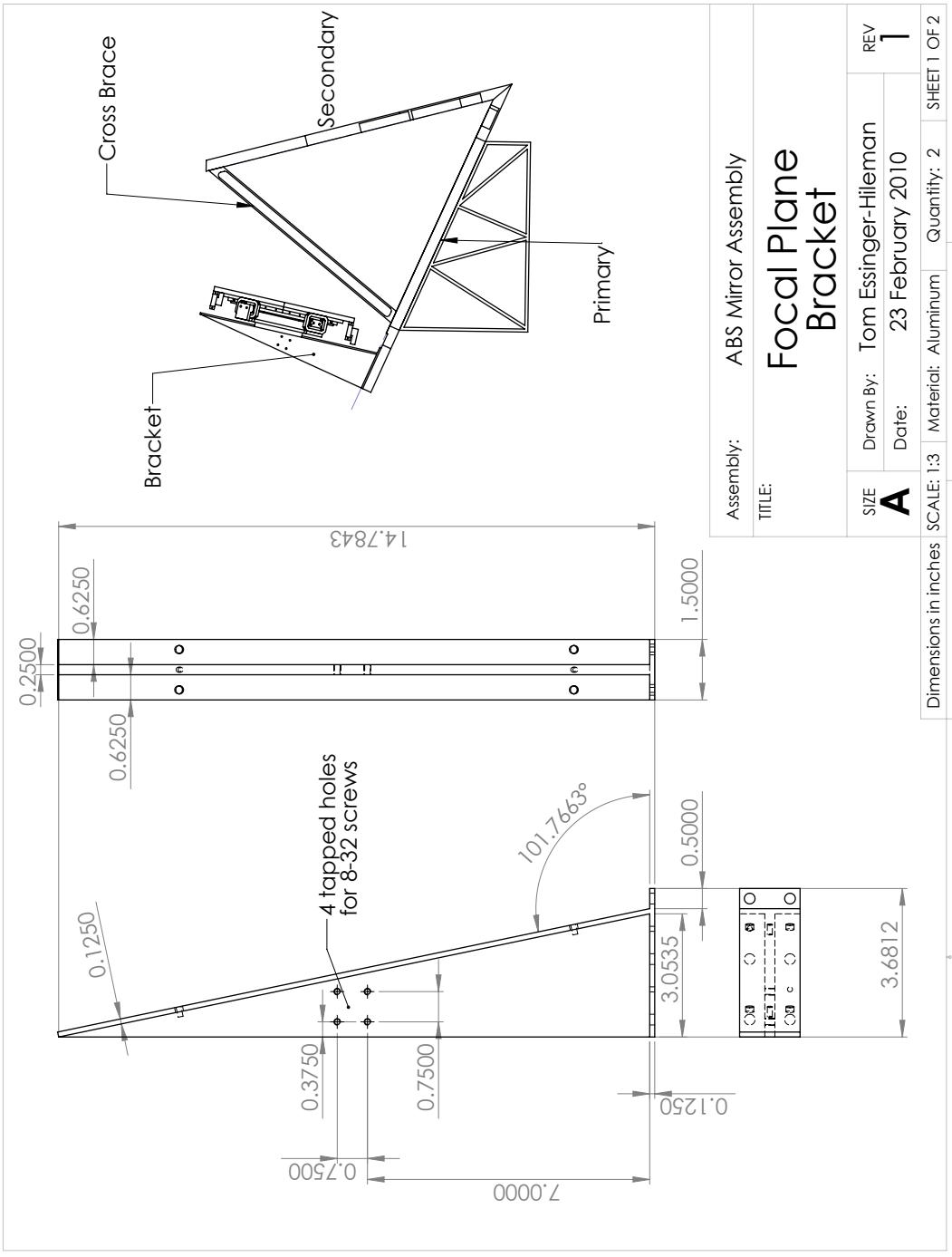
Cross Brace
Secondary
Primary
Bracket
Assembly: ABS Mirror Assembly
TITLE: Focal Plane Bracket
SIZE A
Drawn By: Tom Essinger-Hileman
Date: 23 February 2010
REV 1
Dimensions in inches
SCALE: 1:3
Material: Aluminum
Quantity: 2
SHEET 1 OF 2
14.7843
0.6250
0.2500
0.6250
1.5000
4 tapped holes for 8-32 screws
101.7663°
0.5000
0.1250
3.0535
3.6812
0.3750
0.7500
0.1250
0.7500
7.0000

Figure B.29:

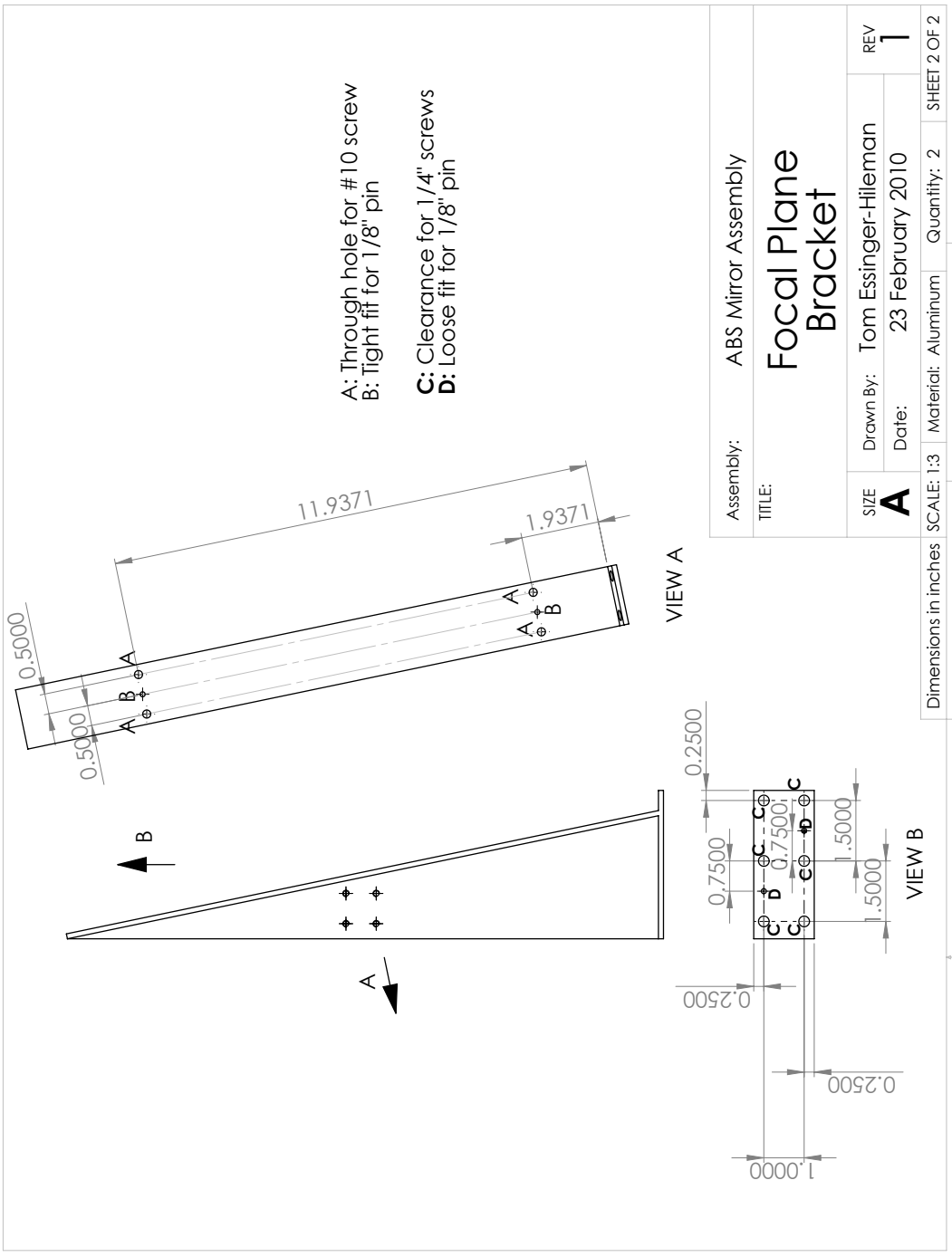
A: Through hole for #10 screw
B: Tight fit for 1/8" pin
C: Clearance for 1/4" screws
D: Loose fit for 1/8" pin
11.9371
1.9371
0.5000
0.5000
VIEW A
VIEW B
0.2500
0.7500
0.7500
1.5000
1.5000
0.2500
0.2500
1.0000
Assembly: ABS Mirror Assembly
TITLE: Focal Plane Bracket
SIZE A
Drawn By: Tom Essinger-Hileman
Date: 23 February 2010
REV 1
Dimensions in inches
SCALE: 1:3
Material: Aluminum
Quantity: 2
SHEET 2 OF 2

Figure B.30:

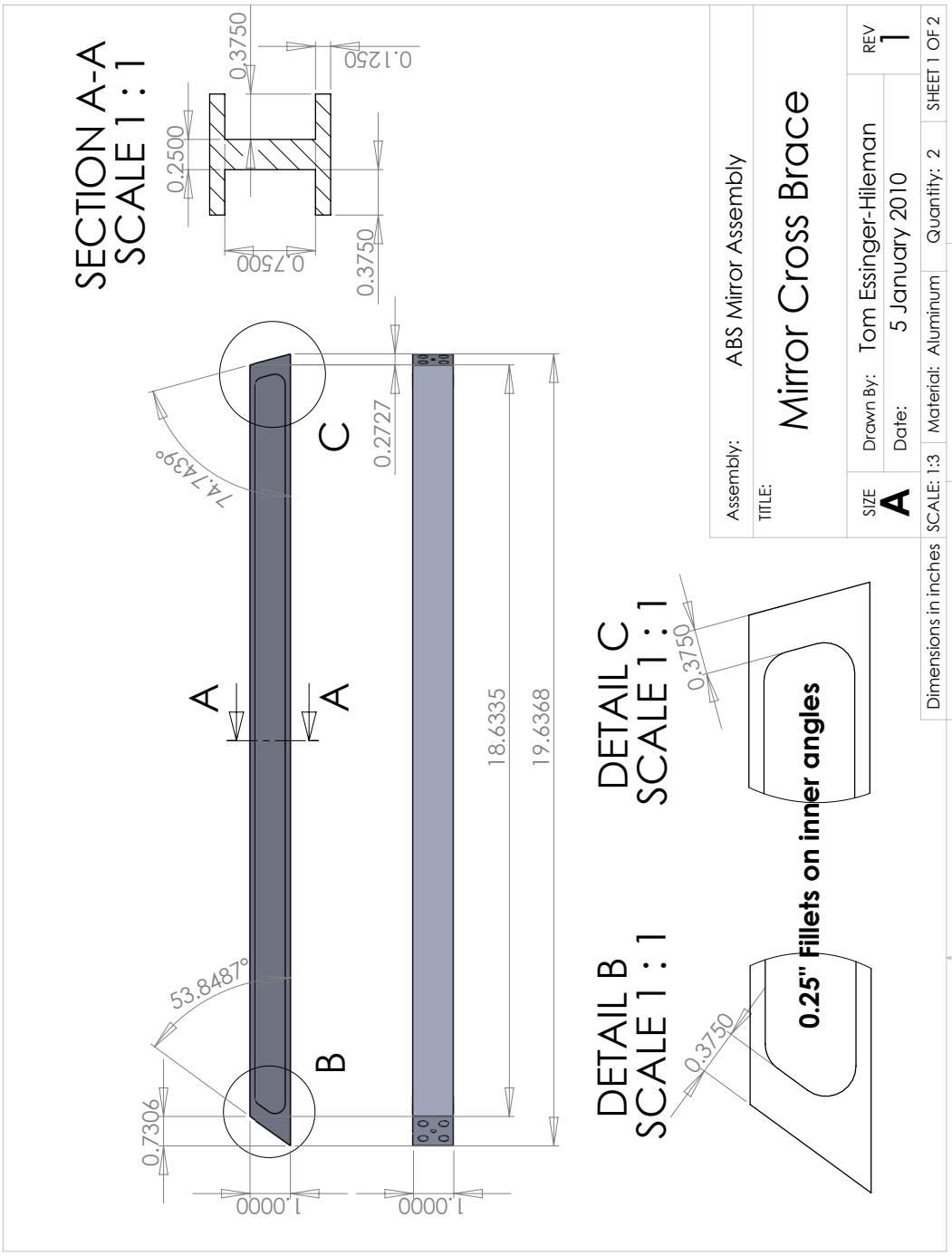
SECTION A-A
SCALE 1 : 1
0.3750
0.1250
0.2500
0.7500
0.3750
0.2727
74.7439°
53.8487°
0.7306
1.0000
1.0000
18.6335
19.6368
A
A
B
C
DETAIL B
SCALE 1 : 1
DETAIL C
SCALE 1 : 1
0.3750
0.3750
0.25" Fillets on inner angles
Assembly: ABS Mirror Assembly
TITLE: Mirror Cross Brace
SIZE A
Drawn By: Tom Essinger-Hileman
Date: 5 January 2010
REV 1
Dimensions in inches
SCALE: 1:3
Material: Aluminum
Quantity: 2
SHEET 1 OF 2

Figure B.31:

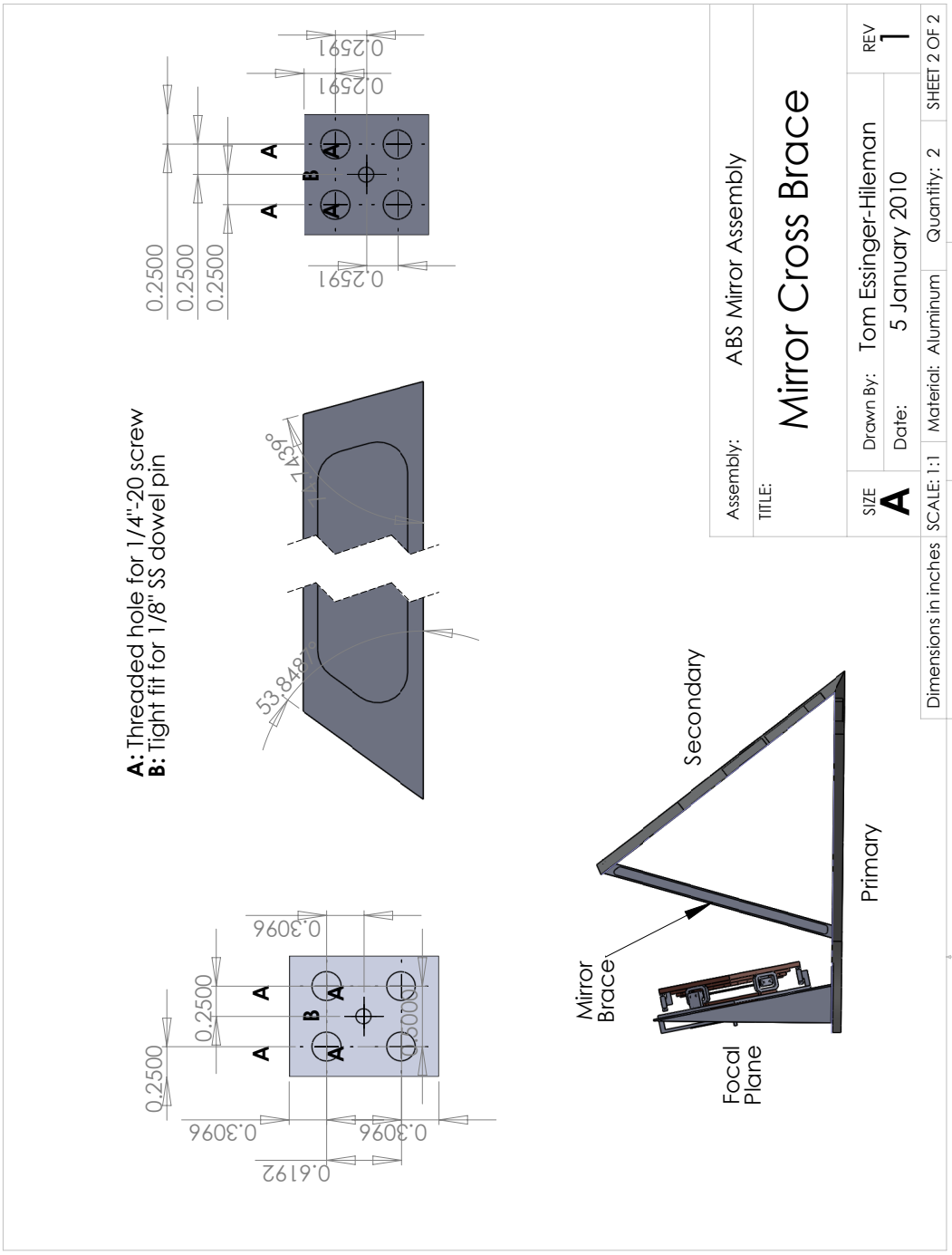
A: Threaded hole for 1/4"-20 screw
B: Tight fit for 1/8" SS dowel pin
0.2500
0.2500
0.2500
0.2591
0.2591
0.2591
0.2500
0.3096
0.3096
0.3096
0.6192
53.848°
14.63°
Secondary
Primary
Mirror Brace
Focal Plane
Assembly: ABS Mirror Assembly
TITLE: Mirror Cross Brace
SIZE A
Drawn By: Tom Essinger-Hileman
Date: 5 January 2010
REV 1
Dimensions in inches
SCALE: 1:1
Material: Aluminum
Quantity: 2
SHEET 2 OF 2

Figure B.32:

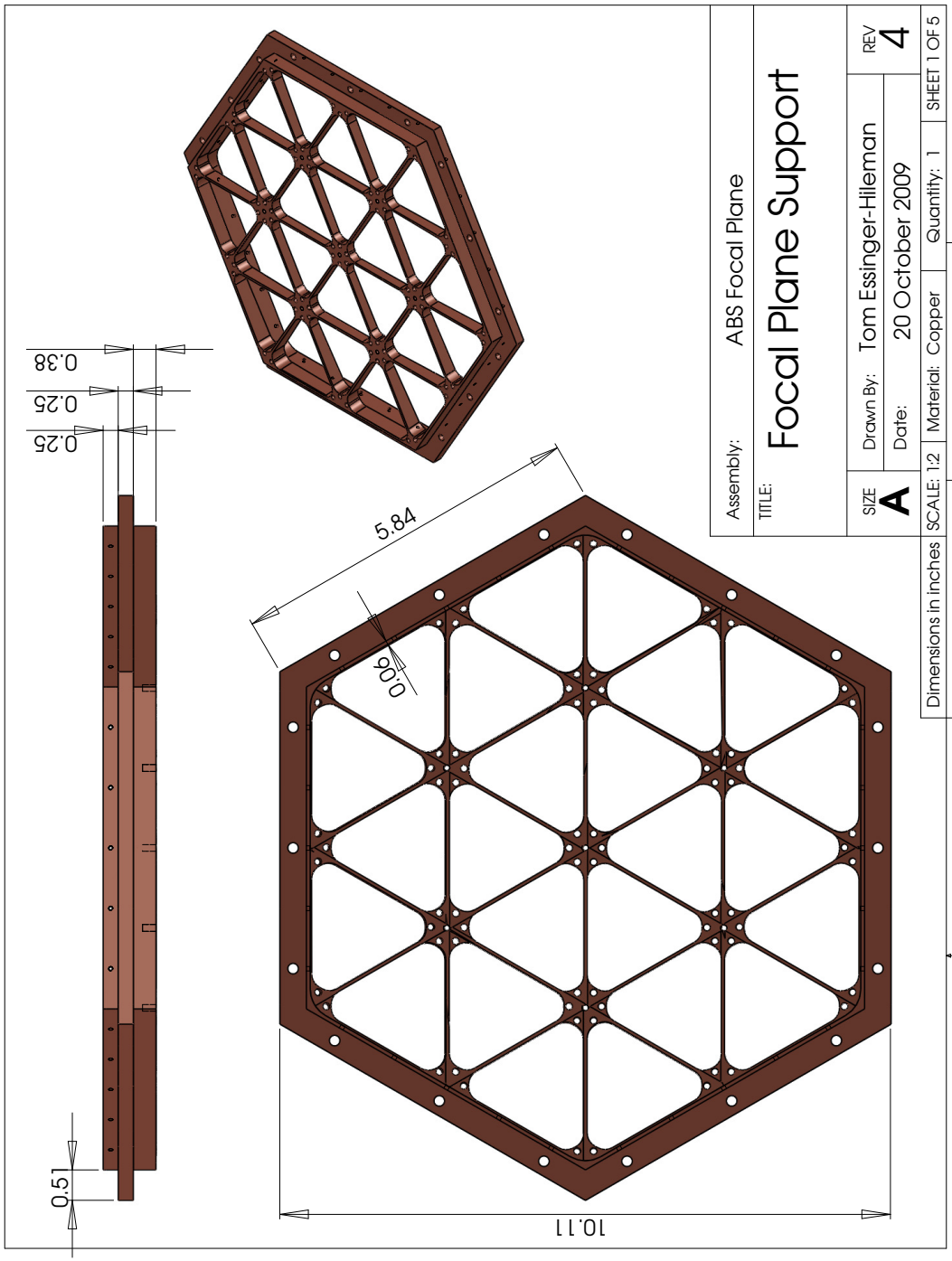
0.38
0.25
0.25
0.51
5.84
0.09
10.11
Assembly:
ABS Focal Plane
TITLE:
Focal Plane Support
SIZE
A
Drawn By:
Tom Essinger-Hileman
Date:
20 October 2009
REV
4
Dimensions in inches
SCALE: 1:2
Material: Copper
Quantity: 1
SHEET 1 OF 5

Figure B.33:

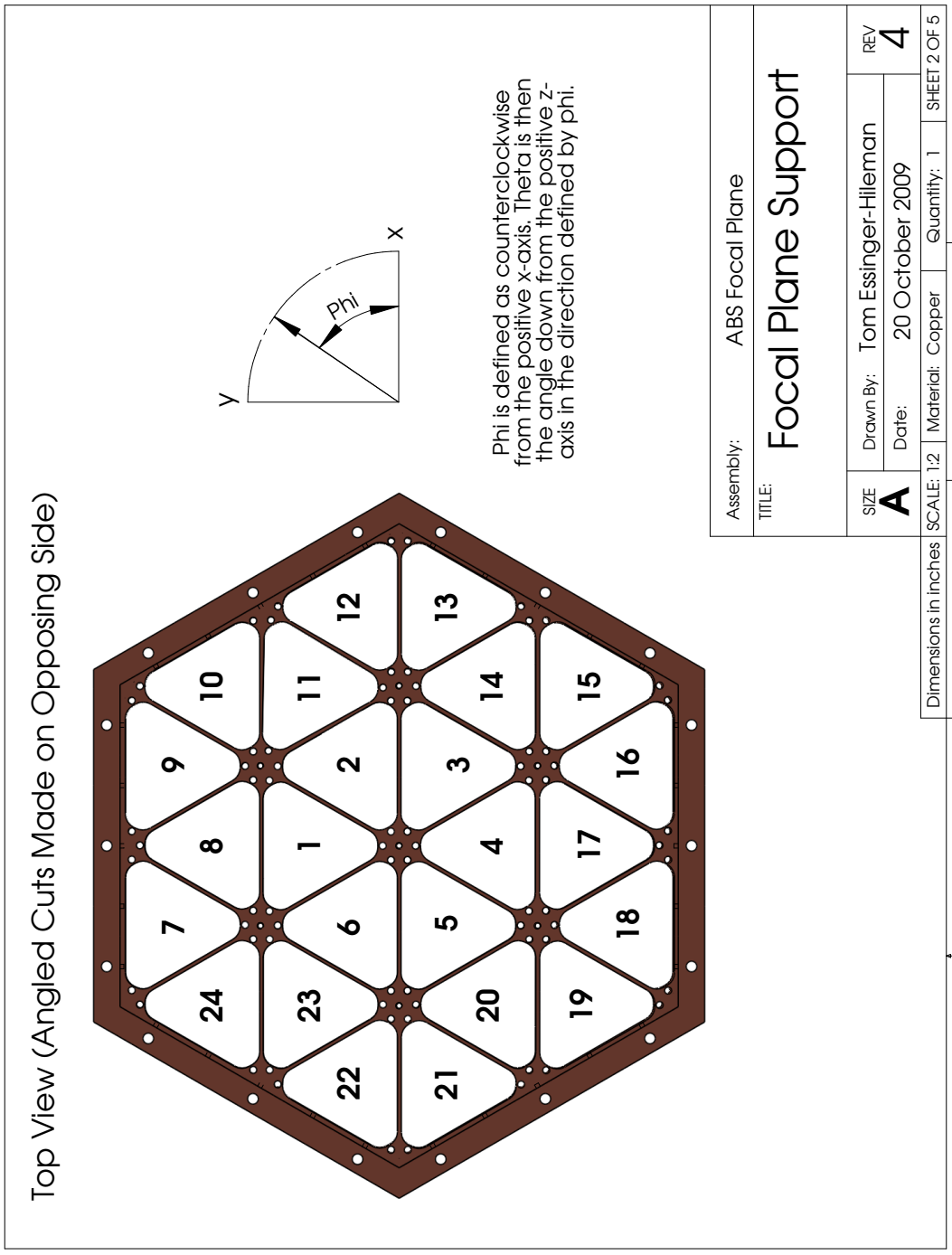
Top View (Angled Cuts Made on Opposing Side)
Phi is defined as counterclockwise from the positive x-axis. Theta is then the angle down from the positive z-axis in the direction defined by phi.
Phi
x
y
1
2
3
4
5
6
7
8
9
10
11
12
13
14
15
16
17
18
19
20
21
22
23
24
Assembly: ABS Focal Plane
TITLE: Focal Plane Support
SIZE A
Drawn By: Tom Essinger-Hileman
Date: 20 October 2009
REV 4
Dimensions in inches
SCALE: 1:2
Material: Copper
Quantity: 1
SHEET 2 OF 5

Figure B.34:

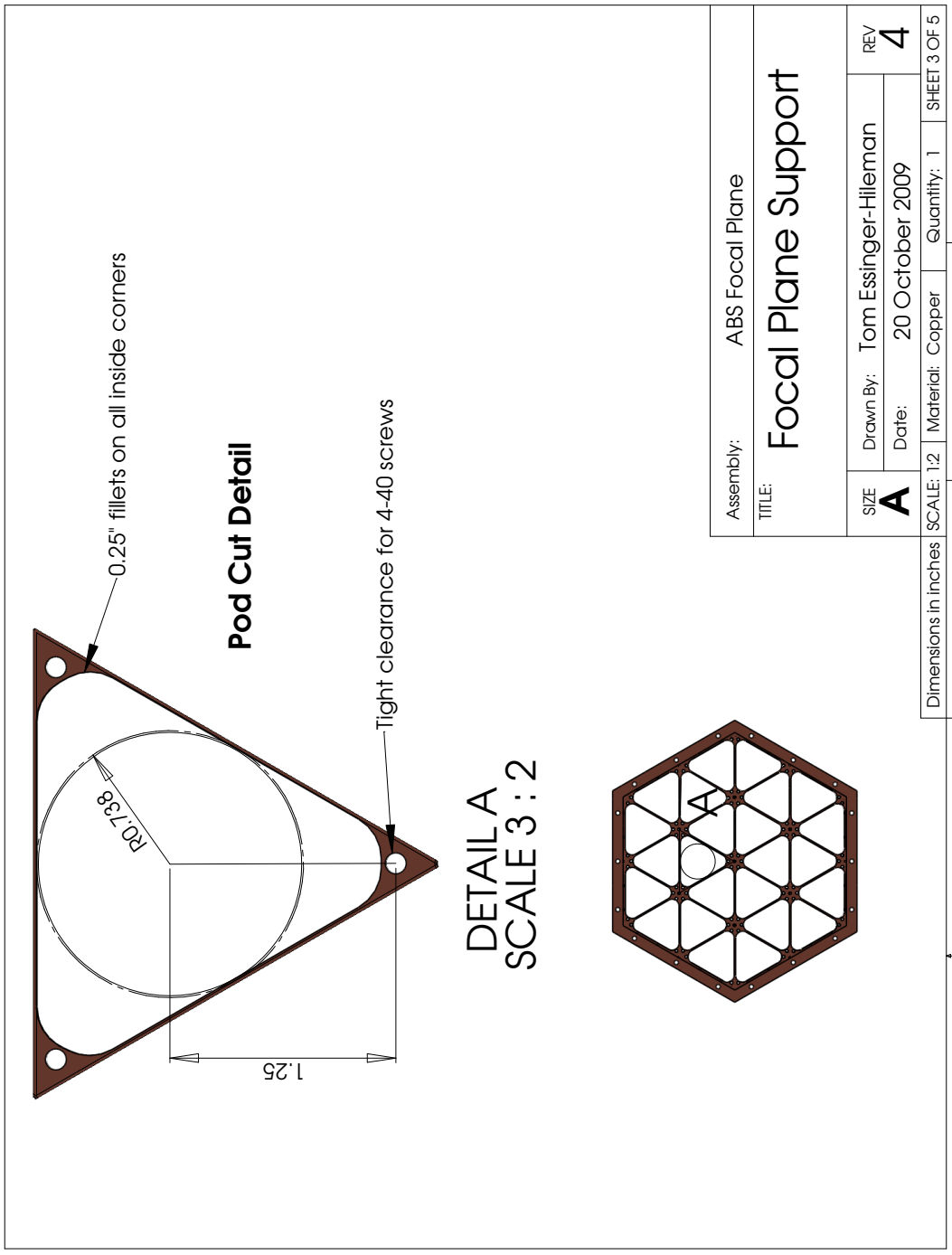
Pod Cut Detail
0.25" fillets on all inside corners
Tight clearance for 4-40 screws
R0.738
1.25
DETAIL A
SCALE 3 : 2
A
Assembly:
ABS Focal Plane
TITLE:
Focal Plane Support
SIZE
A
Drawn By: Tom Essinger-Hileman
Date: 20 October 2009
REV
4
Dimensions in inches
SCALE: 1:2
Material: Copper
Quantity: 1
SHEET 3 OF 5

Figure B.35:

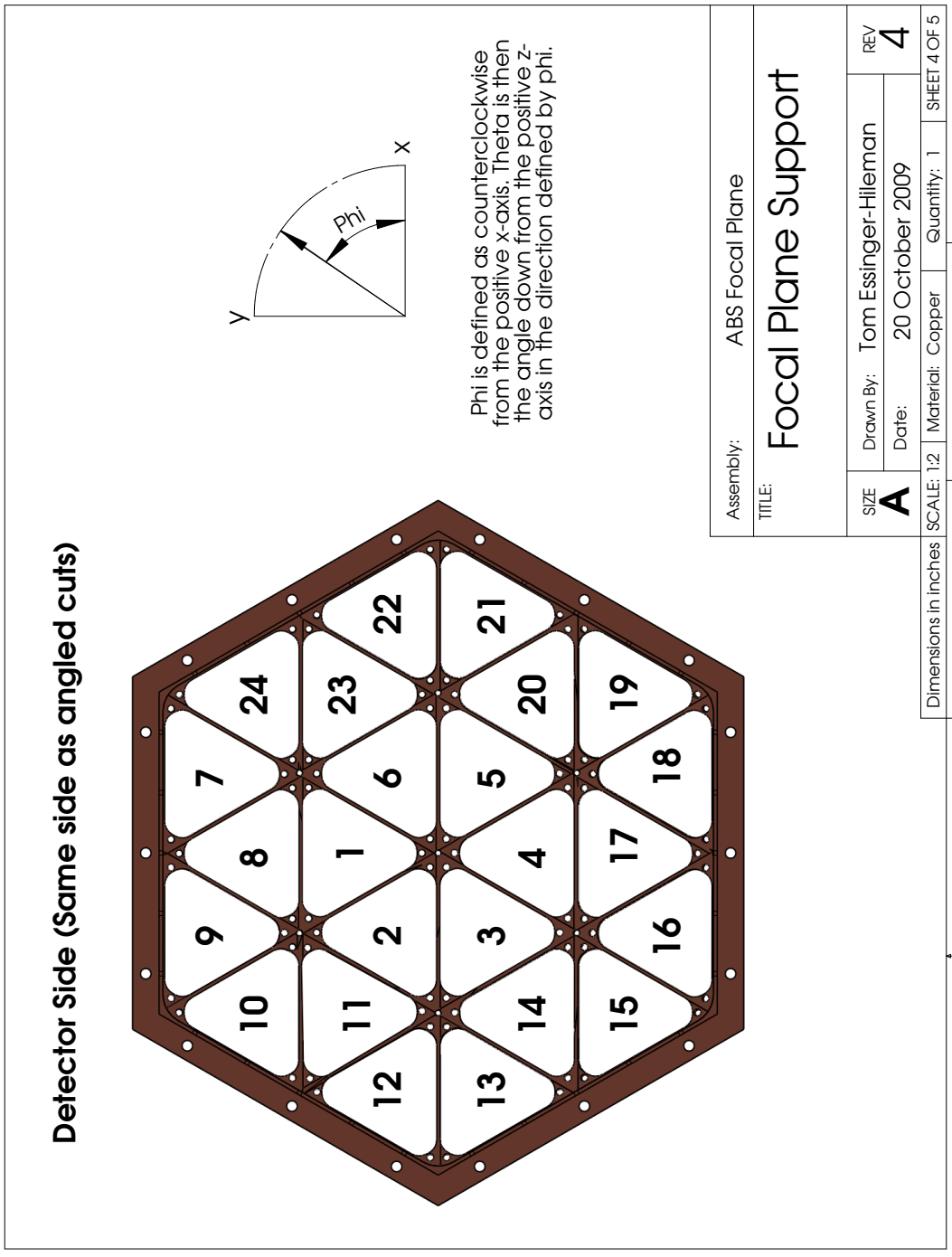
Detector Side (Same side as angled cuts)
Phi is defined as counterclockwise from the positive x-axis. Theta is then the angle down from the positive z-axis in the direction defined by phi.
Phi
x
y
Assembly: ABS Focal Plane
TITLE: Focal Plane Support
SIZE A
Drawn By: Tom Essinger-Hileman
Date: 20 October 2009
REV 4
Dimensions in inches
SCALE: 1:2
Material: Copper
Quantity: 1
SHEET 4 OF 5

Figure B.36:

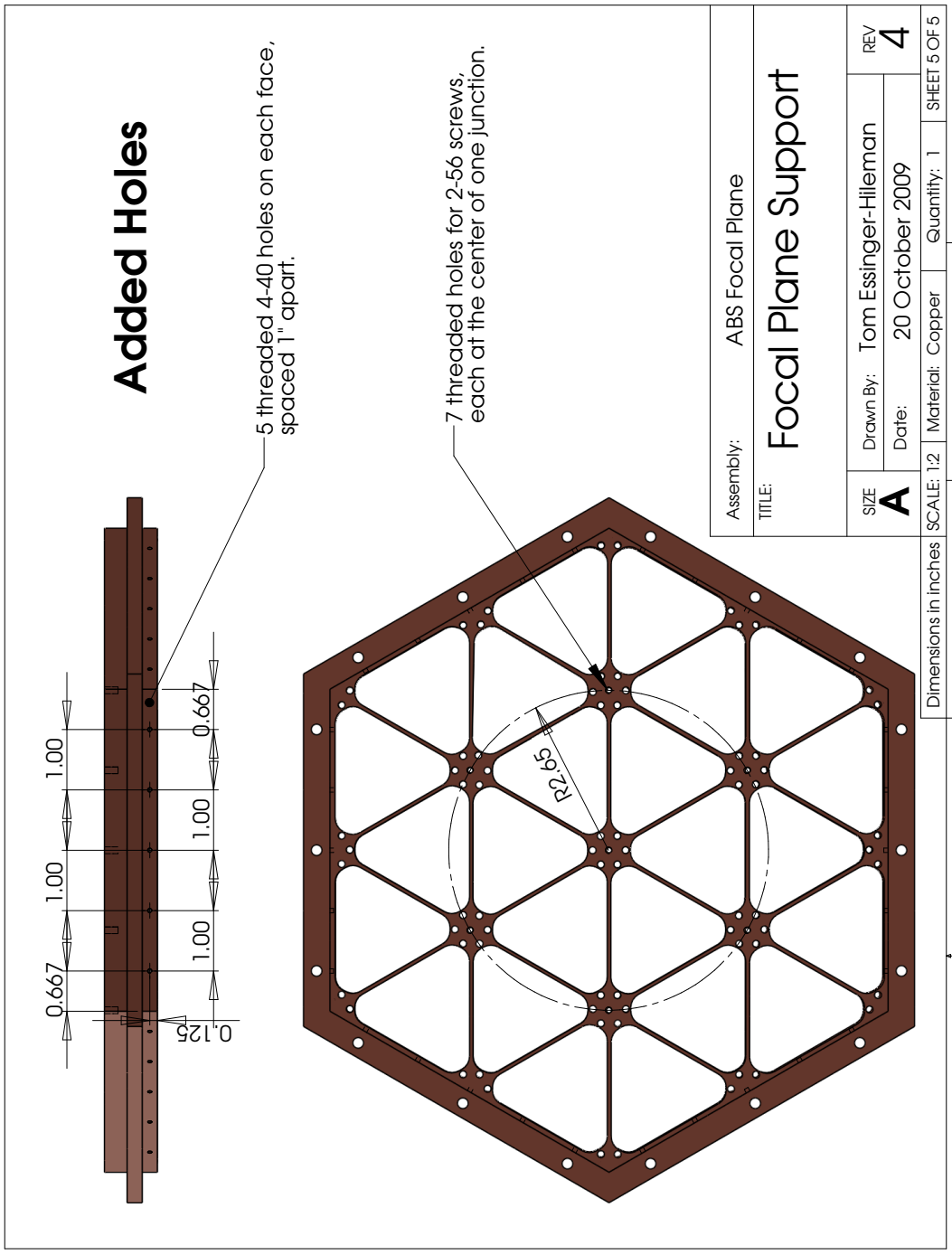
Added Holes
5 threaded 4-40 holes on each face, spaced 1" apart.
7 threaded holes for 2-56 screws, each at the center of one junction.
0.667
1.00
1.00
1.00
1.00
0.667
0.125
R2.65
Assembly: ABS Focal Plane
TITLE: Focal Plane Support
SIZE A
Drawn By: Tom Essinger-Hileman
Date: 20 October 2009
REV 4
Dimensions in inches
SCALE: 1:2
Material: Copper
Quantity: 1
SHEET 5 OF 5

Figure B.37:

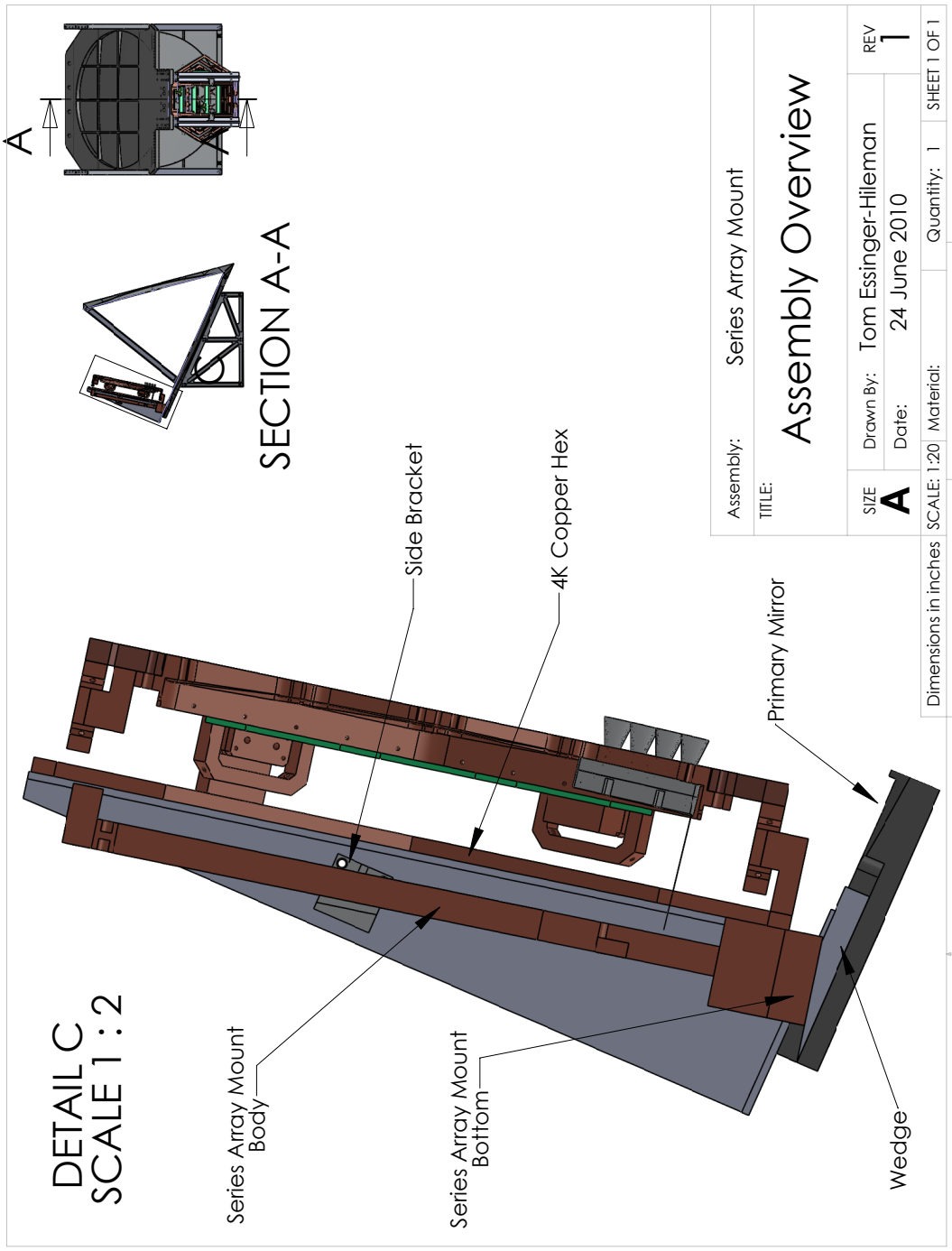
A
SECTION A-A
DETAIL C
SCALE 1 : 2
Side Bracket
4K Copper Hex
Primary Mirror
Series Array Mount Body
Series Array Mount Bottom
Wedge
Assembly: Series Array Mount
TITLE: Assembly Overview
SIZE A
Drawn By: Tom Essinger-Hileman
Date: 24 June 2010
REV 1
Dimensions in inches
SCALE: 1:20
Material:
Quantity: 1
SHEET 1 OF 1

Figure B.38:

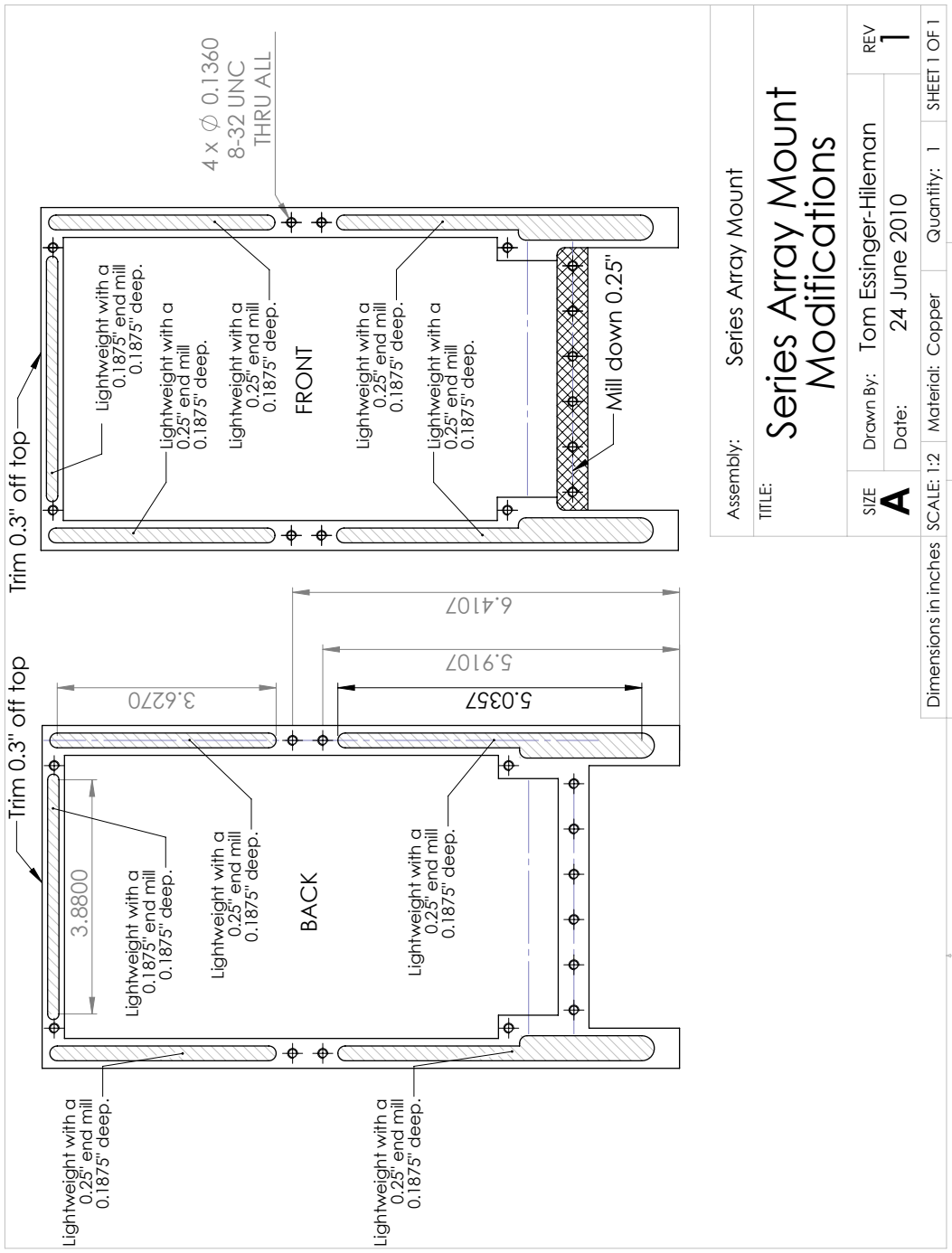
Trim 0.3" off top
Lightweight with a 0.25" end mill 0.1875" deep.
Lightweight with a 0.1875" end mill 0.1875" deep.
Lightweight with a 0.25" end mill 0.1875" deep.
FRONT
Lightweight with a 0.25" end mill 0.1875" deep.
Lightweight with a 0.25" end mill 0.1875" deep.
4 x ∅ 0.1360 8-32 UNC THRU ALL
Mill down 0.25"
Trim 0.3" off top
6.4107
5.9107
5.0357
3.6270
3.8800
Lightweight with a 0.25" end mill 0.1875" deep.
Lightweight with a 0.1875" end mill 0.1875" deep.
Lightweight with a 0.25" end mill 0.1875" deep.
BACK
Lightweight with a 0.25" end mill 0.1875" deep.
Lightweight with a 0.25" end mill 0.1875" deep.
Assembly: Series Array Mount
TITLE: Series Array Mount Modifications
SIZE A
Drawn By: Tom Essinger-Hileman
Date: 24 June 2010
REV 1
Dimensions in inches
SCALE: 1:2
Material: Copper
Quantity: 1
SHEET 1 OF 1

Figure B.39:

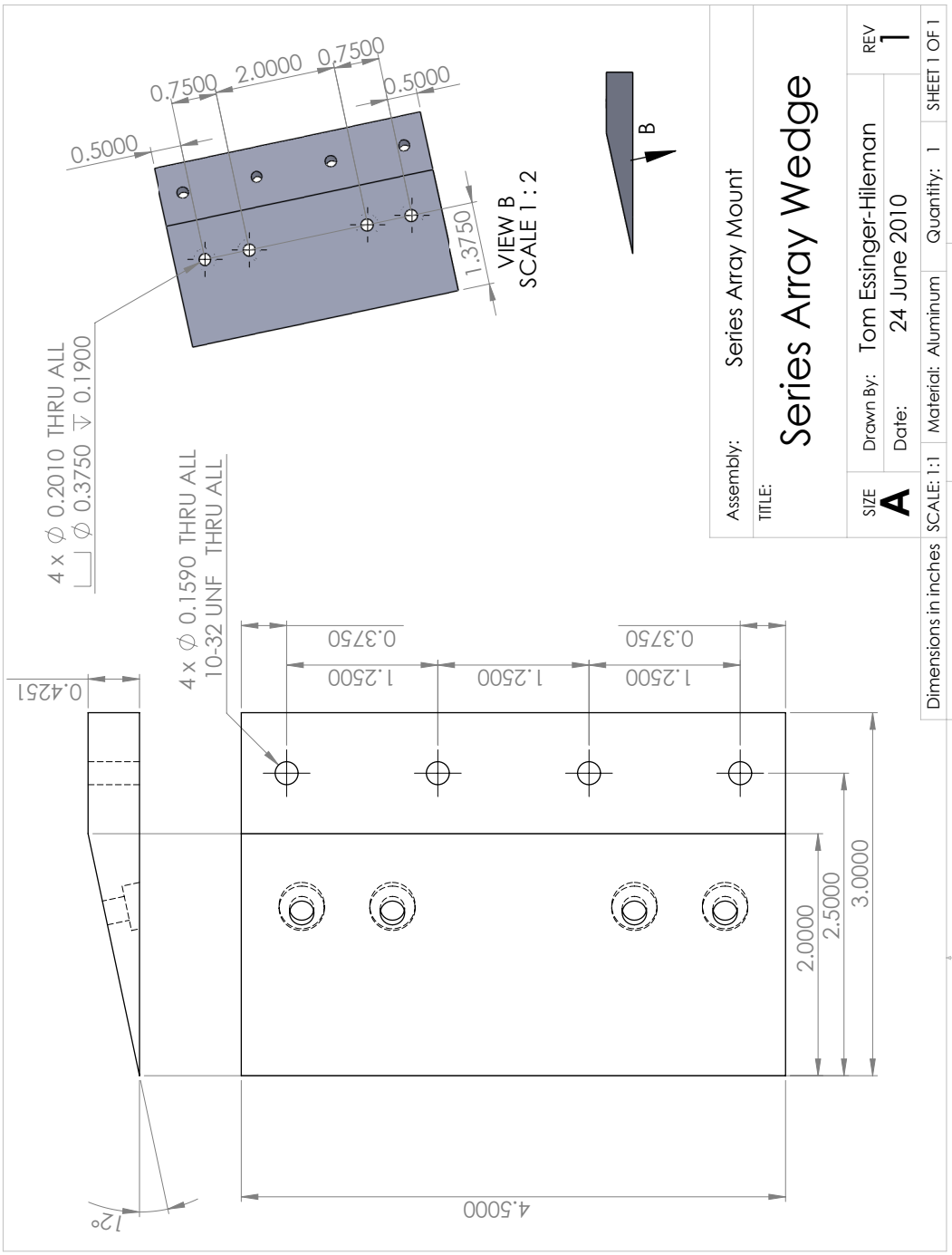
0.5000
0.7500
2.0000
0.7500
0.5000
1.3750
VIEW B
SCALE 1 : 2
B
4 x ⌀ 0.2010 THRU ALL
⌴ ⌀ 0.3750 ▽ 0.1900
4 x ⌀ 0.1590 THRU ALL
10-32 UNF THRU ALL
0.4251
0.3750
1.2500
1.2500
1.2500
0.3750
2.0000
2.5000
3.0000
4.5000
12°
Assembly: Series Array Mount
TITLE: Series Array Wedge
SIZE A
Drawn By: Tom Essinger-Hileman
Date: 24 June 2010
REV 1
Dimensions in inches
SCALE: 1:1
Material: Aluminum
Quantity: 1
SHEET 1 OF 1

Figure B.40:

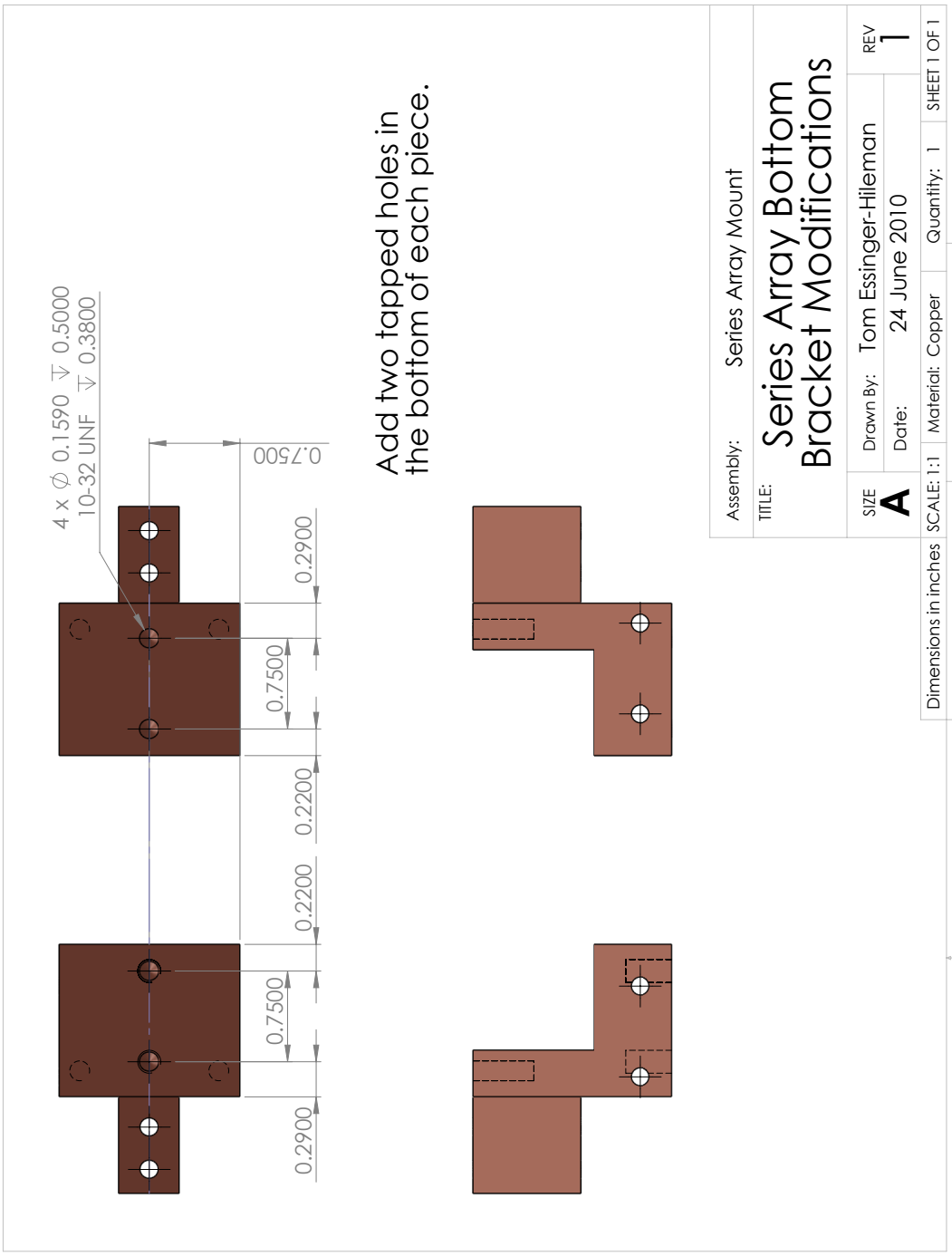
4 x ⌀ 0.1590 ⩛ 0.5000
10-32 UNF ⩛ 0.3800
0.7500
0.2900
0.7500
0.2200
0.2200
0.7500
0.2900
Add two tapped holes in
the bottom of each piece.
Assembly: Series Array Mount
TITLE: Series Array Bottom Bracket Modifications
SIZE A
Drawn By: Tom Essinger-Hileman
Date: 24 June 2010
REV 1
Dimensions in inches
SCALE: 1:1
Material: Copper
Quantity: 1
SHEET 1 OF 1

Figure B.41:

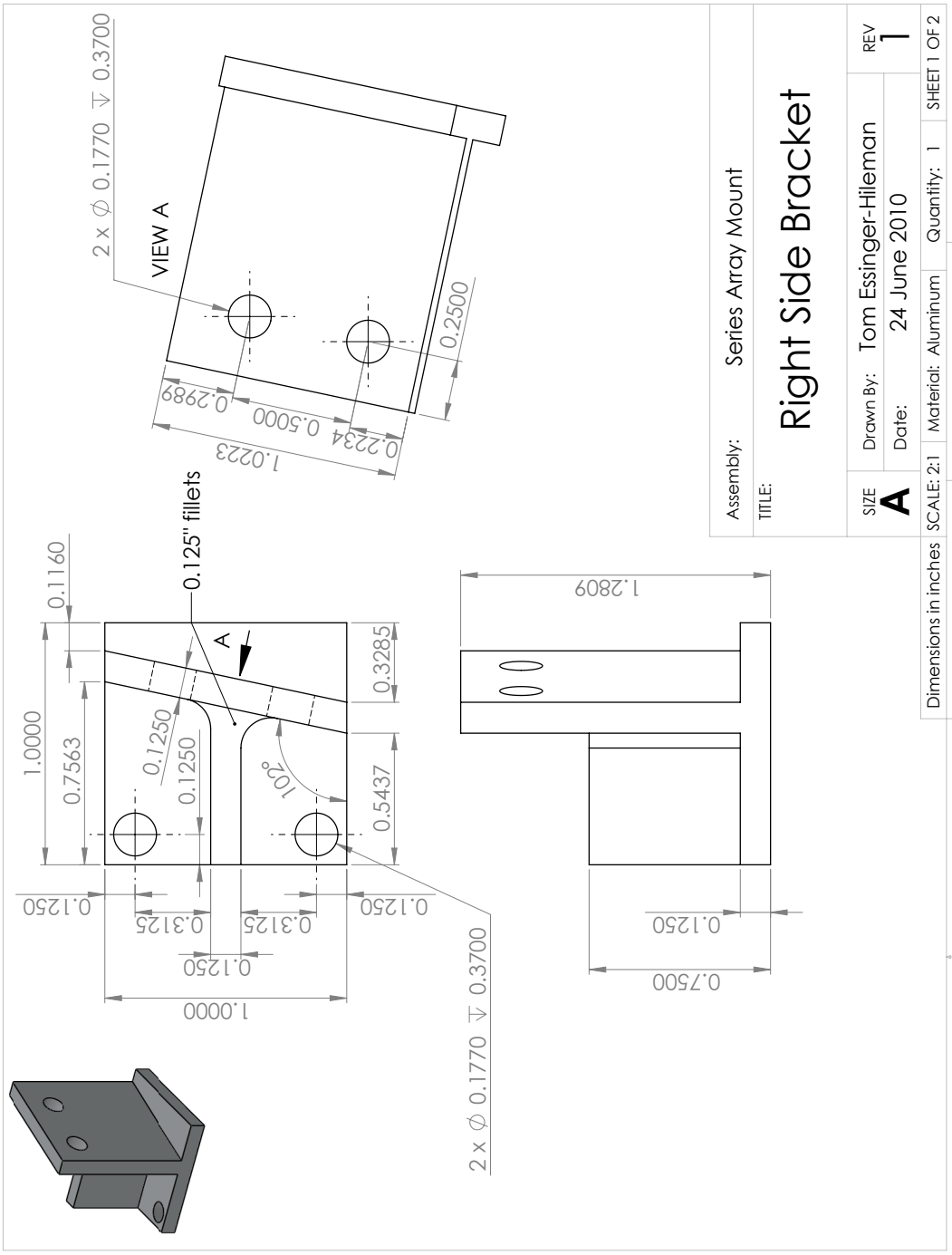
2 x ⌀ 0.1770 ⌯ 0.3700
VIEW A
0.2500
0.2989
0.5000
0.2234
1.0223
0.125" fillets
A
0.1160
1.0000
0.7563
0.1250
0.1250
0.3285
0.5437
20°
0.1250
0.3125
0.3125
0.1250
1.0000
2 x ⌀ 0.1770 ⌯ 0.3700
1.2809
0.1250
0.7500
Assembly: Series Array Mount
TITLE: Right Side Bracket
SIZE A
Drawn By: Tom Essinger-Hileman
Date: 24 June 2010
REV 1
Dimensions in inches
SCALE: 2:1
Material: Aluminum
Quantity: 1
SHEET 1 OF 2

Figure B.42:

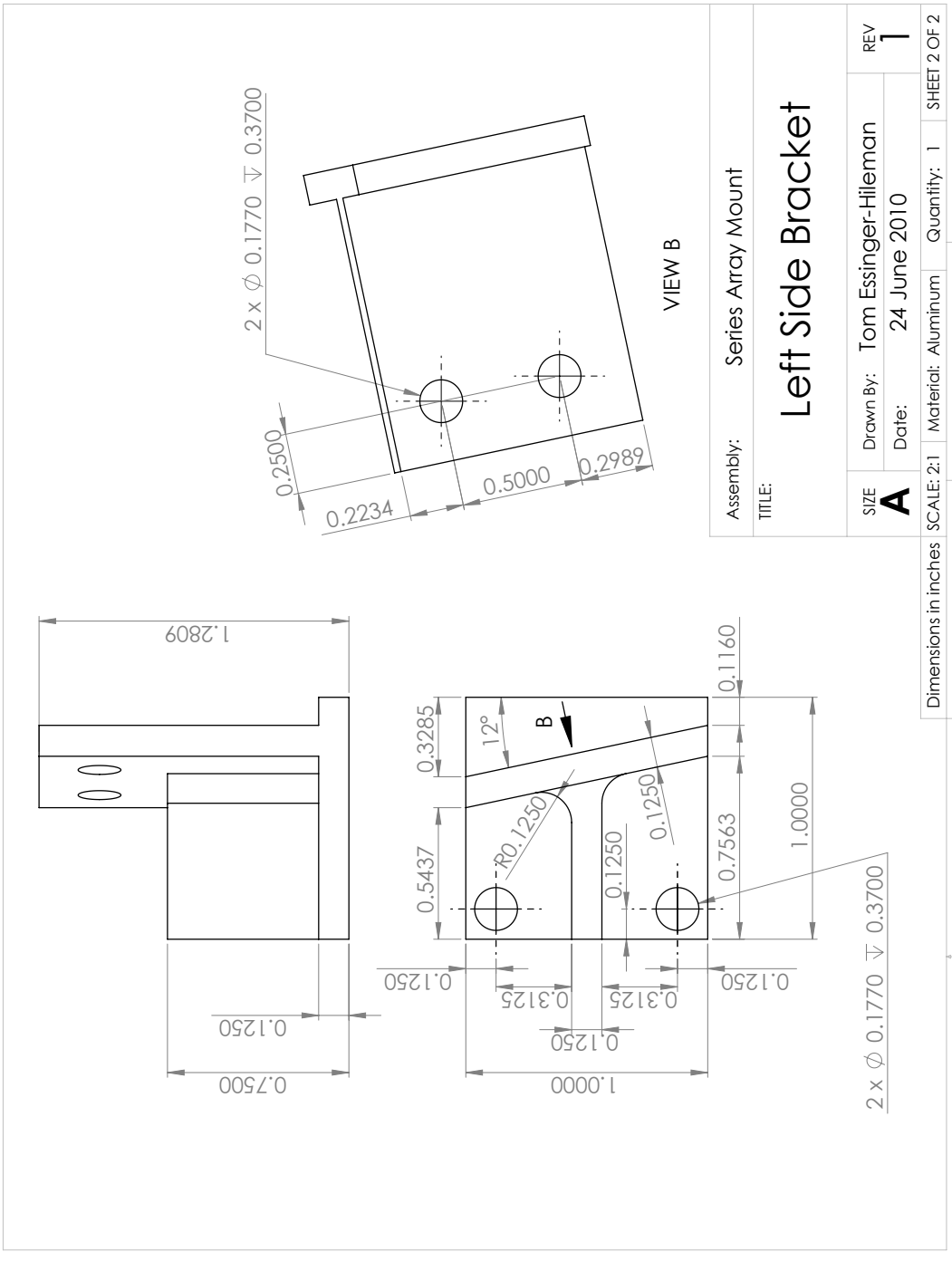
2 x ⌀ 0.1770 ⌵ 0.3700
0.2500
0.2234
0.5000
0.2989
VIEW B
Assembly: Series Array Mount
TITLE: Left Side Bracket
SIZE A
Drawn By: Tom Essinger-Hileman
Date: 24 June 2010
REV 1
Dimensions in inches
SCALE: 2:1
Material: Aluminum
Quantity: 1
SHEET 2 OF 2
1.2809
0.1250
0.7500
0.3285
12°
B
0.1160
0.5437
R0.1250
0.1250
0.1250
0.7563
1.0000
0.1250
0.3125
0.3125
0.1250
1.0000
2 x ⌀ 0.1770 ⌵ 0.3700

Figure B.43:

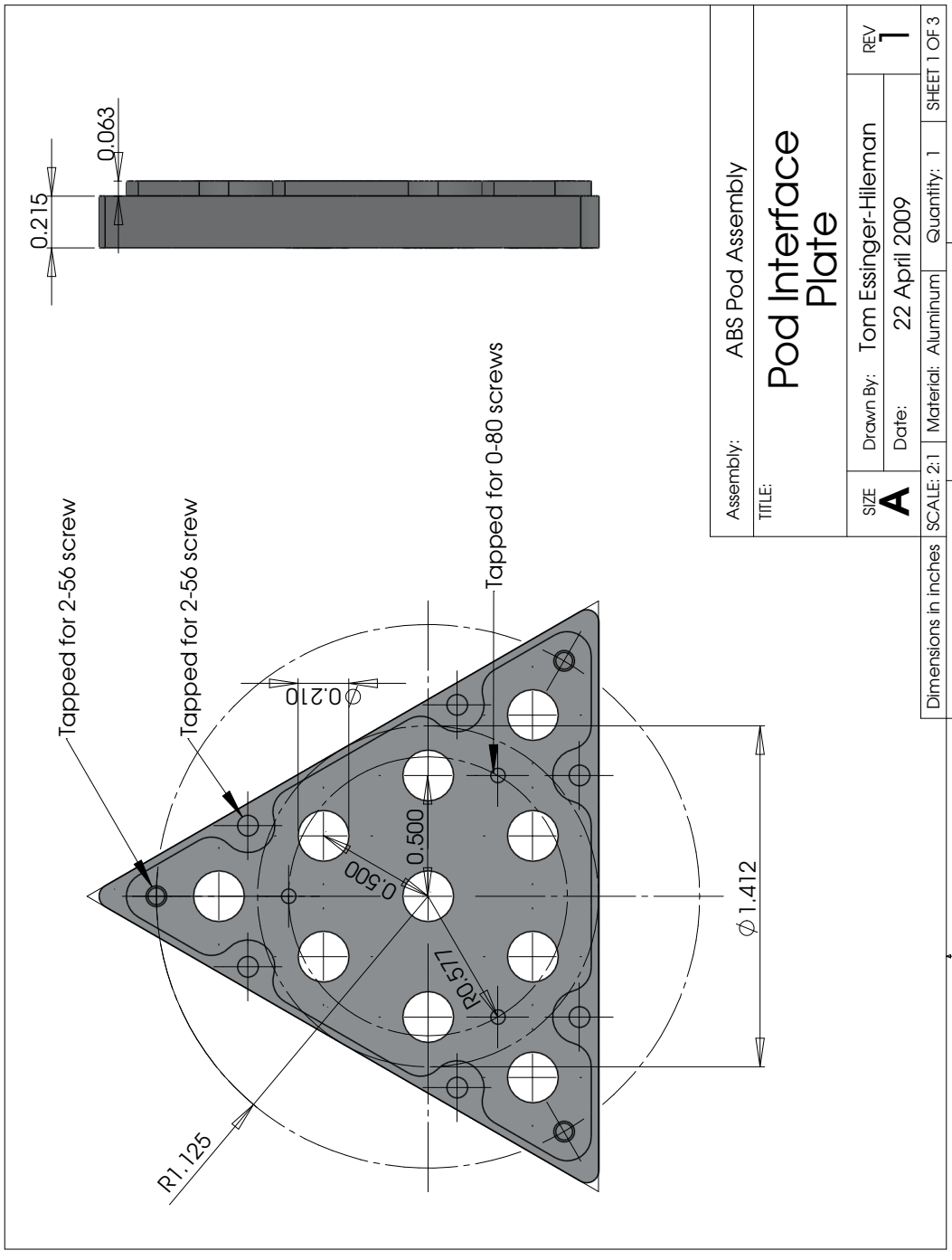
0.063
0.215
Tapped for 2-56 screw
Tapped for 2-56 screw
Tapped for 0-80 screws
∅0.210
0.500
0.500
R0.577
∅1.412
R1.125
Assembly: ABS Pod Assembly
TITLE: Pod Interface Plate
SIZE A
Drawn By: Tom Essinger-Hileman
Date: 22 April 2009
REV 1
Dimensions in inches
SCALE: 2:1
Material: Aluminum
Quantity: 1
SHEET 1 OF 3

Figure B.44:

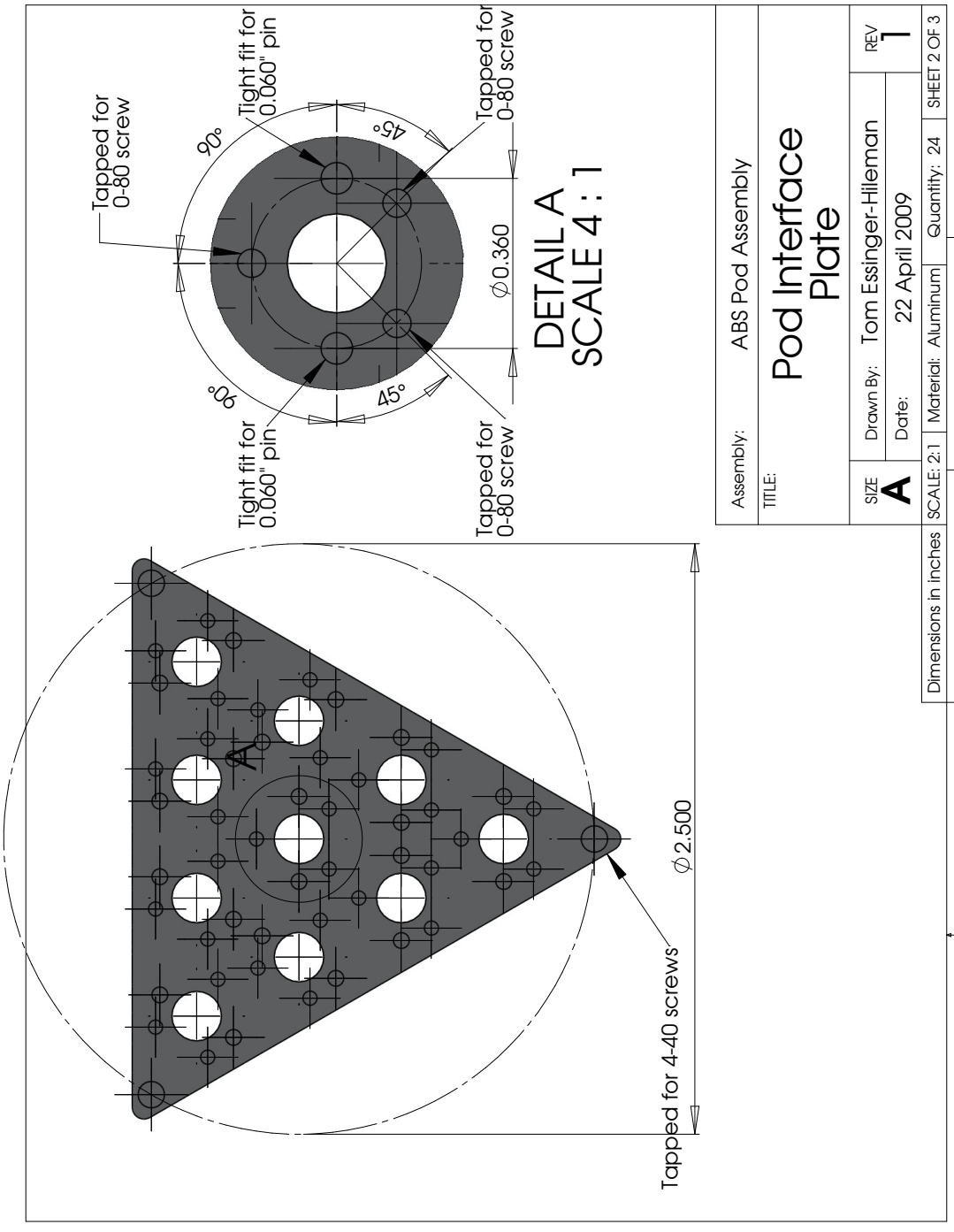
Tapped for 0-80 screw
Tight fit for 0.060" pin
90°
45°
ϕ0.360
DETAIL A
SCALE 4 : 1
Tapped for 0-80 screw
Tight fit for 0.060" pin
Tapped for 0-80 screw
A
ϕ2.500
Tapped for 4-40 screws
Assembly: ABS Pod Assembly
TITLE: Pod Interface Plate
SIZE A
Drawn By: Tom Essinger-Hileman
Date: 22 April 2009
REV 1
Dimensions in inches
SCALE: 2:1
Material: Aluminum
Quantity: 24
SHEET 2 OF 3

Figure B.45:

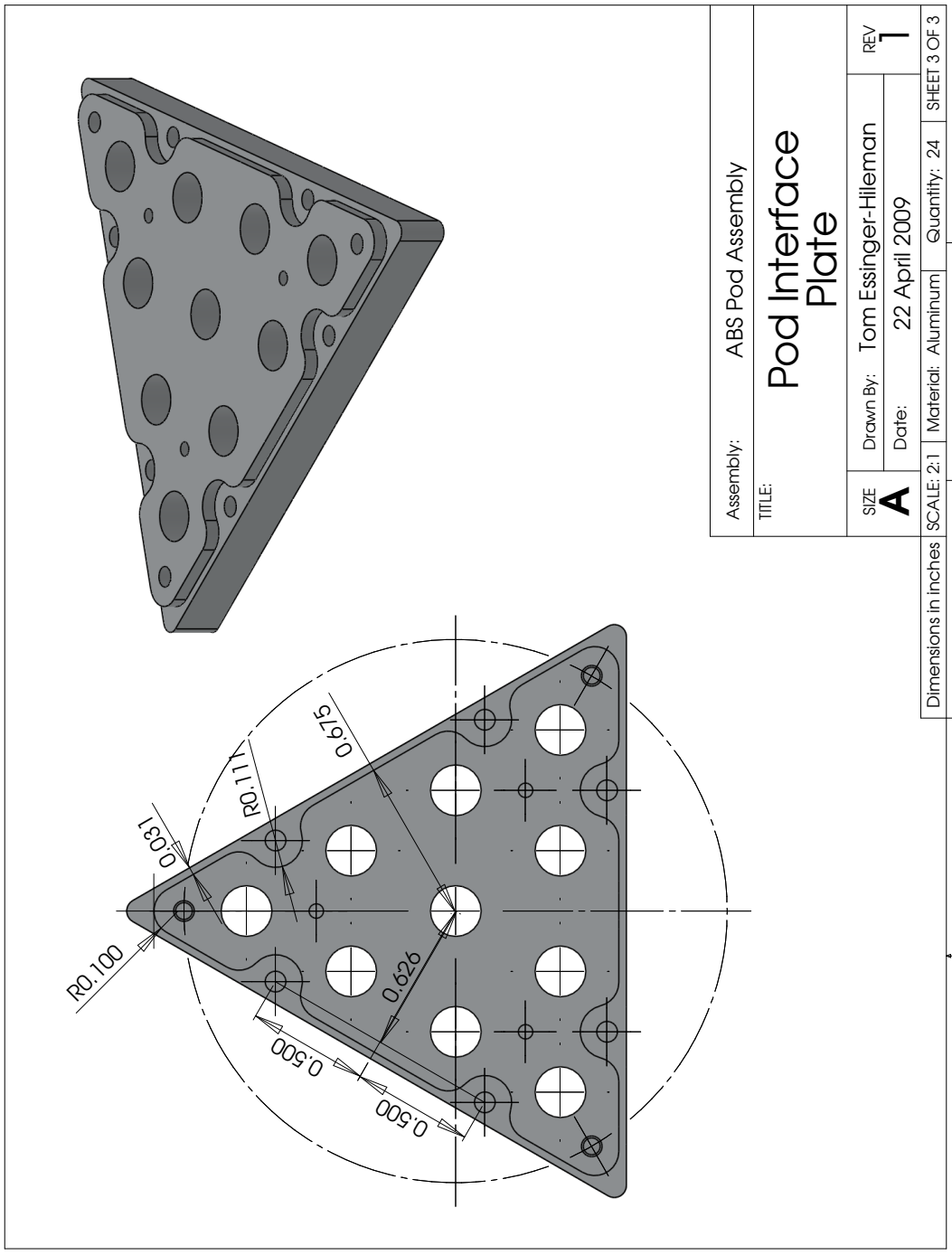
Assembly: ABS Pod Assembly
TITLE: Pod Interface Plate
SIZE A
Drawn By: Tom Essinger-Hileman
Date: 22 April 2009
REV 1
Dimensions in inches
SCALE: 2:1
Material: Aluminum
Quantity: 24
SHEET 3 OF 3
R0.100
0.031
R0.111
0.675
0.626
0.500
0.500

Figure B.46:

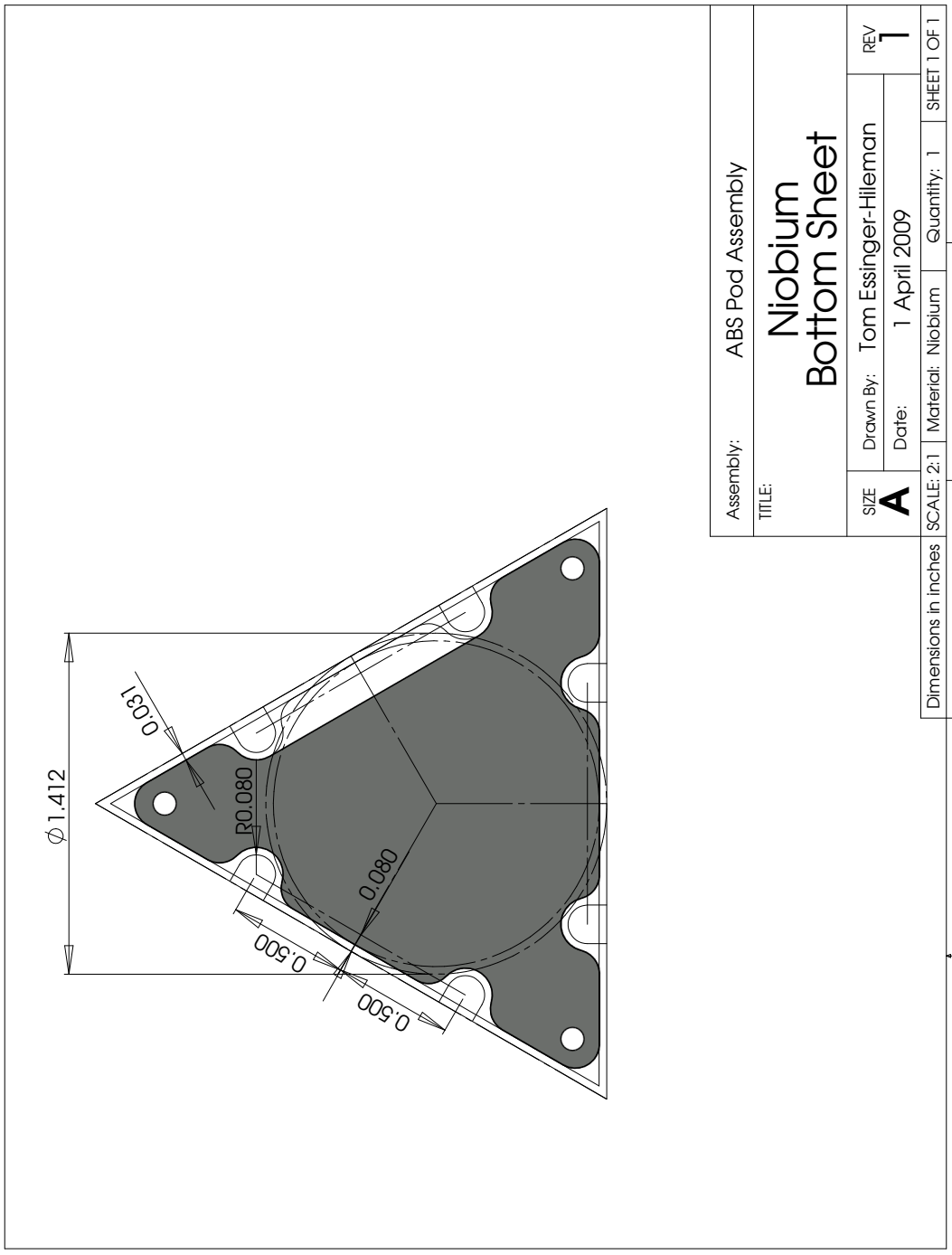
Assembly: ABS Pod Assembly
TITLE: Niobium Bottom Sheet
SIZE A
Drawn By: Tom Essinger-Hileman
Date: 1 April 2009
REV 1
Dimensions in inches
SCALE: 2:1
Material: Niobium
Quantity: 1
SHEET 1 OF 1
ϕ1.412
0.031
R0.080
0.080
0.500
0.500

Figure B.47:

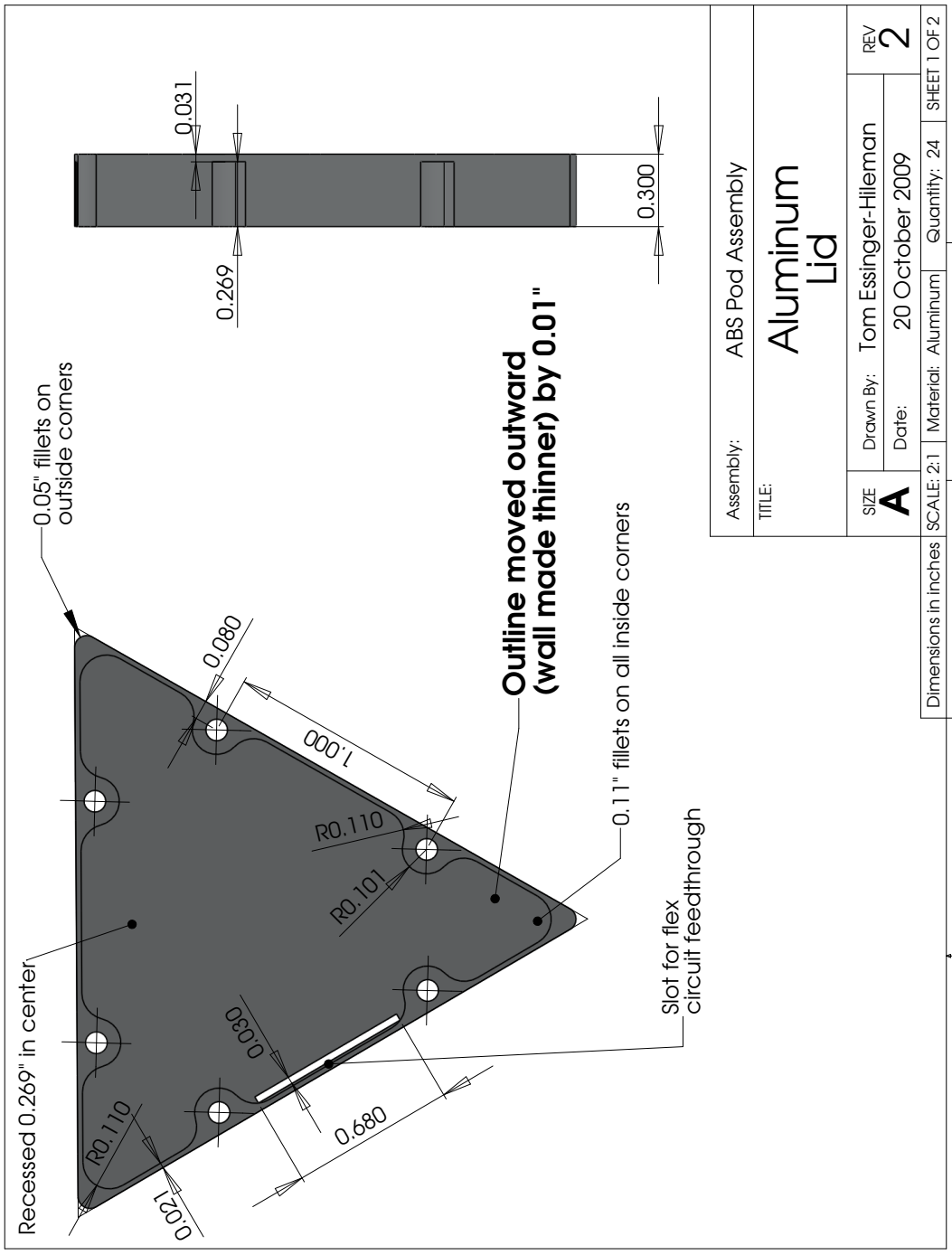
0.031
0.269
0.300
0.05" fillets on
outside corners
0.080
1.000
R0.110
R0.101
Outline moved outward
(wall made thinner) by 0.01"
0.11" fillets on all inside corners
Slot for flex
circuit feedthrough
Recessed 0.269" in center
0.090
0.680
R0.110
0.021
Assembly: ABS Pod Assembly
TITLE: Aluminum Lid
SIZE A
Drawn By: Tom Essinger-Hileman
Date: 20 October 2009
REV 2
Dimensions in inches
SCALE: 2:1
Material: Aluminum
Quantity: 24
SHEET 1 OF 2

Figure B.48:

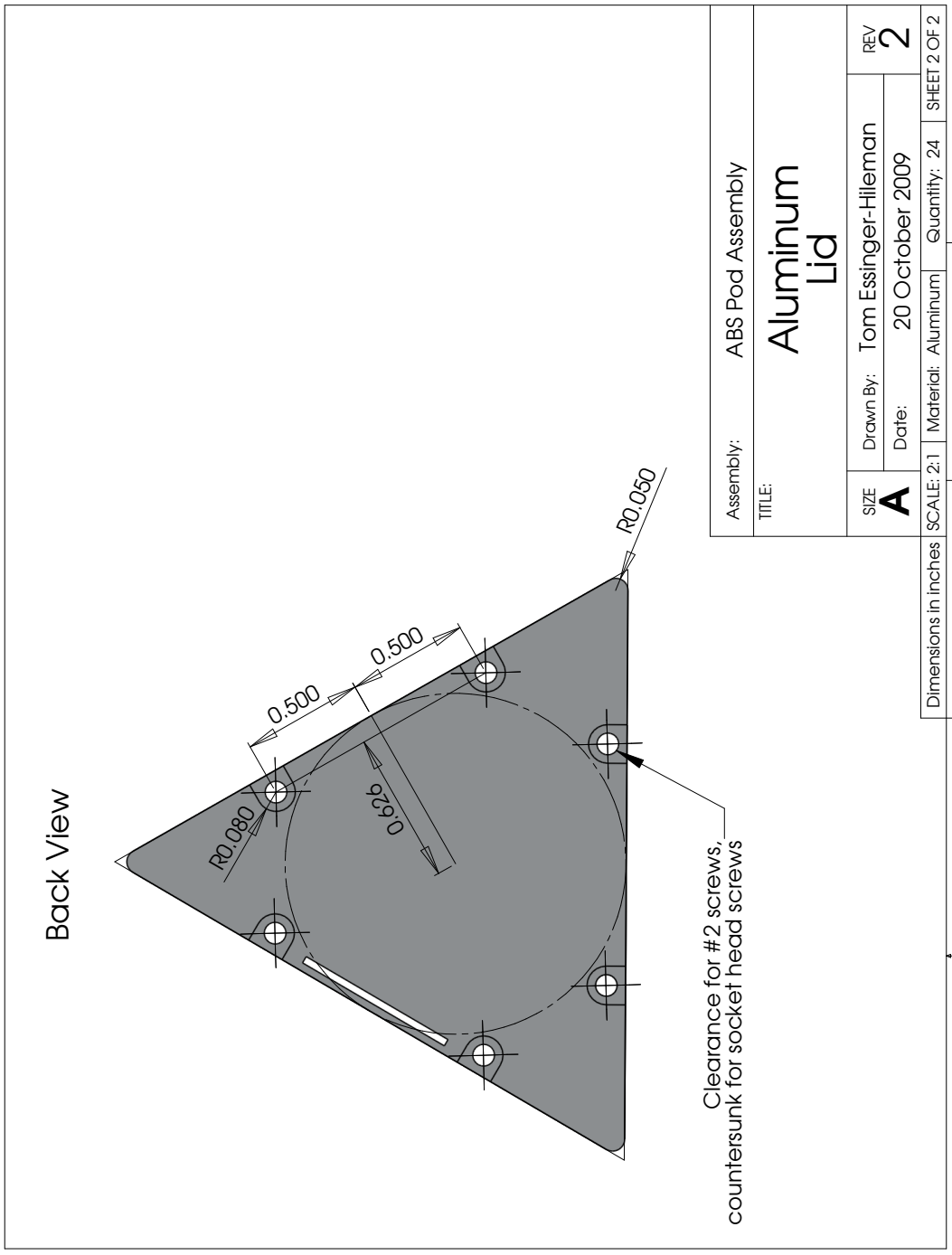
Back View
0.500
0.500
0.620
R0.080
R0.050
Clearance for #2 screws,
countersunk for socket head screws
Assembly: ABS Pod Assembly
TITLE: Aluminum Lid
SIZE A
Drawn By: Tom Essinger-Hileman
Date: 20 October 2009
REV 2
Dimensions in inches
SCALE: 2:1
Material: Aluminum
Quantity: 24
SHEET 2 OF 2

Figure B.49:

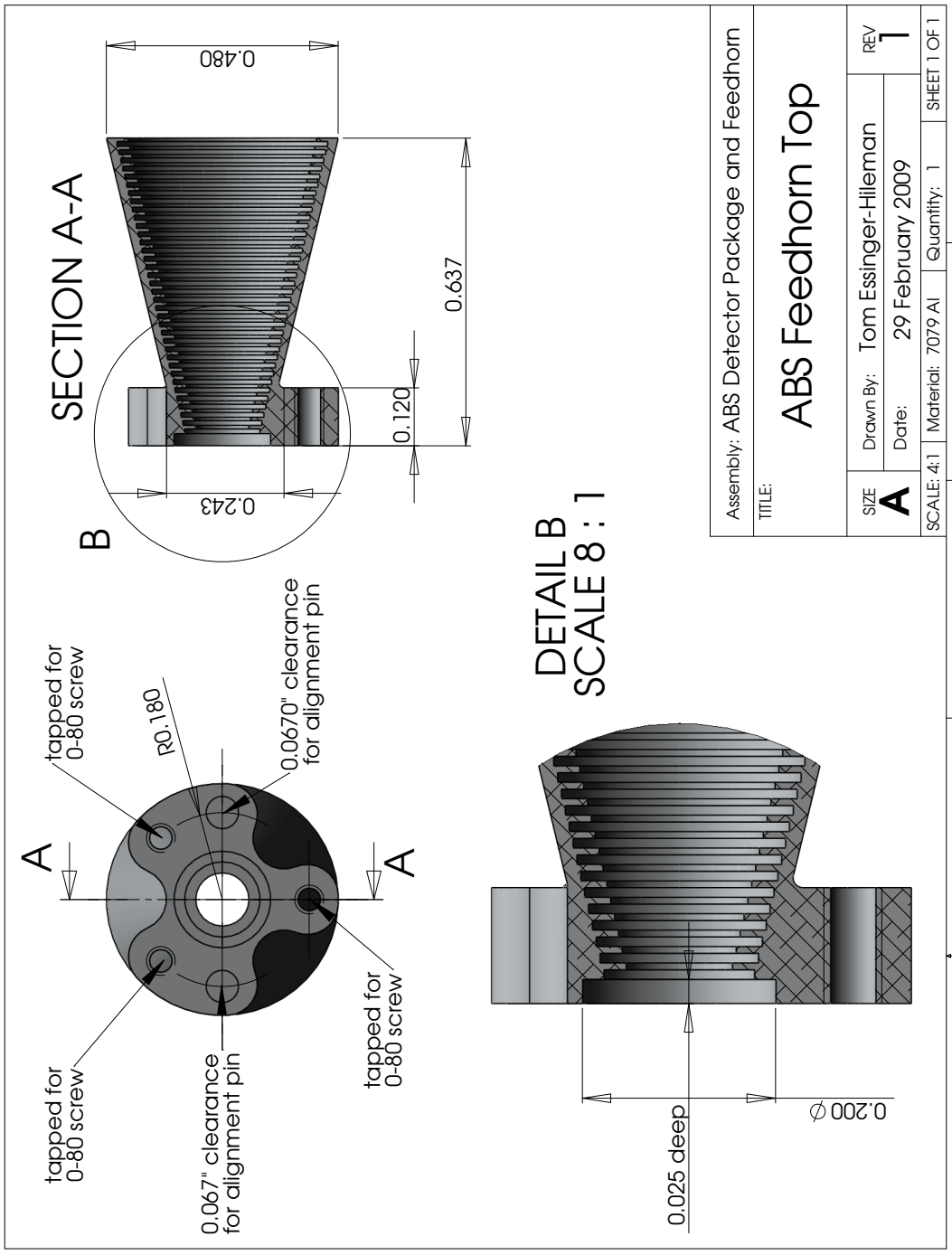
SECTION A-A
B
0.480
0.243
0.120
0.637
DETAIL B
SCALE 8 : 1
A
A
tapped for
0-80 screw
R0.180
0.0670" clearance
for alignment pin
tapped for
0-80 screw
0.067" clearance
for alignment pin
tapped for
0-80 screw
0.025 deep
0.200⌀
Assembly: ABS Detector Package and Feedhorn
TITLE:
ABS Feedhorn Top
SIZE
A
Drawn By: Tom Essinger-Hileman
Date: 29 February 2009
REV
1
SCALE: 4:1
Material: 7079 Al
Quantity: 1
SHEET 1 OF 1

Figure B.50:

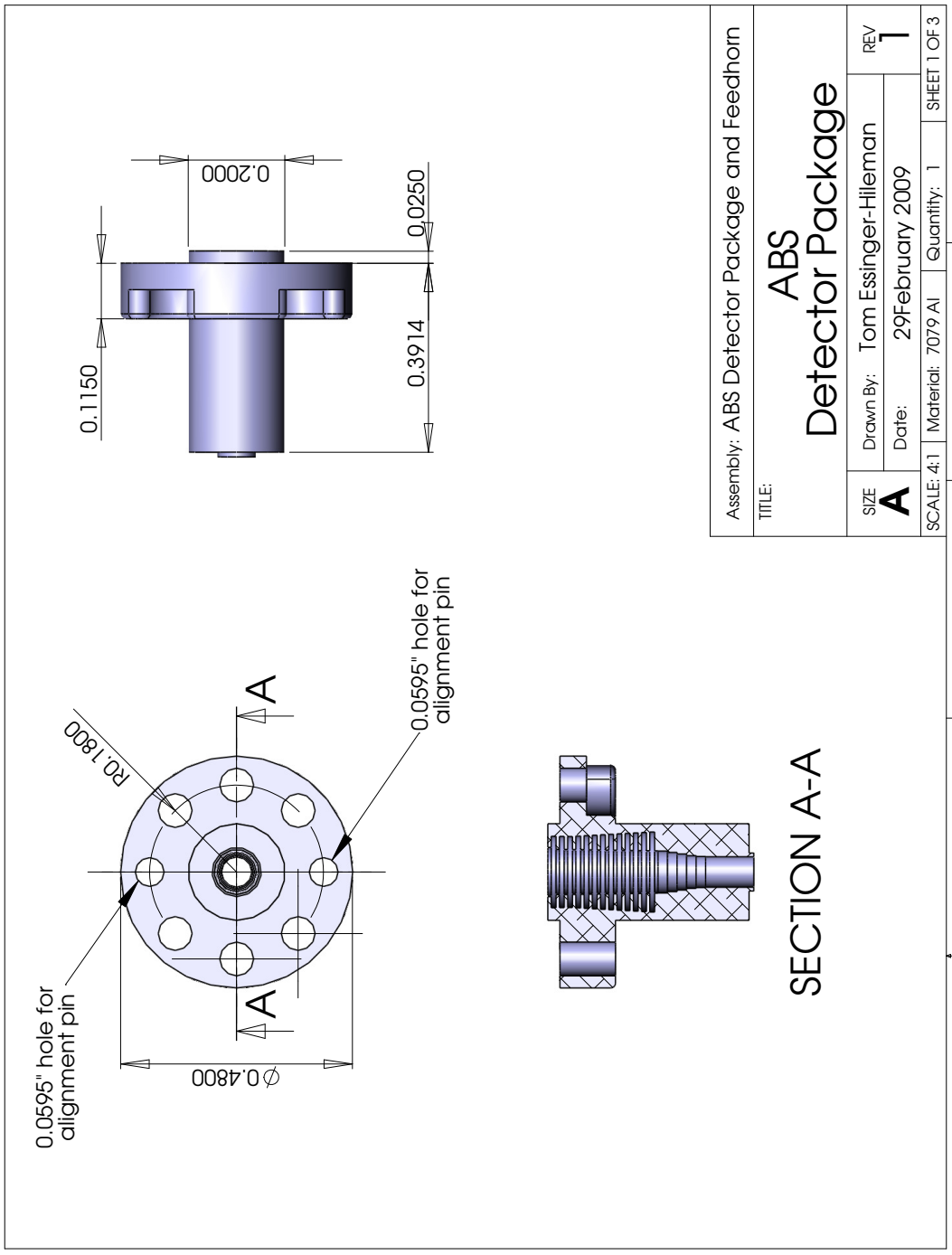
0.2000
0.0250
0.3914
0.1150
0.0595" hole for alignment pin
R0.1800
A
A
0.0595" hole for alignment pin
⌀0.4800
SECTION A-A
Assembly: ABS Detector Package and Feedhorn
TITLE:
ABS Detector Package
SIZE A
Drawn By: Tom Essinger-Hileman
Date: 29February 2009
REV 1
SCALE: 4:1
Material: 7079 Al
Quantity: 1
SHEET 1 OF 3

Figure B.51:

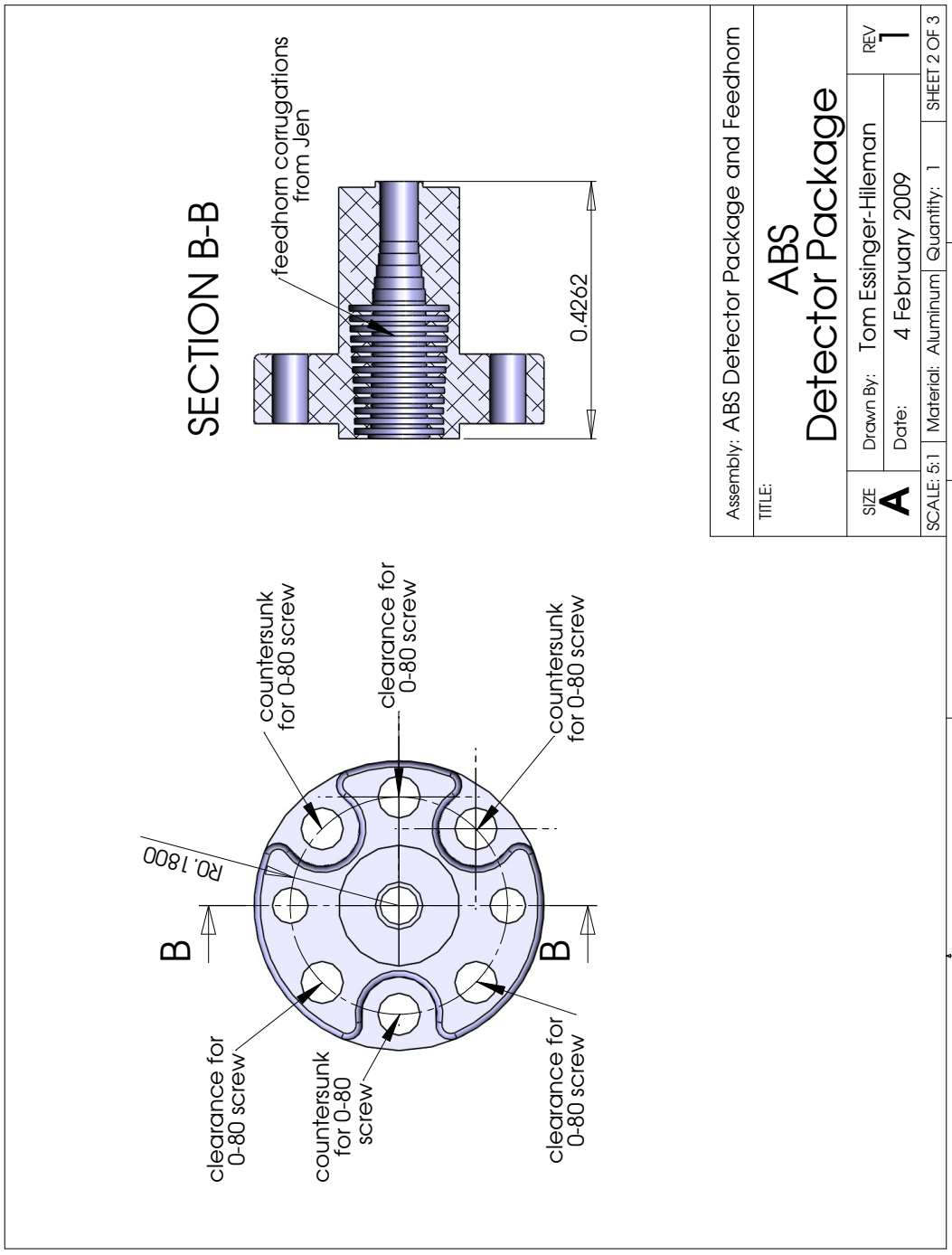
SECTION B-B
feedhorn corrugations from Jen
0.4262
countersunk for 0-80 screw
clearance for 0-80 screw
countersunk for 0-80 screw
R0.1800
B
B
clearance for 0-80 screw
countersunk for 0-80 screw
clearance for 0-80 screw
Assembly: ABS Detector Package and Feedhorn
TITLE:
ABS
Detector Package
SIZE
A
Drawn By: Tom Essinger-Hileman
Date: 4 February 2009
REV
1
SCALE: 5:1
Material: Aluminum
Quantity: 1
SHEET 2 OF 3

Figure B.52:

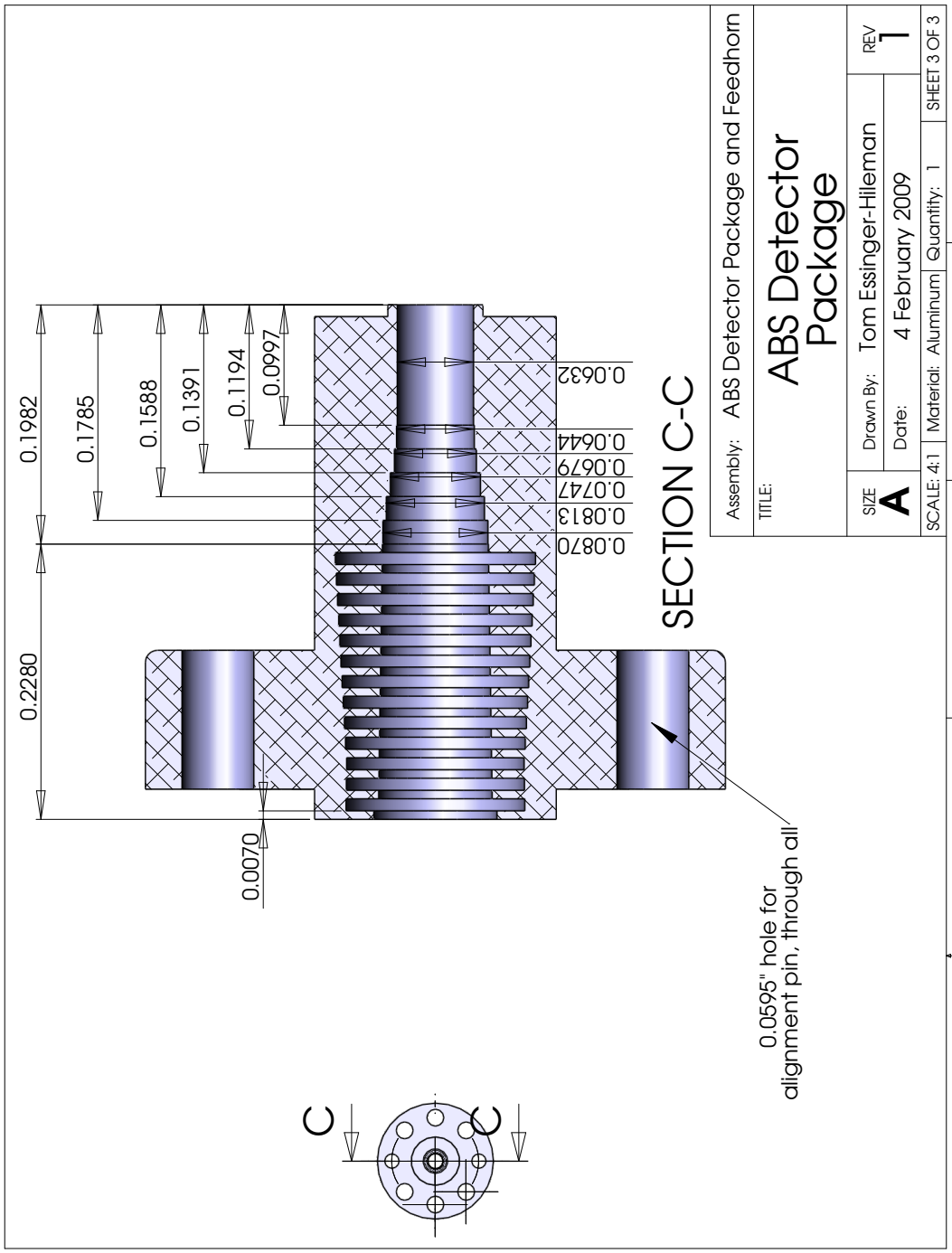
SECTION C-C
0.1982
0.1785
0.1588
0.1391
0.1194
0.0997
0.0632
0.0644
0.0679
0.0747
0.0813
0.0870
0.2280
0.0070
0.0595" hole for
alignment pin, through all
C
C
Assembly: ABS Detector Package and Feedhorn
TITLE:
ABS Detector
Package
SIZE
A
Drawn By: Tom Essinger-Hileman
Date: 4 February 2009
REV
1
SCALE: 4:1
Material: Aluminum
Quantity: 1
SHEET 3 OF 3

Figure B.53:

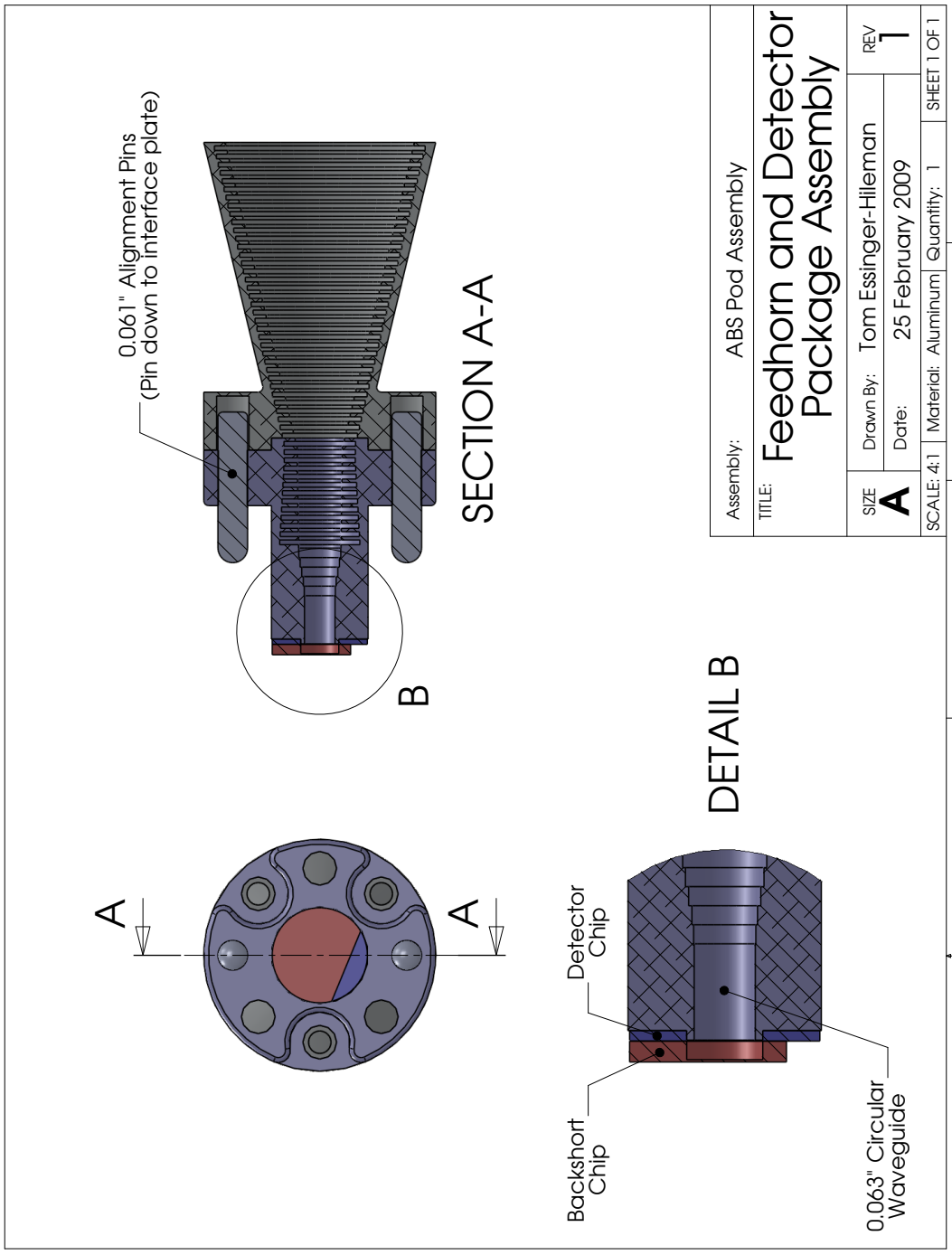
0.061" Alignment Pins
(Pin down to interface plate)
SECTION A-A
B
A
A
DETAIL B
Detector Chip
Backshort Chip
0.063" Circular Waveguide
Assembly: ABS Pod Assembly
TITLE: Feedhorn and Detector Package Assembly
SIZE A
Drawn By: Tom Essinger-Hileman
Date: 25 February 2009
REV 1
SCALE: 4:1
Material: Aluminum
Quantity: 1
SHEET 1 OF 1

Figure B.54:

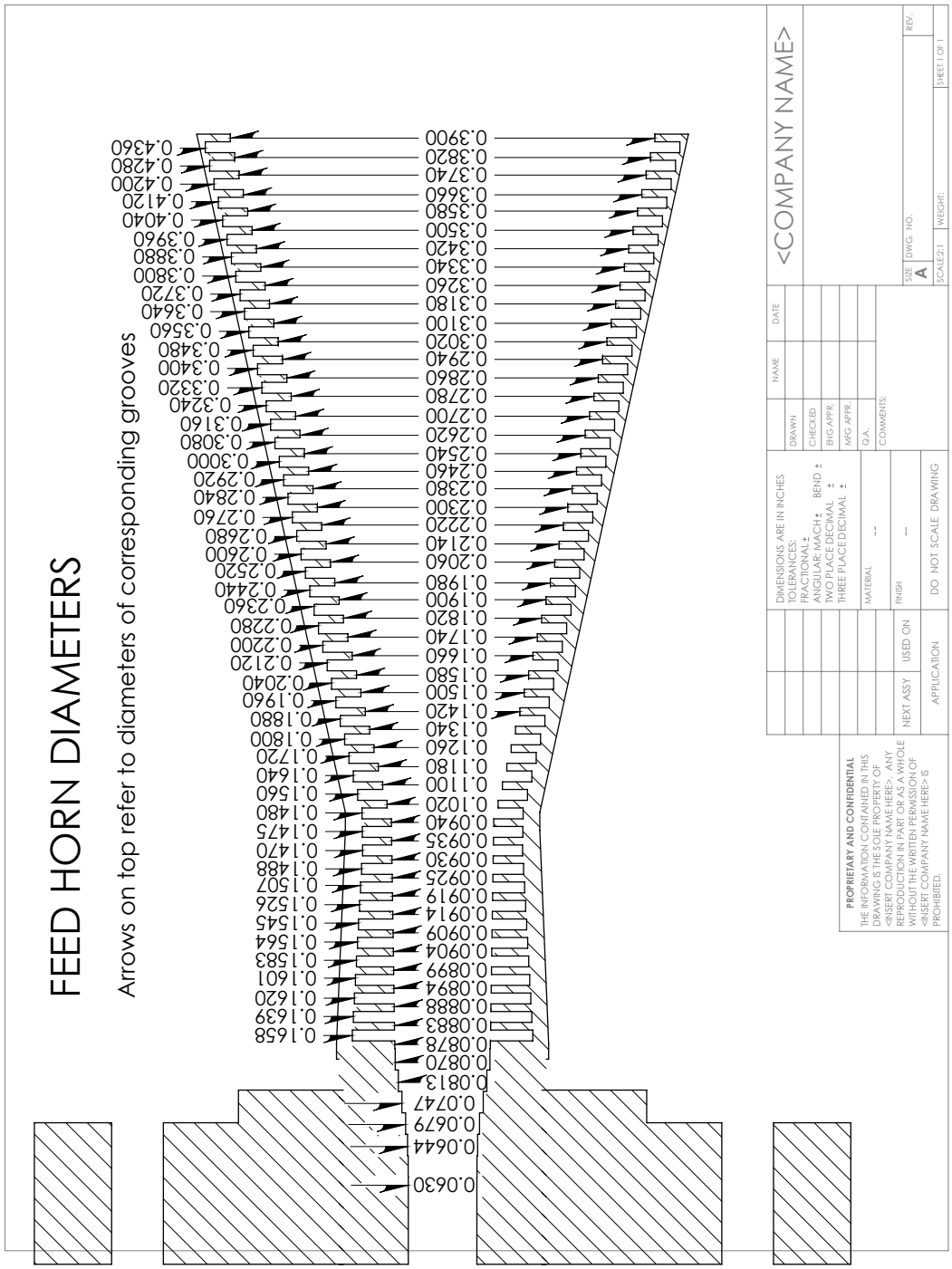
FEED HORN DIAMETERS
Arrows on top refer to diameters of corresponding grooves
0.0630
0.0644
0.0679
0.0747
0.0813
0.0870
0.0878
0.0883
0.0888
0.0894
0.0899
0.0904
0.0909
0.0914
0.0919
0.0925
0.0930
0.0935
0.0940
0.1020
0.1100
0.1180
0.1260
0.1340
0.1420
0.1500
0.1580
0.1660
0.1740
0.1820
0.1900
0.1980
0.2060
0.2140
0.2220
0.2300
0.2380
0.2460
0.2540
0.2620
0.2700
0.2780
0.2860
0.2940
0.3020
0.3100
0.3180
0.3260
0.3340
0.3420
0.3500
0.3580
0.3660
0.3740
0.3820
0.3900
0.1658
0.1639
0.1620
0.1601
0.1583
0.1564
0.1545
0.1526
0.1507
0.1488
0.1470
0.1475
0.1480
0.1560
0.1640
0.1720
0.1800
0.1880
0.1960
0.2040
0.2120
0.2200
0.2280
0.2360
0.2440
0.2520
0.2600
0.2680
0.2760
0.2840
0.2920
0.3000
0.3080
0.3160
0.3240
0.3320
0.3400
0.3480
0.3560
0.3640
0.3720
0.3800
0.3880
0.3960
0.4040
0.4120
0.4200
0.4280
0.4360
PROPRIETARY AND CONFIDENTIAL
THE INFORMATION CONTAINED IN THIS DRAWING IS THE SOLE PROPERTY OF <INSERT COMPANY NAME HERE>. ANY REPRODUCTION IN PART OR AS A WHOLE WITHOUT THE WRITTEN PERMISSION OF <INSERT COMPANY NAME HERE> IS PROHIBITED.
NEXT ASSY
USED ON
APPLICATION
DO NOT SCALE DRAWING
MATERIAL
FINISH
DIMENSIONS ARE IN INCHES
TOLERANCES:
FRACTIONAL ±
ANGULAR: MACH ± BEND ±
TWO PLACE DECIMAL ±
THREE PLACE DECIMAL ±
DRAWN
CHECKED
ENG APPR.
MFG APPR.
Q.A.
COMMENTS:
NAME
DATE
<COMPANY NAME>
SIZE
A
DWG. NO.
REV.
SCALE:2:1
WEIGHT:
SHEET 1 OF 1

Figure B.55:

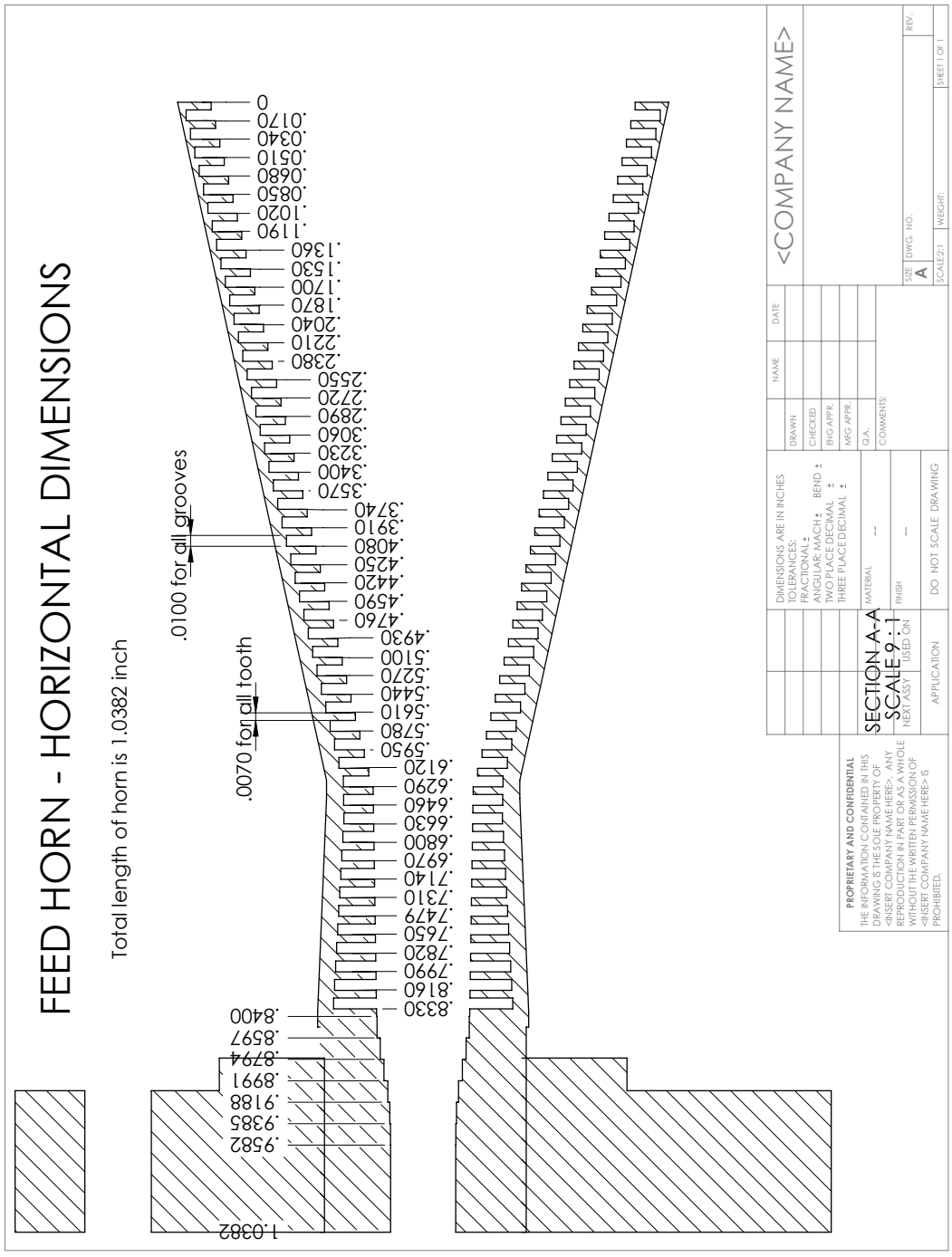
FEED HORN - HORIZONTAL DIMENSIONS
Total length of horn is 1.0382 inch
.0100 for all grooves
.0070 for all tooth
0
.0170
.0340
.0510
.0680
.0850
.1020
.1190
.1360
.1530
.1700
.1870
.2040
.2210
.2380
.2550
.2720
.2890
.3060
.3230
.3400
.3570
.3740
.3910
.4080
.4250
.4420
.4590
.4760
.4930
.5100
.5270
.5440
.5610
.5780
.5950
.6120
.6290
.6460
.6630
.6800
.6970
.7140
.7310
.7479
.7650
.7820
.7990
.8160
.8330
.8400
.8597
.8794
.8991
.9188
.9385
.9582
1.0382
SECTION A-A
SCALE 9 : 1
PROPRIETARY AND CONFIDENTIAL
THE INFORMATION CONTAINED IN THIS DRAWING IS THE SOLE PROPERTY OF <INSERT COMPANY NAME HERE>. ANY REPRODUCTION IN PART OR AS A WHOLE WITHOUT THE WRITTEN PERMISSION OF <INSERT COMPANY NAME HERE> IS PROHIBITED.
MATERIAL --
FINISH --
NEXT ASSY USED ON
APPLICATION
DO NOT SCALE DRAWING
DIMENSIONS ARE IN INCHES
TOLERANCES:
FRACTIONAL ±
ANGULAR: MACH ± BEND ±
TWO PLACE DECIMAL ±
THREE PLACE DECIMAL ±
NAME
DATE
DRAWN
CHECKED
ENG APPR.
MFG APPR.
Q.A.
COMMENTS:
<COMPANY NAME>
SIZE A
DWG. NO.
REV.
SCALE:2:1
WEIGHT:
SHEET 1 OF 1

Figure B.56:

Addendum: Atacama Cosmology Telescope

In addition to the research with the Atacama B-Mode Search (ABS) described in this thesis, I spent considerable time working with the Atacama Cosmology Telescope (ACT) early in my graduate career. ACT is a 6-meter off-axis Gregorian telescope which was built to extend our knowledge of the high-ℓ Cosmic Microwave Background (CMB) temperature anisotropies. ACT has successfully measured the CMB temperature anisotropies out to an ℓ of 8000 [30, 18] and tightened constraints on the tilt of the primordial spectrum and the tensor-to-scalar ratio, as well as other cosmological parameters [26]. The high angular resolution of the ACT telescope has also facilitated the study of galaxy clusters through their Sunyaev-Zel'dovich (SZ) effect on the CMB [38, 63] and allowed the first measurement of the lensing of the CMB by large scale structure [19, 85].

I helped test and build the three detector arrays for ACT, which had bandpasses centered at 148, 218, and 280 GHz. The receiver that housed these three arrays observed at a high-altitude site in the Chilean Andes from October 2007 through January 2011. I was responsible for fabricating many of the aluminum-on-silicon readout cards for the ACT detectors. I also fabricated silicon coupling layers for the three arrays, which were thin silicon membranes that were 50, 40, and 25 μm thick for the 148, 218, and 280 GHz arrays. I made them from silicon-on-insulator (SOI) wafers by reactive-ion etching (RIE) of the handle wafer, followed by a deep potassium-hydroxide etch at an elevated temperature of 40°C.

I made four trips to work on ACT in Chile. While there, I was part of the team that mapped the primary and secondary reflectors and aligned them within 25 μm of their ideal positions. This was a particular challenge for the primary reflector, which consisted of 72 aluminum panels over a 6-meter diameter area. Each panel had four alignment screws. A laser-ranging system was used to map the positions of the mirrors by placing a corner cube mounted to a pole on each of the corners of the 72 panels. Because the ACT reflectors change shape when the sun is out during the day, this work had to be performed at night. During my work with ACT in Chile, I also maintained the observing site, including maintenance of the electrical generators, cryogenic system, telescope motion, and data acquisition systems.

References

[1] P. A. R. Ade, G. Pisano, C. Tucker, and S. Weaver. A review of metal mesh filters. In *Society of Photo-Optical Instrumentation Engineers (SPIE) Conference Series*, volume 6275 of *Society of Photo-Optical Instrumentation Engineers (SPIE) Conference Series*, July 2006.

[2] J. A. Arnaud and F. A. Pelow. Resonant-grid quasi-optical diplexers. *AT T Technical Journal*, 54:263–283, Feb. 1975.

[3] D. J. Benford, M. C. Gaidis, and J. W. Kooi. Optical properties of Zitex in the infrared to submillimeter. Appl. Opt., 42:5118–5122, Sept. 2003.

[4] D. J. Benford, S. H. Moseley, G. J. Stacey, R. A. Shafer, and J. G. Staguhn. Far-infrared imaging spectroscopy with SAFIRE on SOFIA. In R. K. Melugin & H.-P. Roeser, editor, *Society of Photo-Optical Instrumentation Engineers (SPIE) Conference Series*, volume 4857 of *Society of Photo-Optical Instrumentation Engineers (SPIE) Conference Series*, pages 105–114, Feb. 2003.

[5] C. L. Bennett, A. J. Banday, K. M. Gorski, G. Hinshaw, P. Jackson, P. Keegstra, A. Kogut, G. F. Smoot, D. T. Wilkinson, and E. L. Wright. Four-Year COBE DMR Cosmic Microwave Background Observations: Maps and Basic Results. ApJ, 464:L1+, June 1996.

[6] C. L. Bennett, N. W. Boggess, E. S. Cheng, M. G. Hauser, T. Kelsall, J. C. Mather, S. H. Moseley, Jr., T. L. Murdock, R. A. Shafer, and R. F. Silverberg. Scientific results from COBE. *Advances in Space Research*, 13:409–, Dec. 1993.

[7] C. L. Bennett, M. Halpern, G. Hinshaw, N. Jarosik, A. Kogut, M. Limon, S. S. Meyer, L. Page, D. N. Spergel, G. S. Tucker, E. Wollack, E. L. Wright, C. Barnes, M. R. Greason, R. S. Hill, E. Komatsu, M. R. Nolta, N. Odegard, H. V. Peiris, L. Verde, and J. L. Weiland. First-Year Wilkinson Microwave Anisotropy Probe (WMAP) Observations: Preliminary Maps and Basic Results. ApJS, 148:1–27, Sept. 2003.

[8] C. L. Bennett, R. S. Hill, G. Hinshaw, D. Larson, K. M. Smith, J. Dunkley, B. Gold, M. Halpern, N. Jarosik, A. Kogut, E. Komatsu, M. Limon, S. S. Meyer, M. R. Nolta, N. Odegard, L. Page, D. N. Spergel, G. S. Tucker, J. L. Weiland, E. Wollack, and E. L. Wright. Seven-year Wilkinson Microwave Anisotropy Probe (WMAP) Observations: Are There Cosmic Microwave Background Anomalies? ApJS, 192:17–+, Feb. 2011.

[9] J. Birch. The optical constants of some common low-loss polymers between 4 and 40 cm1. *Infrared Physics*, 21:225–228, July 1981.

[10] C. Bischoff, L. Hyatt, J. J. McMahon, G. W. Nixon, D. Samtleben, K. M. Smith, K. Vanderlinde, D. Barkats, P. Farese, T. Gaier, J. O. Gundersen, M. M. Hedman, S. T. Staggs, and B. Winstein. New Measurements of Fine-Scale CMB Polarization Power Spectra from CAPMAP at Both 40 and 90 GHz. ApJ, 684:771–789, Sept. 2008.

[11] J. Bock, S. Church, M. Devlin, G. Hinshaw, A. Lange, A. Lee, L. Page, B. Partridge, J. Ruhl, M. Tegmark, P. Timbie, R. Weiss, B. Winstein, and M. Zaldarriaga. Task Force on Cosmic Microwave Background Research. *ArXiv Astrophysics e-prints*, Apr. 2006.

[12] J. Bock, A. Cooray, S. Hanany, B. Keating, A. Lee, T. Matsumura, M. Milligan, N. Ponthieu, T. Renbarger, and H. Tran. The Experimental Probe of Inflationary

Cosmology (EPIC): A Mission Concept Study for NASA's Einstein Inflation Probe. *ArXiv e-prints*, May 2008.

[13] M. Born and E. Wolf. *Principles of Optics*. Oct. 1999.

[14] S. A. Bryan, T. E. Montroy, and J. E. Ruhl. Modeling dielectric half-wave plates for cosmic microwave background polarimetry using a Mueller matrix formalism. Appl. Opt., 49:6313–+, Nov. 2010.

[15] S. Chang and A. Prata. The Design of Classical Offset Dragonian Reflector Antennas With Circular Apertures. *IEEE Transactions on Antennas and Propagation*, 52:12–19, Jan. 2004.

[16] H. C. Chiang, P. A. R. Ade, D. Barkats, J. O. Battle, E. M. Bierman, J. J. Bock, C. D. Dowell, L. Duband, E. F. Hivon, W. L. Holzapfel, V. V. Hristov, W. C. Jones, B. G. Keating, J. M. Kovac, C. L. Kuo, A. E. Lange, E. M. Leitch, P. V. Mason, T. Matsumura, H. T. Nguyen, N. Ponthieu, C. Pryke, S. Richter, G. Rocha, C. Sheehy, Y. D. Takahashi, J. E. Tolan, and K. W. Yoon. Measurement of Cosmic Microwave Background Polarization Power Spectra from Two Years of BICEP Data. ApJ, 711:1123–1140, Mar. 2010.

[17] G. E. Childs, L. J. Ericks, and R. L. Powell. *Thermal Conductivity of Solids at Room Temperature and Below. A Review and Compilation of the Literature* . National Bureau of Standards, 1973.

[18] S. Das, T. A. Marriage, P. A. R. Ade, P. Aguirre, M. Amiri, J. W. Appel, L. F. Barrientos, E. S. Battistelli, J. R. Bond, B. Brown, B. Burger, J. Chervenak, M. J. Devlin, S. R. Dicker, W. Bertrand Doriese, J. Dunkley, R. Dünner, T. Essinger-Hileman, R. P. Fisher, J. W. Fowler, A. Hajian, M. Halpern, M. Hasselfield, C. Hernández-Monteagudo, G. C. Hilton, M. Hilton, A. D. Hincks, R. Hlozek, K. M. Huffenberger, D. H. Hughes, J. P. Hughes, L. Infante, K. D. Irwin, J. Baptiste Juin, M. Kaul, J. Klein, A. Kosowsky, J. M. Lau, M. Limon, Y.-T. Lin, R. H. Lupton, D. Marsden,

K. Martocci, P. Mauskopf, F. Menanteau, K. Moodley, H. Moseley, C. B. Netterfield, M. D. Niemack, M. R. Nolta, L. A. Page, L. Parker, B. Partridge, B. Reid, N. Sehgal, B. D. Sherwin, J. Sievers, D. N. Spergel, S. T. Staggs, D. S. Swetz, E. R. Switzer, R. Thornton, H. Trac, C. Tucker, R. Warne, E. Wollack, and Y. Zhao. The Atacama Cosmology Telescope: A Measurement of the Cosmic Microwave Background Power Spectrum at 148 and 218 GHz from the 2008 Southern Survey. ApJ, 729:62–+, Mar. 2011.

[19] S. Das, B. D. Sherwin, P. Aguirre, J. W. Appel, J. R. Bond, C. S. Carvalho, M. J. Devlin, J. Dunkley, R. Dünner, T. Essinger-Hileman, J. W. Fowler, A. Hajian, M. Halpern, M. Hasselfield, A. D. Hincks, R. Hlozek, K. M. Huffenberger, J. P. Hughes, K. D. Irwin, J. Klein, A. Kosowsky, R. H. Lupton, T. A. Marriage, D. Marsden, F. Menanteau, K. Moodley, M. D. Niemack, M. R. Nolta, L. A. Page, L. Parker, E. D. Reese, B. L. Schmitt, N. Sehgal, J. Sievers, D. N. Spergel, S. T. Staggs, D. S. Swetz, E. R. Switzer, R. Thornton, K. Visnjic, and E. Wollack. Detection of the Power Spectrum of Cosmic Microwave Background Lensing by the Atacama Cosmology Telescope. *Physical Review Letters*, 107(2):021301–+, July 2011.

[20] P. A. J. de Korte, J. Beyer, S. Deiker, G. C. Hilton, K. D. Irwin, M. Macintosh, S. W. Nam, C. D. Reintsema, L. R. Vale, and M. E. Huber. Time-division superconducting quantum interference device multiplexer for transition-edge sensors. *Review of Scientific Instruments*, 74:3807–3815, Aug. 2003.

[21] M. J. Devlin, S. R. Dicker, J. Klein, and M. P. Supanich. A high capacity completely closed-cycle 250 mK ˆ3He refrigeration system based on a pulse tube cooler. *Cryogenics*, 44:611–616, Sept. 2004.

[22] C. Dragone. Offset multireflector antennas with perfect pattern symmetry and polarization discrimination. *AT T Technical Journal*, 57:2663–2684, Sept. 1978.

[23] C. Dragone. Unique reflector arrangement within very wide field of view for multibeam antennas. *Electronics Letters*, 19:1061–+, Dec. 1983.

[24] J. Dunkley, A. Amblard, C. Baccigalupi, M. Betoule, D. Chuss, A. Cooray, J. Delabrouille, C. Dickinson, G. Dobler, J. Dotson, H. K. Eriksen, D. Finkbeiner, D. Fixsen, P. Fosalba, A. Fraisse, C. Hirata, A. Kogut, J. Kristiansen, C. Lawrence, A. M. Magalha˜Es, M. A. Miville-Deschenes, S. Meyer, A. Miller, S. K. Naess, L. Page, H. V. Peiris, N. Phillips, E. Pierpaoli, G. Rocha, J. E. Vaillancourt, and L. Verde. Prospects for polarized foreground removal. In S. Dodelson, D. Baumann, A. Cooray, J. Dunkley, A. Fraisse, M. G. Jackson, A. Kogut, L. Krauss, M. Zaldarriaga, & K. Smith , editor, *American Institute of Physics Conference Series*, volume 1141 of *American Institute of Physics Conference Series*, pages 222–264, June 2009.

[25] J. Dunkley, R. Hlozek, J. Sievers, V. Acquaviva, P. A. R. Ade, P. Aguirre, M. Amiri, J. W. Appel, L. F. Barrientos, E. S. Battistelli, J. R. Bond, B. Brown, B. Burger, J. Chervenak, S. Das, M. J. Devlin, S. R. Dicker, W. Bertrand Doriese, R. Dunner, T. Essinger-Hileman, R. P. Fisher, J. W. Fowler, A. Hajian, M. Halpern, M. Hasselfield, C. Hernandez-Monteagudo, G. C. Hilton, M. Hilton, A. D. Hincks, K. M. Huffenberger, D. H. Hughes, J. P. Hughes, L. Infante, K. D. Irwin, J. B. Juin, M. Kaul, J. Klein, A. Kosowsky, J. M. Lau, M. Limon, Y. Lin, R. H. Lupton, T. A. Marriage, D. Marsden, P. Mauskopf, F. Menanteau, K. Moodley, H. Moseley, C. B. Netterfield, M. D. Niemack, M. R. Nolta, L. A. Page, L. Parker, B. Partridge, B. Reid, N. Sehgal, B. Sherwin, D. N. Spergel, S. T. Staggs, D. S. Swetz, E. R. Switzer, R. Thornton, H. Trac, C. Tucker, R. Warne, E. Wollack, and Y. Zhao. The Atacama Cosmology Telescope: Cosmological Parameters from the 2008 Power Spectra. *ArXiv e-prints*, Sept. 2010.

[26] J. Dunkley, R. Hlozek, J. Sievers, V. Acquaviva, P. A. R. Ade, P. Aguirre, M. Amiri, J. W. Appel, L. F. Barrientos, E. S. Battistelli, J. R. Bond, B. Brown, B. Burger, J. Chervenak, S. Das, M. J. Devlin, S. R. Dicker, W. Bertrand Doriese, R. Dünner, T. Essinger-Hileman, R. P. Fisher, J. W. Fowler, A. Hajian, M. Halpern, M. Hasselfield, C. Hernández-Monteagudo, G. C. Hilton, M. Hilton, A. D. Hincks, K. M. Huffenberger, D. H. Hughes, J. P. Hughes, L. Infante, K. D. Irwin, J. B. Juin, M. Kaul,

J. Klein, A. Kosowsky, J. M. Lau, M. Limon, Y.-T. Lin, R. H. Lupton, T. A. Marriage, D. Marsden, P. Mauskopf, F. Menanteau, K. Moodley, H. Moseley, C. B. Netterfield, M. D. Niemack, M. R. Nolta, L. A. Page, L. Parker, B. Partridge, B. Reid, N. Sehgal, B. Sherwin, D. N. Spergel, S. T. Staggs, D. S. Swetz, E. R. Switzer, R. Thornton, H. Trac, C. Tucker, R. Warne, E. Wollack, and Y. Zhao. The Atacama Cosmology Telescope: Cosmological Parameters from the 2008 Power Spectrum. ApJ, 739:52–+, Sept. 2011.

[27] J. R. Eimer, P. A. R. Ade, D. J. Benford, C. L. Bennett, D. T. Chuss, D. J. Fixsen, A. J. Kogut, P. Mirel, C. E. Tucker, G. M. Voellmer, and E. J. Wollack. The Primordial Inflation Polarization Explorer (PIPER): optical design. In *Society of Photo-Optical Instrumentation Engineers (SPIE) Conference Series*, volume 7733 of *Society of Photo-Optical Instrumentation Engineers (SPIE) Conference Series*, July 2010.

[28] T. Essinger-Hileman, J. W. Appel, J. A. Beal, H. M. Cho, J. Fowler, M. Halpern, M. Hasselfield, K. D. Irwin, T. A. Marriage, M. D. Niemack, L. Page, L. P. Parker, S. Pufu, S. T. Staggs, O. Stryzak, C. Visnjic, K. W. Yoon, and Y. Zhao. The Atacama B-Mode Search: CMB Polarimetry with Transition-Edge-Sensor Bolometers. In B. Young, B. Cabrera, & A. Miller, editor, *American Institute of Physics Conference Series*, volume 1185 of *American Institute of Physics Conference Series*, pages 494–497, Dec. 2009.

[29] D. J. Fixsen, E. S. Cheng, J. M. Gales, J. C. Mather, R. A. Shafer, and E. L. Wright. The Cosmic Microwave Background Spectrum from the Full COBE FIRAS Data Set. ApJ, 473:576–+, Dec. 1996.

[30] J. W. Fowler, V. Acquaviva, P. A. R. Ade, P. Aguirre, M. Amiri, J. W. Appel, L. F. Barrientos, E. S. Battistelli, J. R. Bond, B. Brown, B. Burger, J. Chervenak, S. Das, M. J. Devlin, S. R. Dicker, W. B. Doriese, J. Dunkley, R. Dünner, T. Essinger-Hileman, R. P. Fisher, A. Hajian, M. Halpern, M. Hasselfield, C. Hernández-Monteagudo, G. C. Hilton, M. Hilton, A. D. Hincks, R. Hlozek, K. M. Huffenberger,

D. H. Hughes, J. P. Hughes, L. Infante, K. D. Irwin, R. Jimenez, J. B. Juin, M. Kaul, J. Klein, A. Kosowsky, J. M. Lau, M. Limon, Y.-T. Lin, R. H. Lupton, T. A. Marriage, D. Marsden, K. Martocci, P. Mauskopf, F. Menanteau, K. Moodley, H. Moseley, C. B. Netterfield, M. D. Niemack, M. R. Nolta, L. A. Page, L. Parker, B. Partridge, H. Quintana, B. Reid, N. Sehgal, J. Sievers, D. N. Spergel, S. T. Staggs, D. S. Swetz, E. R. Switzer, R. Thornton, H. Trac, C. Tucker, L. Verde, R. Warne, G. Wilson, E. Wollack, and Y. Zhao. The Atacama Cosmology Telescope: A Measurement of the 600 ell 8000 Cosmic Microwave Background Power Spectrum at 148 GHz. ApJ, 722:1148–1161, Oct. 2010.

[31] J. W. Fowler, W. B. Doriese, T. A. Marriage, H. T. Tran, A. M. Aboobaker, C. Dumont, M. Halpern, Z. D. Kermish, Y.-S. Loh, L. A. Page, S. T. Staggs, and D. H. Wesley. Cosmic Microwave Background Observations with a Compact Heterogeneous 150 GHz Interferometer in Chile. ApJS, 156:1–11, Jan. 2005.

[32] W. L. Freedman, B. F. Madore, B. K. Gibson, L. Ferrarese, D. D. Kelson, S. Sakai, J. R. Mould, R. C. Kennicutt, Jr., H. C. Ford, J. A. Graham, J. P. Huchra, S. M. G. Hughes, G. D. Illingworth, L. M. Macri, and P. B. Stetson. Final Results from the Hubble Space Telescope Key Project to Measure the Hubble Constant. ApJ, 553:47–72, May 2001.

[33] C. J. Glassbrenner and G. A. Slack. Thermal Conductivity of Silicon and Germanium from 3degK to the Melting Point. *Physical Review*, 134:1058–1069, May 1964.

[34] B. Gold, N. Odegard, J. L. Weiland, R. S. Hill, A. Kogut, C. L. Bennett, G. Hinshaw, X. Chen, J. Dunkley, M. Halpern, N. Jarosik, E. Komatsu, D. Larson, M. Limon, S. S. Meyer, M. R. Nolta, L. Page, K. M. Smith, D. N. Spergel, G. S. Tucker, E. Wollack, and E. L. Wright. Seven-Year Wilkinson Microwave Anisotropy Probe (WMAP) Observations: Galactic Foreground Emission. *ArXiv e-prints*, Jan. 2010.

[35] P. F. Goldsmith. *Quasioptical Systems: Guassian Beam Quasioptical Propagation and Applications*. IEEE Press, New York, 1998.

[36] D. H. Goldstein. *Polarized Light*. CRC Press, Boca Raton, FL, 2011.

[37] M. Halpern, H. P. Gush, E. Wishnow, and V. de Cosmo. Far infrared transmission of dielectrics at cryogenic and room temperatures - Glass, Fluorogold, Eccosorb, Stycast, and various plastics. Appl. Opt., 25:565–570, Feb. 1986.

[38] N. Hand, J. W. Appel, N. Battaglia, J. R. Bond, S. Das, M. J. Devlin, J. Dunkley, R. Dünner, T. Essinger-Hileman, J. W. Fowler, A. Hajian, M. Halpern, M. Hasselfield, M. Hilton, A. D. Hincks, R. Hlozek, J. P. Hughes, K. D. Irwin, J. Klein, A. Kosowsky, Y.-T. Lin, T. A. Marriage, D. Marsden, M. McLaren, F. Menanteau, K. Moodley, M. D. Niemack, M. R. Nolta, L. A. Page, L. Parker, B. Partridge, R. Plimpton, E. D. Reese, F. Rojas, N. Sehgal, B. D. Sherwin, J. L. Sievers, D. N. Spergel, S. T. Staggs, D. S. Swetz, E. R. Switzer, R. Thornton, H. Trac, K. Visnjic, and E. Wollack. The Atacama Cosmology Telescope: Detection of Sunyaev-Zel'Dovich Decrement in Groups and Clusters Associated with Luminous Red Galaxies. ApJ, 736:39–+, July 2011.

[39] R. Hlozek, J. Dunkley, G. Addison, J. W. Appel, J. R. Bond, C. Sofia Carvalho, S. Das, M. Devlin, R. Dünner, T. Essinger-Hileman, J. Fowler, P. Gallardo, A. Hajian, M. Halpern, M. Hasselfield, M. Hilton, A. D. Hincks, J. P. Hughes, K. Irwin, J. Klein, A. Kosowsky, T. A. Marriage, D. Marsden, F. Menanteau, K. Moodley, M. D. Niemack, M. R. Nolta, L. Page, L. Parker, B. Partridge, F. Rojas, N. Sehgal, B. Sherwin, J. Sievers, D. Spergel, S. Staggs, D. Swetz, E. Switzer, R. Thornton, and E. Wollack. The Atacama Cosmology Telescope: a measurement of the primordial power spectrum. *ArXiv e-prints*, May 2011.

[40] W. Hu and S. Dodelson. Cosmic Microwave Background Anisotropies. ARA&A, 40:171–216, 2002.

[41] E. Hubble. A Relation between Distance and Radial Velocity among Extra-Galactic Nebulae. *Proceedings of the National Academy of Science*, 15:168–173, Mar. 1929.

[42] K. D. Irwin and G. C. Hilton. Transition-Edge Sensors. In C. Enss, editor, *Cryogenic Particle Detection*. Springer.

[43] P. G. J. Irwin, P. A. R. Ade, S. B. Calcutt, F. W. Taylor, J. S. Seeley, R. Hunneman, and L. Walton. Investigation of dielectric spaced resonant mesh filter designs for PMIRR. *Infrared Physics*, 34:549–563, Dec. 1993.

[44] W. C. Jones, T. E. Montroy, B. P. Crill, C. R. Contaldi, T. S. Kisner, A. E. Lange, C. J. MacTavish, C. B. Netterfield, and J. E. Ruhl. Instrumental and analytic methods for bolometric polarimetry. A&A, 470:771–785, Aug. 2007.

[45] N. Katayama and E. Komatsu. Simple Foreground Cleaning Algorithm for Detecting Primordial B-mode Polarization of the Cosmic Microwave Background. ApJ, 737:78–+, Aug. 2011.

[46] J. B. Keller. Geometrical theory of diffraction. *Journal of the Optical Society of America (1917-1983)*, 52:116–+, Feb. 1962.

[47] E. M. Kennaugh and S. Adachi. The Analysis of a Broad-Band Circular Polarizer Including Interface Reflections. *IEEE Transactions on Microwave Theory Techniques*, 8:520–525, Sept. 1960.

[48] M. Kök and Y. Aydoğdu. The Thermal Conductivity Measurements of Solid Samples by Heat Flux Differantial Scanning Calorimetry. In S. A. Cetin & I. Hikmet, editor, *Sixth International Conference of the Balkan Physical Union*, volume 899 of *American Institute of Physics Conference Series*, pages 580–580, Apr. 2007.

[49] E. Komatsu, K. M. Smith, J. Dunkley, C. L. Bennett, B. Gold, G. Hinshaw, N. Jarosik, D. Larson, M. R. Nolta, L. Page, D. N. Spergel, M. Halpern, R. S. Hill, A. Kogut, M. Limon, S. S. Meyer, N. Odegard, G. S. Tucker, J. L. Weiland, E. Wollack, and E. L. Wright. Seven-Year Wilkinson Microwave Anisotropy Probe (WMAP) Observations: Cosmological Interpretation. *ArXiv e-prints*, Jan. 2010.

[50] J. M. Kovac, E. M. Leitch, C. Pryke, J. E. Carlstrom, N. W. Halverson, and W. L. Holzapfel. Detection of polarization in the cosmic microwave background using DASI. Nature, 420:772–787, Dec. 2002.

[51] M. Krejny, D. T. Chuss, G. Novak, G. M. Voellmer, E. J. Wollack, C. K. Walker, M. Jackson, D. J. Benford, J. G. Staguhn, S. H. Moseley, Jr., C. Kulesa, C. Y. Drouet d'Aubigny, D. R. Golish, and R. F. Loewenstein. The variable-delay polarization modulator. In *Society of Photo-Optical Instrumentation Engineers (SPIE) Conference Series*, volume 6275 of *Society of Photo-Optical Instrumentation Engineers (SPIE) Conference Series*, July 2006.

[52] J. W. Lamb. Infrared filters for cryogenic millimeterwave receivers. *International Journal of Infrared and Millimeter Waves*, 14:959–967, May 1993.

[53] J. W. Lamb. Miscellaneous data on materials for millimetre and submillimetre optics. *International Journal of Infrared and Millimeter Waves*, 17:1997–2034, Dec. 1996.

[54] D. Larson, J. Dunkley, G. Hinshaw, E. Komatsu, M. R. Nolta, C. L. Bennett, B. Gold, M. Halpern, R. S. Hill, N. Jarosik, A. Kogut, M. Limon, S. S. Meyer, N. Odegard, L. Page, K. M. Smith, D. N. Spergel, G. S. Tucker, J. L. Weiland, E. Wollack, and E. L. Wright. Seven-Year Wilkinson Microwave Anisotropy Probe (WMAP) Observations: Power Spectra and WMAP-Derived Parameters. *ArXiv e-prints*, Jan. 2010.

[55] J. Lau, M. Benna, M. Devlin, S. Dicker, and L. Page. Experimental tests and modeling of the optimal orifice size for a closed cycle ^{4}He sorption refrigerator. *Cryogenics*, 46:809–814, Nov. 2006.

[56] J. Lau, J. Fowler, T. Marriage, L. Page, J. Leong, E. Wishnow, R. Henry, E. Wollack, M. Halpern, D. Marsden, and G. Marsden. Millimeter-wave antireflection coating for cryogenic silicon lenses. Appl. Opt., 45:3746–3751, June 2006.

[57] J. M. Lau. *CCAM: A Novel Millimeter-Wave Instrument Using a Close-Packed TES Bolometer Array*. PhD thesis, Princeton University, New Jersey, 2007.

[58] E. M. Leitch, J. M. Kovac, N. W. Halverson, J. E. Carlstrom, C. Pryke, and M. W. E. Smith. Degree Angular Scale Interferometer 3 Year Cosmic Microwave Background Polarization Results. ApJ, 624:10–20, May 2005.

[59] J. Lekner. Reflection and refraction by uniaxial crystals. *Journal of Physics Condensed Matter*, 3:6121–6133, Aug. 1991.

[60] J. Lekner. Normal-incidence reflection and transmission by uniaxial crystals and crystal plates. *Journal of Physics Condensed Matter*, 4:1387–1398, Feb. 1992.

[61] A. R. Liddle and D. H. Lyth. *Cosmological Inflation and Large-Scale Structure*. Apr. 2000.

[62] T. A. Marriage, V. Acquaviva, P. A. R. Ade, P. Aguirre, M. Amiri, J. W. Appel, L. F. Barrientos, E. S. Battistelli, J. R. Bond, B. Brown, B. Burger, J. Chervenak, S. Das, M. J. Devlin, S. R. Dicker, W. B. Doriese, J. Dunkley, R. Dunner, T. Essinger-Hileman, R. P. Fisher, J. W. Fowler, A. Hajian, M. Halpern, M. Hasselfield, C. Hern'andez-Monteagudo, G. C. Hilton, M. Hilton, A. D. Hincks, R. Hlozek, K. M. Huffenberger, D. H. Hughes, J. P. Hughes, L. Infante, K. D. Irwin, J. B. Juin, M. Kaul, J. Klein, A. Kosowsky, J. M. Lau, M. Limon, Y. Lin, R. H. Lupton, D. Marsden, K. Martocci, P. Mauskopf, F. Menanteau, K. Moodley, H. Moseley, C. B. Netterfield, M. D. Niemack, M. R. Nolta, L. A. Page, L. Parker, B. Partridge, H. Quintana, E. D. Reese, B. Reid, N. Sehgal, B. D. Sherwin, J. Sievers, D. N. Spergel, S. T. Staggs, D. S. Swetz, E. R. Switzer, R. Thornton, H. Trac, C. Tucker, R. Warne, G. Wilson, E. Wollack, and Y. Zhao. The Atacama Cosmology Telescope: Sunyaev Zel'dovich Selected Galaxy Clusters at 148 GHz in the 2008 Survey. *ArXiv e-prints*, Oct. 2010.

[63] T. A. Marriage, J. Baptiste Juin, Y.-T. Lin, D. Marsden, M. R. Nolta, B. Partridge, P. A. R. Ade, P. Aguirre, M. Amiri, J. W. Appel, L. F. Barrientos, E. S. Battistelli, J. R. Bond, B. Brown, B. Burger, J. Chervenak, S. Das, M. J. Devlin, S. R. Dicker, W. Bertrand Doriese, J. Dunkley, R. Dünner, T. Essinger-Hileman, R. P. Fisher,

J. W. Fowler, A. Hajian, M. Halpern, M. Hasselfield, C. Hernández-Monteagudo, G. C. Hilton, M. Hilton, A. D. Hincks, R. Hlozek, K. M. Huffenberger, D. Handel Hughes, J. P. Hughes, L. Infante, K. D. Irwin, M. Kaul, J. Klein, A. Kosowsky, J. M. Lau, M. Limon, R. H. Lupton, K. Martocci, P. Mauskopf, F. Menanteau, K. Moodley, H. Moseley, C. B. Netterfield, M. D. Niemack, L. A. Page, L. Parker, H. Quintana, B. Reid, N. Sehgal, B. D. Sherwin, J. Sievers, D. N. Spergel, S. T. Staggs, D. S. Swetz, E. R. Switzer, R. Thornton, H. Trac, C. Tucker, R. Warne, G. Wilson, E. Wollack, and Y. Zhao. The Atacama Cosmology Telescope: Extragalactic Sources at 148 GHz in the 2008 Survey. ApJ, 731:100–+, Apr. 2011.

[64] T. A. Marriage, J. A. Chervenak, and W. B. Doriese. Testing and assembly of the detectors for the Millimeter Bolometric Array Camera on ACT. *Nuc Inst & Meth. in Phys Res A*, 559:551–553, 2006.

[65] J. C. Mather, D. J. Fixsen, R. A. Shafer, C. Mosier, and D. T. Wilkinson. Calibrator Design for the COBE Far-Infrared Absolute Spectrophotometer (FIRAS). ApJ, 512:511–520, Feb. 1999.

[66] T. E. Montroy, P. A. R. Ade, J. J. Bock, J. R. Bond, J. Borrill, A. Boscaleri, P. Cabella, C. R. Contaldi, B. P. Crill, P. de Bernardis, G. De Gasperis, A. de Oliveira-Costa, G. De Troia, G. di Stefano, E. Hivon, A. H. Jaffe, T. S. Kisner, W. C. Jones, A. E. Lange, S. Masi, P. D. Mauskopf, C. J. MacTavish, A. Melchiorri, P. Natoli, C. B. Netterfield, E. Pascale, F. Piacentini, D. Pogosyan, G. Polenta, S. Prunet, S. Ricciardi, G. Romeo, J. E. Ruhl, P. Santini, M. Tegmark, M. Veneziani, and N. Vittorio. A Measurement of the CMB EE Spectrum from the 2003 Flight of BOOMERANG. ApJ, 647:813–822, Aug. 2006.

[67] S. H. Moseley, E. Dwek, R. F. Silverberg, W. Glaccum, J. R. Graham, and R. F. Loewenstein. Far-infrared spectrophotometry of SN 1987A - Days 265 and 267. ApJ, 347:1119–1127, Dec. 1989.

[68] S. H. Moseley, A. Kutyrev, D. Rapchun, R. Silverberg, D. Sohl, and Microshutter Team. The Microshutter Array for JWST NIRSpec. In *American Astronomical Society Meeting Abstracts #213*, volume 41 of *Bulletin of the American Astronomical Society*, pages 426.06–+, Jan. 2009.

[69] B. A. Munk. *Frequency Selective Surfaces: Theory and Design.* John Wiley & Sons, New York, 2000.

[70] National Academy of Sciences. *NASA's Beyond Einstein Program: An Architecture for Implementation.* the National Academy of Sciences, 2007.

[71] National Research Council. *New Worlds, New Horizons in Astronomy and Astrophysics.* National Academies Press, 2010.

[72] L. B. Newburgh, B. C. UC, Caltech Collaboration, Columbia U. Collaboration, GSFC Collaboration, Harvard-Smithsonian CfA Collaboration, JPL Collaboration, U. C. C. Kavli Inst., S. U. C. Kavli Inst., U. Miami Collaboration, U. Oxford Collaboration, and Princeton U. Collaboration. QUIET: Q U Imaging Experiment for Detection of the CMBR Polarization. In *American Astronomical Society Meeting Abstracts*, volume 37 of *Bulletin of the American Astronomical Society*, pages 170.15–+, Dec. 2005.

[73] NIST. *Cryogenic Materials Properties.* The National Institute of Standards and Technology, 2011.

[74] R. W. Ogburn, IV, P. A. R. Ade, R. W. Aikin, M. Amiri, S. J. Benton, J. J. Bock, J. A. Bonetti, J. A. Brevik, B. Burger, C. D. Dowell, L. Duband, J. P. Filippini, S. R. Golwala, M. Halpern, M. Hasselfield, G. Hilton, V. V. Hristov, K. Irwin, J. P. Kaufman, B. G. Keating, J. M. Kovac, C. L. Kuo, A. E. Lange, E. M. Leitch, C. B. Netterfield, H. T. Nguyen, A. Orlando, C. L. Pryke, C. Reintsema, S. Richter, J. E. Ruhl, M. C. Runyan, C. D. Sheehy, Z. K. Staniszewski, S. A. Stokes, R. V. Sudiwala, G. P. Teply, J. E. Tolan, A. D. Turner, P. Wilson, and C. L. Wong. The BICEP2

CMB polarization experiment. In *Society of Photo-Optical Instrumentation Engineers (SPIE) Conference Series*, volume 7741 of *Society of Photo-Optical Instrumentation Engineers (SPIE) Conference Series*, July 2010.

[75] E. Pascale, P. A. R. Ade, J. J. Bock, E. L. Chapin, J. Chung, M. J. Devlin, S. Dicker, M. Griffin, J. O. Gundersen, M. Halpern, P. C. Hargrave, D. H. Hughes, J. Klein, C. J. MacTavish, G. Marsden, P. G. Martin, T. G. Martin, P. Mauskopf, C. B. Netterfield, L. Olmi, G. Patanchon, M. Rex, D. Scott, C. Semisch, N. Thomas, M. D. P. Truch, C. Tucker, G. S. Tucker, M. P. Viero, and D. V. Wiebe. The Balloon-borne Large Aperture Submillimeter Telescope: BLAST. ApJ, 681:400–414, July 2008.

[76] A. A. Penzias and R. W. Wilson. A Measurement of Excess Antenna Temperature at 4080 Mc/s. ApJ, 142:419–421, July 1965.

[77] L. Piccirillo, P. Ade, M. D. Audley, C. Baines, R. Battye, M. Brown, P. Calisse, A. Challinor, W. D. Duncan, P. Ferreira, W. Gear, D. M. Glowacka, D. Goldie, P. K. Grimes, M. Halpern, V. Haynes, G. C. Hilton, K. D. Irwin, B. Johnson, M. Jones, A. Lasenby, P. Leahy, J. Leech, S. Lewis, B. Maffei, L. Martinis, P. D. Mauskopf, S. J. Melhuish, C. E. North, D. O'Dea, S. Parsley, G. Pisano, C. D. Reintsema, G. Savini, R. V. Sudiwala, D. Sutton, A. Taylor, G. Teleberg, D. Titterington, V. N. Tsaneva, C. Tucker, R. Watson, S. Withington, G. Yassin, and J. Zhang. The ClOVER experiment. In *Society of Photo-Optical Instrumentation Engineers (SPIE) Conference Series*, volume 7020 of *Society of Photo-Optical Instrumentation Engineers (SPIE) Conference Series*, Aug. 2008.

[78] F. Pobell and J. Brooks. Matter and Methods at Low Temperatures. *Physics Today*, 45:116–+, 1992.

[79] S. Pufu. Optical Design for a new CMB polarization experiment. *Experimental Project, Princeton University*, 2008.

[80] A. G. Riess, L. Macri, S. Casertano, H. Lampeitl, H. C. Ferguson, A. V. Filippenko, S. W. Jha, W. Li, and R. Chornock. A 3% Solution: Determination of the Hubble Constant with the Hubble Space Telescope and Wide Field Camera 3. ApJ, 730:119–+, Apr. 2011.

[81] A. G. Riess, L. Macri, S. Casertano, M. Sosey, H. Lampeitl, H. C. Ferguson, A. V. Filippenko, S. W. Jha, W. Li, R. Chornock, and D. Sarkar. A Redetermination of the Hubble Constant with the Hubble Space Telescope from a Differential Distance Ladder. ApJ, 699:539–563, July 2009.

[82] B. Rulf. Transmission of microwaves through layered dielectrics-Theory, experiment, and application. *American Journal of Physics*, 56:76–80, Jan. 1988.

[83] G. Savini, G. Pisano, and P. A. R. Ade. Achromatic half-wave plate for submillimeter instruments in cosmic microwave background astronomy: modeling and simulation. Appl. Opt., 45:8907–8915, Dec. 2006.

[84] C. D. Sheehy, P. A. R. Ade, R. W. Aikin, M. Amiri, S. Benton, C. Bischoff, J. J. Bock, J. A. Bonetti, J. A. Brevik, B. Burger, C. D. Dowell, L. Duband, J. P. Filippini, S. R. Golwala, M. Halpern, M. Hasselfield, G. Hilton, V. V. Hristov, K. Irwin, J. P. Kaufman, B. G. Keating, J. M. Kovac, C. L. Kuo, A. E. Lange, E. M. Leitch, M. Lueker, C. B. Netterfield, H. T. Nguyen, R. W. Ogburn, IV, A. Orlando, C. L. Pryke, C. Reintsema, S. Richter, J. E. Ruhl, M. C. Runyan, Z. Staniszewski, S. Stokes, R. Sudiwala, G. Teply, K. L. Thompson, J. E. Tolan, A. D. Turner, P. Wilson, and C. L. Wong. The Keck Array: a pulse tube cooled CMB polarimeter. In *Society of Photo-Optical Instrumentation Engineers (SPIE) Conference Series*, volume 7741 of *Society of Photo-Optical Instrumentation Engineers (SPIE) Conference Series*, July 2010.

[85] B. D. Sherwin, J. Dunkley, S. Das, J. W. Appel, J. R. Bond, C. S. Carvalho, M. J. Devlin, R. Dünner, T. Essinger-Hileman, J. W. Fowler, A. Hajian, M. Halpern, M. Hasselfield, A. D. Hincks, R. Hlozek, J. P. Hughes, K. D. Irwin, J. Klein, A. Kosowsky,

T. A. Marriage, D. Marsden, K. Moodley, F. Menanteau, M. D. Niemack, M. R. Nolta, L. A. Page, L. Parker, E. D. Reese, B. L. Schmitt, N. Sehgal, J. Sievers, D. N. Spergel, S. T. Staggs, D. S. Swetz, E. R. Switzer, R. Thornton, K. Visnjic, and E. Wollack. Evidence for Dark Energy from the Cosmic Microwave Background Alone Using the Atacama Cosmology Telescope Lensing Measurements. *Physical Review Letters*, 107(2):021302–+, July 2011.

[86] M. Shimon, B. Keating, N. Ponthieu, and E. Hivon. CMB polarization systematics due to beam asymmetry: Impact on inflationary science. Phys. Rev. D, 77(8):083003–+, Apr. 2008.

[87] J. L. Sievers, C. Achermann, J. R. Bond, L. Bronfman, R. Bustos, C. R. Contaldi, C. Dickinson, P. G. Ferreira, M. E. Jones, A. M. Lewis, B. S. Mason, J. May, S. T. Myers, N. Oyarce, S. Padin, T. J. Pearson, M. Pospieszalski, A. C. S. Readhead, R. Reeves, A. C. Taylor, and S. Torres. Implications of the Cosmic Background Imager Polarization Data. ApJ, 660:976–987, May 2007.

[88] A. Sommerfeld. Mathematische Theorie der Diffraction. *Math. Ann*, 47:317–374, 1896.

[89] N. Suzuki, D. Rubin, C. Lidman, G. Aldering, R. Amanullah, K. Barbary, L. F. Barrientos, J. Botyanszki, M. Brodwin, N. Connolly, K. S. Dawson, A. Dey, M. Doi, M. Donahue, S. Deustua, P. Eisenhardt, E. Ellingson, L. Faccioli, V. Fadeyev, H. K. Fakhouri, A. S. Fruchter, D. G. Gilbank, M. D. Gladders, G. Goldhaber, A. H. Gonzalez, A. Goobar, A. Gude, T. Hattori, H. Hoekstra, E. Hsiao, X. Huang, Y. Ihara, M. J. Jee, D. Johnston, N. Kashikawa, B. Koester, K. Konishi, M. Kowalski, E. V. Linder, L. Lubin, J. Melbourne, J. Meyers, T. Morokuma, F. Munshi, C. Mullis, T. Oda, N. Panagia, S. Perlmutter, M. Postman, T. Pritchard, J. Rhodes, P. Ripoche, P. Rosati, D. J. Schlegel, A. Spadafora, S. A. Stanford, V. Stanishev, D. Stern, M. Strovink, N. Takanashi, K. Tokita, M. Wagner, L. Wang, N. Yasuda, and H. K. C. Yee. The Hubble Space Telescope Cluster Supernova Survey: V. Improving the Dark

Energy Constraints Above z1 and Building an Early-Type-Hosted Supernova Sample. *ArXiv e-prints*, May 2011.

[90] D. S. Swetz, P. A. R. Ade, M. Amiri, J. W. Appel, E. S. Battistelli, B. Burger, J. Chervenak, M. J. Devlin, S. R. Dicker, W. B. Doriese, R. Dünner, T. Essinger-Hileman, R. P. Fisher, J. W. Fowler, M. Halpern, M. Hasselfield, G. C. Hilton, A. D. Hincks, K. D. Irwin, N. Jarosik, M. Kaul, J. Klein, J. M. Lau, M. Limon, T. A. Marriage, D. Marsden, K. Martocci, P. Mauskopf, H. Moseley, C. B. Netterfield, M. D. Niemack, M. R. Nolta, L. A. Page, L. Parker, S. T. Staggs, O. Stryzak, E. R. Switzer, R. Thornton, C. Tucker, E. Wollack, and Y. Zhao. Overview of the Atacama Cosmology Telescope: Receiver, Instrumentation, and Telescope Systems. ApJS, 194:41–+, June 2011.

[91] Y. D. Takahashi, P. A. R. Ade, D. Barkats, J. O. Battle, E. M. Bierman, J. J. Bock, H. C. Chiang, C. D. Dowell, L. Duband, E. F. Hivon, W. L. Holzapfel, V. V. Hristov, W. C. Jones, B. G. Keating, J. M. Kovac, C. L. Kuo, A. E. Lange, E. M. Leitch, P. V. Mason, T. Matsumura, H. T. Nguyen, N. Ponthieu, C. Pryke, S. Richter, G. Rocha, and K. W. Yoon. Characterization of the BICEP Telescope for High-precision Cosmic Microwave Background Polarimetry. ApJ, 711:1141–1156, Mar. 2010.

[92] T. Timusk and P. L. Richards. Near millimeter wave bandpass filters. Appl. Opt., 20:1355–1360, Apr. 1981.

[93] H. Tran, B. Johnson, M. Dragovan, J. Bock, A. Aljabri, A. Amblard, D. Bauman, M. Betoule, T. Chui, L. Colombo, A. Cooray, D. Crumb, P. Day, C. Dickenson, D. Dowell, S. Golwala, K. Gorski, S. Hanany, W. Holmes, K. Irwin, B. Keating, C.-L. Kuo, A. Lee, A. Lange, C. Lawrence, S. Meyer, N. Miller, H. Nguyen, E. Pierpaoli, N. Ponthieu, J.-L. Puget, J. Raab, P. Richards, C. Satter, M. Seiffert, M. Shimon, B. Williams, and J. Zmuidzinas. Optical design of the EPIC-IM crossed Dragone telescope. In *Society of Photo-Optical Instrumentation Engineers (SPIE) Conference*

Series, volume 7731 of *Society of Photo-Optical Instrumentation Engineers (SPIE) Conference Series*, July 2010.

[94] H. Tran, A. Lee, S. Hanany, M. Milligan, and T. Renbarger. Comparison of the crossed and the Gregorian Mizuguchi-Dragone for wide-field millimeter-wave astronomy. Appl. Opt., 47:103–109, Jan. 2008.

[95] P. T. Tsilingiris. Comparative Evaluation of the Infrared Transmission of Polymer Films. *Energy Conversion and Management*, 711:2839–2856, 2003.

[96] C. E. Tucker and P. A. R. Ade. Thermal filtering for large aperture cryogenic detector arrays. In *Society of Photo-Optical Instrumentation Engineers (SPIE) Conference Series*, volume 6275 of *Society of Photo-Optical Instrumentation Engineers (SPIE) Conference Series*, July 2006.

[97] R. Ulrich. Effective low-pass filters for far infrared frequencies. *Infrared Physics*, 7:65–74, June 1967.

[98] R. Ulrich. Far-infrared properties of metallic mesh and its complementary structure. *Infrared Physics*, 7:37–50, Mar. 1967.

[99] L. B. Whitbourn and R. C. Compton. Equivalent-circuit formulas for metal grid reflectors at a dielectric boundary. Appl. Opt., 24:217–220, Jan. 1985.

[100] E. J. Wollack, D. T. Chuss, and S. H. Moseley. Electromagnetic considerations for pixellated planar bolometer arrays in the single-mode limit. In *Society of Photo-Optical Instrumentation Engineers (SPIE) Conference Series*, volume 6275 of *Society of Photo-Optical Instrumentation Engineers (SPIE) Conference Series*, July 2006.

[101] E. J. Wollack, D. J. Fixsen, R. Henry, A. Kogut, M. Limon, and P. Mirel. Electromagnetic and Thermal Properties of a Conductively Loaded Epoxy. *International Journal of Infrared and Millimeter Waves*, 29:51–61, Jan. 2008.

[102] J. H. P. Wu, J. Zuntz, M. E. Abroe, P. A. R. Ade, J. Bock, J. Borrill, J. Collins, S. Hanany, A. H. Jaffe, B. R. Johnson, T. Jones, A. T. Lee, T. Matsumura, B. Rabii, T. Renbarger, P. L. Richards, G. F. Smoot, R. Stompor, H. T. Tran, and C. D. Winant. MAXIPOL: Data Analysis and Results. ApJ, 665:55–66, Aug. 2007.

[103] K. W. Yoon, P. A. R. Ade, D. Barkats, J. O. Battle, E. M. Bierman, J. J. Bock, J. A. Brevik, H. C. Chiang, A. Crites, C. D. Dowell, L. Duband, G. S. Griffin, E. F. Hivon, W. L. Holzapfel, V. V. Hristov, B. G. Keating, J. M. Kovac, C. L. Kuo, A. E. Lange, E. M. Leitch, P. V. Mason, H. T. Nguyen, N. Ponthieu, Y. D. Takahashi, T. Renbarger, L. C. Weintraub, and D. Woolsey. The Robinson Gravitational Wave Background Telescope (BICEP): a bolometric large angular scale CMB polarimeter. In *Society of Photo-Optical Instrumentation Engineers (SPIE) Conference Series*, volume 6275 of *Society of Photo-Optical Instrumentation Engineers (SPIE) Conference Series*, July 2006.

[104] K. W. Yoon, J. W. Appel, J. E. Austermann, J. A. Beall, D. Becker, B. A. Benson, L. E. Bleem, J. Britton, C. L. Chang, J. E. Carlstrom, H. Cho, A. T. Crites, T. Essinger-Hileman, W. Everett, N. W. Halverson, J. W. Henning, G. C. Hilton, K. D. Irwin, J. McMahon, J. Mehl, S. S. Meyer, S. Moseley, M. D. Niemack, L. P. Parker, S. M. Simon, S. T. Staggs, K. U-Yen, C. Visnjic, E. Wollack, and Y. Zhao. Feedhorn-Coupled TES Polarimeters for Next-Generation CMB Instruments. In B. Young, B. Cabrera, & A. Miller, editor, *American Institute of Physics Conference Series*, volume 1185 of *American Institute of Physics Conference Series*, pages 515–518, Dec. 2009.

[105] M. Zaldarriaga. Polarization of the microwave background in reionized models. Phys. Rev. D, 55:1822–1829, Feb. 1997.

[106] M. Zaldarriaga. The Polarization of the Cosmic Microwave Background. *Measuring and Modeling the Universe*, pages 309–+, 2004.